

UNIVERSITÀ DELLA CALABRIA



UNIVERSITA' DELLA CALABRIA

Dipartimento di Fisica

Dottorato in Scienze e Tecnologie Fisiche, Chimiche e dei Materiali, in
convenzione con il CNR

CICLO XXXII

**Electronic structure investigation of Dirac materials and
layered semiconductors**

Settore Scientifico Disciplinare FIS/01

Coordinatore:

Prof.ssa Gabriella Cipparrone

 Firma oscurata in base alle linee
guida del Garante della privacy

Supervisore:

Dott.ssa Daniela Pacilé

 Firma oscurata in base alle linee
guida del Garante della privacy


Dottoranda:

Ilenia Grimaldi

Firma oscurata in base alle linee
guida del Garante della privacy

Co-supervisore:

Dott. Marco Papagno


Firma oscurata in base alle linee
guida del Garante della privacy

Contents	i
Introduction	1
Introduzione	4
1 Topological Insulators	9
1.1 Introduction	9
1.2 Experimental details	11
1.3 Structural and electronic properties	12
1.3.1 PbBi_4Te_7 and $\text{PbBi}_6\text{Te}_{10}$	13
1.3.2 PbBi_4Te_7 , SnBi_4Te_7 and $\text{PbBi}_4\text{Te}_6\text{Se}$	20
1.4 Robustness against contaminants	27
1.5 Conclusion	30
References	32
2 Graphene-based systems and heterostructures	37
2.1 Introduction	37
2.2 Graphene-based ferromagnetic junctions	38
2.2.1 Experimental details	38
2.2.2 Results and discussion	41
2.3 Silver <i>sp</i> -derived quantum well states between graphene and metallic substrates	46
2.3.1 Experimental details	47
2.3.2 Results and discussion	48
2.4 Electronic structure of graphene/ <i>4f</i> rare-earth/FM system	57
2.4.1 Experimental details	58
2.4.2 Results and discussion	58
References	62
3 III-VI layered semiconductors	68
3.1 Introduction	68
3.2 Structural investigation of III-VI layered semiconductors	69
3.2.1 Experimental details	69
3.2.2 Results and Discussion	70
3.3 Electronic investigation of InSe and GaSe layered semiconductors	76
3.3.1 Experimental details	77

3.3.2	Results and discussion	77
References	84
4	Black-Phosphorus and analogue materials	89
4.1	Introduction	89
4.2	TR-ARPES investigation of Black Phosphorus	90
4.2.1	Experimental details	91
4.2.2	Results and discussion	92
4.3	Electronic structure of SnSe, SnS and analogue materials	98
4.3.1	Experimental details	99
4.3.2	Results and discussion	99
References	103
Appendix		108
A	Basic principles of Angle-Resolved PhotoEmission Spectroscopy and Synchrotron Radiation	109
A.1	Introduction to PhotoEmission Spectroscopy	109
A.2	Angle-resolved Photoemission Spectroscopy	111
A.3	Experimental ARPES setup	115
A.4	Introduction to Synchrotron radiation	116
A.4.1	VUV beamline	119
A.4.2	APE beamline	120
A.5	Time-resolved ARPES Spectroscopy	120
A.5.1	Experimental TR-ARPES setup	121
A.5.2	ASTRA end station	122
References	124
Conclusions		125
List of Publications		127

An increasing number of materials displaying low-energy electronic excitations have emerged in the last decade. This rapid expansion has defined a new class of materials called "Dirac materials". The low energy quasi-particles, in this class of materials, move as if they had no mass and obeying the Dirac-like equation: massless Dirac particles. This behavior results in a completely new set of physical phenomena. One of the most important common feature of Dirac materials are the Dirac points that usually affect the response of material to external probes. They have captured the attention of the scientific community, mainly because they are perfect candidates for applications in quantum computers, spintronic devices due to their excellent transport properties and peculiar spin-texture. The benchmark of this class of materials is graphene, followed by silicene, germanene, hexagonal boron nitrite (h-BN), layered heterostructures. Dirac physics has been extended also to the non-trivial topological properties of materials such as Topological insulators (TIs), superconductors, Dirac and Weyl semimetals.

The interest on new materials went far beyond graphene; although graphene (and graphene-based systems) remains the cornerstone in both experimental and theoretical research, in the last years, many other members have joined, such as the 2D layered semiconductors. Small dimensionality (atomic thickness) is one of the most important request for future emerging technologies, which combined with high anisotropy, mechanical flexibility and optical transparency provide great opportunities for developing new optical and electronic devices. Most of them present also electron confinement effects which confer intriguing electronic properties. The two-dimensional nature makes them extremely sensitive to probe surface interactions; it represents also a unique opportunity to tune materials properties through surface modification and also to understand how contaminants can affect or degrade the material properties.

The electronic band dispersion is a keystone in identifying and understanding the proper-

ties of materials. Angle-Resolved PhotoEmission Spectroscopy (ARPES) is the most advanced spectroscopic method to probe electronic band dispersion, since it provides a direct measurement of energy and momentum of electrons in materials. In the last decades, the improvements in instrumentation allow to superior resolution (in both energy and momentum) and ARPES has become the best choice in band structure investigation, among all PhotoElectron Spectroscopies (PESs).

This thesis represents a summary of research accomplishments, work in progress, and future perspectives on ARPES investigation of different materials belonging to the class of Dirac materials and layered semiconductors. In this thesis I also wanted to include measurements and results on research-in-progress in order to give a complete overview of all the experimental investigations, I performed during my PhD. Most of the data reported in this thesis were acquired in Synchrotron Radiation facilities and by means of Angle-Resolved PhotoEmission Spectroscopy technique.

Outline of the thesis

The thesis is structured as follows:

- Chapter 1 is focused on the study of a new class of Topological Insulators (TIs). In particular, I focus the attention on the possibility to obtain a new class of *tunable* compounds, with different electronic properties. This has been attempted by controlling either the stoichiometry and the atomic composition of Topological Insulators. We provide a detailed comparative experimental and theoretical investigation, showing the high potential of this family of compounds for novel topological phenomena which require the tunability of Dirac states.
- In Chapter 2, I report the electronic band structure of different graphene-based systems. In the first part I report the results on the study of the magnetic coupling between different ferromagnetic metals, focusing mainly on understanding the role of graphene as a "screening" layer. I report also an ARPES study on the electron quantum confinement effects of Ag-film underneath a graphene layer; this investigation proves the possibility to create uniform films with well-defined electronic states under graphene. Then, a work in progress on the interaction between graphene and a $4f$ rare-earth metal is presented.
- Chapter 3 presents the results of the investigation on InSe and GaSe layered semiconductors; we started the analysis of this class of materials from the crystal structure and morphology, since their properties strongly depend on their structure. The second part deals with the electronic properties and main differences between InSe and GaSe; we focus on the study of the top valence band (crucial for optical and optoelectronic

applications) of the two compounds along main symmetry directions and on the effect of spin-orbit coupling and contribution of third group metals.

- Chapter 4 presents the results of the investigation on Black Phosphorus (BP), layered semiconductor. This material has attracted a great interest because of peculiar anisotropic structure and optoelectronic properties. We perform Time- and Angle-Resolved PhotoElectron Spectroscopy measurements with the aim to study out-of-equilibrium dynamics and to shed light on the electronic response to an ultrafast laser excitation. The effect of band gap renormalization is shown. Last part of the Chapter is devoted to a work in progress on BP analogous materials, such as SnSe, SnS and $\text{Pb}_{1-x}\text{Sn}_x\text{S}$ ($x=0.25, 0.5, 1$).
- The last part of this thesis, Appendix A, is devoted to the description of the experimental technique and set-up. I report basic fundamental aspects on Time- and Angle-Resolved PhotoEmission Spectroscopy and Synchrotron Light facilities.

The compilation of this thesis is exclusively to the author. The presented results are based on work carried out in collaboration with national and international research groups, which provided valuable support for my PhD.

The studies regarding Topological Insulators described in Chapter 1 were performed in collaboration with: Prof. Evgeny Chulkov¹ and Dr. Sergey V. Eremeev², which provided DFT calculations; Dr. Ziya S. Aliev³ and Dr. Mahammad B. Babanly⁴ which performed syntheses and characterization of the investigated samples; the research group lead by Dr. Carlo Carbone⁵; the group lead by Prof. Raffaele G. Agostino⁶; Dr. Marco Caputo⁷; Dr. Andrea Goldoni⁸, Dr. Jun Fujii⁸ and Dr. Ivana Vobornik⁸ of Elettra Synchrotron of Trieste.

The studies regarding graphene-based systems and heterostructures, reported in Chapter 2, were performed in collaboration with the research group lead by Dr. Carlo Carbone, with Dr. Luisa Ferrari⁹ and with the group lead by Dr. Gustav Bihlmayer¹⁰.

The studies regarding III-VI layered semiconductors, described in Chapter 3 were performed in collaboration with: Dr. Ida D. Perrotta, Dr. Federica Ciuchi, the group lead by Dr. Marco Castriota, from University of Calabria; the group lead by Dr. Carlo Carbone; Prof. Evgeny Chulkov, Dr. Sergey Eremeev; the group lead by Prof. Marco Gioni¹¹.

During my PhD, I had the opportunity to do a nine-month research period at Laboratory of Electron Spectroscopy (LSE) of École Polytechnique Fédérale de Lausanne. I greatly appreciate the support received from the group lead by Prof. Marco Gioni. The results of the joint measurements, in collaboration with the group lead by Dr. Luca Petaccia⁸, are reported in Chapter 4.

Finally, I greatly benefited from the support given by my supervisors, Dr. Daniela Pacilè⁶ and Dr. Marco Papagno⁶; by Dr. Alberto Crepaldi¹¹ and Dr. Oreste De Luca⁶. I would like to thank them for their suggestions and helpful criticism.

¹Donostia International Physics Center (DIPC) 20018 San Sebastián/Donostia, 20080, Basque Country, Spain - Departamento de Física de Materiales UPV/EHU, Centro de Física de Materiales CFM - MPC and Centro Mixto CSIC-UPV/EHU, San Sebastián/Donostia, 20080, Basque Country, Spain

²Institute of Strength Physics and Materials Science, 634055, Tomsk, Russia - Tomsk State University, 634050, Tomsk, Russia - Saint Petersburg State University, Saint Petersburg, 198504, Russia

³Azerbaijan State Oil and Industry University, AZ1010, Baku, Azerbaijan - Materials Science and Nanotechnology Department, Near East University, North Cyprus, Mersin 10, 99138, Nicosia, Turkey

⁴Institute Catalysis and Inorganic Chemistry, Azerbaijan National Academy of Science, AZ1143 Baku, Azerbaijan

⁵Istituto di Struttura della Materia, Consiglio Nazionale delle Ricerche, Trieste, Italy

⁶Dipartimento di Fisica, Università della Calabria, 87036 Arcavacata di Rende (Cs), Italy

⁷Swiss Light Source, Paul Scherrer Institute, CH-5232 Villigen-PSI, Switzerland

⁸Elettra Sincrotrone Trieste, s.s. 14 km 163.5 in Area Science Park, 34149 Trieste, Italy

⁹Istituto di Struttura della Materia, Consiglio Nazionale delle Ricerche, 00133 Roma, Italy

¹⁰Forschungszentrum Jülich GmbH, Peter Grünberg Institute (PGI-1 & PGI-7), 52425, Jülich, Germany - Forschungszentrum Jülich GmbH, JARA, Fundamentals of Future Information Technologies, 52425, Jülich, Germany - Forschungszentrum Jülich GmbH, Institute of Advanced Simulation (IAS-1), 52425, Jülich, Germany

¹¹Institute of Physics, École Polytechnique Fédérale de Lausanne (EPFL), CH-1015 Lausanne, Switzerland - Lausanne Centre for Ultrafast Science (LACUS), École Polytechnique Fédérale de Lausanne (EPFL), CH-1015 Lausanne, Switzerland

Un sempre crescente numero di materiali che mostrano eccitazioni elettroniche a bassa energia sono emersi nell'ultimo decennio. Questa rapida espansione ha definito una nuova classe di materiali chiamati "materiali di Dirac". Le quasi-particelle a bassa energia, in questa classe di materiali, si muovono come se non avessero massa e obbediscono all'equazione di Dirac: sono definite *massless Dirac particles*. Questo comportamento si traduce in una serie di fenomeni fisici completamente nuovi e di grande interesse. Una delle caratteristiche comuni più importanti di questa classe di composti sono i punti Dirac, i quali influenzano la risposta del materiale a perturbazioni esterne. Questi materiali hanno catturato l'attenzione della comunità scientifica, principalmente perché rappresentano i candidati perfetti per possibili applicazioni in computer quantistici e dispositivi spintronici grazie alle loro eccellenti proprietà di trasporto e alla particolare *spin-texture*. Il caposaldo di questa classe di materiali è certamente il grafene, seguito da silicene, germanene, nitrito di boro esagonale (h-BN) ed eterostrutture *layered*. La fisica di Dirac è stata estesa anche alle proprietà topologiche non-banali di materiali quali gli isolanti topologici (Topological Insulators - TIs), superconduttori, semimetalli di Dirac e di Weyl.

L'interesse per i nuovi materiali è andato ben oltre il grafene; sebbene il grafene (e i sistemi basati sul grafene) rimanga la pietra angolare della ricerca, sia sperimentale che teorica, negli ultimi anni, molti altri materiali si sono uniti, come i semiconduttori *layered* bidimensionali. La bassa dimensionalità (ci riferiamo a materiali 2D, con spessore atomico) è una delle richieste più importanti per le future tecnologie emergenti, che combinata all'elevata anisotropia, alla flessibilità meccanica e trasparenza ottica offrono grandi opportunità per lo sviluppo di nuovi dispositivi ottici ed elettronici. La maggior parte di essi presenta anche effetti di confinamento quantistico di elettroni che conferisce loro interessanti proprietà elettroniche. La natura bidimensionale, inoltre, li rende estremamente sensibili per sondare interazioni di superficie; offrono anche la possibilità di ottimizzare le proprietà dei materiali attraverso

modifiche della superficie e per capire come i contaminanti possono influenzarne le proprietà.

La struttura elettronica a bande è di fondamentale importanza nell'identificare e conoscere le proprietà dei materiali. *Angle-Resolved PhotoEmission Spectroscopy* (ARPES), ossia la spettroscopia di fotoemissione risolta in angolo, risulta essere la tecnica spettroscopica più avanzata per sondare la dispersione elettronica nei materiali, dal momento che fornisce simultaneamente una misura diretta dell'energia e del momento degli elettroni fotoemessi. Negli ultimi anni, i progressi tecnologici e miglioramenti della strumentazione hanno progressivamente portato a ottenere misure con risoluzione (in energia e momento) sempre più spinta, e la tecnica ARPES è divenuta così la scelta migliore per analizzare le strutture dei materiali.

Questa tesi rappresenta una raccolta dei principali lavori, pubblicati e in corso, sull'indagine ARPES effettuata su materiali di Dirac e semiconduttori *layered*. In questa tesi ho voluto includere misure e risultati ancora in corso al fine di fornire una panoramica completa di tutte le indagini sperimentali che ho svolto durante il mio dottorato. La maggior parte dei dati riportati in questa tesi sono stati acquisiti utilizzando principalmente la tecnica ARPES, presso il Sincrotrone Elettra di Trieste.

Struttura della tesi

Questa tesi è strutturata nel seguente modo:

- Il Capitolo 1 è incentrato sullo studio di una nuova classe di Isolanti Topologici. In particolare, ci siamo focalizzati sulla possibilità di ottenere una classe di composti le cui proprietà elettroniche (posizione del punto di Dirac, band gap, velocità di gruppo) siano tunabili. Questo è stato possibile mediante il controllo della stechiometria e della composizione atomica dei composti. In questo capitolo riporto uno confronto tra i risultati sperimentali e i calcoli DFT. La nostra indagine sperimentale mostra l'alto potenziale di questa famiglia di composti nella realizzazione di materiali topologici che richiedono la tunabilità degli stati di Dirac.
- Nel Capitolo 2, riporto la struttura elettronica a bande di diversi sistemi basati su grafene. Nella prima parte del capitolo, ho riportato lo studio dell'accoppiamento magnetico tra diversi metalli ferromagnetici, concentrandomi principalmente sulla comprensione del ruolo del grafene come mediatore dell'interazione di scambio. Riporto anche uno studio ARPES sugli effetti del confinamento quantico di elettroni del film Ag al di sotto di un layer di grafene; questa indagine dimostra la possibilità di creare film uniformi con stati elettronici ben definiti sotto il layer di grafene. Infine, presento delle misure preliminari sull'interazione tra grafene e substrato metallico mediata da intercalazione di terre rare.

-
- Il Capitolo 3 presenta i risultati dell'indagine su semiconduttori *layered* III-VI, InSe e GaSe; abbiamo iniziato lo studio di questa classe di materiali dalla struttura cristallina e dalla loro morfologia, poiché è noto che le loro proprietà dipendono fortemente dalla loro struttura. La seconda parte del capitolo è incentrata sulle proprietà elettroniche e sulle principali differenze tra i due semiconduttori, InSe e GaSe; la nostra analisi sperimentale si è focalizzata sullo studio del top della banda di valenza (la cui posizione e forma è cruciale per le applicazioni nel campo dell'optoelettronica) dei due composti lungo le principali direzioni di simmetria, sull'effetto dell'accoppiamento spin-orbita e sul contributo sulla struttura a bande del metallo del terzo gruppo.
 - Il Capitolo 4 presenta i risultati dell'indagine su *Black Phosphorus* (BP), semiconduttore *layered*. Questo materiale ha suscitato un grande interesse per via della peculiare struttura anisotropa e delle interessanti proprietà optoelettroniche. Abbiamo effettuato misure di spettroscopia fotoelettronica risolte in tempo (TR-ARPES) e angolo (ARPES) con l'obiettivo di estrarre e studiare la dinamica fuori dall'equilibrio e osservare la risposta elettronica a un'eccitazione laser ultraveloce. Sono stati osservati effetti dovuti al fenomeno della rinormalizzazione della *band gap*. L'ultima parte del capitolo è dedicata a un lavoro in corso su materiali con struttura analoga a BP, vale a dire SnSe, SnS e $\text{Pb}_{1-x}\text{Sn}_x\text{S}$ ($x=0.25, 0.5, 1$).
 - L'ultima parte della tesi, Appendice A, è incentrata sulla descrizione della tecnica e del set-up sperimentale. Ho riportato gli aspetti fondamentali delle tecniche di spettroscopia risolta in tempo (TR-ARPES) e angolo (ARPES), e sulla radiazione di Sincrotrone.

La compilazione di questa tesi è esclusivamente dell'autore. I risultati presentati si basano sul lavoro svolto in collaborazione con gruppi di ricerca nazionali e internazionali, che hanno fornito un prezioso supporto per il mio dottorato di ricerca.

Gli studi che riguardano gli Isolanti Topologici, descritti nel Capitolo 1 sono stati realizzati in collaborazione con il gruppo guidato dal Prof. Evgeny Chulkov¹² e con il Dr. Sergey V. Eremeev¹³, che hanno effettuato le simulazioni DFT; Dr. Ziya S. Aliev¹⁴ e Dr. Mahammad B. Babanly¹⁵ che hanno sintetizzato e caratterizzato i campioni analizzati; il gruppo guidato dal Dr. Carlo Carbone¹⁶; il gruppo guidato dal Prof. Raffaele G. Agostino¹⁷; Dr. Marco Caputo¹⁸; Dr. Andrea Goldoni¹⁹, Dr. Jun Fujii¹⁹ e Dr. Ivana Vobornik¹⁹ del Sincrotrone Elettra di Trieste.

Gli studi che riguardano sistemi ed eterostrutture basate su grafene, riportate nel Capitolo 2, sono stati effettuati in collaborazione con: il gruppo guidato dal Dr. Carlo Carbone, Dr. Luisa Ferrari²⁰ e il gruppo guidato dal Dr. Gustav Bihlmayer²¹.

Gli studi sui conduttori *layered* III-VI, descritti nel Capitolo 3, sono stati effettuati in collaborazione con: Dr. Ida D. Perrotta, Dr. Federica Ciuchi e il gruppo guidato dal Dr. Marco Castriota, dell'Università della Calabria; il gruppo guidato dal Dr. Carlo Carbone; Prof. Evgevy Chulkov, Dr. Sergey Eremeev; il gruppo guidato dal Prof. Marco Grioni²².

Durante il mio dottorato, ho avuto l'opportunità di fare un periodo di ricerca di nove mesi presso il Laboratory of Electron Spectroscopy (LSE) dell'École Polytechnique Fédérale de Lausanne. Ho beneficiato molto dell'esperienza trascorsa nel gruppo di ricerca guidato dal Prof. Marco Grioni. I risultati delle misurazioni congiunte, in collaborazione con il gruppo guidato dal Dr. Luca Petaccia¹⁹, sono riportati nel Capitolo 3.

Infine, ho beneficiato notevolmente del sostegno fornito dai miei supervisori, Dr. Daniela Pacilè¹⁷ e Dr. Marco Papagno¹⁷; dal Dr. Alberto Crepaldi²² e dal Dr. Oreste De Luca¹⁷. Vorrei ringraziarli per i loro preziosi suggerimenti e critiche costruttive.

¹²Donostia International Physics Center (DIPC) 20018 San Sebastián/Donostia, 20080, Basque Country, Spain - Departamento de Física de Materiales UPV/EHU, Centro de Física de Materiales CFM - MPC and Centro Mixto CSIC-UPV/EHU, San Sebastián/Donostia, 20080, Basque Country, Spain

¹³Institute of Strength Physics and Materials Science, 634055, Tomsk, Russia - Tomsk State University, 634050, Tomsk, Russia - Saint Petersburg State University, Saint Petersburg, 198504, Russia

¹⁴Azerbaijan State Oil and Industry University, AZ1010, Baku, Azerbaijan - Materials Science and Nanotechnology Department, Near East University, North Cyprus, Mersin 10, 99138, Nicosia, Turkey

¹⁵Institute Catalysis and Inorganic Chemistry, Azerbaijan National Academy of Science, AZ1143 Baku, Azerbaijan

¹⁶Istituto di Struttura della Materia, Consiglio Nazionale delle Ricerche, Trieste, Italy

¹⁷Dipartimento di Fisica, Università della Calabria, 87036 Arcavacata di Rende (Cs), Italy

¹⁸Swiss Light Source, Paul Scherrer Institute, CH-5232 Villigen-PSI, Switzerland

¹⁹Elettra Sincrotrone Trieste, s.s. 14 km 163.5 in Area Science Park, 34149 Trieste, Italy

²⁰Istituto di Struttura della Materia, Consiglio Nazionale delle Ricerche, 00133 Roma, Italy

²¹Forschungszentrum Jülich GmbH, Peter Grünberg Institute (PGI-1 & PGI-7), 52425, Jülich, Germany - Forschungszentrum Jülich GmbH, JARA, Fundamentals of Future Information Technologies, 52425, Jülich, Germany - Forschungszentrum Jülich GmbH, Institute of Advanced Simulation (IAS-1), 52425, Jülich, Germany

²²Institute of Physics, École Polytechnique Fédérale de Lausanne (EPFL), CH-1015 Lausanne, Switzerland - Lausanne Centre for Ultrafast Science (LACUS), École Polytechnique Fédérale de Lausanne (EPFL), CH-1015 Lausanne, Switzerland

In this chapter, a systematic investigation of the electronic band structure of a new family of three-dimensional topological insulators (TIs) is reported mainly by Angle-Resolved PhotoEmission Spectroscopy measurements. We proved that a tailoring of the topological states is made possible by controlling the variation of stoichiometry or atomic components through the replacement of heavy atoms. In order to unveil the effect of the stoichiometry, we report the investigation on two topological insulators with the same atomic composition but different atomic ratio. To shed light on the effect of the atomic composition, in the second part of the chapter, a detailed comparison of three topological insulators with the same ratio stoichiometry but different atomic composition is reported.

By means of Angle-Resolved PhotoEmission Spectroscopy, Scanning Tunnelling Microscopy and Density Functional Theory calculations we proved the existence of topological states deriving from different surface terminations, displaying distinct electronic band dispersion, different constant energy contours and Dirac point energies. Our measurements reveal also the presence of Rashba-like split states close to the Fermi level.

We also provide evidence that the electronic band structures of the investigated systems are almost *unaffected* by contaminants exposure making them good candidates for construction of novel TIs-based devices operating in environmental conditions.

1.1 Introduction

Topological insulators (TIs) have recently emerged as a new state of quantum matter. TIs are materials that are insulators in its interior but whose surface contains peculiar conduction states (Topological State: TS) with massless Dirac cone dispersion. In the bulk, topological insulators have the same electronic band structure of an ordinary band insulator, i.e. with the Fermi level falling between the conduction and valence bands; beyond that, on the surface there are special states that fall into the bulk energy gap and allow surface metallic conduction and continuously connect bulk conduction and valence bands [1–3]. These states show linear dispersing features, crossing the Fermi level, and forming a Dirac cone with a crossing point called Dirac point D_p . Surface carriers, in these states, have their spin locked at a right-angle

to their momentum (spin-momentum locking). This is interesting for several reasons, among them that this could allow for electrical manipulation of spins and spin currents. However, the conducting surface it is not referable only to topological insulators, since ordinary band insulators can also support conductive surface states. The main difference between TIs and ordinary band insulators is related to the topological distinction of these two classes of materials and we usually refer to them as trivial and non-trivial. The term *topological* here defines a bulk invariant (an integer which typically derived from the topology involved in the map from the momentum space to the energy spectrum given by the Hamiltonian of the system) which differentiates these phases of matter and classifies them accordingly [4].

Another intuitive way to get into topological insulators is to start from *Quantum Hall state* (QH), because it represents the simplest topologically ordered state. Basically, we can define QH as a state of the material in the presence of a magnetic field where the interior part is insulating and the edges are conducting. Unlike the QH effect, which is only seen when a strong magnetic field is present, TIs occur even in the absence of a magnetic field. In these materials, the role of the magnetic field is played by strong spin-orbit coupling (SOC). An important consequence of the SOC in TIs is the band inversion, in which the usual ordering of the conduction band and valence band is inverted by spin-orbit coupling. Such inversion is usually assumed to result from the band splitting at the Γ point. While some topological materials classes exist without spin-orbit coupling, many topological behaviours are related to SOC induced band inversion. Consequently, the search for new topological insulators is focused on materials with strong SOC due to heavy elements. However, the band inversion can also be induced by lattice strain, without any SOC, as reported in ref. [5].

The Dirac-like state and the peculiar spin-texture play an essential role in manipulating spin-polarization and spin-current of TI-based devices; the Dirac state position with respect to the bulk states and the shape of the Dirac cone can affect the conduction properties of the topological insulator. For practical applications, a fine tailoring of its properties (such as band gap, group velocity, the position of the Dirac point energy with respect to the Fermi level) is required. So far, the tuning or modification of the topological state has been attempted mainly by doping or intercalation, but with relevant modifications of the electronic band structure [6–11].

A number of materials have been theoretically proposed and experimentally confirmed as topological insulators, such as the well known $\text{Bi}_{1-x}\text{Sb}_x$, Bi_2Te_3 , Bi_2Se_3 . Motivated by their peculiar electronic properties and future possible applications, the search of new topological insulators has been extended to ternary/quaternary compounds.

In contrast to the well known binary compounds (Bi_2Se_3 , Bi_2Te_3) [12–15], composed by five atomic planes (Te(Se)-Bi-Te(Se)-Bi-Te(Se)) to form quintuple layers (QL), the ternary/quaternary compounds have a tetradymitelike layered structures including sequences of quintuple and septuple blocks (SL). Each block is characterized by covalent bonding between the atoms of the basal plane and van der Waals interlayer bonding between adjacent blocks [16–18]. By varying the sequence of the blocks within the crystal¹ it is possible to modify the topological

¹"Varying the sequence of the blocks" stands for varying the stoichiometry of the compound in order to obtain different structural properties.

insulator electronic and structural properties.

Another possibility to take control over the TIs electronic properties relies on the variation of the atomic composition, in particular by the replacements of heavy atoms by lighter isoelectronic ones. Such variation involves a change in the electronic position of the Dirac point with respect to the Fermi level and consequently their related electronic properties [19–21]. This procedure suggests the efficient possibility of controlling the conduction states of this class of materials.

In this context, we have performed a systematic comparative investigation of the electronic band structure of a new family of three-dimensional topological insulators by means Angle-Resolved PhotoEmission Spectroscopy (ARPES) investigations. ARPES is the ideal experimental tool to study the electronic structure, as it gives direct measure of the spectral weight function, providing information about band dispersion, constant energy surfaces, energy electronic gaps, and quasi-particle excitations in solids.

In order to unveil the effect of the stoichiometry, we first report ARPES results on Pb-based TIs with the same atomic composition (Pb, Bi, Te) but different atomic ratio: PbBi_4Te_7 and $\text{PbBi}_6\text{Te}_{10}$. The presented results are supported by Density Functional Theory calculations (DFT) and Scanning Tunneling Microscopy (STM) measurements.

In the second part of the chapter, we report the electronic band structure of $A^{IV}\text{Bi}_4\text{Te}_{7-x}\text{Se}_x$ ($A^{IV} = \text{Sn, Pb}$; $x=0, 1$) TIs having the same atomic ratio stoichiometry (1:4:7) but different atomic composition.

1.2 Experimental details

Sample growth and X-ray diffraction (XRD) characterization were done by Ziya S. Aliev at Azerbaijan State Oil and Industry University. Single crystalline ingots of the TIs (i) $\text{PbBi}_6\text{Te}_{10}$, (ii) PbBi_4Te_7 , (iii) SnBi_4Te_7 and (iv) $\text{PbBi}_4\text{Te}_6\text{Se}$ were grown from non-stoichiometric composition by the vertical Bridgman-Stockbarger technique. The synthesis was performed into two steps. At first, the polycrystalline composition was synthesized from high purity (5N) elements in evacuated quartz ampoule at about 1000 K for 8 h mixing incessantly, followed by air cooling. The as obtained polycrystalline samples are then placed in a conical-bottom quartz ampoule, which was sealed under vacuum better than 10^{-4} Pa. At the beginning of the growing process, the ampoule was held in the "hot" zone (at about ~ 900 K) of a specially designed two-zone tube furnace for 24 hours for a complete melting of the composition. The charged ampoule moves from the "hot" zone to the narrow "cold" one with the required rate of 1 mm per hour. In this way, layered single crystal was obtained, with the average dimensions of about 4 cm in length and 0.8 cm of diameter. The high quality of the as-grown ingot was accurately checked by XRD preliminary measurements.

The experiments on PbBi_4Te_7 and $\text{PbBi}_6\text{Te}_{10}$ samples were performed ad APE-IOM beamline of the Elettra Synchrotron of Trieste (see section A.4.2 for the beamline experimental set-up description). ARPES investigations were carried out in the photon energy range of 15 - 60 eV at low temperature (77 K) and with a base pressure below 1×10^{-10} Torr. Core level photoemission measurements have been recorded at RT using 830 eV, 700 eV and

370 eV oh photon energies. STM measurements were carried out by using a home-built room-temperature microscope at room temperature and in UHV condition (base pressure of 1×10^{-10} mbar). All the STM acquired images were processed using the WSxM software (8.3 version).

The photoemission experiments performed on SnBi_4Te_7 and $\text{PbBi}_4\text{Te}_6\text{Se}$ were collected at the VUV-Photoemission beamline of the Elettra synchrotron radiation facility in Trieste (see section A.4.1 for the beamline experimental set-up description). ARPES and core level photoemission measurements were performed at RT. The energy and angular resolution of ARPES were set to 15 meV and 0.3° , respectively.

All presented measurements were performed on fresh mirror-like surfaces obtained by cleavage *in-situ* at room temperature and in UHV conditions (base pressure of 1×10^{-11} mbar), just before the ARPES measurements. The high quality of the achieved (111) surfaces were verified and confirmed by the 1×1 sharp features in the low-energy electron diffraction (LEED) pattern. All the spectra were recorded within 12 hours after cleavage and *aging* effects were monitored over time. To unveil possible contaminants at the surface, we performed core level photoemission measurements before and after the ARPES investigations.

The ARPES results have been compared with electronic structure calculations, provided by Evgueni Chulkov and Sergey V. Eremeev. The DFT calculations were performed by using the Vienna Ab initio Simulation Package (VASP) [22, 23], with core electrons represented by projector augmented wave (PAW) potentials [24, 25] with the generalized gradient approximation [26] to the exchange correlation (XC) potential. To take into account the effect of dispersion interactions and for structure optimization, DFT-D3 van der Waals correction [27] was applied. Spin-orbit interaction (SOI) was included in structure optimization and electronic band calculations. To simulate surfaces of $A^{IV}\text{Bi}_4\text{Te}_{7-n}\text{Se}_n$ ($A^{IV} = \text{Sn, Pb}; n=0, 1$) compounds composed by alternating QL and SL blocks we used asymmetric slabs with QL and SL terminations on the opposite surfaces.

1.3 Structural and electronic properties

In Fig. 1.1 the crystal structure of $\text{PbBi}_6\text{Te}_{10}$, PbBi_4Te_7 is reported. The pink and yellow balls correspond to Bi and Te atoms, while the grey balls stand for Pb atoms. The crystal structure of the SnBi_4Te_7 and $\text{PbBi}_4\text{Te}_6\text{Se}$ is similar to the one here depicted for PbBi_4Te_7 . For the SnBi_4Te_7 sample the substitution of Pb with Sn occurs, while for $\text{PbBi}_4\text{Te}_6\text{Se}$ in the central atomic layer of the QL block, one Te atom is replaced by Se atom. The crystal structure of the compounds with stoichiometry ratio 1:4:7 has hexagonal primitive cell with alternating stacking of one quintuple (QL), Te-Bi-Te-Bi-Te, and one septuple layer (SL) block, Te-Bi-Te-Pb-Te-Bi-Te [21, 28]. The crystal structure of $\text{PbBi}_6\text{Te}_{10}$ with stoichiometry ratio 1:6:10 has hexagonal crystal structure but it consists of alternate stacking of two types of five-layer blocks (QL₁ and QL₂), and one seven-layer block. In these compounds, QLs and SLs blocks are bonded together by van der Waals forces and each atomic layer has only one hexagonal arranged type of atom (Te, Bi or Pb). Because of the weak interaction between the blocks, each crystal can be easily cleaved and the surface exposed after cleavage have therefore two

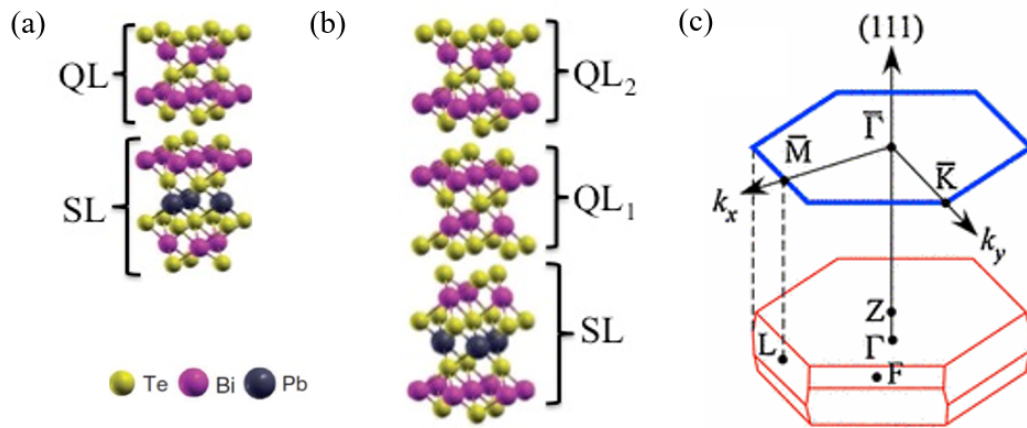


Figure 1.1: Atomic structure of (a) PbBi_4Te_7 and (b) $\text{PbBi}_6\text{Te}_{10}$. The blocks are separated each other by van der Waals gap. (c) The bulk (red lines) and the corresponding (111) surface (blue lines) Brillouin zone.

or three possible terminations, QL (QL 1 or 2) or SL blocks [18].

During ARPES experiments, all surface blocks are illuminated at the same time since the average size of the surface terraces (about 10^4 nm^2) are typically smaller than the beam spot of conventional apparatus (about $100 \mu\text{m}$); therefore, since each surface state supports a Dirac cone, the band structure of different surface terminations is captured at the same time during the photoemission experiment.

1.3.1 PbBi_4Te_7 and $\text{PbBi}_6\text{Te}_{10}$

In Fig. 1.2 the representative topographic images of fresh cleaved (111) surface of PbBi_4Te_7 - panel (a)- and $\text{PbBi}_6\text{Te}_{10}$ - panel (b)- is reported. The line profile along the grey line extracted from panel (a) of Fig. 1.2 and reported in panel (c), confirms that, in the case of PbBi_4Te_7 , the topmost surface after cleavage can be QL or SL-termination. The two blocks have different step heights of about 1.2 and 1.7 nm, respectively. These two terminated blocks always alternate themselves in a QL-SL-QL-SL... sequence. The crystal structure of $\text{PbBi}_6\text{Te}_{10}$ is slightly more complex. The line profile, extracted from panel (b) of Fig. 1.2 and displayed in panel (d), clearly evidences the presence of two different steps: two quintuple-layers (QL_1 and QL_2) and one septuple layer block. The calculated step height is 1.2 nm for QL_1 and QL_2 , and 1.7 nm for the SL block. The three blocks alternate themselves according to the QL_1 - QL_2 -SL sequence [18].

Fig. 1.3 presents the measured electronic band structure along the $\text{M}\bar{\Gamma}\text{K}$ direction of the first Brillouin zone of PbBi_4Te_7 and $\text{PbBi}_6\text{Te}_{10}$. All surface layered blocks are illuminated simultaneously during the ARPES experiments, and thus the band structure of different surface terminations is captured at the same time. For both compounds, the topological states have been labeled by comparison with DFT calculation, which will be discussed later in the text and reported in the Figs. 1.7 and 1.8.

In panel (a) of Fig. 1.3 we can observe two well-defined and distinct topological states, labeled QL- and SL-term of PbBi_4Te_7 ; these two features are due to QL- and SL- terminations,

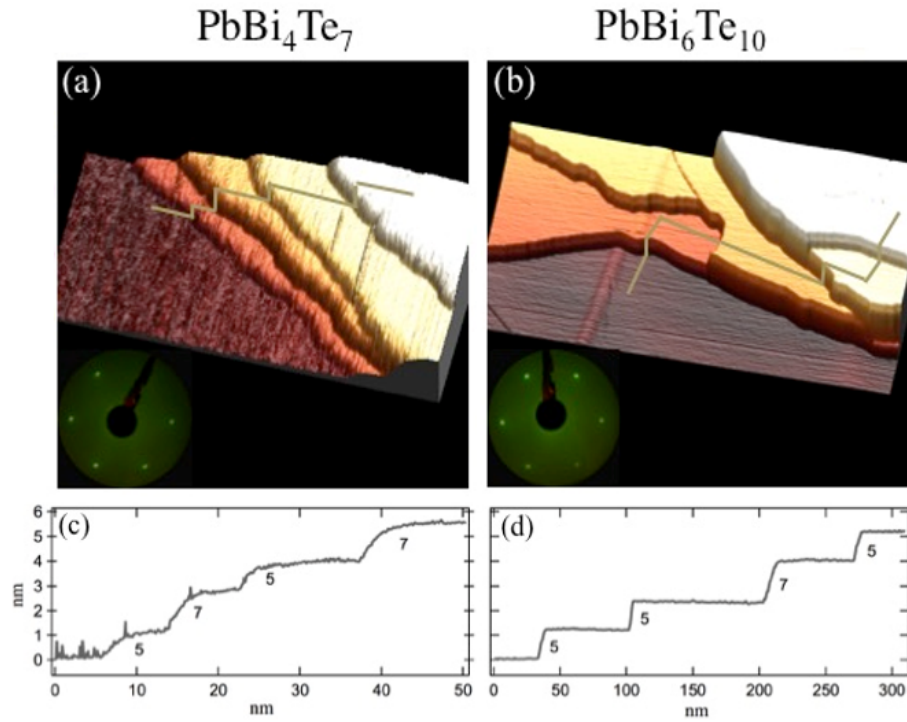


Figure 1.2: Constant-current STM image of fresh cleaved (111) surface of (a) PbBi_4Te_7 and (b) $\text{PbBi}_6\text{Te}_{10}$ ($V_B=1.0$ V; $I_t=0.2$ nA; $T=300$ K; size 400 nm \times 200 nm). The line profiles in panels (c) and (d) represent the apparent height profiles of surfaces extracted from panels (a) and (b) respectively. The inset of panels (a) and (b) show the low-energy electron diffraction patterns of the topological insulators collected with 55 eV of electron beam

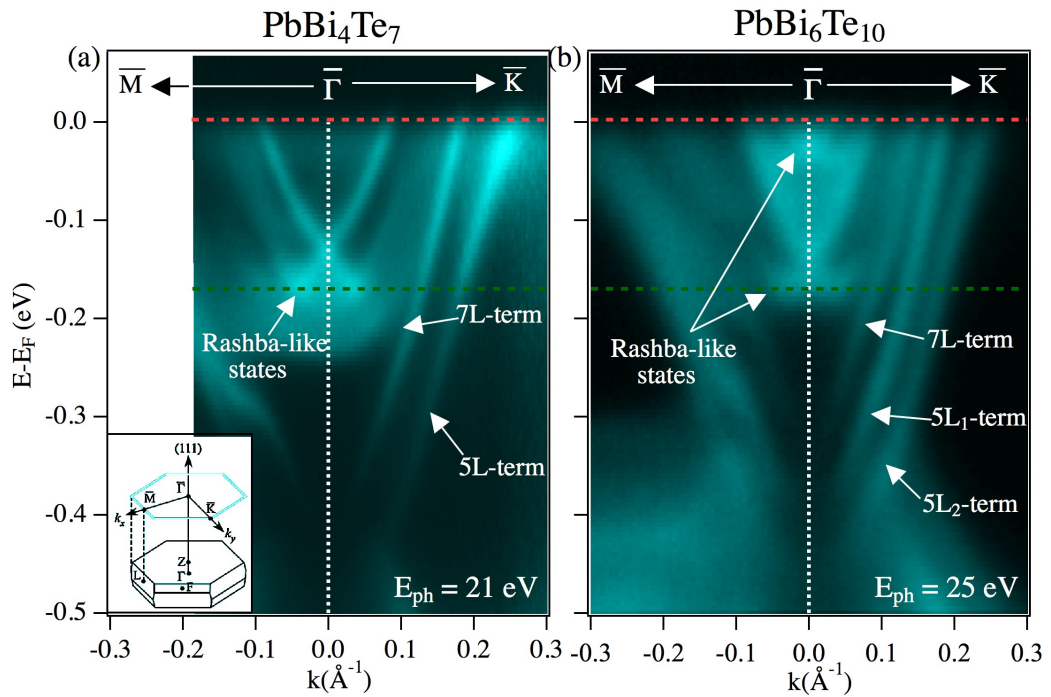


Figure 1.3: ARPES band structure for (a) PbBi_4Te_7 and (b) $\text{PbBi}_6\text{Te}_{10}$ along the $\text{M}\bar{\Gamma}\text{K}$ direction of the first Brillouin zone (shown in the inset of panel (a)) performed at 21 eV and 25 eV of photon energy, respectively. Dotted red and green lines in panels indicate the binding energy of the constant energy cuts reported in Fig.1.4.

respectively [17]. In the ARPES spectrum of $\text{PbBi}_6\text{Te}_{10}$, in Fig. 1.3(b), we can observe three distinctive and defined Dirac cone like states, labeled QL_1 , QL_2 and SL as the compound possesses three different surface terminations, each one supporting a Dirac state.

The topological surface states of both compounds present almost linear dispersion along the ΓK direction up to the Fermi level, whereas along ΓM they present a change in Dirac cone slope of the inner features: this is due to rhombohedral crystal structure [18].

For $\text{PbBi}_6\text{Te}_{10}$, the warping of the topological states are observed at $k_{\parallel} = -0.10 \text{ \AA}^{-1}$ and at about 0.26 eV of binding energy for the QL- terminated surface and at $k_{\parallel} = -0.08 \text{ \AA}^{-1}$ and about 0.2 eV of binding energy for the SL- state. The warping in PbBi_4Te_7 is observed for the SL- term at $k_{\parallel} = -0.08 \text{ \AA}^{-1}$ and $\simeq 0.30$ eV of binding energy.

The SL terminated surface for both compounds is well resolved, allowing an easy estimation of the Dirac point position: for $\text{PbBi}_6\text{Te}_{10}$ the $D_p(\text{SL})$ is located at $\simeq 0.36$ eV and for PbBi_4Te_7 we have $D_p(\text{SL})$ at $\simeq 0.45$ eV of binding energy. Due to the overlapping of the topological state with the valence band, the determination of the Dirac point of the outer Dirac cones can be estimated by linear interpolation of the data; we estimate that the $D_p(\text{QL}_2)$ is at about 0.48 eV for $\text{PbBi}_6\text{Te}_{10}$ and $D_p(\text{QL})$ at about 0.55 eV for PbBi_4Te_7 below the Fermi level. The topological states display similar group velocity of the Dirac Fermions close to the Fermi level. By momentum distribution curves (MDCs) fitting, we estimate the group velocity along ΓK direction for each feature of the $\text{PbBi}_6\text{Te}_{10}$ compound and we obtain $v_g(\text{QL}_1) \simeq 5.3 \times 10^5$ m/s, $v_g(\text{QL}_2) \simeq 4.8 \times 10^5$ m/s and $v_g(\text{SL}) \simeq 4.5 \times 10^5$ m/s. Similar values have been obtained for both surface terminations of the PbBi_4Te_7 compound. The hallmark of the observed topological states (band dispersion, Dirac point energy, group velocity, and kink like structure) are in perfect agreement with earlier studies [17, 18, 29].

In Fig. 1.3(b) for $\text{PbBi}_6\text{Te}_{10}$ TI, we observe diffuse photoemission intensity at about 20 meV below the Fermi level at the Γ point, which is assigned to the bottom of the conduction band.

In Fig. 1.4 the constant energies contours are reported for different binding energies. These maps reveal the nature of the TSs. The energy contours are very similar for both compounds. The external structures present an almost hexagonal shape, while the inner ones have the peculiar *snowflakes* pattern for energies between the Fermi level down to about 200 meV of binding energy (Fig. 1.4 panels A-D). The *snowflakes* contour, which reflects the 6-fold symmetry of these systems, progressively turns into a circular shape centered at Γ point: this change of the energy contour shape highlights the warping of the more internal structures, in analogy with similar compounds.

In addition to the topological states, ARPES measurements reported in Fig. 1.3 reveal Rashba-like states for both samples at the zone center and in the energy region between Fermi level and $\simeq 0.20$ eV of binding energy. These states have parabolic dispersion with a minimum located at 0.17 eV of binding energy and momentum offset of $\pm k_0$ with $k_0 = 0.035 \text{ \AA}^{-1}$; the origin of the aforementioned states have already been widely studied in Ref. [18]. The estimated Rashba energy and coupling constant have approximately the same values for both topological insulators ($\simeq 0.03$ eV and $\simeq 1.7 \text{ eV \AA}^{-1}$, respectively), in agreement with earlier measurements [17, 18].

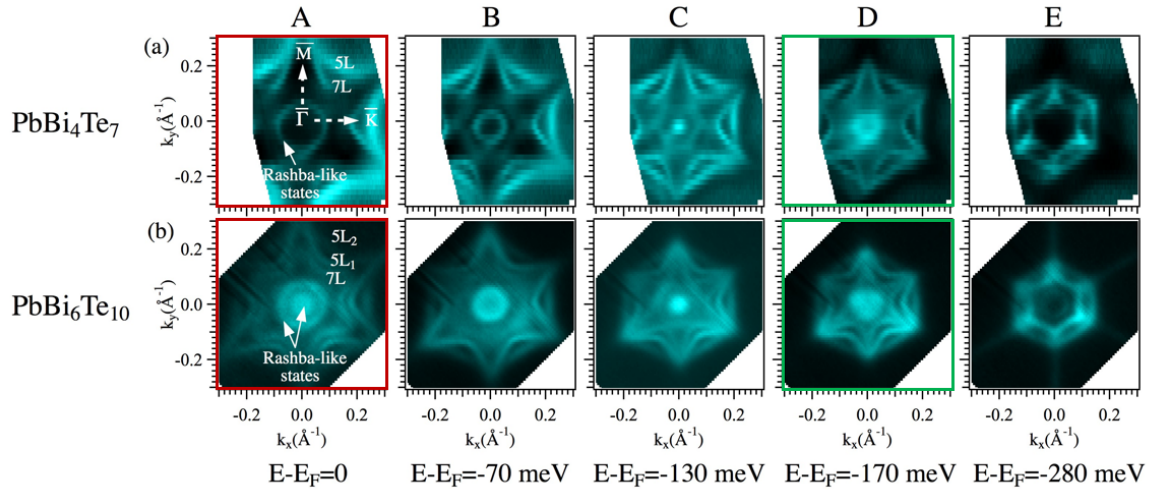


Figure 1.4: Constant energy cuts for PbBi_4Te_7 (a) and $\text{PbBi}_6\text{Te}_{10}$ (b) at different binding energies.

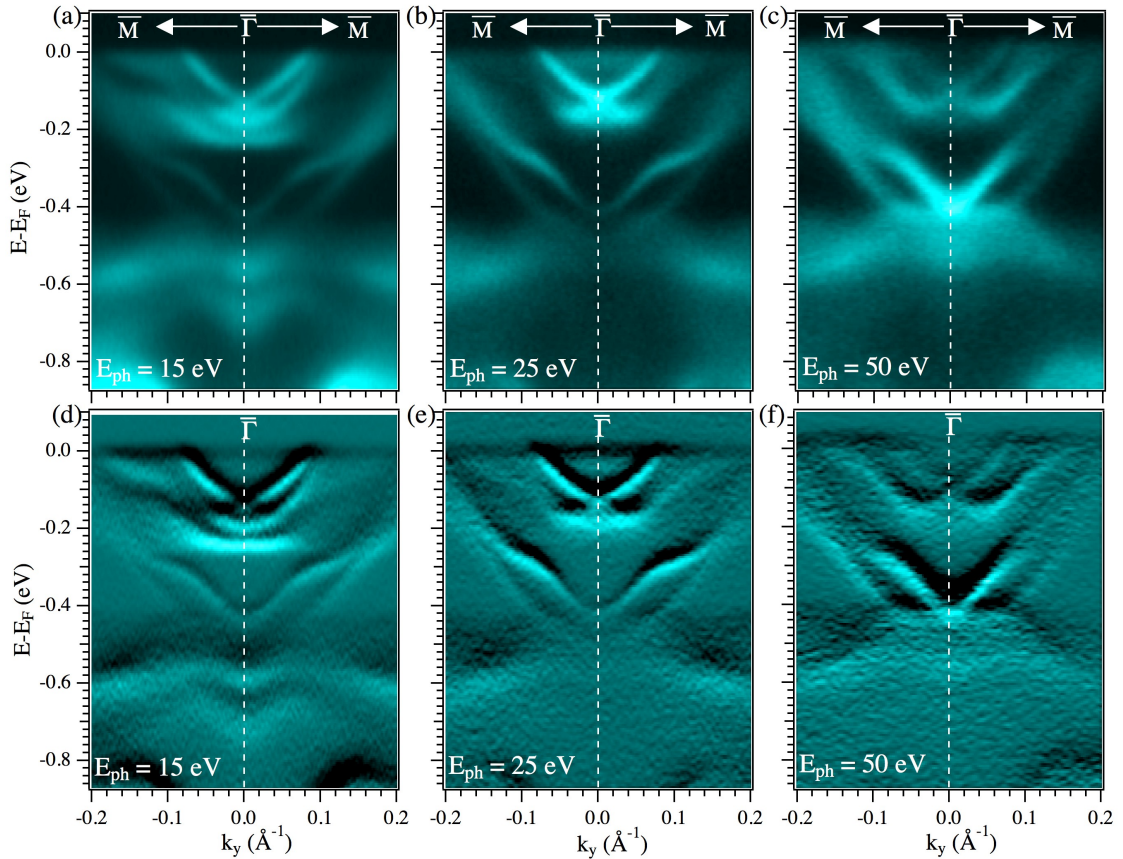


Figure 1.5: Electronic states of PbBi_4Te_7 along the ΓM direction for (a) 15 eV, (b) 25 eV and (c) 50 eV of photon energies and the same spectra differentiated along the energy axis in panels (d), (e) and (f), respectively.

The spectra reported in Fig. 1.5, panels (a)-(c), show the band structure of PbBi_4Te_7 along the ΓM direction of the first Brillouin zone detected at different photon energies, i.e. (a) 15 eV, (b) 25 eV and (c) 50 eV, respectively. In order to better resolve the topological states features, in panels (d), (e) and (f) of Fig.1.5 we present also the corresponding second derivatives along the binding energy axis. The present measurements prove that both the topological states and the Rashba-like states do not vary with the photon energy, evidencing a poor k_z dispersion of the observed features.

In addition, at deeper binding energy (in the energy range of 0.4 - 0.7 eV), we see the M-shaped bulk band structure for both topological insulators. Such M-shaped replicated bands in the valence band spectra are due to an intrinsic quantization effects of the electronic states [8, 30–33], and are also been observed for similar parental compound, such as $\text{PbBi}_4\text{Te}_4\text{S}_3$ [34].

As mentioned before, while the presence of the topological states is due to the different surface terminations of the crystal, the origin of the observed Rashba-like states² is less clear. These states can arise because of the *aging effect* of the sample or due to van der Waals gaps. The *aging effect* is related to donor-type contaminants adsorbed on surface during the ARPES experiments on the n -doped TIs. The contaminated surface can result in a sort of "donor-type" surface state that induces spatial regions of space charge or screening charges which can extend tens of Å into the crystal. If the redistribution of screening charges is strong enough, the conduction band minimum crosses the Fermi level and produces a downward band bending (eV_{bb}) and a plasma of electrons within the space charge region. However, this free-electron gas is trapped by the band bending potential V_{bb} and it results in quantized electronic states and spin-split bands. The second possible cause of the origin of Rashba-like states, it is an expansion of the van der Waals gaps induced by imperfections or defects which are trapped between adjacent blocks during the growth process. Such expansion affects the band structure inducing a spin-split of the electronic states [33, 36, 37].

At first, to unveil the presence of possible contaminants on surface and the *aging effect* of the sample, we have performed detailed core level photoemission measurements on the two cleaved surfaces. We observed that both compounds are contaminants-free within the detection limits of the technique³. The photoemission wide spectra, recorded at 700 eV of photon energy and reported in Fig. 1.6(a), do not show any presence of impurities, chemical shift or added peaks referable to a possible sample contamination after cleavage (red and blue curves for PbBi_4Te_7 and $\text{PbBi}_6\text{Te}_{10}$, respectively). Subsequently, the same crystal surface of PbBi_4Te_7 has been intentionally exposed to air for 15 minutes. The recorded wide spectrum, measured at 830 eV of photon energy and reported in panel (b) of Fig. 1.6, show oxygen and carbon peaks (green curve); the inset of panel (b) shows the Te $3d$ -states for the as-cleaved clean surface (red curve) splitted by spin-orbit interaction into the doublet $3d_{3/2}$ and $3d_{5/2}$ at

²The Rashba effect is a momentum-dependent spin-split of bands in bulk crystals or low-dimensional systems (such as heterostructures and surface states); the splitting is the result of spin-orbit coupling and asymmetry of the crystal potential [35].

³In general, detection limits for core level photoemission measurements is from 0.1 to 1 atomic percent (parts per thousand). This is the reason why core level photoemission is a technique widely employed to measure the chemical composition of material surfaces.

582.07 and 571.65 eV binding energy. After the air exposure (green curve), we can observe new components shifted by 3.62 eV toward higher binding energy. In Fig. 1.6 panel (c), Bi and Pb 4*f*-states for the clean PbBi₄Te₇ surface (red curve) collected at 370 eV; these peaks are splitted by spin-orbit interaction into Bi 4*f*_{5/2} at 162.30 eV, Bi 4*f*_{7/2} at 157.00 eV, and Pb 4*f*_{5/2} and Pb 4*f*_{7/2} at 141.50 eV and 136.65 eV, respectively. After air exposure (green curve) Bi 4*f*-states present new resonance components shifted by 1.2 eV toward lower binding energy. We collected also the valence band spectrum of the sample at 50 eV of photon energy after air exposure, reported in panel (d) of Fig. 1.6. Importantly, the valence band remains protected: no remarkable energy shifts of the electronic states nor additional electronic (Rashba-like) bands are observed in the valence band. This is the first example of spin-split electronic states unaffected by prolonged air exposure.

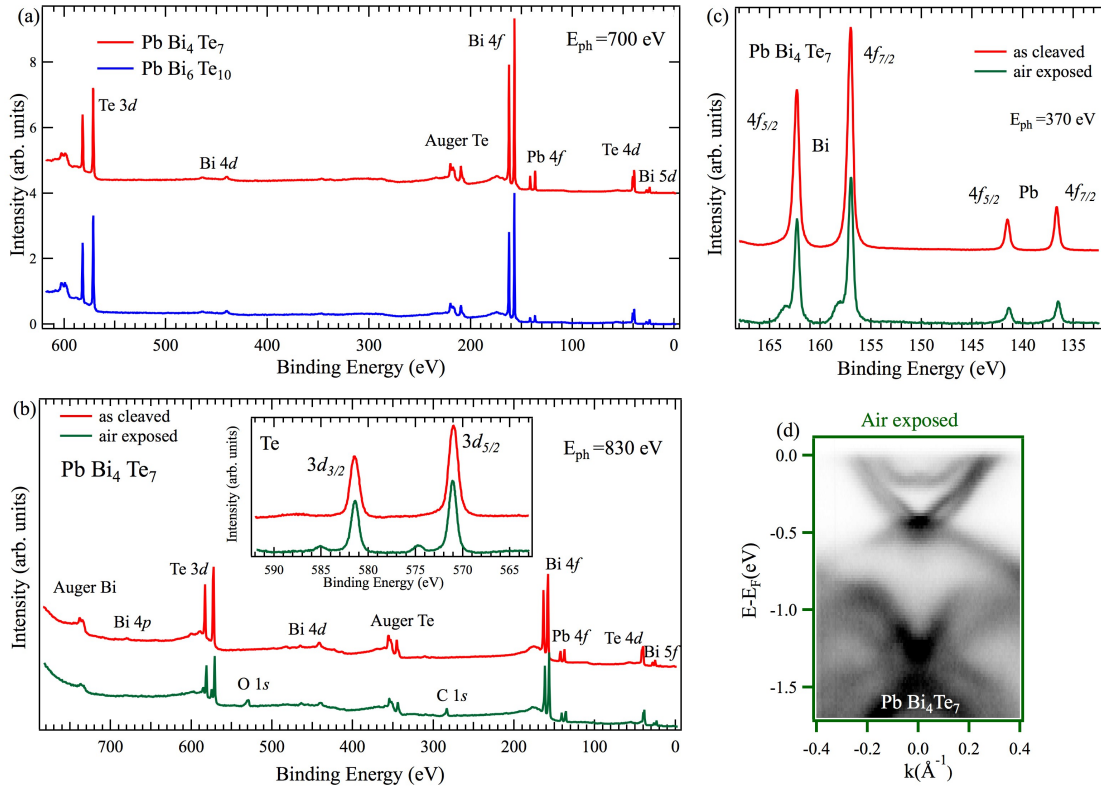


Figure 1.6: (a) Core level photoemission measurements on PbBi₄Te₇ (red curve) and PbBi₆Te₁₀ (blue curve) measured with 700 eV photons after cleavage. (b) Wide spectra recorded at 830 eV of photon energy of PbBi₄Te₇ before (red curve) and after (green curve) air exposure; in the inset Te 3*d*-states before (red curve) and after (green curve) air exposure. (c) Bi and Pb 4*f*-states for the clean (red curve) and air exposed (green curve) surface of PbBi₄Te₇, collected at 370 eV. (d) ARPES spectrum of PbBi₄Te₇ measured with photons of 50 eV after exposure to air.

These results suggest that the investigated systems do not undergo to the *aging effect*, and that foreign atoms adsorbed at surface cannot be responsible of the observed Rashba-like bands.

In order to unveil the effect of the van der Waals gap expansion as the cause of the

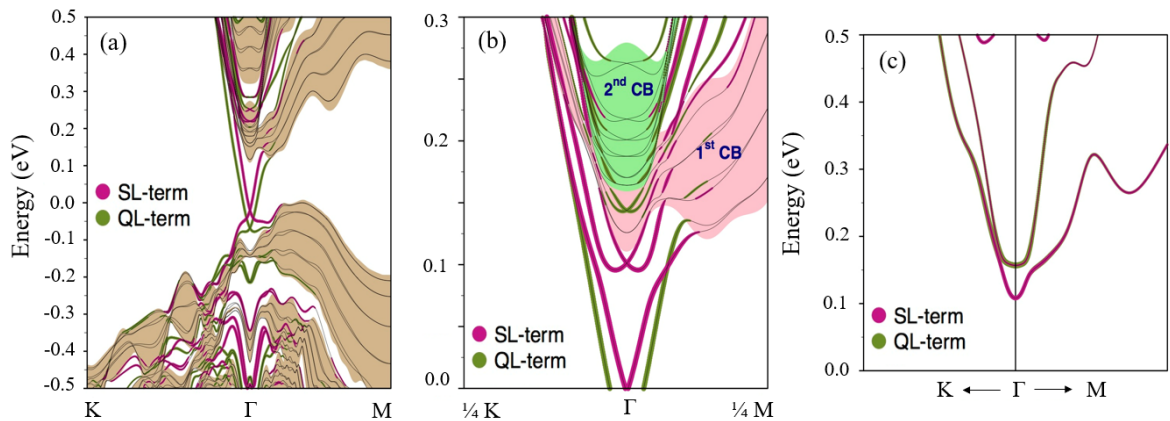


Figure 1.7: (a) DFT calculation of the surface electronic structure of PbBi_4Te_7 slab with SL and QL surface terminations on the opposite side of the slab; shaded area identify the bulk-projected band. (b) The electronic structure of the PbBi_4Te_7 slab with outer SL (QL) detached by 20%. (c) Close view of the bulk conduction band near the Γ where the thickness of the lines indicate the weights of p_z orbitals for the atoms forming on SL and QL terminations.

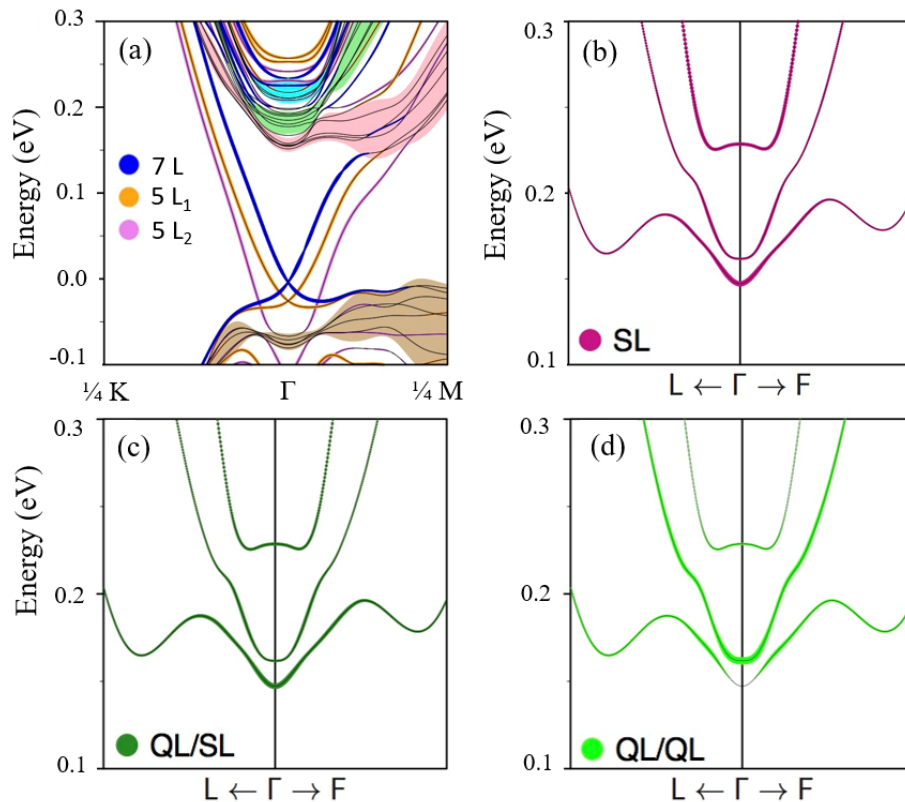


Figure 1.8: (a) DFT calculation of the surface electronic structure of $\text{PbBi}_6\text{Te}_{10}$; shaded area identify the bulk-projected band. (b)-(d) The bulk conduction band near Γ point for SL, QL/SL and QL/QL van der Waals spacing, respectively; the thickness of the lines gives the indication of the relative weights of the p_z orbitals.

Rashba-like states, we have performed DFT calculations for PbBi_4Te_7 TI.

The first spectrum reported in Fig.1.7 well reproduces the dispersion of the Dirac cone-like state along the KTM direction of the presented ARPES measurements but these calculations do not show any Rashba-like states. In order to predict the formation of such states, we performed simulations assuming a van der Waals gap expansion of the 20% on both side of the slabs for both QL- and SL- terminations. The result is reported in panel (b) of Fig. 1.7: such expansion leads to the formation of two Rashba-states. The first one is located in the bulk band gap; it resides at the SL- terminated surface (pink lines) and it arises due to the splitting of the bottom of the first conduction band (shaded pink band). The second Rashba-state is located on the QL- terminated surface (green lines) and comes from the split of the bottom of the second conduction band (shaded green band); however, these states lie in the bulk continuum region and are not detectable experimentally. The shaded area outlines the bulk-projected bands.

Since the Rashba-states have predominantly p_z character, we added the contributions (with the relative weights) of the p_z orbitals of the atoms that constitute the two blocks; in Fig. 1.7(c) we report a close view of the bulk band conduction near the Γ point: the thickness of the pink and green lines gives an indication of the relative weights of the p_z orbitals. We can observe that the first lowest band has predominantly SL- character while the second band is mainly composed by atomic orbitals of the QL- termination. The case of the $\text{PbBi}_6\text{Te}_{10}$ is more complicated due to the presence of more contributions from the QL_1 -, QL_2 - and SL- blocks. In Fig. 1.8 we report the calculated surface electronic structure of $\text{PbBi}_6\text{Te}_{10}$ along the KTM direction; shaded area identify the bulk-projected band. Panel (a) of Fig. 1.8 shows three Dirac states and three different bulk bands (pink, green and cyan) which contribute to the lower bulk band formation. In panels (b), (c) and (d) of Fig. 1.8 we report a close view of the bulk conduction band near the Γ point by summing the contributions of the p_z orbital weights for SL, QL/SL and QL/QL van der Waals spacing, respectively. From panels (b), (c) and (d) of Fig. 1.8 we can see that the lowest part of the first conduction band (at about 0.15 eV) is equally composed by the contributions of the SL and QL/SL orbitals, while the contribution from QL/QL is absent; the second band is mainly composed by QL/QL and the third is constituted equally by all orbitals. The Rashba-states originated from the two lowest band appear in the gap, as we can observe from ARPES measurements in Fig.1.3(b), while the third state, which should be originated from the third bulk band, is located in the continuum region and it is not detectable experimentally.

1.3.2 PbBi_4Te_7 , SnBi_4Te_7 and $\text{PbBi}_4\text{Te}_6\text{Se}$

In this section the effect of the replacements of heavy atoms with lighter isoelectronic ones is presented. In particular, starting from the measurements performed on PbBi_4Te_7 and reported in section 1.3.1, we proceeded with the analysis of SnBi_4Te_7 , in which Pb atoms have been substituted by Sn. Finally, we compare the results collected on $\text{PbBi}_4\text{Te}_6\text{Se}$, in which one Te atom in the central atomic layer of the QL block were substituted by Se atom.

In Fig. 1.9 we report the first experimental evidence of the topological nature of SnBi_4Te_7 ,

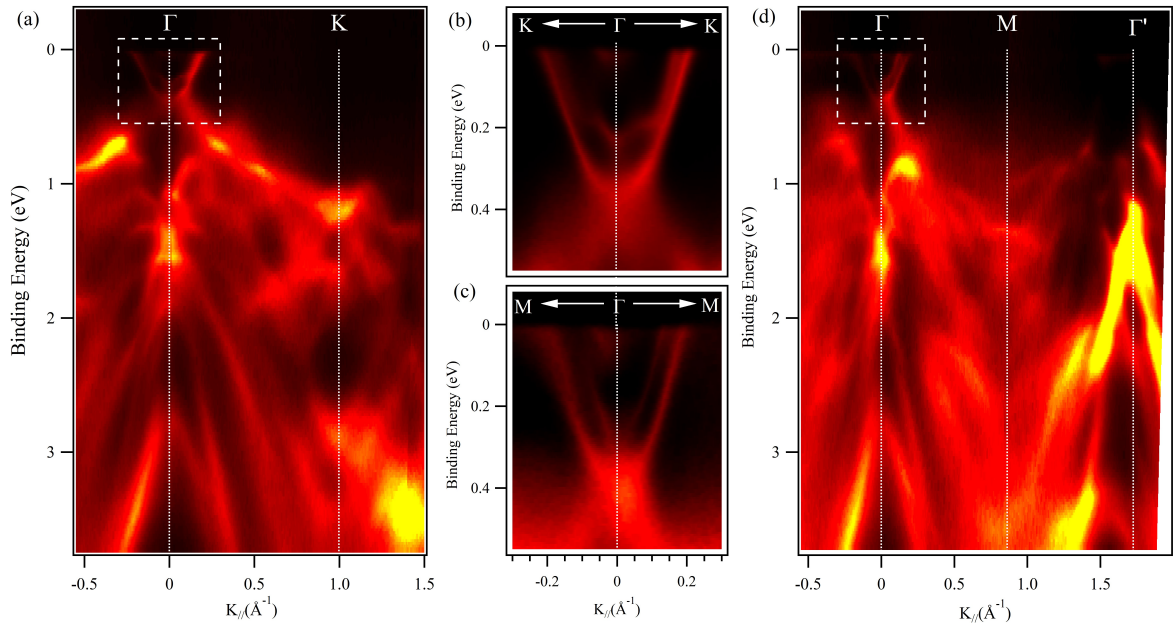


Figure 1.9: Experimental band dispersion of SnBi_4Te_7 in a wide energy and momentum range along (a) ΓK and (d) ΓM directions of the Brillouin zone. (b) and (c) panels show a magnified view of the Dirac states along $\text{K}\Gamma\text{K}$ and $\text{M}\Gamma\text{M}$ directions, respectively. All measurements were performed with 50 eV of photon energy.

which has been theoretically proposed as promising 3D TI in Refs. [21, 28]. Panels (a) and (d) show the band structure in a wide energy range along ΓK and $\Gamma\text{M}\Gamma'$ direction of the Brillouin zone, respectively. Panels (b) and (c) were acquired in a narrow range of energy and momentum in order to better resolve the Dirac states. The K symmetry point is located at $k_{\parallel} \simeq 1.0 \text{ \AA}^{-1}$ and M point is at $k_{\parallel} \simeq 0.85 \text{ \AA}^{-1}$. The two branches along ΓM direction in Fig. 1.9(c) display the typical Dirac linear dispersion, while along ΓK it deviates from linear at $k_{\parallel} \simeq 0.1 \text{ \AA}^{-1}$ and $\simeq 0.2 \text{ eV}$ of binding energy. Such warping highlights the manifestation of the hexagonal distortion of the Dirac cone, which will be discussed later by comparing topological insulators with different atomic composition.

In Fig. 1.10 (a) and (b) we present the comparison between the second derivative along the energy axis of the band structure collected along the ΓM direction of the surface Brillouin zone (BZ) for the two compounds SnBi_4Te_7 and $\text{PbBi}_4\text{Te}_6\text{Se}$. The presented ARPES images were recorded at 50 eV and 30 eV of photon energy respectively. These data clearly evidence the characteristic signature of the topological surface states: two sharply linear dispersing features, crossing the Fermi level and with a minimum at the Γ point. The position of the symmetry points M and K of $\text{PbBi}_4\text{Te}_6\text{Se}$ are almost the same as those reported above for SnBi_4Te_7 topological insulator.

We compared the experimental results with DFT calculations reported in Fig. 1.11. The SnBi_4Te_7 and $\text{PbBi}_4\text{Te}_6\text{Se}$ compounds demonstrate complicated band inversion in the bulk, as we can observe from panels (a) and (b) of Fig. 1.11. For both QL and SL blocks of the two TIs, the p_z orbitals of the Te atoms occupy the two lowest conduction bands at Γ point (red curves) while the p_z orbitals of Bi atoms, of both terminations, occur in the first and second valence

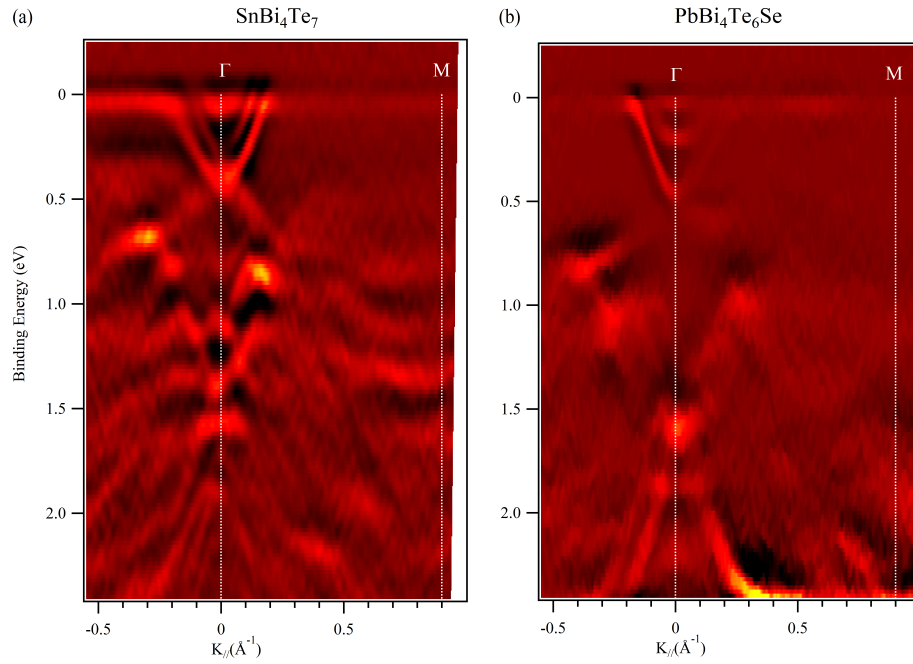


Figure 1.10: Second derivative along the energy axis of the wide energy and momentum dispersions along the Γ M direction of the Brillouin zone for (a) SnBi_4Te_7 and (b) $\text{PbBi}_4\text{Te}_6\text{Se}$ compounds, recorded at 50 eV and 30 eV of photon energy respectively.

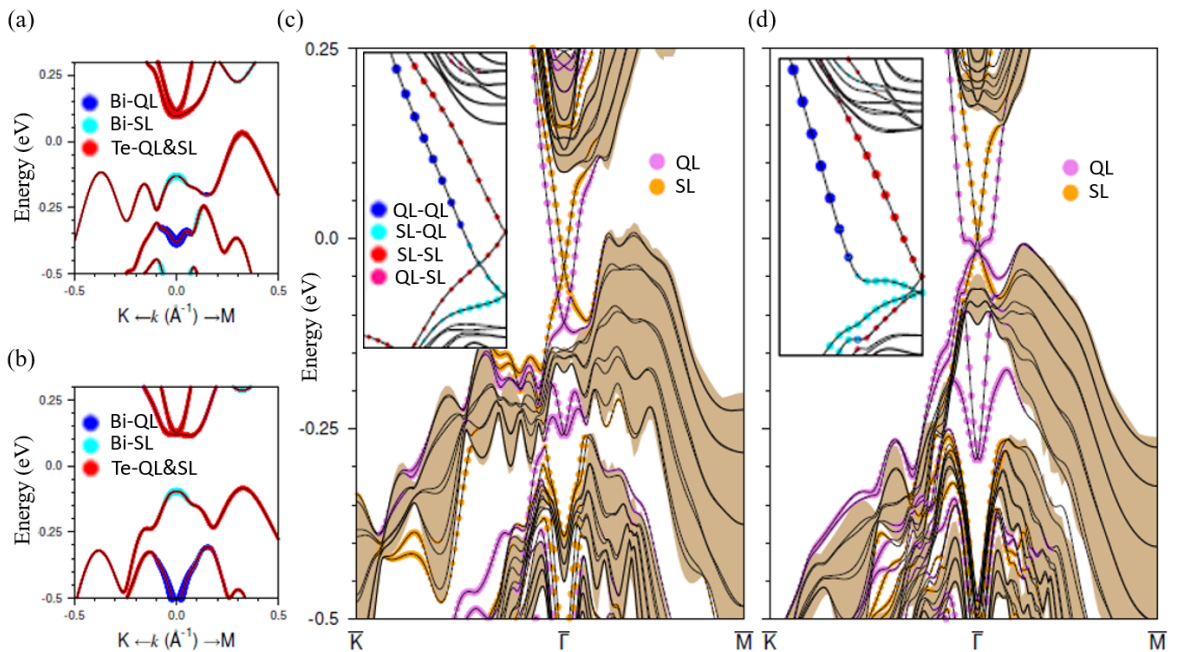


Figure 1.11: Bulk electronic spectra of (a) SnBi_4Te_7 and (b) $\text{PbBi}_4\text{Te}_6\text{Se}$. Color circles denote weights of Bi and Te p_z orbitals. Surface electronic spectra of (c) SnBi_4Te_7 and (d) $\text{PbBi}_4\text{Te}_6\text{Se}$. Insets in (c) and (d) show magnified view of the Dirac states (in Γ K direction). The size of color circles represents the weight of the states in the surface and subsurface building blocks, respectively.

bands (blue and light blue curves), respectively, like in other topological compounds with the same alternating QL/SL structure [17]. Such bulk band inversion results in the formation of the single Dirac states on the SL and QL-terminated surface of SnBi_4Te_7 (Fig. 1.11 (c)) and $\text{PbBi}_4\text{Te}_6\text{Se}$ (Fig. 1.11 (d)), completely localized on the surface of the respective blocks. The lowest one arises in the local valence band completely stemming from the inversion of the Bi-QL states and the second state resides in the bulk gap demonstrating changing localization (insets of panels (c) and (d) of Fig. 1.11). In the vicinity of the Dirac point, this state is localized predominantly in the subsurface of SL block while at larger k_{\parallel} it relocates into the surface of the QL termination. The band gap state of the QL-terminated surface of SnBi_4Te_7 has typical Dirac dispersion, which is characteristic of the Bi_2Te_3 -derived compounds. For the $\text{PbBi}_4\text{Te}_6\text{Se}$ topological insulator, in contrast to usual Bi_2Te_3 -based systems, the deeper Γ dispersion in the bulk valence band shows a pronounced cusp: the Dirac state has a kink-like (dog-leg) dispersion similar to that found in $(\text{SnTe})_{n>1}(\text{Bi}_2\text{Te}_3)_{m=1}$ [38] where competitive bulk band gap inversion occurs also.

In the following, we discuss the tunable property of the topological surface states of these class of ternary/quaternary topological insulators, $A^{IV}\text{Bi}_4\text{Te}_{7-n}\text{Se}_n$ ($A^{IV} = \text{Sn, Pb}; x=0, 1$).

To take a closer look at the Dirac-cone like dispersion and in order to catch the effect of stoichiometry on the electronic properties of the TIs, in Fig.1.12 we report the ARPES images in a smaller range of binding energies for the three compounds along the ΓM direction: SnBi_4Te_7 , $\text{PbBi}_4\text{Te}_6\text{Se}$ and PbBi_4Te_7 , in panel (a), (c) and (e), respectively. The measured electronic states have been recorded at 50 eV, 30 eV and 50 eV of photon energy. To better visualize the band dispersion and to enhance the contrast, we reported also the corresponding second derivatives along the energy axis of each ARPES images in Fig.1.12(b), (d) and (f). Two main dispersing features crossing the Fermi level and with the minimum centered at the Γ point are observed for SnBi_4Te_7 and PbBi_4Te_7 . In accordance with DFT calculations showed in Fig. 1.11, we can assign these feature as follow: the outer dispersing structure is related to the QL surface termination, while the inner one to the SL-term. The derivative of the ARPES measurements proves that, apart from final state effect (matrix-element effects), we are able also to solve the topological state localized on SL-terminated terraces of $\text{PbBi}_4\text{Te}_6\text{Se}$.

In the case of SnBi_4Te_7 and PbBi_4Te_7 , the overlap of the Dirac states resided on the QL-terminated terraces with the bulk band dispersions, in the energy region of 0.4 - 0.6 eV below the Fermi level, does not allow the accurate determination of the Dirac point energies. However, following the dispersion of the second derivative and by linear interpolation of the data, extracted from the peak positions of MDCs, we can estimate the Dirac point energies. Conversely, the Dirac points of the topological states resided on the SL-terminates terraces are well-resolved and highlighted by the derivatives for the $\text{PbBi}_4\text{Te}_6\text{Se}$ compound. In Fig.1.13(a) and (b) we report the extracted band dispersions for SL and QL terminated surfaces of the three topological insulators.

For SnBi_4Te_7 , both Dirac states have almost linear dispersion above the Dirac point up to the Fermi level. The dispersion of the Dirac cone in the case of QL-terminated surface is wider than in the SL ones; we estimated the following values of k_{\parallel} for the surface bands crossing the Fermi level: $k_F(\text{QL}) \simeq \pm 0.20 \text{ \AA}^{-1}$ and $k_F(\text{SL}) \simeq \pm 0.135 \text{ \AA}^{-1}$. The Dirac points of the QL-

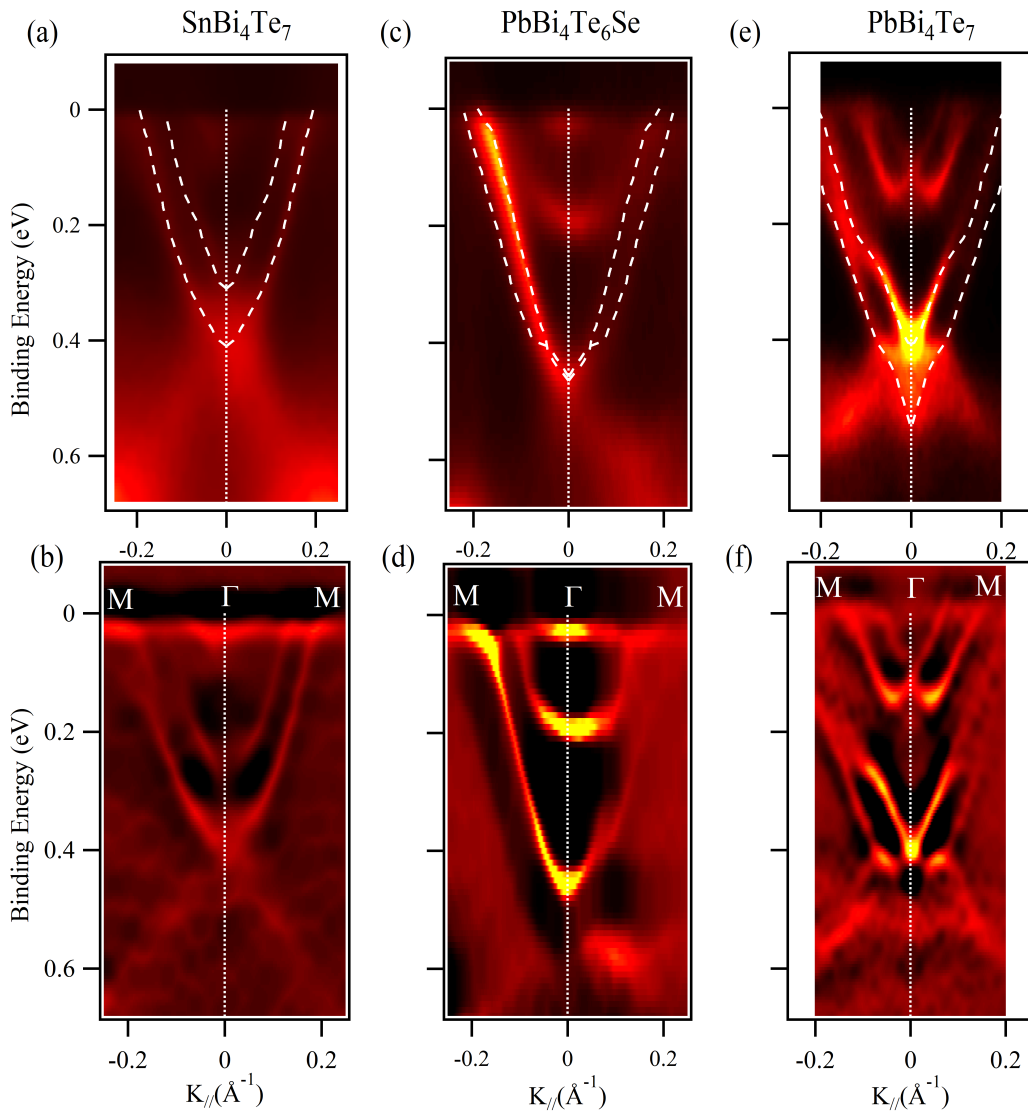


Figure 1.12: ARPES images and corresponding second derivatives along the energy axis of (a)-(b) SnBi_4Te_7 , (c)-(d) $\text{PbBi}_4\text{Te}_6\text{Se}$ and (e)-(f) PbBi_4Te_7 recorded at 50 eV, 30 eV and 50 eV of photon energy, respectively. The band dispersions extracted from the MDCs peak positions have been superimposed on the corresponding as-acquired spectra.

and SL-terminated surface are well separated for this compound; the estimated positions are $DP_{SL} \simeq 0.31$ eV and $DP_{QL} \simeq 0.40$ eV of BE. We also observe diffuse photoemission spectral-weight intensity at about 100 meV below the Fermi level and centered at the Γ point, which is assigned to the bottom of the conduction band. By MDCs fitting, we estimate the group velocity of the Dirac Fermions close to Fermi level along the showed ΓM direction: $v_g(QL) \simeq 4.5 \times 10^5$ m/s and $v_g(SL) \simeq 4.8 \times 10^5$ m/s. The obtained values are in good agreement with the group velocity estimated for other topological insulators [16, 18, 34, 39].

ARPES measurements performed on $PbBi_4Te_6Se$ and reported in Fig.1.12 (c) and (d), reveal a strongly linear dispersion of the inner Dirac state (assigned to SL terminated surface) from the Dirac point up to $\simeq 0.05$ eV of BE. In contrast, the dispersion of the Dirac state stemming from the QL-terminated terraces is linear close to the Fermi level and display a change in the slope close to the Dirac point, demonstrating kink-like behaviour in agreement with calculated spectrum (see Fig. 1.11). The dispersion of the outer Dirac surface state (QL term) is slightly wider with respect to that from SL termination; we estimate the following values of momentum: $k_F(QL) \simeq \pm 0.22 \text{ \AA}^{-1}$ and $k_F(SL) \simeq \pm 0.19 \text{ \AA}^{-1}$. The state centered at Γ and with a minimum located at about 0.2 eV of binding energy has been assigned to the two-dimensional electron gas (2DEG) state, according with DFT calculations and with previous works [30, 36, 40, 41]. We estimate that the topological states, stemming from QL and SL-terminated surfaces, have similar group velocities to those of Sn-compound: $v_g(QL) \simeq 4.3 \times 10^5$ m/s and $v_g(SL) \simeq 5 \times 10^5$ m/s, respectively. By linear interpolation of the data extracted from MDCs, we have estimate also the Dirac points position, which is the same for both topological states and it is located at $\simeq 0.45$ eV below the Fermi level; this values is in accordance with our DFT calculations, which revealed only 19 meV energy difference between Dirac points energy.

The $PbBi_4Te_7$ compound has already been widely discussed in section 1.3.1. Here we add more information about electronic properties in order to highlights the differences with the compared topological insulators. As clearly observed in Fig.1.12 panels (e) and (f), the SL term is well separated from the bulk band gap, while the QL term, which has a wider and deeper dispersion, energetically overlaps with bulk valence band. Then, for the latter, the energy position of the Dirac point has been obtained by linear interpolation of the data extracted from MDCs. We found the Dirac points located at $\simeq 0.40$ eV and $\simeq 0.55$ eV below the Fermi level for SL and QL, respectively. The estimated group velocities have also similar value with respect to those evaluated for the other compounds $v_g \simeq 4 \times 10^5$ m/s.

To highlight the effects of the replacement of heavy atoms with lighter isoelectronic ones, we report in panels (a) and (b) of Fig.1.13, the band dispersions extracted from the peak maximum positions of the MDCs of the related ARPES spectra showed in Fig. 1.12, for both surface terminations. Such extracted band dispersions are also superimposed to the corresponding as-acquired spectra. The data presented in Fig.1.13 prove that the Dirac point energy can be significantly shifted by changing the stoichiometry of the crystal. One can recognized that the energy shift proceeds *approximately* in a rigid manner, starting from $PbBi_4Te_7$ and by changing the composition; this effect results more clear by observing the trend of the position of the DP for the QL-termination surface. This suggests the efficient

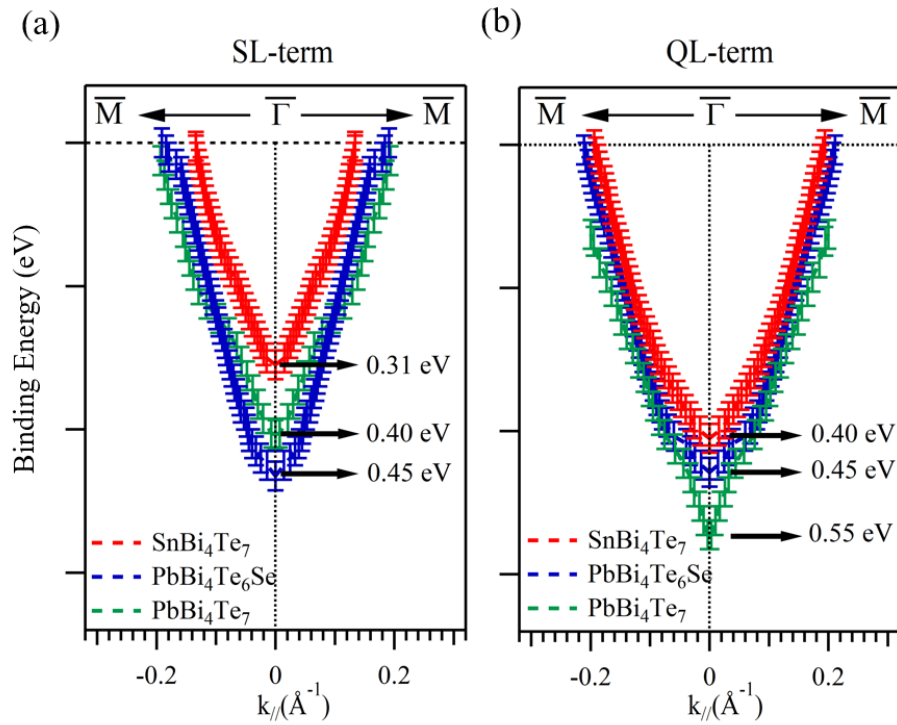


Figure 1.13: The band dispersions of the three topological insulators extracted from the maximum peak positions in the MDCs of the ARPES images for (a) SL and (b) QL-terminated surfaces, respectively.

possibility of controlling the conduction states by means of the variation of the component. Such shift indicates a modification of the concentration of n -type bulk carriers.

From a directly comparison between SnBi_4Te_7 and PbBi_4Te_7 topological insulators, an upward shift of the Dirac cones with respect to the Fermi level, when the lighter element is present, has been observed. In particular, in the SL block, it is possible to shift the topological state of the SL-terminated state by 0.10 eV toward lower binding energy (Fig. 1.13(a)); the topological state of the QL-terminated domain moves instead up by 0.15 eV (Fig. 1.13(b)). These behaviour has been theoretically proposed for MBi_2Te_4 ($M = \text{Ge}, \text{Sn}, \text{Pb}$ and Yb)⁴ compounds [19, 20]. Also in this case, the substitution of the M (Sn or Pb) component affects the shape of the Dirac cone and also the related position in energy with respect to the Fermi level. In addition, the manifestation of the hexagonal warping of the Dirac cone in PbBi_4Te_7 is visible for the Dirac state from the SL-terminated terraces along the showed direction of the Brillouin zone, while for SnBi_4Te_7 it is present along the ΓK direction (as we can see in Fig. 1.9). Such difference highlights the strong dependence and directional anisotropy because of the different stoichiometry, which affect the group velocity.

The Dirac points of $\text{PbBi}_4\text{Te}_6\text{Se}$ are well separated from the bulk states (upward shift of more than 100 meV), compared to PbBi_4Te_7 where QL Dirac point is buried inside the valence bands. This is crucial for applications of topological insulators in the Dirac transport

⁴The calculation of the surface structure of these compounds reveal a strong dependence of the dispersion on the M component, and besides the rigid upward shift, it has been proved that Ge and Pb noticeably improved the shape of the Dirac cone.

regime. The Dirac state stemming from the SL-terminated surface, of the two Pb-based TIs, is located almost at the same position (within less than 10 meV): we estimate 0.45 eV of binding energy for $\text{PbBi}_4\text{Te}_6\text{Se}$, compared to 0.40 eV for PbBi_4Te_7 , as we can see from panel (a) of Fig. 1.13. The substitution of Te atoms with the lighter Se has the most important effect on the QL-terminated surface, shifting it by 100 meV toward lower binding energy (Fig. 1.13(b)). The two lattice parameters a and c decrease in case of the substitution of the Te atom with Se; we report $a=4.3842 \text{ \AA}$ $c=23.841 \text{ \AA}$ for $\text{PbBi}_4\text{Te}_6\text{Se}$ and $a=4.500 \text{ \AA}$ $c=24.438 \text{ \AA}$ calculated for PbBi_4Te_7 [42], which it is in line with the smaller size of selenium atoms. Furthermore, our experimental observations suggest the different roles of selenium atoms: beside the rigid shift, the slope of the two Dirac cones increase and so does the velocity group [43] from $\simeq 4 \times 10^5 \text{ m/s}$ to $\simeq 4.3 \times 10^5 \text{ m/s}$ for the QL-terminated surfaces and from $4.5 \times 10^5 \text{ m/s}$ up to $5 \times 10^5 \text{ m/s}$ for the SL terms. The Te to Se substitution leads also to an increasing of the band gap value according to other ternary compounds [40, 43, 44].

We note that Dirac state position with respect to Fermi level and the shape of the Dirac cone strongly influence the conduction properties of the topological insulators. The presented results demonstrate that the replacement of heavy atoms (Pb and Te) by lighter isoelectronic ones (Sn and Se) results in a change of the positions of Dirac point and in the slope of the Dirac cones. Such experimental realization denotes the high potential of this new family of topological insulators for investigation of novel topological phenomena which requires the tunability of the Dirac states.

1.4 Robustness against contaminants

The possible engineering applications of topological insulators depend on how the sample surface states can be manipulated, in order to be able to control the electronic and physical properties. While the ARPES, STM and core level photoemission measurements involve fresh cleaved surfaces obtained, for example, by cleaving the sample *in situ* and in UHV conditions, for other techniques, such as transport and optical techniques, the sample surface is usually exposed to ambient conditions. The critical point is how the topological states behave under such conditions.

Therefore it is crucial to study the possible modifications of the electronic properties against contaminants so that these materials can be employed at RT and under ambient condition. To this purpose, we carried out ARPES and core level photoemission measurements on the as-cleaved samples and also after contaminants exposure.

The reported ARPES measurements performed on PbBi_4Te_7 after exposing the sample surface to air were mandatory in order to investigate and discard the *aging effect* as a possible cause of the appearance of Rashba states; however, they also helped us understand the behaviour of these air-exposed surfaces. At first, the sample has been cleaved and measured in the UHV chamber. The same measured sample surface, whose band structure has been reported in Fig. 1.3(a), was subsequently exposed to air for about 15 minutes, transferring back to the UHV chamber to perform again the ARPES measurements. We observe the presence of C and O in the related wide core level spectrum and/or inset and other panels, see Fig.

1.6, but there were no remarkable shifts or modification of the electronic band structure of the topological insulators. These results allowed us to demonstrate that the band structure remains *protected* against air exposure. For further details, see section 1.3.1.

A recent ARPES study performed on a similar compound, $\text{PbBi}_4\text{Te}_4\text{S}_3$, reported the vanishing of the QL-related TS after exposure to 100 Langmuir (L) of oxygen at room temperature [46]; since there are some contradicting results concerning the robustness of the ternary/quaternary compound TSs to external agents, to study the effects of the surface reactivity and the level of protection of the TSs of the investigated compounds, the crystal surfaces of both compounds, SnBi_4Te_7 and $\text{PbBi}_4\text{Te}_6\text{Se}$ samples, were exposed up to 1000 Langmuir (L) of oxygen atmosphere at RT.

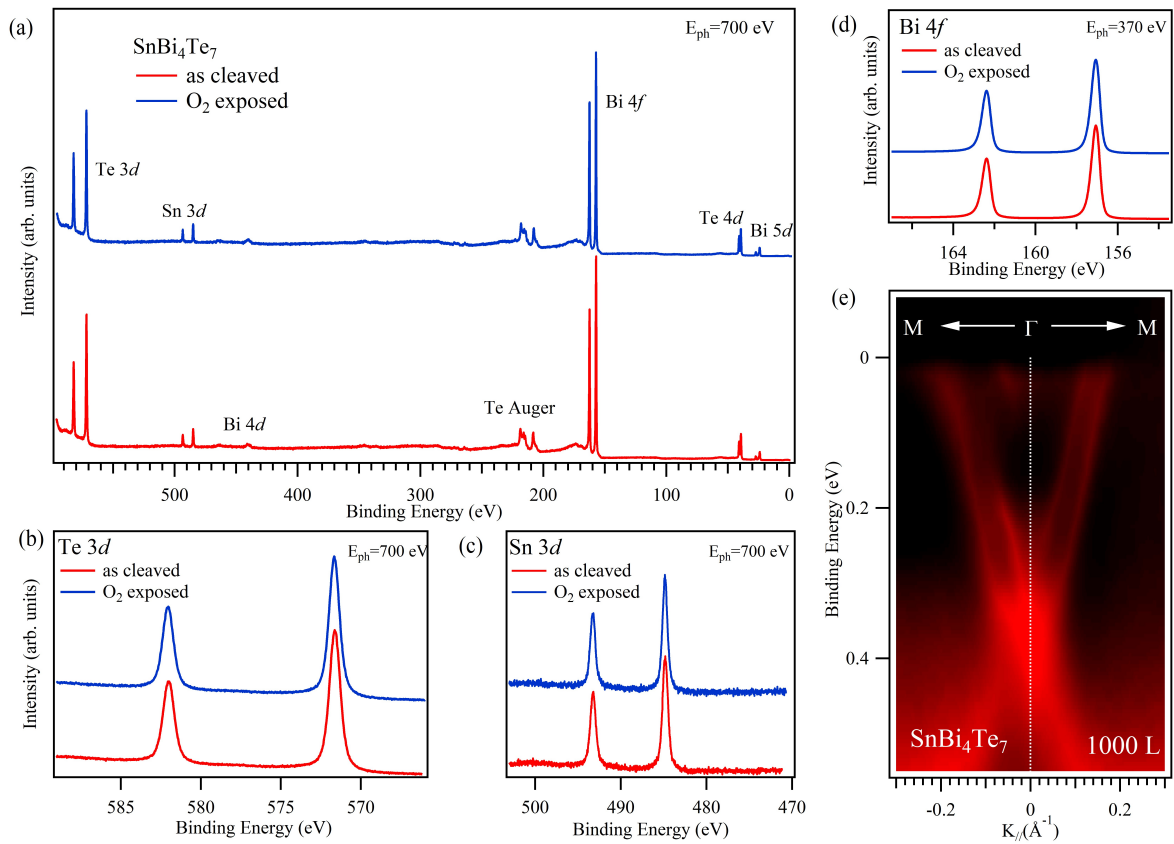


Figure 1.14: (a) Core level photoemission wide spectra recorded at 700 eV of photon energy on the as-cleaved (red curve) and after oxygen exposure (blue curve) surface of SnBi_4Te_7 . (b) Te 3 d -states and (c) Sn 3 d -states for the as-cleaved (red curve) and oxygen exposure (green curve) surface collected at 700 eV of photon energy. (d) Bi 4 f -states for the as-cleaved (red curve) and oxygen exposure (blue curve) surface collected at 370 eV. (e) ARPES spectrum of SnBi_4Te_7 measured with photons of 50 eV after oxygen exposure.

The photoemission spectra, recorded at 700 eV of photon energy and reported in Fig. 1.14(a), compare the wide spectra of the as-cleaved and after oxygen exposure SnBi_4Te_7 . The wide spectrum recorded after the exposure (blue curve), does not show any presence of oxygen, chemical shift or added peaks referable to a possible sample contamination. We conclude that SnBi_4Te_7 is contaminants-free within the detection limits of the technique (parts per thousand). Panel (b) of Fig. 1.14 shows the Te 3 d -states for the as-cleaved clean surface

(red curve) splitted by spin-orbit interaction into the doublet $3d_{3/2}$ and $3d_{5/2}$ at 582.05 and 571.62 eV binding energy, respectively. No added components or shift were observed after the air exposure (blue curve), at odd with the spectra recorded for PbBi_4Te_7 , see Fig. 1.6. Also the measured spectra of the Bi $4f$ -states, $4f_{5/2}$ and $4f_{7/2}$ at 162.38 and 157.06 eV of binding energy, and the Sn $3d$ -states, splitted in $3d_{3/2}$ and $3d_{5/2}$ at 493.22 and 484.80 eV binding energy reported in Fig. 1.14 (d) and in Fig. 1.14 (c), do not show remarkable differences before and after exposure.

Fig. 1.14 (e) reports the experimental band structure along the ΓM direction after oxygen exposure. The valence band remains protected and unaffected by oxygen exposure: no remarkable energy shifts or modifications of the electronic states nor additional electronic (Rashba-like) bands were observed in the valence band.

Very similar results have been obtained for $\text{PbBi}_4\text{Te}_6\text{Se}$, as we can see from Fig. 1.15.

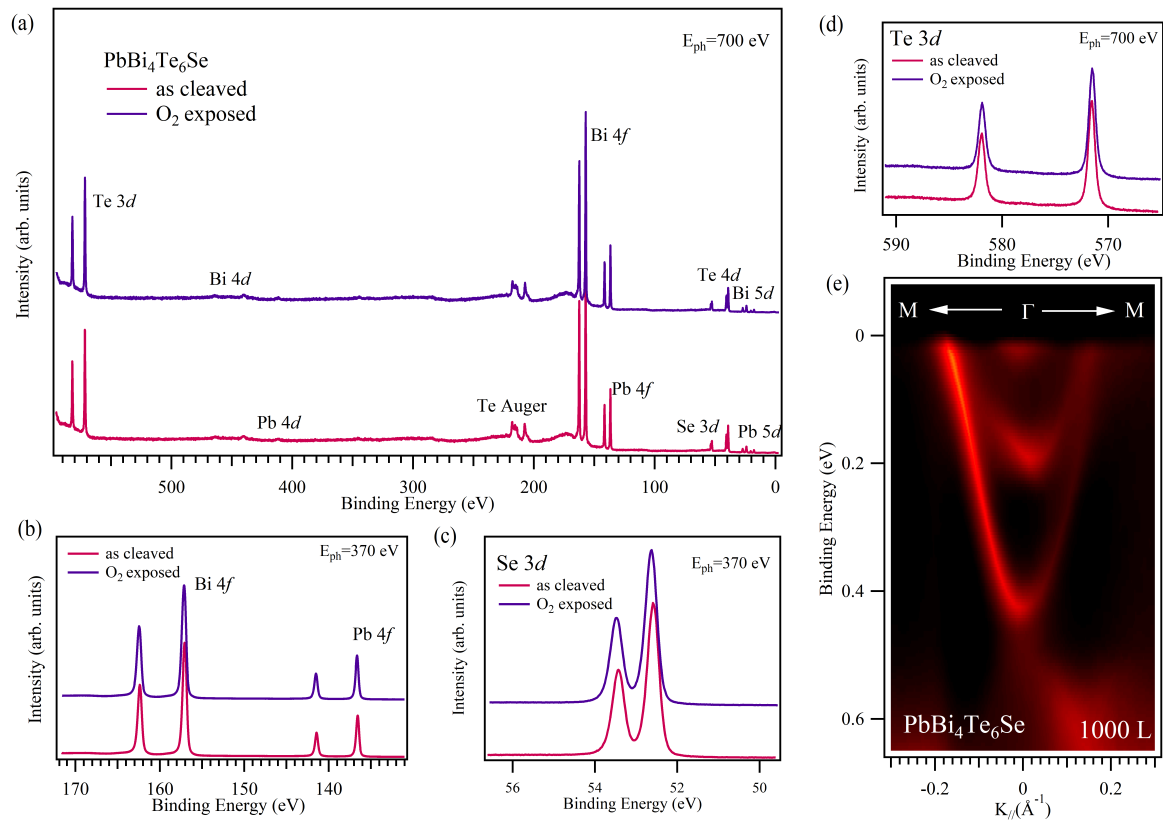


Figure 1.15: (a) Core level photoemission wide spectra recorded at 700 eV of photon energy on the as-cleaved (pink curve) and after oxygen exposure (purple curve) surface of $\text{PbBi}_4\text{Te}_6\text{Se}$. (b) Bi and Pb $4f$ -states, and (c) Se $3d$ -states for the as-cleaved (pink curve) and oxygen exposure (purple curve) surface collected at 370 eV. (d) Te $3d$ -states for the as-cleaved (pink curve) and oxygen exposure (purple curve) surface collected at 700 eV of photon energy. (e) ARPES spectrum of $\text{PbBi}_4\text{Te}_6\text{Se}$ measured with photons of 30 eV after oxygen exposure.

In panel (a), we compare the wide spectra of the $\text{PbBi}_4\text{Te}_6\text{Se}$, recorder at at 700 eV of photon energy. The spectrum recorded after oxygen exposure (purple curve) does not show notably effect of contaminants, such as peaks, added structure or remarkable shifts. In panel (b), we report the Bi $4f$ -states, splitted into $4f_{5/2}$ and $4f_{7/2}$ at 162.40 and 157.00 eV binding

energy, and Pb 4*f*-states, 4*f*_{5/2} and 4*f*_{7/2} at 141.50 and 136.55 eV, before and after O exposure. Panel (c) shows the Se 3*d*-states, 3*d*_{5/2} and 3*d*_{3/2} at 52.60 and 53.48 eV binding energy, barely affected by O. Also Te 3*d*-states reported in panel (d) splitted into 3*d*_{5/2} at 571.50 and 3*d*_{3/2} at 581.95 eV, confirm no observable effects. We collected also the experimental band structure of the sample at 30 eV of photon energy along the Γ M direction after oxygen exposure, reported in panel (e) of Fig. 1.15. No remarkable energy shifts or modifications of the electronic states nor additional electronic (Rashba-like) bands were observed.

The present study demonstrate that the exposure to molecular oxygen, in the case of SnBi₄Te₇ and PbBi₄Te₆Se compounds, or to air, as reported for sample PbBi₄Te₇, does not change the electronic structure of the compounds and reveal that the surfaces are chemically inert to contamination. This is due to the high crystalline quality of the cleaved surface (surface with low concentration of defects) and to the absence of dangling bonding at the surface. This is a great advantage with respect to other TIs, where TSs are strongly modified or disappear [45, 46].

1.5 Conclusion

In this chapter a systematic comparative study of the electronic band structure of a new family of three-dimensional topological insulators has been reported.

Starting by Pb-based topological insulators with the same atomic composition (Pb, Bi and Te) but different ratio stoichiometry we performed a combined theoretical and experimental investigation to shed light on the effect of stoichiometry on the band structure of the compounds. We proved that, by changing the stoichiometry, it is in principle possible to built a topological insulator with the desired properties and to have a fine tailoring of the topological states and related electronic properties. Our ARPES measurements clearly reveal coexisting topological states stemming from different surface terminations and Rashba-like split states close to the Fermi level for both systems. Valence band photoemission measurements proved the origin of the aforementioned Rashba-like states, whose stem from the van der Waals gap expansion, as it was predicted by density functional theory calculations.

In the second part of this chapter, we report the electronic band structure of A^{IV}Bi₄Te_{7-x}Se_x (A^{IV} = Sn, Pb; *x*=0, 1) topological insulators by means ARPES measurements and DFT calculations. We show that it is possible to tailor the electronic properties of that compounds by varying the atomic composition. Indeed the substitution of heavy atoms, such as Pb and Te, by lighter isoelectronic ones, Sn and Se, involves a change in the position of the Dirac point with respect to the Fermi level and consequently the related electronic properties. We observed the existence of multiple Dirac-cone like surface band structures, stemming from different terminations, in all samples. Aside from this result, we report the first experimental evidence of the topological nature of Sn-based topological insulator, SnBi₄Te₇, which has been theoretically proposed as a promising 3D candidate.

We also proved by combined core level photoemission spectroscopy and ARPES measurements, that the electronic structure remain protected and barely unaffected by contaminants exposure (air and oxygen environment).

Our results provide an innovative approach that may allow to design topological insulators with tunable electronic states.

The results related to the PbBi_4Te_7 and $\text{PbBi}_6\text{Te}_{10}$ topological insulators discussed in section 1.3.1, are reported in the manuscript: "*Deep Insight Into the Electronic Structure of Ternary Topological Insulators: A Comparative Study of PbBi_4Te_7 and $\text{PbBi}_6\text{Te}_{10}$* ", D. Pacile', S. V. Eremeev, M. Caputo, M. Pisarra, O. De Luca, **I. Grimaldi**, J. Fujii, Z. S. Aliev, M. B. Babanly, I. Vobornik, R. G. Agostino, A. Goldoni, E. V. Chulkov and M. Papagno, *Physica Status Solidi - Rapid Research Letter* Volume **12**, 10 October 2018, Page 1800341. The manuscript is available [here](#).

The results here shown related to the SnBi_4Te_7 , PbBi_4Te_7 and $\text{PbBi}_4\text{Te}_6\text{Se}$ topological insulators discussed in section 1.3.2, are reported in the manuscript: "*Electronic band structure of three-dimensional topological insulators with different stoichiometry composition*", **I. Grimaldi**, D. Pacilè, S. V. Eremeev, O. De Luca, A. Policicchio, P. Moras, P. M. Sheverdyaeva, A. Kumar Kundu, Z. S. Aliev, P. Rudolf, R. G. Agostino, E. V. Chulkov and M. Papagno, *Physical Review B*, *Accepted*.

References

- [1] L. Fu, C. L. Kane, and E. J. Mele. “Topological Insulators in Three Dimensions”. In: *Physical Review Letters* 98.10 (Mar. 2007). DOI: 10.1103/physrevlett.98.106803.
- [2] M. Z. Hasan and C. L. Kane. “Colloquium: Topological insulators”. In: *Rev. Mod. Phys.* 82 (4 Nov. 2010), pp. 3045–3067. DOI: 10.1103/RevModPhys.82.3045.
- [3] X.-L. Qi and S.-C. Zhang. “Topological insulators and superconductors”. In: *Rev. Mod. Phys.* 83 (4 Oct. 2011), pp. 1057–1110. DOI: 10.1103/RevModPhys.83.1057.
- [4] M. Z. Hasan and C. L. Kane. “Colloquium: Topological insulators”. In: *Rev. Mod. Phys.* 82 (4 Nov. 2010), pp. 3045–3067. DOI: 10.1103/RevModPhys.82.3045.
- [5] Zhiyong Zhu, Yingchun Cheng, and Udo Schwingenschlögl. “Band inversion mechanism in topological insulators: A guideline for materials design”. In: *Phys. Rev. B* 85 (23 June 2012), p. 235401. DOI: 10.1103/PhysRevB.85.235401.
- [6] H. M. Benia, C. Lin, K. Kern, and C. R. Ast. “Reactive Chemical Doping of the Bi₂Se₃ Topological Insulator”. In: *Physical Review Letters* 107.17 (Oct. 2011). DOI: 10.1103/physrevlett.107.177602.
- [7] P. D. C. King, R. C. Hatch, M. Bianchi, R. Ovsyannikov, C. Lupulescu, G. Landolt, B. Slomski, J. H. Dil, D. Guan, J. L. Mi, E. D. L. Rienks, J. Fink, A. Lindblad, S. Svensson, S. Bao, G. Balakrishnan, B. B. Iversen, J. Osterwalder, W. Eberhardt, F. Baumberger, and P. Hofmann. “Large Tunable Rashba Spin Splitting of a Two-Dimensional Electron Gas in Bi₂Se₃”. In: *Physical Review Letters* 107.9 (Aug. 2011). DOI: 10.1103/physrevlett.107.096802.
- [8] T. Valla, Z.-H. Pan, D. Gardner, Y. S. Lee, and S. Chu. “Photoemission Spectroscopy of Magnetic and Nonmagnetic Impurities on the Surface of the Bi₂Se₃ Topological Insulator”. In: *Physical Review Letters* 108.11 (Mar. 2012). DOI: 10.1103/physrevlett.108.117601.
- [9] M. Bianchi, R. C. Hatch, Z. Li, P. Hofmann, F. Song, J. Mi, B. B. Iversen, Z. M. Abd El-Fattah, P. Löptien, L. Zhou, A. A. Khajetoorians, J. Wiebe, R. Wiesendanger, and J. W. Wells. “Robust Surface Doping of Bi₂Se₃ by Rubidium Intercalation”. In: *ACS Nano* 6.8 (Aug. 2012), pp. 7009–7015. DOI: 10.1021/nn3021822.
- [10] J. Henk, A. Ernst, S. V. Ereameev, E. V. Chulkov, I. V. Maznichenko, and I. Mertig. “Complex Spin Texture in the Pure and Mn-Doped Topological Insulator Bi₂Te₃”. In: *Physical Review Letters* 108.20 (May 2012). DOI: 10.1103/physrevlett.108.206801.
- [11] J. Henk, M. Flieger, I. V. Maznichenko, I. Mertig, A. Ernst, S. V. Ereameev, and E. V. Chulkov. “Topological Character and Magnetism of the Dirac State in Mn-Doped Bi₂Te₃”. In: *Physical Review Letters* 109.7 (Aug. 2012). DOI: 10.1103/physrevlett.109.076801.

- [12] D. Hsieh, Y. Xia, D. Qian, L. Wray, F. Meier, J. H. Dil, J. Osterwalder, L. Patthey, A. V. Fedorov, H. Lin, A. Bansil, D. Grauer, Y. S. Hor, R. J. Cava, and M. Z. Hasan. “Observation of Time-Reversal-Protected Single-Dirac-Cone Topological-Insulator States in Bi_2Te_3 and Sb_2Te_3 ”. In: *Physical Review Letters* 103.14 (Sept. 2009). DOI: 10.1103/physrevlett.103.146401.
- [13] R. C. Hatch, M. Bianchi, D. Guan, S. Bao, J. Mi, B. B. Iversen, L. Nilsson, L. Hornekær, and P. Hofmann. “Stability of the $\text{Bi}_2\text{Se}_3(111)$ topological state: Electron-phonon and electron-defect scattering”. In: *Physical Review B* 83.24 (June 2011). DOI: 10.1103/physrevb.83.241303.
- [14] H. Zhang, C.-X. Liu, X.-L. Qi, X. Dai, Z. Fang, and S.-C. Zhang. “Topological insulators in Bi_2Se_3 , Bi_2Te_3 and Sb_2Te_3 with a single Dirac cone on the surface”. In: *Nature Physics* 5.6 (May 2009), pp. 438–442. DOI: 10.1038/nphys1270.
- [15] Y. L. Chen, J. G. Analytis, J.-H. Chu, Z. K. Liu, S.-K. Mo, X. L. Qi, H. J. Zhang, D. H. Lu, X. Dai, Z. Fang, S. C. Zhang, I. R. Fisher, Z. Hussain, and Z.-X. Shen. “Experimental Realization of a Three-Dimensional Topological Insulator, Bi_2Te_3 ”. In: *Science* 325.5937 (June 2009), pp. 178–181. DOI: 10.1126/science.1173034.
- [16] K. Kuroda, H. Miyahara, M. Ye, S. V. Eremeev, Yu. M. Koroteev, E. E. Krasovskii, E. V. Chulkov, S. Hiramoto, C. Moriyoshi, Y. Kuroiwa, K. Miyamoto, T. Okuda, M. Arita, K. Shimada, H. Namatame, M. Taniguchi, Y. Ueda, and A. Kimura. “Experimental Verification of PbBi_2Te_4 as a 3D Topological Insulator”. In: *Physical Review Letters* 108.20 (May 2012). DOI: 10.1103/physrevlett.108.206803.
- [17] S. V. Eremeev, G. Landolt, T. V. Menshchikova, B. Slomski, Y. M. Koroteev, Z. S. Aliev, M. B. Babanly, J. Henk, A. Ernst, L. Patthey, A. Eich, A. A. Khajetoorians, J. Hagemester, O. Pietzsch, J. Wiebe, R. Wiesendanger, P. M. Echenique, S. S. Tsirkin, I. R. Amiraslanov, J. H. Dil, and E. V. Chulkov. “Atom-specific spin mapping and buried topological states in a homologous series of topological insulators”. In: *Nature Communications* 3.1 (Jan. 2012). DOI: 10.1038/ncomms1638.
- [18] M. Papagno, S. V. Eremeev, J. Fujii, Z. S. Aliev, M. B. Babanly, S. Kr. Mahatha, I. Vobornik, N. T. Mamedov, D. Pacilè, and E. V. Chulkov. “Multiple Coexisting Dirac Surface States in Three-Dimensional Topological Insulator $\text{PbBi}_6\text{Te}_{10}$ ”. In: *ACS Nano* 10.3 (Feb. 2016), pp. 3518–3524. DOI: 10.1021/acsnano.5b07750.
- [19] T. V. Menshchikova, S. V. Eremeev, Yu. M. Koroteev, V. M. Kuznetsov, and E. V. Chulkov. “Ternary compounds based on binary topological insulators as an efficient way for modifying the Dirac cone”. In: *JETP Letters* 93.1 (Mar. 2011), pp. 15–20. DOI: 10.1134/s002136401101005x.
- [20] T.V. Menshchikova, S.V. Eremeev, and E.V. Chulkov. “Electronic structure of SnSb_2Te_4 and PbSb_2Te_4 topological insulators”. In: *Applied Surface Science* 267 (Feb. 2013), pp. 1–3. DOI: 10.1016/j.apsusc.2012.04.048.

- [21] M. G. Vergniory, T. V. Menshchikova, I. V. Silkin, Yu. M. Koroteev, S. V. Eremeev, and E. V. Chulkov. “Electronic and spin structure of a family of Sn-based ternary topological insulators”. In: *Physical Review B* 92.4 (July 2015). DOI: 10.1103/physrevb.92.045134.
- [22] G. Kresse and J. Hafner. “Ab initio molecular dynamics for open-shell transition metals”. In: *Physical Review B* 48.17 (Nov. 1993), pp. 13115–13118. DOI: 10.1103/physrevb.48.13115.
- [23] G. Kresse and J. Furthmüller. “Efficient iterative schemes for ab initio total-energy calculations using a plane-wave basis set”. In: *Physical Review B* 54.16 (Oct. 1996), pp. 11169–11186. DOI: 10.1103/physrevb.54.11169.
- [24] P. E. Blochl. “Projector augmented-wave method”. In: *Physical Review B* 50.24 (Dec. 1994), pp. 17953–17979. DOI: 10.1103/physrevb.50.17953.
- [25] G. Kresse and D. Joubert. “From ultrasoft pseudopotentials to the projector augmented-wave method”. In: *Physical Review B* 59.3 (Jan. 1999), pp. 1758–1775. DOI: 10.1103/physrevb.59.1758.
- [26] J. P. Perdew, K. Burke, and M. Ernzerhof. “Generalized Gradient Approximation Made Simple”. In: *Physical Review Letters* 77.18 (Oct. 1996), pp. 3865–3868. DOI: 10.1103/physrevlett.77.3865.
- [27] S. Grimme, J. Antony, S. Ehrlich, and H. Krieg. “A consistent and accurate ab initio parametrization of density functional dispersion correction (DFT-D) for the 94 elements H-Pu”. In: *The Journal of Chemical Physics* 132.15 (Apr. 2010), p. 154104. DOI: 10.1063/1.3382344.
- [28] M.G. Vergniory, T.V. Menshchikova, S.V. Eremeev, and E.V. Chulkov. “Bulk and surface electronic structure of SnBi₄Te₇ topological insulator”. In: *Applied Surface Science* 267 (Feb. 2013), pp. 146–149. DOI: 10.1016/j.apsusc.2012.08.073.
- [29] T. Okuda, T. Maegawa, M. Ye, K. Shirai, T. Warashina, K. Miyamoto, K. Kuroda, M. Arita, Z. S. Aliev, I. R. Amiraslanov, M. B. Babanly, E. V. Chulkov, S. V. Eremeev, A. Kimura, H. Namatame, and M. Taniguchi. “Experimental Evidence of Hidden Topological Surface States in PbBi₄Te₇”. In: *Physical Review Letters* 111.20 (Nov. 2013). DOI: 10.1103/physrevlett.111.206803.
- [30] M. Bianchi, D. Guan, S. Bao, J. Mi, B. B. Iversen, P. D. C. King, and P. Hofmann. “Coexistence of the topological state and a two-dimensional electron gas on the surface of Bi₂Se₃”. In: *Nature Communications* 1.1 (Nov. 2010). DOI: 10.1038/ncomms1131.
- [31] M. Bianchi, R. C. Hatch, J. Mi, B. B. Iversen, and P. Hofmann. “Simultaneous Quantization of Bulk Conduction and Valence States through Adsorption of Nonmagnetic Impurities on Bi₂Se₃”. In: *Physical Review Letters* 107.8 (Aug. 2011). DOI: 10.1103/physrevlett.107.086802.

- [32] L. A. Wray, S.-Y. Xu, Y. Xia, D. Hsieh, A. V. Fedorov, Y. S. Hor, R. J. Cava, A. Bansil, H. Lin, and M. Z. Hasan. “A topological insulator surface under strong Coulomb, magnetic and disorder perturbations”. In: *Nature Physics* 7.1 (Dec. 2010), pp. 32–37. DOI: 10.1038/nphys1838.
- [33] C. Chen, S. He, H. Weng, W. Zhang, L. Zhao, H. Liu, X. Jia, D. Mou, S. Liu, J. He, Y. Peng, Y. Feng, Z. Xie, G. Liu, X. Dong, J. Zhang, X. Wang, Q. Peng, Z. Wang, S. Zhang, F. Yang, C. Chen, Z. Xu, X. Dai, Z. Fang, and X. J. Zhou. “Robustness of topological order and formation of quantum well states in topological insulators exposed to ambient environment”. In: *Proceedings of the National Academy of Sciences* 109.10 (Feb. 2012), pp. 3694–3698. DOI: 10.1073/pnas.1115555109.
- [34] L. Bao, L. He, N. Meyer, X. Kou, P. Zhang, Z.-G. Chen, A. V. Fedorov, J. Zou, T. M. Riedemann, T. A. Lograsso, K. L. Wang, G. Tuttle, and F. Xiu. “Weak Anti-localization and Quantum Oscillations of Surface States in Topological Insulator $\text{Bi}_2\text{Se}_2\text{Te}$ ”. In: *Scientific Reports* 2.1 (Oct. 2012). DOI: 10.1038/srep00726.
- [35] G. Bihlmayer, O. Rader, and R. Winkler. “Focus on the Rashba effect”. In: *New Journal of Physics* 17.5 (May 2015), p. 050202. DOI: 10.1088/1367-2630/17/5/050202.
- [36] S. V. Eremeev, M. G. Vergniory, T. V. Menshchikova, A. A. Shaposhnikov, and E. V. Chulkov. “The effect of van der Waal’s gap expansions on the surface electronic structure of layered topological insulators”. In: *New Journal of Physics* 14.11 (Nov. 2012), p. 113030. DOI: 10.1088/1367-2630/14/11/113030.
- [37] L. Plucinski, A. Herdt, S. Fahrendorf, G. Bihlmayer, G. Mussler, S. Döring, J. Kampmeier, F. Matthes, D. E. Bürgler, D. Grützmacher, S. Blügel, and C. M. Schneider. “Electronic structure, surface morphology, and topologically protected surface states of Sb_2Te_3 thin films grown on Si(111)”. In: *Journal of Applied Physics* 113.5 (Feb. 2013), p. 053706. DOI: 10.1063/1.4789353.
- [38] S. V. Eremeev, T. V. Menshchikova, I. V. Silkin, M. G. Vergniory, P. M. Echenique, and E. V. Chulkov. “Sublattice effect on topological surface states in complex $(\text{SnTe})_{n>1}(\text{Bi}_2\text{Te}_3)_{m=1}$ compounds”. In: *Physical Review B* 91.24 (June 2015). DOI: 10.1103/physrevb.91.245145.
- [39] J. Sánchez-Barriga, M. R. Scholz, E. Golias, E. Rienks, D. Marchenko, A. Varykhalov, L. V. Yashina, and O. Rader. “Anisotropic effect of warping on the lifetime broadening of topological surface states in angle-resolved photoemission from Bi_2Te_3 ”. In: *Physical Review B* 90.19 (Nov. 2014). DOI: 10.1103/physrevb.90.195413.
- [40] I. A. Shvets, I. I. Klimovskikh, Z. S. Aliev, M. B. Babanly, J. Sánchez-Barriga, M. Krivenkov, A. M. Shikin, and E. V. Chulkov. “Impact of stoichiometry and disorder on the electronic structure of the $\text{PbBi}_2\text{Te}_{4-x}\text{Se}_x$ topological insulator”. In: *Physical Review B* 96.23 (Dec. 2017). DOI: 10.1103/physrevb.96.235124.
- [41] M. G. Vergniory, T. V. Menshchikova, S. V. Eremeev, and E. V. Chulkov. “Ab initio study of 2DEG at the surface of topological insulator Bi_2Te_3 ”. In: *JETP Letters* 95.4 (Apr. 2012), pp. 213–218. DOI: 10.1134/s0021364012040108.

- [42] S. V. Eremeev, Yu. M. Koroteev, and E. V. Chulkov. “On possible deep subsurface states in topological insulators: The PbBi_4Te_7 system”. In: *JETP Letters* 92.3 (Aug. 2010), pp. 161–165. DOI: 10.1134/s0021364010150087.
- [43] A. M. Shikin, I. I. Klimovskikh, S. V. Eremeev, A. A. Rybkina, M. V. Rusinova, A. G. Rybkin, E. V. Zhizhin, J. Sánchez-Barriga, A. Varykhalov, I. P. Rusinov, E. V. Chulkov, K. A. Kokh, V. A. Golyashov, V. Kamyshlov, and O. E. Tereshchenko. “Electronic and spin structure of the topological insulator $\text{Bi}_2\text{Te}_{2.4}\text{Se}_{0.6}$ ”. In: *Physical Review B* 89.12 (Mar. 2014). DOI: 10.1103/physrevb.89.125416.
- [44] M. Neupane, S.-Y. Xu, L. A. Wray, A. Petersen, R. Shankar, N. Alidoust, Chang Liu, A. Fedorov, H. Ji, J. M. Allred, Y. S. Hor, T.-R. Chang, H.-T. Jeng, H. Lin, A. Bansil, R. J. Cava, and M. Z. Hasan. “Topological surface states and Dirac point tuning in ternary topological insulators”. In: *Physical Review B* 85.23 (June 2012). DOI: 10.1103/physrevb.85.235406.
- [45] K. Park, C. De Beule, and B. Partoens. “The ageing effect in topological insulators: evolution of the surface electronic structure of Bi_2Se_3 upon K adsorption”. In: *New Journal of Physics* 15.11 (Nov. 2013), p. 113031. DOI: 10.1088/1367-2630/15/11/113031.
- [46] K. Sumida, T. Natsumeda, K. Miyamoto, I. V. Silkin, K. Kuroda, K. Shirai, S. Zhu, K. Taguchi, M. Arita, J. Fujii, A. Varykhalov, O. Rader, V. A. Golyashov, K. A. Kokh, O. E. Tereshchenko, E. V. Chulkov, T. Okuda, and A. Kimura. “Enhanced surface state protection and band gap in the topological insulator $\text{PbBi}_4\text{Te}_4\text{S}_3$ ”. In: *Physical Review Materials* 2.10 (Oct. 2018). DOI: 10.1103/physrevmaterials.2.104201.

Graphene-based systems and heterostructures

In this chapter, investigations of the electronic band structure of different graphene-based systems have been reported. Despite the well-known exceptional properties of free-standing graphene, its role in heterogeneous structures is still under investigation. The versatility of graphene and its ability to improve the electronic properties of heterostructures is useful for various electronic and spintronic applications.

By means of Angle-Resolved PhotoEmission Spectroscopy, X-ray Photoemission Spectroscopy and by Density Functional Theory calculations, we investigate the role of graphene within different systems and heterostructures.

In the first part of the chapter I report the study of the magnetic coupling between different ferromagnetic metals (FMs) across a graphene layer and the role of graphene as a thin covalent spacer; in the second part I show electronic confinement effects underneath a graphene layer; in the last part, I report a work in progress focused on the interaction between graphene and a *4f* rare-earth metal.

2.1 Introduction

Since the first isolation of graphene in 2004 [1], the interest on atomically thin materials has increased, revealing a wide spectrum of unusual properties and novel physics that are not accessible in their 3D counterparts. Besides the discovery of 2D atomic materials has been considerably expanded over the past years, the research into graphene remains a cornerstone in academic and industrial research. Thanks to its unique electronic structure, graphene continues to offer opportunities for exploration of novel 2D physics.

The versatility of combining a graphene layer with other components provides an efficient method to design graphene-based system, heterostructures or junctions, by physical or chemical interaction. When graphene is combined with other materials, the result can bring to new materials with "novel hybrid properties" or to an improvement of graphene properties. These kind of phenomena take innovation in scientific knowledge and in materials science.

The ability to manipulate and tune these functionalities is an important target, and although much has been done in this context, still so much has to be discovered.

I report the investigation of the electronic band structure of selected ferromagnetic graphene-based junctions (FM/Gr/FM) in order to unveil the role of graphene and its "screening" effect of the interlayer magnetic coupling (section 2.2). In the second part of the chapter, the study of the electron quantum confinement effects of Ag-film between graphene and metallic substrates has been reported (section 2.3); the graphene passivation efficiency may offer the opportunity to transfer the longstanding expertise on quantum well states of noble metal thin films in application research areas. Finally, in the last part of the chapter (section 2.4) I report a work in progress focused on the interaction between graphene and a 4f rare-earth metal.

2.2 Graphene-based ferromagnetic junctions

Graphene has been proposed as an ideal material for spintronic devices due to the weak intrinsic spin-orbit interaction which support lateral spin transport and due to the high tunability of its electronic and magnetic properties. The electronic transport and the magnetic coupling between different magnetic species (such as isolated atoms, cluster, molecules) separated by a graphene layer has recently triggered interest for spintronics applications in vertical magneto devices [2–6]. Spin dependent transport perpendicular to the graphene plane results in tunneling magnetoresistance. According to the literature, concerning the behaviour of different ferromagnetic metals (FMs) chemically separated by a graphene layer, it has been predicted that the coupling can be either ferromagnetic or antiferromagnetic, depending on the choice of the two FM species, on the adsorption sites for isolated atoms and varies also in a complex way for dimers and larger aggregates [7–9].

In this context, aim of this work is to unveil the role of graphene in selected FM/Gr/FM junctions. In this part of the chapter, we examine the magnetic coupling between FM adsorbates (Fe, Co and Ni) deposited at room temperature (RT) on both Gr/Co(0001) and Gr/Ni(111) substrates and measured in remanent magnetization. By measuring the line shape of $3p$ core levels as a function of the direction of magnetization and along different symmetry directions of the substrate, we are able to investigate the dichroic effect in photoemission lines and detect the magnetic coupling across the graphene layer or its absence.

Our results show that for the selected FM/Gr/FM junctions, grown and measured at RT, no magnetic coupling is attained through the graphene layer. Therefore, the graphene inhibits the magnetic alignment that normally occurs when two FMs are put in contact.

2.2.1 Experimental details

The presented experiments were performed at the VUV beamline of the Elettra synchrotron radiation laboratory (Trieste, Italy), described in section A.4.1. We used W(110) crystal surface as substrate for the preparation of the ferromagnetic films. Such crystal was prepared by repeated high temperature flash-annealing cycles in oxygen atmosphere at a

base pressure of 5×10^{-6} mbar; the cleanliness of the W(110) surface was confirmed by the appearance of a sharp (1×1) LEED pattern and well-defined W 4f surface core level components, reported in Fig. 2.1.

The Co(0001) and Ni(111) films were grown *in-situ*, in the preparation chamber, on the W(110) crystal surface by evaporation of 10-25 monolayers of Co (or Ni) at RT from an electron-bombarded rod. The resulting ferromagnetic thin films showed a well-ordered (1×1) hexagonal pattern for both Co and Ni films, with sharp diffraction spots upon annealing at about 420 K.

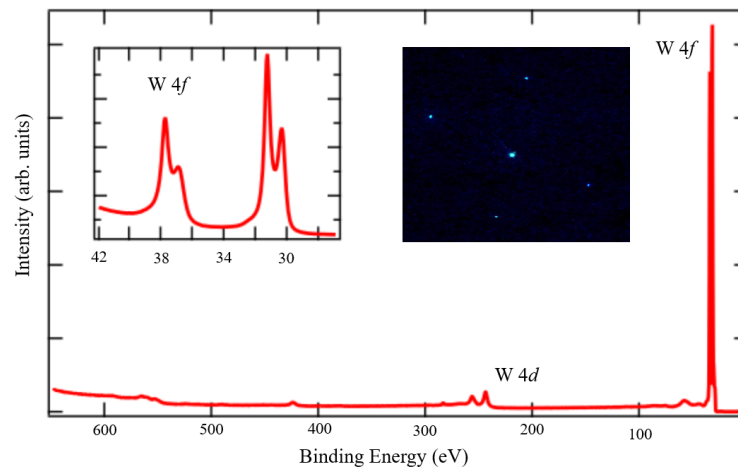


Figure 2.1: Photoemission wide spectrum taken on W(110) crystal at 730 eV of photon energy. In the inset we report the measurement of W 4f core levels taken with 70 eV photons and LEED image at 90 eV of electron beam energy.

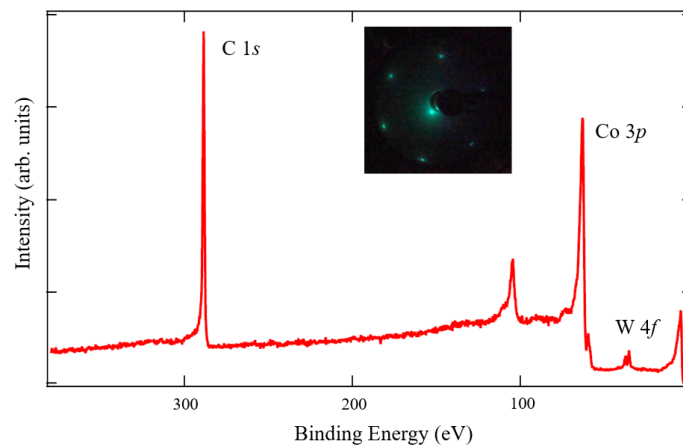


Figure 2.2: Photoemission wide spectrum taken at 730 eV of photon energy on Gr/Co/W(110). In the inset we report the corresponding LEED image at 90 eV of electron beam energy.

The graphene layer was grown, according to the procedure reported in Refs. [10–12], by chemical vapour deposition of ethylene (C_2H_4) for about 10 minutes at the base pressure of 5×10^{-6} mbar and at temperature of about 700 K, which seems to be the lower limit of temperature to avoid local breaking of the film. Surface quality, order and cleanliness were checked by LEED and core level measurements. The aforementioned procedure leads

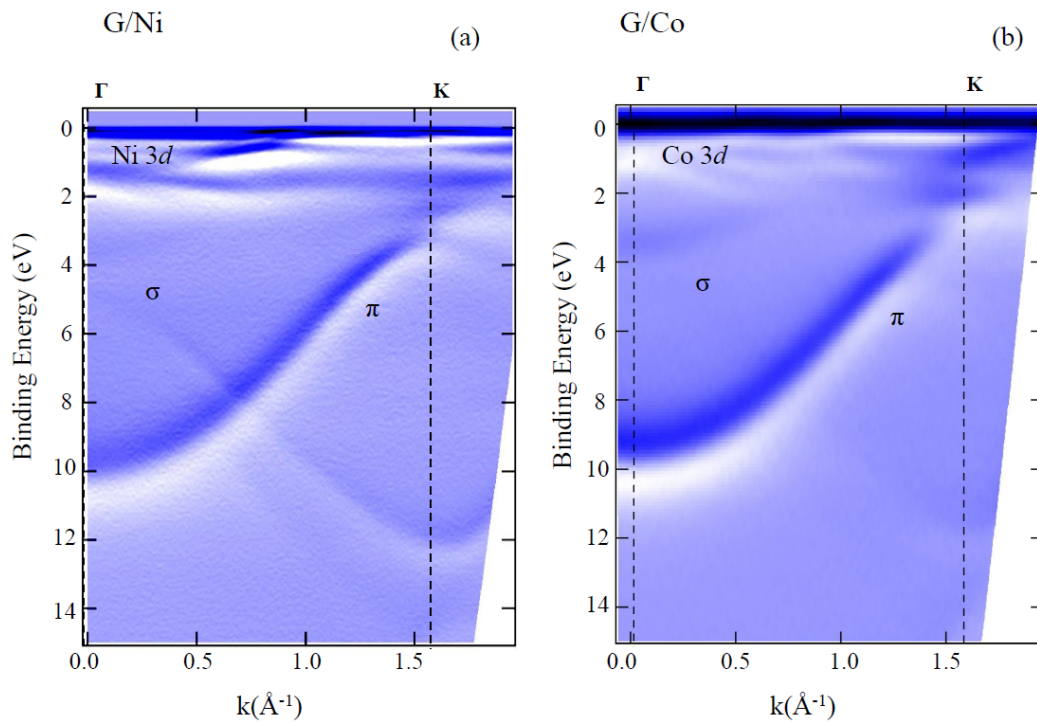


Figure 2.3: Second derivative along the energy axis of (a) Gr/Ni and (b) Gr/Co systems measured along the ΓK direction and at 60 eV of photon energy.

us to grow a single graphene domain on Co or Ni substrate and to obtain a sharp (1×1) LEED diffraction pattern and a single well-defined component of C 1s, as depicted in Fig. 2.2, which is the fingerprint of a single graphene domain. Since Ni(111), Co(0001) and graphene have nearly similar lattice parameters, the graphene forms an hexagonal (1×1) structure. By optimizing the preparation procedure, the graphene layer exhibits a highly ordered crystallographic structure without any visible defects even over large areas, as deduced from the LEED pattern.

In Fig. 2.3 we report the second derivative along the energy axis of the as-obtained Gr/Co and Gr/Ni structures; the ARPES measurements were taken along the ΓK direction of the Brillouin zone and with 60 eV of photon energy. The strong interaction between the graphene layer and the substrate manifests itself as a considerable modification of the graphene states and both Ni or Co related valence-band states as a result of the hybridization of the graphene π and metals 3d states, accompanied by a partial charge transfer from the FM substrate to graphene. Due to this strong interaction, the π -state of graphene is modified and shifted away from Fermi level. The Dirac cone results splitted in several parts, above and below the Fermi level, due to the mentioned interaction between C $2p_z$ and d states of the metallic substrate, and retains some similarities to the Dirac cone of free-standing graphene [11, 12].

The samples were magnetically saturated by applying a pulsed current to a coil wrapped around the sample holder, and always measured in remanent magnetization at RT. The Ni(111) and Co(0001) films were found to be in-plane magnetized respectively along the $[1\bar{1}0]$ and $[1\bar{1}00]$ symmetry directions. Along the magnetization directions, core level spectra exhibit a large dichroic effect when the magnetization direction was reversed from M_{up} to

M_{down} .

Ferromagnets (Fe, Co or Ni) were finally deposited on Gr/Co and Gr/Ni magnetized substrates at RT by evaporation of about 1 minute from an electron-bombarded rod at a base pressure of 2×10^{-10} mbar. These experimental conditions lead to form 3D clusters of FMs on the substrates without long-range order [13–17]. By measuring the intensity ratio of $3p$ photoemission components of the substrates and adsorbates, we estimate a coverage of FM below 1 ML. Core levels photoemission spectra were collected using a photon energy of 150 eV in order to minimize the photoelectron mean free path and to reduce the secondary electrons contribution.

Magnetic linear dichroism (MLD) measurements were performed preserving the non-coplanar three vector geometry: the incoming light polarization, the magnetization direction and the direction of the outgoing photoelectrons are not on the same plane. Light with linear horizontal polarization was impinging on the sample at 45° with respect to the normal direction. Electrons were collected under normal emission with about 30° full acceptance along the scattering plane (xy). The scattering geometry of our experiments is reported in Fig. 2.4(a). All spectra were measured at RT which is far below the Curie temperature¹, required condition for the investigation of the ferromagnetic films.

The Co or Ni easy magnetization axis² is set to lie at different angles with respect to the scattering plane by means of azimuthal rotation of the sample. If the easy magnetization axis is oriented along z , namely perpendicularly to the scattering plane, the core levels spectra exhibit a large dichroic signal when the magnetization is reversed from positive (M_{up}) to negative (M_{down}) z values. The M_{down} magnetization was achieved by azimuthal rotation of the sample of 180° , which is equivalent of reversing the sample during the magnetization. This leads to an interchange of the energetic positions of the multiplet sublevels, due to dipole matrix element effects [19], i.e. reversing the magnetization will not change the intensity of the states but the energetic position of the multiplets and consequently the resulting line shape (which is a convolution of sublevels) will be different for M_{up} and M_{down} . The dichroic signal is obtained by calculating the asymmetry, i.e. the difference between spectra acquired with different magnetization divided by their sum, $A = (I^{M_{up}} - I^{M_{down}}) / (I^{M_{up}} + I^{M_{down}})$ ³. This quantity is proportional to the surface magnetization, i.e. to the average orientation of magnetic moments at surface, thus defining an element-specific order parameter.

2.2.2 Results and discussion

In Fig. 2.4 we report the MLD measurements taken on the Ni/Gr/Co system. The sample was prepared by depositing 0.2 ML of Ni on the G/Co substrate remanently magnetized (i.e. magnetization before FM deposition). In both (b) and (d) panels, the line shape of Co $3p$ and Ni $3p$ photoemission peaks were monitored along different azimuthal directions, starting from the easy magnetization axis direction up to the perpendicular one, and pair spectra

¹The Curie temperature is defined as the transition temperature between a ferromagnetic and paramagnetic phase [18]; For Ni and Co, Curie temperatures are 620 K and 1390 K, respectively.

²The Easy axis is an energetically favourable direction of spontaneous magnetization.

³All MLD spectra were normalized to the background intensity before calculating asymmetry spectra.

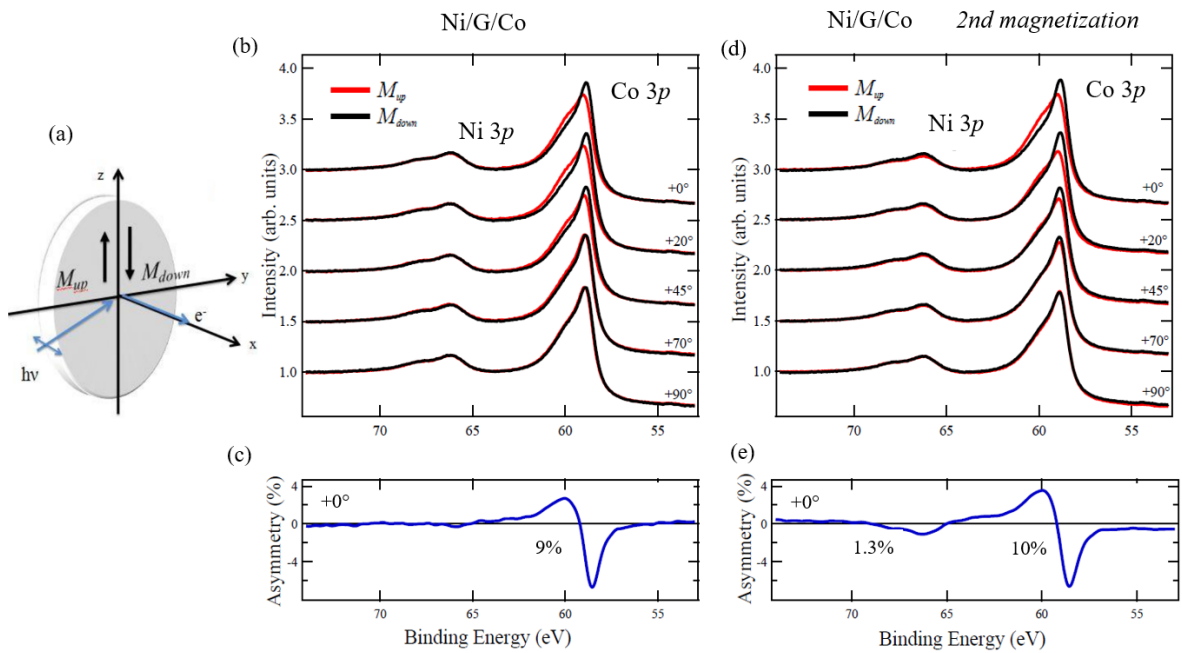


Figure 2.4: (a) MLD chiral geometry. Core level measurements taken on (b) 0.2 ML Ni/Gr/Co in remanent magnetization prior to the Ni deposition, and (d) after the Ni deposition, showing Co 3*p* and Ni 3*p* photoemission peaks acquired along selected azimuthal directions and for different magnetizations (M_{up} and M_{down}); (c)-(e) asymmetry curves extracted from data taken at $+0^\circ$ from panels (b) and (d), respectively.

were obtained by reversing the magnetization. In Fig. 2.4 (a), the dichroic signal is present for the Co 3*p* photoemission peak, while is not observed for the Ni 3*p* peak, as confirmed by the asymmetry curve reported below in panel (c). The dichroism signal measured for the Co 3*p* peak consists in a plus/minus feature about 1.5 eV wide, and a maximum peak-to-peak asymmetry of about 9% (see panel (c)), in agreement with previous results [20]. Extrema (minimum and maximum) correspond to $m_j = \pm 3/2$ sublevels of the Co 3*p* multiplets [21]. Our MLD results show that while the Co substrate is magnetized, no magnetic coupling is transmitted to the Ni clusters.

In order to check the capability of the Ni clusters to align their magnetic moments, we applied a second magnetic pulse to the Ni/Gr/Co system. The result is reported in Fig. 2.4(d): besides a slightly increased asymmetry of Co 3*p* extracted from data taken at $+0^\circ$ (from about 9% up to 10%) a detectable asymmetry of Ni 3*p* is extracted (about 1.3%) as we can appreciate from panel (e) and the similarity between the shape of the dichroic signals, with a prominent minus feature, indicates that Ni and Co moments are parallelly aligned, i.e. Ni-Co ferromagnetic coupling.

Similar MLD experiments were performed when Fe clusters were deposited on top of Gr/Co and Gr/Ni substrates and in remanent magnetization conditions. With respect to the Ni 3*p* photoemission peak, the Fe 3*p* peak is expected to exhibit a strong dichroic behaviour, according to Ref. [22], allowing us to detect also faint line shape variation induced by the substrate magnetization. Similarly to the previous measurements, in Fig. 2.5 we can observe that while the substrates (Co in panel (a) and Ni in (b)) exhibit the expected magnetization,

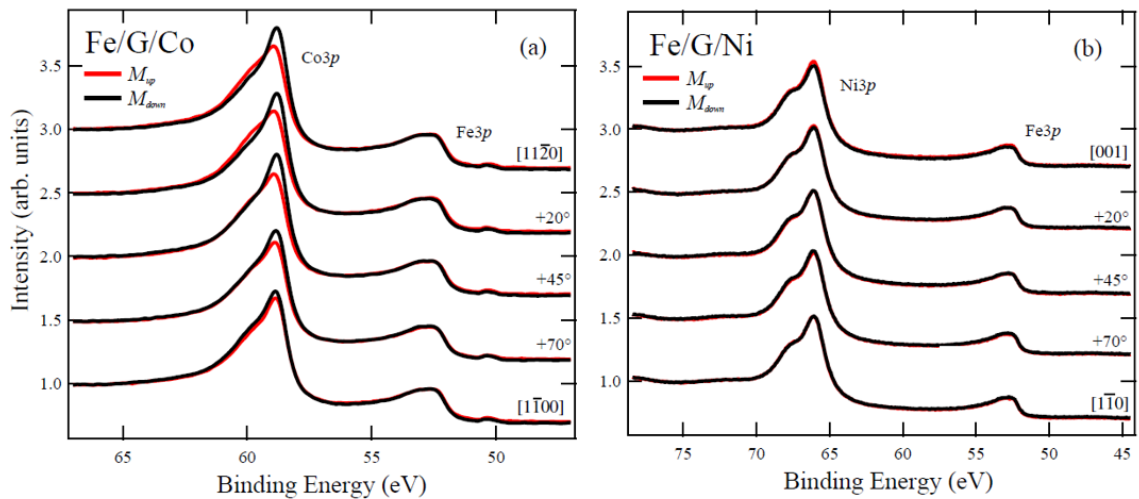


Figure 2.5: Core level measurements taken on (a) 0.4 ML Fe/Gr/Co and on (b) 0.3 ML Fe/Gr/Ni showing $3p$ photoemission peaks acquired along selected azimuthal directions and for different magnetizations (M_{up} and M_{down}).

with the easy magnetization axis along $[1\bar{1}00]$ and $[1\bar{1}0]$, respectively, no dichroic effect is seen for the Fe $3p$ photoemission peak related to the absorbed ferromagnetic clusters. Once again, our results confirm that the remanently magnetized substrate (either Co or Ni) is screened by the graphene layer.

To shed light on the "screening" effect of graphene, we compared our previous results with those obtained for a partially graphene covered substrate, see Fig. 2.6. The uncovered Co surface was estimated to be below 10% by evaluating the ratio of C $1s$ /Co $3p$ photoemission peaks, taken at 730 eV of photon energy, with respect to the ratio obtained at the saturation coverage, Fig. 2.7(c).

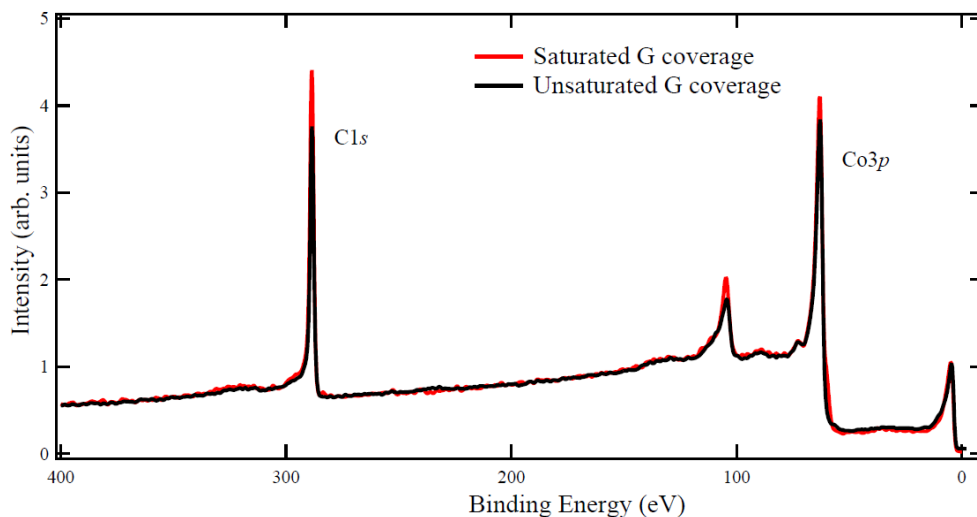


Figure 2.6: Comparison between the core level measurements of the saturate (red curve) and unsaturated (black curve) Gr coverage, referred to fig. 2.7 (a) and (c), respectively. The measurements have been performed with 730 eV of photon energy.

The starting point relies in the analysis of the dichroic behavior of Fe clusters, of about

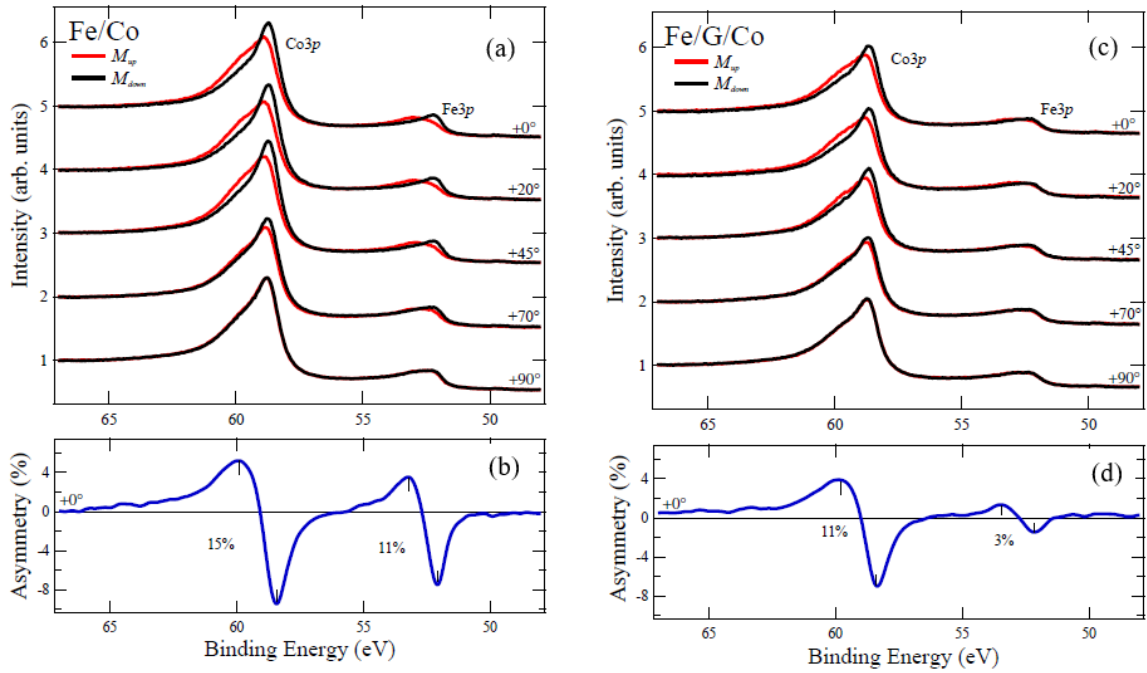


Figure 2.7: Core level measurements taken on (a) 0.2 ML Fe/Co, (c) partially covered 0.2 ML Fe/0.9 ML Gr/Co, showing Fe 3p and Co 3p photoemission peaks acquired along selected azimuthal directions and for different magnetizations; (b) and (d) asymmetry curves extracted from data taken +0° of panels (a) and (c), respectively.

0.2 ML, deposited on a pristine magnetically saturated Co film. As we can deduce from Fig. 2.7(a), Co atoms and Fe overlayer both produce a significant ferromagnetic coupling, highlighted by the corresponding asymmetry spectrum in panel (b) with a maximum peak-to-peak asymmetry of about 11% and 15% for Fe 3p and Co 3p, respectively. Moreover, the similarity between the shape of the respective dichroic signals, with a prominent minus feature, indicates that Co and Fe moments are parallelly aligned, i.e. Fe-Co ferromagnetic coupling. Further, we show the partially covered Gr/Co surface reported in Fig. 2.7(c)-(d), achieved by means of exposures to ethylene below the saturation condition (Fig. 2.6). What stands out at first sight is the drastic reduction of the maximum peak-to-peak asymmetry, as reported in Fig. 2.7 (d), related to the Fe atoms: from 11% to 3%. By comparison of the corresponding MLD measurements with those obtained for a fully covered substrate, we can deduce that the strong Fe-Co ferromagnetic coupling seen in Fig. 2.7 (c)-(d), is due to a direct contact of the two metals in the reduced uncovered regions. Therefore, we conclude that the presence of graphene in our junctions weakens the exchange interactions between the ferromagnets, leading to a decoupling of their magnetic moments. In a defect-free Gr/Ni system the net magnetic moment of carbon was evaluated to be of about $0.01 \mu_B$ per atom [23, 24], taking into account that in the two different absorption sites on Ni(111) carbon atoms acquire opposite polarization compared to the substrate. The magnetic interactions through the graphene layer is based on the direct exchange, and has therefore a different origin from the well-known interlayer oscillatory coupling through non-magnetic and metallic spacers.

In some earlier XMCD experiments [25], it was observed a significant graphene mediated exchange coupling between Co isolated atoms and Ni(111). The experiments were performed on similar junctions, Co/Gr/Ni and the exchange coupling between Co isolated atoms and Ni (111) film substrate, was found to change from ferromagnetic to antiferromagnetic. Such junctions were prepared and measured at low temperature ($T < 5$ K). Therein, it was found that the coupling depends on the adsorption site of the single Co atoms and on the coverage of the adlayer. The Co-porphyrin molecules display a different magnetic coupling mechanisms with a Ni(111) crystal via graphene, at temperature of about 10 K [3, 8]. These systems show the sensitivity of exchange interaction mediated by graphene to the geometrical arrangement and local coordination of magnetic adatoms.

In the present experiments, we performed MLD measurements on different kind of FM/G/FM junctions, achieved at RT by depositing 3D FM clusters on selected substrates. From the analysis of the MLD response, we find that such Gr-mediated exchange coupling is not sufficient to align the magnetic moment of the deposited $3d$ metals and consequently they do not exhibit any magnetic alignment. By comparison with other experiments (such as Ref. [9]) we can deduce that the effective magnitude of the coupling is reduced due to the 3D nature (cluster) of our FM. The absence of remanent magnetization can find explanation both in the different growth mode of the 3D metals and on the measurement conditions. On one side, the sign of the magnetic coupling depends on the adsorption sites with respect to the graphene lattice [25]. The magnetic coupling of 3D aggregates through graphene therefore results by an averaging effect between ferro- and antiferromagnetic exchange interactions. The effective magnitude of the coupling is expected to be further reduced for overlayers grown at RT, where 3D clustering can be favoured with respect to a 2D growth. If 3D cluster growth prevails, the number of atoms in contact with graphene is reduced and the effective exchange interaction proportionally decreased with respect to ideal 2D growth [7].

The absence of adlayer magnetization suggests that disordered ferromagnetic domains of the 3D cluster form but they point in different spatial directions or, less likely, the presence of fluctuating paramagnetic units. In fact, by applying a magnetic pulse to the Ni/Gr/Co junction (Fig. 2.4(d)), we found that the secondly applied field partially orients the magnetization of the overlayer to the substrate and a weak magnetic coupling appears, indicating that at least a significant fraction of the metal is blocked at RT with respect to thermal fluctuations.

We can conclude that in our experiments a shielding effect of a saturated graphene layer towards FM clusters, with respect to a direct contact between the same metals, has been observed. These results add useful information to the existing literature and confirm the complex behaviour of the exchange interaction mediated by a graphene layer.

The results here shown are reported in the manuscript: "*Magnetic decoupling of ferromagnetic metals through a graphene spacer*", **I. Grimaldi**, M. Papagno, L. Ferrari, P. M. Sheverdyeva, S. K. Mahatha, D. Pacilé and C. Carbone, *Journal of Magnetism and Magnetic Materials* Volume **426**, 15 March 2017, Pages 440-443. The manuscript is available [here](#).

2.3 Silver *sp*-derived quantum well states between graphene and metallic substrates

The discrete quantum well (QW) states formed between thin metal films grown on appropriate supporting metal substrates can be easily understood in simple terms by using the particle-in-a-box picture [26, 27]. In the case of metallic films deposited on metal surfaces, the boundaries which are the substrate/film interface and the film/vacuum interface, define a one-dimensional potential well of width corresponding to the film thickness. The valence electrons of the films can acquire a standing wave character and present a discrete QW energy spectrum under two conditions. First of all, an ordered film of uniform thickness is required. To this end, optimized growth conditions such as the deposition rate, temperature, absence of contaminants, etc., are necessary to get clean and flat films over large areas of the substrate. Secondly, the electron reflectivity at the interface must be different from zero. This condition avoids the full propagation of the electron waves into the bulk of the supporting material. It was shown that even for closely matched materials (Ag and Au), a reflectivity of few percent leads to observable effects of electron confinement [28, 29]. Microscopic techniques, such as scanning tunneling spectroscopy [30, 31] and low-energy electron microscopy [32], allow to reveal and study the presence of discrete QW states in films of reduced lateral dimensions (few tens of nm) with limited momentum resolution. Angle-resolved photoemission spectroscopy, through its energy and momentum conservation selection rules, provides us valuable information on QW states such as the photon energy dependence, the role of the atomic potential within the films etc. ARPES provides high energy and momentum resolutions at once, but averages over few to hundreds of μm (mainly depending on the optical focusing of the photon beam). Therefore, the growth of atomically flat films on large areas of the substrate is mandatory for the study of electron confinement effects by means of spectroscopy technique. Indeed, many *sp*- and *d*-like metal films, grown according to optimized procedures, display well-defined QW state peaks in ARPES spectra. Conversely, the coexistence of multiple film thicknesses (and/or roughness) over the area scanned by ARPES result in ill-defined confinement conditions and broad spectral features [33].

Starting from these premises, the intercalation of metals underneath a graphene layer, which has been widely studied, appears as an uncertain method for the creation of flat and uniform films and the consequently observation of electron confinement effects by ARPES. In fact, the intercalation process involves mass transport through defects of the graphene layer and should favour an inhomogeneous film growth. Until now, a lot of experimental studies examined the intercalation of thin metal films underneath a graphene layer with microscopic and surface sensitive probes [10, 34–39]. For instance, scanning tunneling microscopy/spectroscopy (STM/STS) pointed out the weak interaction of intercalated Ag(111) or Au(111) films with ordered graphene flakes [37–39]. At present, specific information about the properties of deeper lying layers of the metal is not available.

In the present study we analyse by means of ARPES technique the electronic band structure of silver films intercalated in the Gr/Co(0001) interface, and we compared the

results with those obtained for the bare Ag/Co(0001) interface. The observation of Ag *sp*-derived QW states allow us to affirm that the intercalation process is a viable route for the production of atomically uniform Ag(111) films. The interaction between graphene and the underlying films gives rise to a large π - π^* band gap opening, and a hybridization gap between π and Ag 4*d* levels. Other signature of that coupling are the shift of the Ag(111) surface state and the downward shift of the Dirac point (*n*-type doping).

Beside the fundamental interest of these findings, the creation of uniform films with well-defined electronic states may simplify the understanding of the electron transport properties across the Gr/metal contact interface. Moreover, many physical properties (among them transport properties) and ultimate applications require surfaces that are exposed to ambient environment (1 atm and RT). One critical issue is then how the thin films will behave under such ambient conditions. While this problem has been overcome in selected semiconductor heterostructures [40], it is certainly still open for thin metal films. In this respect, thanks to the graphene passivation efficiency, the present study may offer the opportunity to transfer the longstanding expertise on QW states of noble metal thin films in application research areas. These systems can be considered as useful prototypes of graphene-protected thin metal films displayed electron quantum confinement effects.

2.3.1 Experimental details

The present experiments were carried out at the VUV-Photoemission beamline of the Elettra synchrotron radiation facility in Trieste, see section A.4.1. We used as substrate a W(110) crystal, which has been prepared following the procedure reported in section 2.2.1.

A thick Co film of about 5-6 nm was grown on the clean W(110) crystal by evaporation of Co at RT and followed by a post-annealing to approximately 420 K; this procedure has been described also in section 2.2.1. Starting from the as-prepared Co(0001)/W(110) substrate, we prepared two different systems, Gr/Ag/Co and Ag/Co(0001), in order to compare the electronic band structures of the system without graphene layer with the Ag intercalated system. The Ag intercalated system was prepared by Ag intercalation in graphene on thick Co(0001) films, as described in [10]. At first, the Ag was evaporated on top of the graphene layer at RT. Then, the sample was repeatedly annealed at about 700 K for a total time of about 30 minutes; this process leads to the formation of Gr/Ag(111), as previously reported [38, 39]. In Fig. 2.8(a) we report the LEED image of the as-prepared system; we can clearly observe the $(7 \times 7)/(6 \times 6)$ moiré superstructure of graphene on a Ag film on Co(0001): the inner yellow arrows indicate the spots of the superstructure, while the outer white ones indicate Gr multidomains. The intercalation process was also monitored by core levels and valence band spectra.

The Ag films were directly grown on bare Co(0001) substrate using a resistively heated drop on a tungsten filament, with the substrate kept at 80 K and successively annealed at RT, in order to favour the formation of layers with atomically uniform thickness. Due to the lattice mismatch (13.1%; $a_{Co} = 2.51 \text{ \AA}$ and $a_{Ag} = 2.89 \text{ \AA}$ are the nearest neighbour distances), few-layers Ag films display a moiré superstructure with the axis aligned to the main directions of

Co(0001) substrate, as showed in Fig. 2.8(b). Above 6 monolayers (ML) (1ML = 2.36 Å) the (1×1) of Ag(111) is recovered in the low-energy electron diffraction (LEED) pattern.

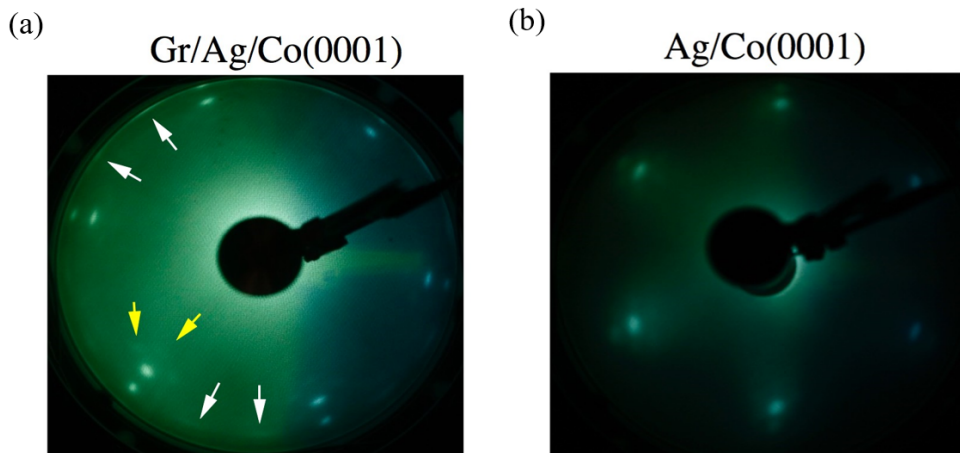


Figure 2.8: LEED images performed at 110 eV of electron beam energy: (a) the $(7 \times 7)/(6 \times 6)$ moiré superstructure of the system with Ag film intercalated on Gr/Co(0001), where yellow arrows indicate the spots of the superstructure while white ones indicate Gr multidomains; (b) the moiré superstructure of a Ag film of 2.5 ML thickness grown on Co(0001) substrate.

We have performed the intercalation of Ag using two different substrates, Gr/Co(0001) and Gr/Pt(111), in order to shed light on the substrate effect; Pt(111) crystal was prepared by repeated Ar^+ sputtering at 1.5 keV of beam energy and high temperature flash-annealing cycles in oxygen atmosphere, until a sharp (1×1) LEED pattern and well-developed core level components were observed. The graphene layer was grown by exposing the as-obtained Pt(111) surface to a partial pressure of 5×10^{-7} mbar of ethylene, with the temperature kept at about 1100 K in order to grow the $(\sqrt{3} \times \sqrt{3})R30^\circ$ graphene domain [41, 42]. The intercalation of Ag deposits on Gr/Pt(111) was achieved as previously described for the Co substrate.

Representative XPS data are reported in Fig. 2.9. In the upper spectra we report the XPS data recorded at 636 eV of photon energy on the Gr/Ag/Co(0001) system, with 2.5 ML of Ag intercalated. The black curve is related to the Co(0001) bare substrate; no peaks related to the W(110) substrate are visible, which indicate a thick coverage of the Co film. In addition to LEED measurements, the growth of the graphene layer on Co substrate is confirmed by a single and well defined C 1s core level peak, as shown by red curve reported in Fig. 2.9(a). The blue curve has been measured after the Ag intercalation: Ag 4d related peaks are visible. In Fig. 2.9(b), we report similar measurements performed on Gr/Ag/Pt(111), monitoring the following steps: Pt(111) (black curve), Gr/Pt(111) (red curve) and Gr/Ag/Pt(111) (blue curve).

2.3.2 Results and discussion

The structural properties of graphene on intercalated Ag multilayers have been reported in the literature [38]. Due to the mismatch between the planar lattice constants of graphene and Ag(111) (14.9%; $a_{\text{Gr}} = 2.46 \text{ \AA}$, $a_{\text{Ag}} = 2.89 \text{ \AA}$), a $(7 \times 7)/(6 \times 6)$ moiré structure with a periodicity of 16.4 Å, has been observed in LEED measurements and reported in Fig. 2.8(a); yellow arrows

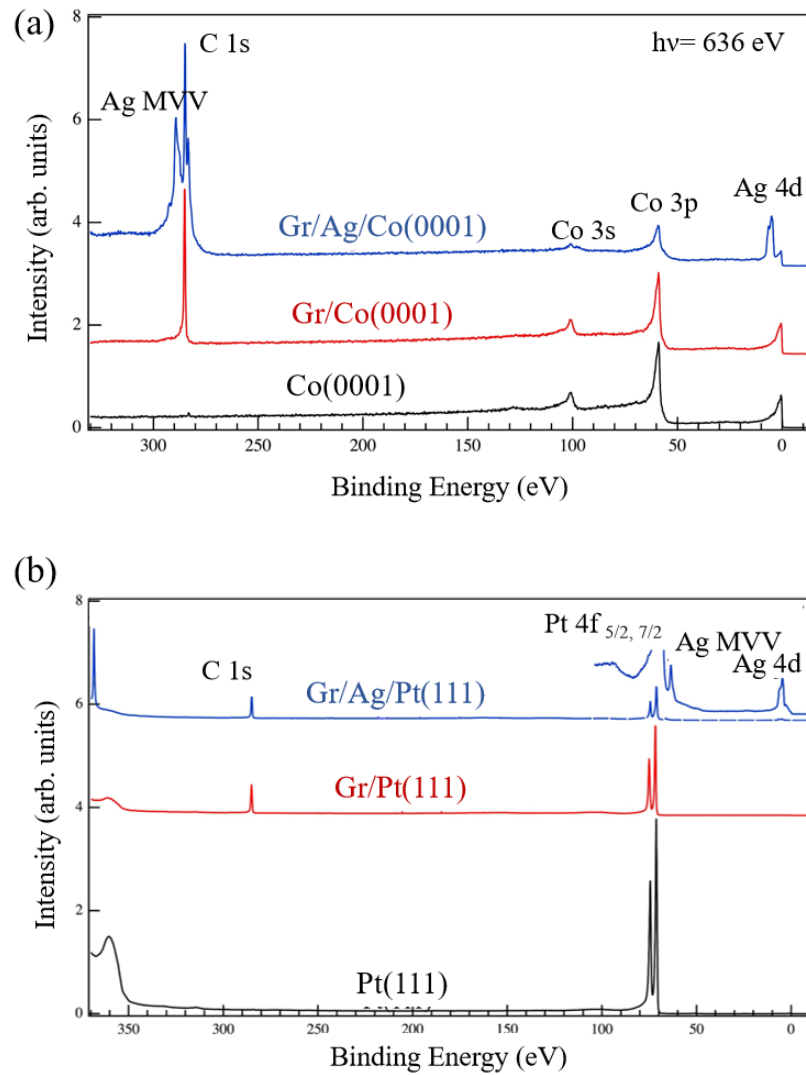


Figure 2.9: (a) Representative XPS measurements on Co(0001) (black curve), Gr/Co(0001) (red curve) and Gr/2.5ML Ag/Co(0001) (blue curve) taken with 636 eV of photon energy. (b) Representative XPS measurements on Pt(111) (black curve), Gr/Pt(111) (red curve) and Gr/0.5ML Ag/Pt(111) (blue curve) taken with 425 eV of photon energy. The last curve has been amplified below 100 eV to highlight Ag 4d related peaks.

indicate the spots of the superstructure, while the white ones the Gr multidomains. We achieved the intercalation of Ag using two different substrates, Gr/Co(0001) and Gr/Pt(111). The electronic structure of Gr/Co(0001) has been widely characterized by means of ARPES measurements in previous studies [10, 11].

Starting from the Gr/Co interface, we proceeded with Ag intercalation by following the annealing procedure previously described and reported in section 2.3.1. In Fig. 2.10 we show the second derivative along the energy axis of the related ARPES measurements performed on Gr/Ag/Co, acquired at 18 K and 55 eV of photon energy and centered at Γ point. We can clearly observe the presence of two main dispersing feature, with the minimum located at the Γ point and highlighted by white arrows, which are the *sp*-derived QW states arising from the intercalated Ag film. In the case of free-standing Ag(111) films, the QW states would appear with parabolic dispersion but more packed to each other and closer to Fermi level as the film thickness increases. If Ag films are grown on single crystals, the hybridization effects with the surface-projected bands of the substrate modify the ideal behaviour in specific region of the energy-momentum space [43–45]. In order to catch the similarity with Ag *sp*-derived QW states on Co(0001) and to quantify by comparison the number of intercalated layers, we performed the same ARPES investigation on the second prepared system, i.e. Ag/Co(0001), starting from 0.5 ML of Ag on bare Co substrate and by progressively increasing the Ag coverage. In Fig. 2.11 we report the second derivative along the energy axis of the ARPES measurements, taken at 18 K with photon energy of 55 eV and centered at Γ point for different Ag coverage: (a) 2 ML Ag/Co(0001) and (b) 6-7 ML Ag/Co. In Fig. 2.12 the second derivative of the ARPES images of the estimated coverage of 2.5 ML Ag/Co(0001), accompanied by the related extracted EDC curves.

At first glance, we recognize the same main dispersing feature, i.e. the deeper QW state, with the minimum located at about 2.64 eV of binding energy for (i) the Gr/Ag/Co(0001) system in Fig. 2.10 (a), for (ii) the Ag films grown on bare Co for an estimated coverage of 2 ML reported in Fig. 2.11(a) and for (iii) 2.5 ML in Fig. 2.12(a). As we can clearly observe, this state is the only seen for a thickness of 2 ML while the higher one, with minimum at 2.12 eV of binding energy, is characteristic of 3 ML uniform coverage, as also deduced from comparison with existing literature on Ag/Ni(111) [46]. Therefore, we can deduce from the analysis of their parabolic trend and binding energy position that the number of Ag QWs seen in Fig. 2.10(a) are comparable to the results obtained for a Ag coverage on bare Co(0001) substrate between 2 and 3 ML. Weaker QWs with minimum located between 1.2 and 1.4 eV of binding energy, clearly detected in the same Fig. 2.10(a), are instead signature of regions with a higher number of intercalated layers, as also deduced by comparison with the coverage of 6-7 ML of Ag on bare Co(0001), reported in Fig. 2.11(b). However, the typical coherence length required to observe QW states is in the order of 50 Å, therefore we can assume that in our system there are mainly homogeneous and flat regions of 2 or 3 ML coverage of the Ag film, each of which must have this minimum required size. Moreover, by comparing our ARPES results, we can attribute the non-dispersing state close to the Fermi level in Fig. 2.10(a) to the Co *3d* bands.

More interestingly, the comparison of our data also shows the shift of the surface state in

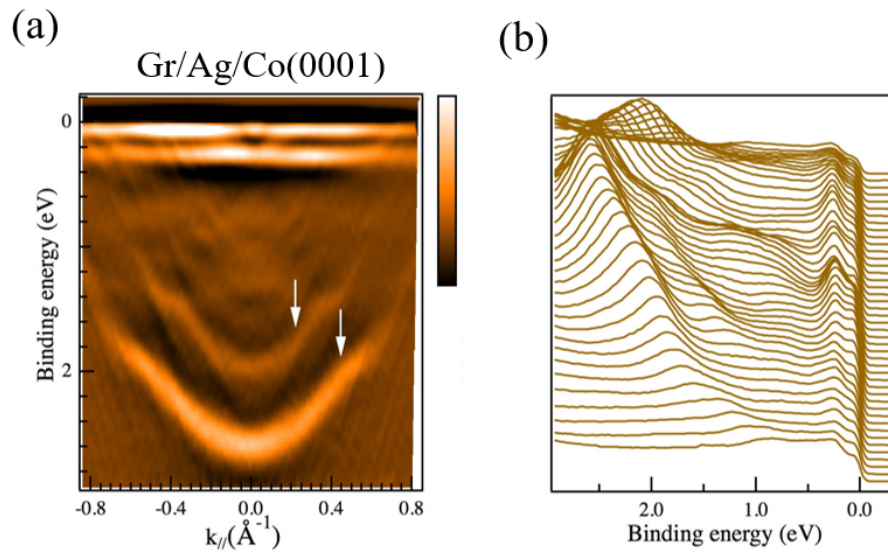


Figure 2.10: (a) Second derivative along the energy axis of the ARPES measurements, taken with photon energy of 55 eV and centered at Γ point of Gr/2.5ML Ag/Co(0001) system. White arrows highlight the Ag *sp*-QW states. (b) Energy distribution curves extracted from the presented measurements.

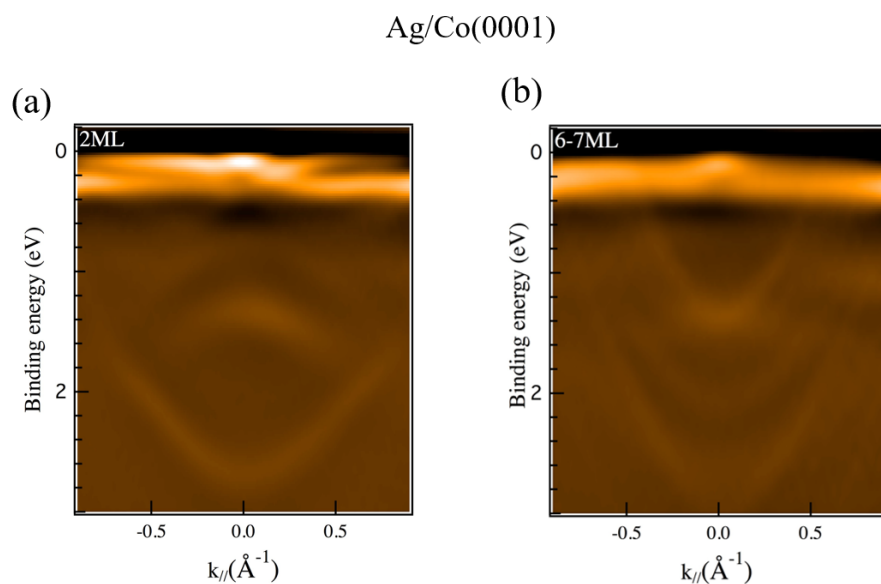


Figure 2.11: Second derivative along the energy axis of the ARPES measurements, taken with photon energy of 55 eV and centered at Γ point of (a) 2 ML Ag/Co(0001) and (b) 6-7 ML Ag/Co.

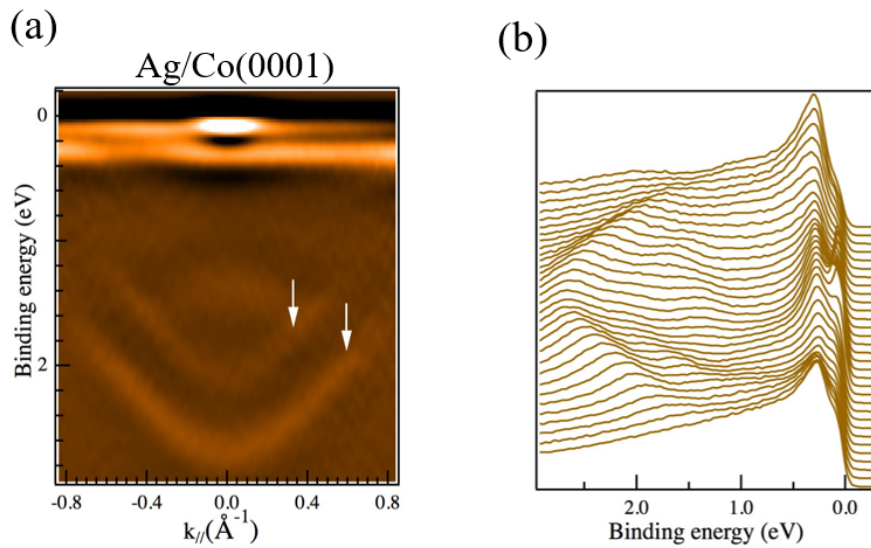


Figure 2.12: (a) Second derivative along the energy axis of the ARPES measurements, taken with photon energy of 55 eV and centered at Γ point of 2.5ML Ag/Co(0001) system. White arrows highlight the Ag *sp*-QW states. (b) Energy distribution curves extracted from the presented measurements.

Gr/Ag/Co system which is expected for Ag(111) single-crystal upward dispersing feature around the Γ point, with a minimum located at about 67 meV at 5 K [47–49].

In the Ag films grown directly on bare Co(0001) the surface state is the most prominent feature observed across the Fermi level, dispersing around Γ within $k = \pm 0.15 \text{ \AA}^{-1}$, as seen from Fig. 2.12(b) and highlighted also from the extracted EDC. Several studies have shown that the adsorption of graphene on weakly interacting metals (i.e. Pt, Ir, Au) preserve the surface states [35, 49]. In the present system, the shift of the Ag surface state is in agreement with previous STM and STS measurements performed on Gr/15 ML Ag/Ir(111) [36]; in that case the surface of 15 ML Ag(111)/Ir(111) exhibits a surface state shifted up in energy when located under graphene, from -0.075 eV up to 0.011 eV of binding energy. For this reason, in analogy with what has been reported in the literature, we can interpret the small intensity near Fermi level at the Γ point as the tail of the surface state, as visible also from Fig. 2.12(a). Such shift toward unoccupied states has been explained as two combined factors: (i) as due to the net epitaxial strain of the Ag lattice constant [50, 51] and (ii) the perturbation introduced by the Gr layer in changing the boundary conditions for both surface states (from vacuum to a graphene boundary). In the first case, the strain exerted on the lattice concomitant with the formation of epitaxial Ag(111) films is expected to change the (111)-in-plane lattice constant, as in the case of Ag(111) on Si(111) with a strain of the 0.95% [50] or for 15 ML Ag(111)/Ir(111) with a strain of 1.06% evaluating from the moiré pattern [36]. Similar results have been obtained for graphene nanoflakes on Ag/Ir(111) by STS investigations [38]. Uncovered Ag films on Ir(111) substrate exhibit already a shift above the Fermi level of the surface state, which is further increased in graphene-covered regions. For the present system, we can rule out that the effect of strain is responsible of the shift, as Ag films on bare Co(0001) exhibit the surface state below Fermi level, as highlighted by measurements reported in Fig. 2.12.

Therefore, we can conclude that the interaction of the graphene layer on Ag multilayers is strong enough to change the surface potential, in analogy with the adsorption of Xe on Ag(111) substrate, for which has been measured an upward shift of the surface state from -67 to +52 meV [52].

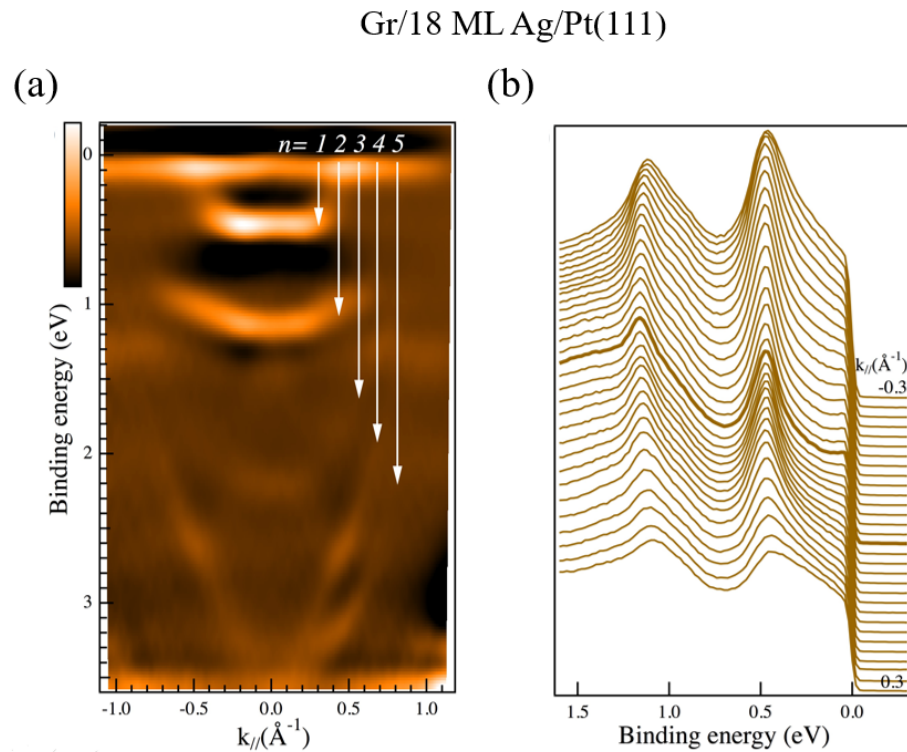


Figure 2.13: (a) Second derivative along the energy axis of the ARPES measurements, taken with photon energy of 70 eV and centered at Γ point and taken along ΓM direction of Gr/18 ML Ag/Pt(111) system. White arrows and quantum number n highlight the Ag *sp*-QW states. (b) Energy distribution curves extracted from the presented measurements in a range of $\pm 0.3 \text{ \AA}^{-1}$.

To shed light on the role of the supporting substrate, we have performed similar experiments on Ag multi-layers intercalated in Gr/Pt(111) system, as reported in Fig. 2.13. In analogy with the trend observed on bare Pt(111) [43], in panel (a) of Fig. 2.13 we observed the presence of Ag *sp*-derived QW states arising from the intercalated multi-layers Ag film, highlighted by white arrows and labelled with quantum numbers n . By comparing the position of QW states with existing literature [43], we estimate a silver film thickness of about 18 monolayers. Analogies with the bare Ag/Pt interface are also a flat bottom for first bands, in the region of about 0.45 eV of binding energy, and a significant lowering of spectral weight intensity at higher binding energy, in a triangular region around the Γ point. This fact reflects the hybridization effects between Ag and the surface-projected bands of the substrate. Moreover, we can observe that the dispersions of all QW bands seem to exhibit a kink at the edges of the triangular area, as in the case of Ag on bare Pt(111). The deviation from a parabolic dispersion of $n=4$ and $n=5$ bands is also due to the presence of a poorly

reflecting region. Moreover, the sequence of energy distribution curves (EDCs) of Fig. 2.13(b) shows the absence of the Ag surface state, in analogy with the results discussed above for Gr/Ag/Co(0001).

By comparing the experiments here reported using Co(0001) and Pt(111) substrates, we conclude that Ag multi-layers intercalated on graphene remind the growth properties of Ag films on the bare substrate and, consequently, the energy-dispersion curves of QWs mainly reflect the supporting metal rather than the graphene layer on top. Such observations lead us to assert that a graphene-protected film is achievable on different supporting metals.

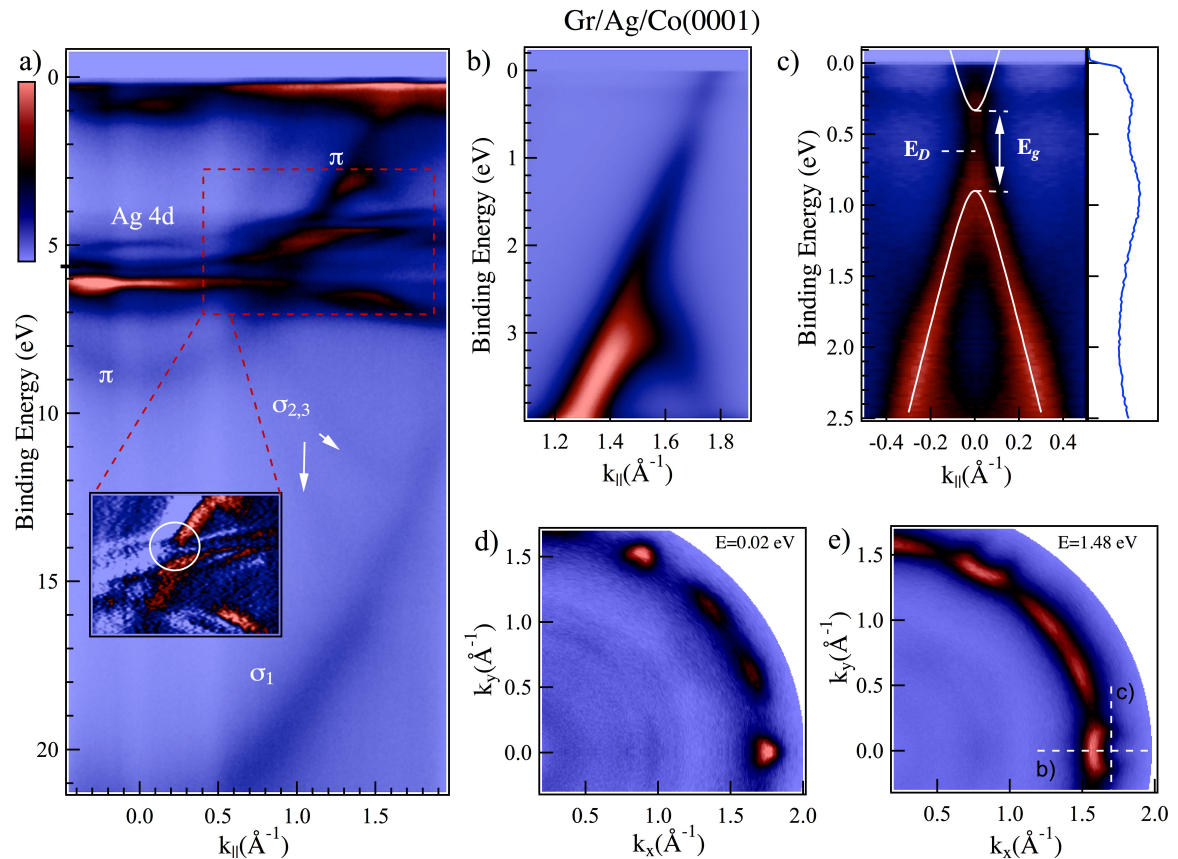


Figure 2.14: ARPES measurements taken on Gr/2.5 ML Ag/Co(0001). (a) Extended photoemission intensity plot along ΓK direction of the main domains of Gr, taken at 120 eV of photon energy. The inset shows the first derivative of the region enclosed by dashed red lines. (b) and (c) Photoemission intensity plots taken at 55 eV of photon energy, along main ΓK direction of Gr and perpendicularly to it, respectively. On the right side of panel (c), we report the energy distribution curve extracted at $k = 0$ is reported. (d) and (e) panels report the constant-energy maps taken 0.02 eV below the Fermi level, and at 1.48 eV of binding energy, respectively. In panel (e) the dashed lines indicate the directions along which parts (b) and (c) are taken.

Finally, we move the attention to the electronic properties of graphene on intercalated Ag multi-layers. In Figure 2.14(a) we report a wide photoemission intensity plot taken at 120 eV of photon energy, along ΓK direction of main domains of Gr/Ag/Co system: we can clearly observe the dispersion of Gr π and σ states and the presence of the Ag 4d bands. The latter bands, i.e. 4d Ag states, confirm the good crystalline quality of the Ag intercalated films. We noticed that the decoupling of the graphene layer from the Co substrate is proved by

the minimum of the π state at the Γ point, which has been found here at 8.72 eV of binding energy, against 10.10 eV reported on previously measurements of Gr/Co(0001) [10].

However, according to a previous investigation [53] where a considerable Gr-Ag interaction has been detected, we confirm here a significant and detectable hybridization between the graphene π band and Ag 4*d* bands, which results in the formation of a band gap at about 4.5 eV of binding energy in the present experiment. This results has been highlighted by the first derivative of the ARPES data and reported in the inset of Figure 2.14(a) enclosed by a dashed line; the formed band gap has been indicated within a white circle.

Panels (b) and (c) of Fig. 2.14 show the *n*-doped π and π^* Dirac cones of graphene in proximity of the Fermi level, along the ΓK direction and orthogonally to it, respectively.

The doping effect and band gap opening of epitaxial noble-metal contacts on graphene have been widely discussed in the literature within different first-principles DFT calculations. The adsorption of graphene on Al, Cu, Ag, Au and Pt(111) surfaces is weak; this facts preserves the typical graphene electronic structure, including the conical points. Even in this physisorbed case, there is a short-range graphene-metal interaction, as well as a charge transfer between the graphene and metal states which results in a doping of graphene, i.e. a shift of the Fermi level with respect to the conical points, driven by the work function difference (W) of the graphene-covered metal surfaces as compared to the clean metal surface [54–56]. Taking into account a physisorbed graphene layer located at large distance of about $d = 5 \text{ \AA}$ from a metal surface, one would expect a rigid charge transfer from the metal to graphene, or in the opposite direction, only due to the difference of corresponding work functions. Specifically, since values of the Ag and graphene work function have the value of $W_{Ag} = 4.92 \text{ eV}$, and $W_{Gr} = 4.60 \text{ eV}$, the Gr/Ag interface is expected to be close to the neutral point at large distance, with a slight *p*-doping. Actually, at a typical equilibrium separation of $d = 3.3 \text{ \AA}$ for weakly interacting metals, there is also a contribution coming from the overlap integral between wave functions of metal and Gr, which can account for the failure of a simple picture of charge transfer.

In the present experiment, the linear extrapolation of the π and π^* band dispersions of graphene towards the \bar{K} point do not overlap, as showed in the cut reported in Fig. 2.14(b) and perpendicular to it, panel (c). The two band dispersions are misaligned along the momentum axis and separated by a depression of the photoemission intensity, giving a clear signature of an energy band-gap, as highlighted by interpolation of the dispersions superimposed to our ARPES data in Fig. 2.14(c). The anomalous behaviour near the Dirac point of epitaxial graphene has been first observed on SiC(0001), and through a controversial interpretation of data inferred to electron-plasmon scattering [57], or symmetry breaking caused by substrate bonding [58]. A similar gap-like spectrum was also seen in disordered graphene, leading to the information that a high number of defects or small graphene domain size cause a broadening of the intrinsic spectral function [qw38, 59, 60]. Energy gaps partially hidden by non-vanishing intensity have been observed in other intercalated Gr-systems [61, 62], first discussed for Gr/Au(1ML)/Ru(0001) and ascribed to the breaking of the C sub-lattice symmetry [63].

Back to our experiments, previous ARPES studies on Gr/Ag systems showed that

graphene on one interlayer of Ag(111) becomes heavy electron doped, with a Dirac point (E_D) located at about 400 meV (± 100 meV) and a band gap E_g of 450 meV (± 100 meV) when Re(0001) is used as supporting substrate [53] and with $E_D = 560$ meV (± 5 meV) and $E_g = 320$ meV (± 5 meV) on Ni(111) [62]. The present system differs for the number of Ag interlayers, the supporting substrate, and thus the graphene superstructure. However, from the photoemission intensity plot taken along ΓK direction of the main graphene domain and in the direction perpendicular to it, Figs. 2.14(b) and (c), and from EDC extracted at the center of the Dirac cones, we estimate for Gr/Ag/Co(0001) $E_D = 620$ meV (± 15 meV) and $E_g = 560$ meV (± 15 meV); these values are in agreement with STS results for Gr/Ag(111) [38] which reports E_D of about 560 meV (± 80 meV).

Moreover, in Figure 2.14(d) and (e), photoemission measurements of constant-energy surface close to Fermi level, i.e. 0.02 eV of binding energy, and down to 1.48 eV binding energy, are displayed. Close to the Fermi surface, the red spots located in correspondence of the K points are related to the constant energy cuts of the π^* band of Gr. Weaker signs of the π^* bands located at $20^\circ \pm 1^\circ$ and $40^\circ \pm 1^\circ$ are originated from the rotated graphene domains. The cut at higher binding energy (i.e. 1.48 eV in Fig. 2.14(e)), clearly show the characteristic triangular contour of π band of graphene for the main domain, fully described within the tight-binding approach [64], and a spread of the signal along circular segments for the rotated domains. Notably, in both constant energy cuts, faint inner circles visible within $|k| \simeq 1.00 \text{ \AA}^{-1}$ correspond to Ag *sp*-derived QW states.

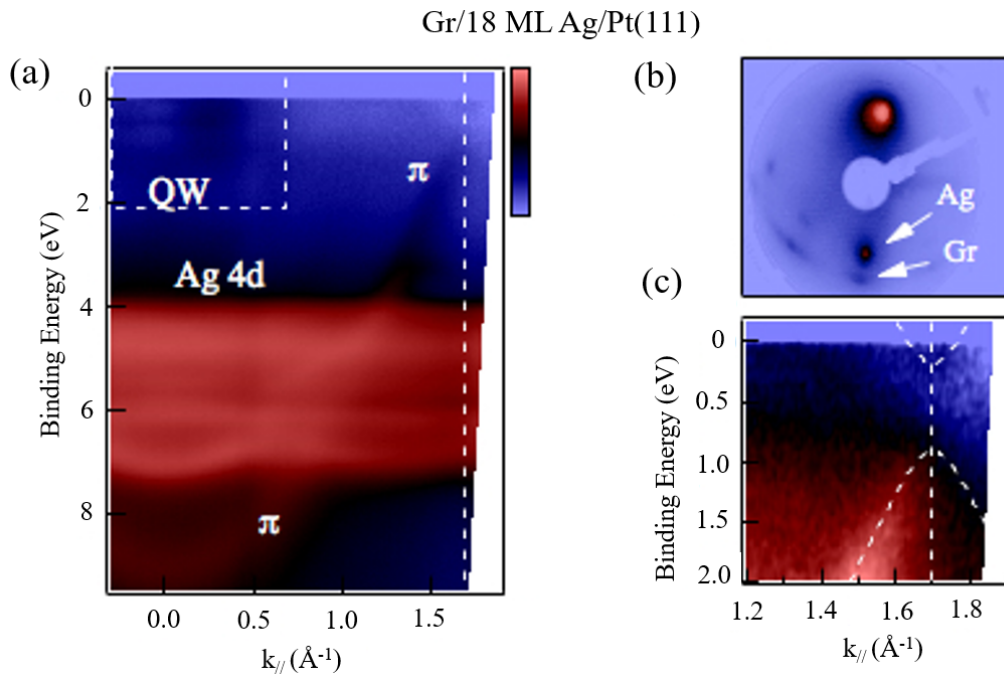


Figure 2.15: ARPES measurements taken on Gr/Ag/Pt(111). (a) Extended photoemission intensity plot in logarithmic intensity scale along ΓK direction of the main domains of Gr, taken at 70 eV of photon energy. (b) LEED image taken off normal at 65 eV of electron beam energy, showing the superstructure of Gr on Ag multi-layers grown on Pt(111) substrate. (c) Photoemission intensity plot in logarithmic intensity scale along ΓK direction of the main domains of Gr, with 70 eV of photon energy.

A similar behaviour has been observed using Pt(111) as a supporting substrate, as reported in Fig. 2.15. The first panel (a) shows the wide extended ARPES spectrum along the Γ K direction of the main graphene domain, taken at 70 eV of photon energy. We can clearly distinguish the π dispersion of graphene, with a minimum at Γ point located at about 9 eV of binding energy, which proves a weak coupling of the Gr layer with the Ag substrate. The good crystalline quality of the Ag films is again confirmed by the appearance of dispersive 4d Ag states. The LEED measurement, reported in Fig. 2.15(b) and taken at 65 eV of electron beam energy, shows the superstructure of graphene on Ag multilayers, grown on Pt(111) substrate; inner white arrow indicates the spot related to the superstructure while the outer one indicates the Gr multidomain. In panel (c) of Fig. 2.15 we show the n -doped π and π^* Dirac cones in proximity of the Fermi level in the direction perpendicular to Γ K. As in the case of Gr/2.5 ML Ag/Co(0001), π and π^* band dispersion do not overlap each other and are separated by a depression of the photoemission intensity; we are able to distinguish the band gap opening, as highlighted by the dashed white linear interpolation superimposed on AREPS measurements.

The results here shown were reported in the manuscript: "*Electron Confinement Effects in Silver Films Embedded between Graphene and Metallic Substrates*", L. Ferrari, I. Grimaldi, P. M. Sheverdyayeva, Asish K. Kundu, P. Moras, M. Papagno, C. Carbone and D. Pacile, *Journal of Physical Chemistry C* Volume **123**, 29 March 2019, Pages 9764-9769. The manuscript is available [here](#).

2.4 Electronic structure of graphene/4f rare-earth/FM system

In the last few years, many works were addressed to the study of the structural, electronic and magnetic properties of the graphene/metal systems; some examples are also reported in previous sections of this chapter. As mentioned before, the ferromagnetic transition metals (such as Fe, Co and Ni) possess localized valence orbitals of d symmetry that interact with the C p_z orbitals and thereby destroy the linear dispersion of π state of graphene. The strong hybridization of the (Ni, Co, or Fe) $3d$ electrons of FMs with the π band of graphene modifies the graphene band structure at the K point. At odd, a hybrid $3d$ - $4f$ system with graphene- $4f$ metal interface could leave the graphene electronic band structure nearly intact, due to the absence of d -electrons available for interaction.

In this context, rare earth elements are of interest; most of them do not possess d electrons available for interaction and their magnetic moment is very robust against chemical environment. Recently, two studies have been published regarding the intercalation of europium underneath Gr [65, 66]. It has been demonstrated that, depending on the coverage, the intercalated Eu atoms on Gr/Ir(111) can form a (2×2) or $(\sqrt{3} \times \sqrt{3})R 30^\circ$ superstructure. Compared to the base system with Gr on Ir(111), the graphene bands in both superstructure systems are rigidly shifted to higher binding energies, indicating a n -doping. Beside a similar electronic behaviour, the magnetic properties of the two intercalated systems are different: the (2×2) structure displays a paramagnetic behaviour, while $(\sqrt{3} \times \sqrt{3})R 30^\circ$ superstructure allows to a ferromagnetic Eu/Ir coupling. The last superstructure is more interesting for applications

in the field of spintronics, also due to the fact that Eu has a large magnetic moment (about $7 \mu_B$). The electronic band structure of systems with graphene-4f rare-earth is still poorly studied. We report some preliminary ARPES results on the electronic structure of the Gr/1ML Eu/Ni system.

2.4.1 Experimental details

The present experiments were carried out at the VUV-Photoemission beamline (section A.4.1). We used as substrate a W(110) or Ir(111) crystal; the W(110) crystal has been prepared following the procedure reported in section 2.2.1, while Ir(111) was prepared by repeating high temperature flash-annealing cycle in oxygen atmosphere and by cycles of Ar ion sputtering and annealing to about 1500 K at a base pressure of of 5×10^{-6} mbar; the cleanliness of surfaces was confirmed by the appearance of a sharp (1×1) LEED pattern and by XPS measurements.

A thick Ni film was grown in situ, in the preparation chamber on the clean substrate (W(110) or Ir(111)) by evaporation of about 10 ML of Ni from an electron-bombarded rod at RT. The resulting ferromagnetic thin films showed a well-ordered (1×1) hexagonal pattern with sharp diffraction spots upon annealing at about 420 K.

Graphene on Ni film were grown by chemical vapour deposition of ethylene (C_2H_4) at a temperature of about 700 K, the minimum temperature to avoid local breaking of the film (see section 2.2.1). The Eu monolayer was evaporated from a Knudsen cell on top of the graphene layer while the sample has been held at a temperature of about 700 K. The intercalation process was monitored by LEED measurements and core levels photoemission spectra. In Fig. 2.16(a) we report the sketch of the superstructure of Eu intercalated between graphene and Ni(111) film. The black hexagons indicate the Ni(111) pattern structure, while those in red are related to the superstructure $(\sqrt{3} \times \sqrt{3})R 30^\circ$ of Eu intercalated. In panel (b) we report the LEED measurements performed at about 80 eV of electron energy; white arrow indicates the Gr/Ni structure while the yellow one indicates the $(\sqrt{3} \times \sqrt{3})R 30^\circ$ Eu superstructure with respect to graphene.

ARPES measurements have been performed with a photon energy of about 50 eV, in order to minimize the Ni background signal and to favour the detection of the π states of graphene. Total-energy and angular resolution were set to 15 meV and 0.3° , respectively.

2.4.2 Results and discussion

In Fig. 2.17 we report the DFT calculations, performed by the research group lead by Dr. G. Bihlmayer, of the band structure of graphene on Eu, panel (a), and Eu intercalated on Gr/Ni(111) film, panel (b). The comparison between the two panels helps us to highlight the role of the ferromagnetic substrate.

In both panels, red curves are related to the majority spin of graphene, while the blue curves to the minority ones. In panel (a) of Fig. 2.17, the thick shaded red bands around -3 eV of binding energy are related to 4f states of Eu. The Eu 4f bands are lower in energy and they do not cross the π states of graphene at the Dirac point. In this case the intersections occur

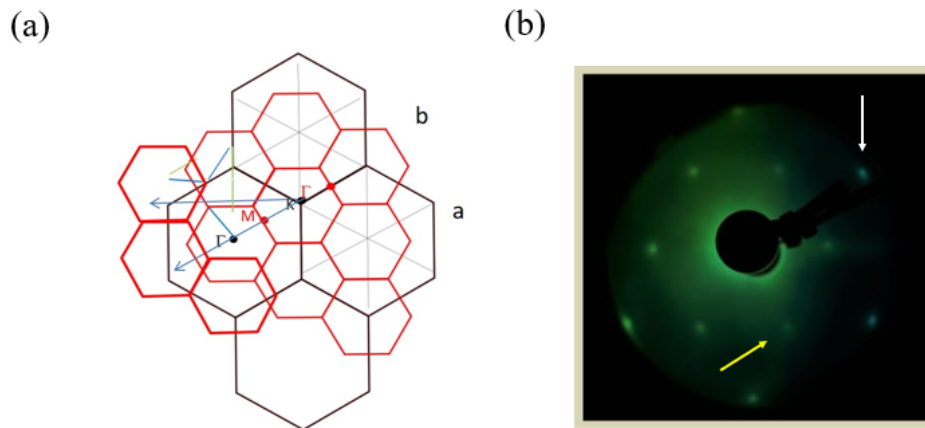


Figure 2.16: (a) Sketch of the superstructure of Eu intercalated between graphene and Ni film. Black hexagons show the Ni(111) structure, red ones the $(\sqrt{3} \times \sqrt{3})R 30^\circ$ Eu superstructure. (b) LEED measurements performed at about 80 eV of electron energy; white arrow indicates the Gr/Ni structure while the yellow one indicates the $(\sqrt{3} \times \sqrt{3})R 30^\circ$ Eu superstructure.

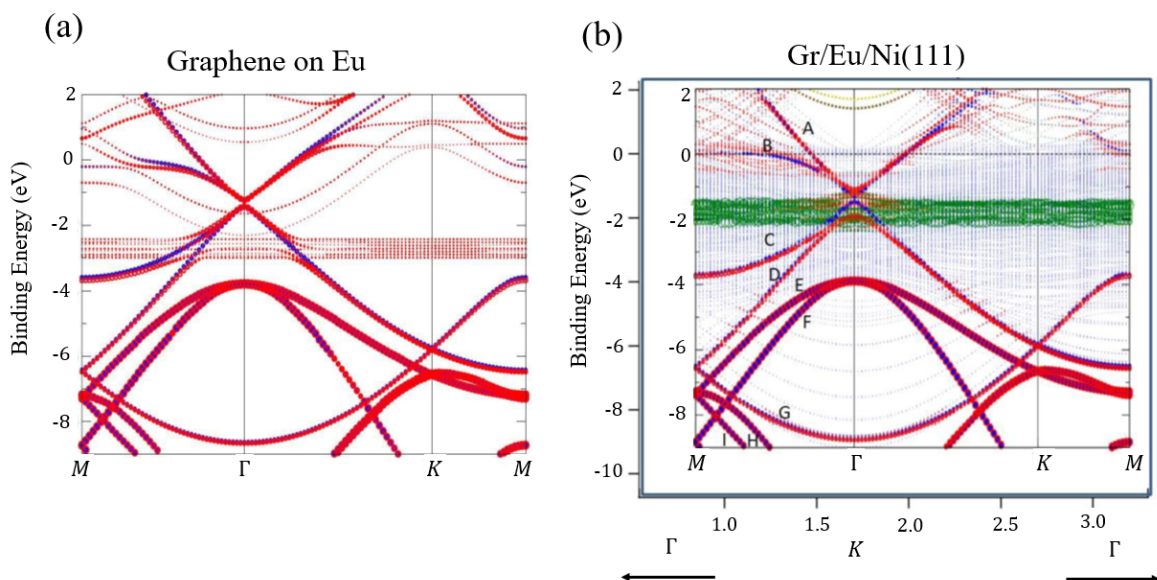


Figure 2.17: Calculated band structure of (a) graphene on Eu and (b) Eu/Gr/Ni(111). Red (blue) lines indicate the majority (minority) spin of graphene.

far from the K point (of graphene) and in these points (about -2.5 eV of BE) we observe a gap opening for the spin up electrons (red curves) while the spin down (blue curves) remain undisturbed by the interaction. In system with Eu intercalated on Gr/Ni(111), panel (b) of Fig. 2.17, the Eu 4f states are represented by green shaded band, which are located almost 1 eV upper, at about -1.8 eV of binding energy and about 0.8 eV wide. The thick and light blue bands located between the Fermi level and about -4 eV of binding energy are related to the Ni electronic states, as well as those with upward parabolic dispersion located between -4.5 eV and -9 eV. The graphene bands are indicated with A-I letters; in the bottom part of the spectra, the bands are all degenerate in spin, while in the upper part some spin-split of the bands and opening of gaps occur: we can observe that the B band has predominantly spin down character while the C band, going from Γ to K point, is splitted by crossing the Eu 4f states. The gap opening of about 430 meV affects only the spin up electrons.

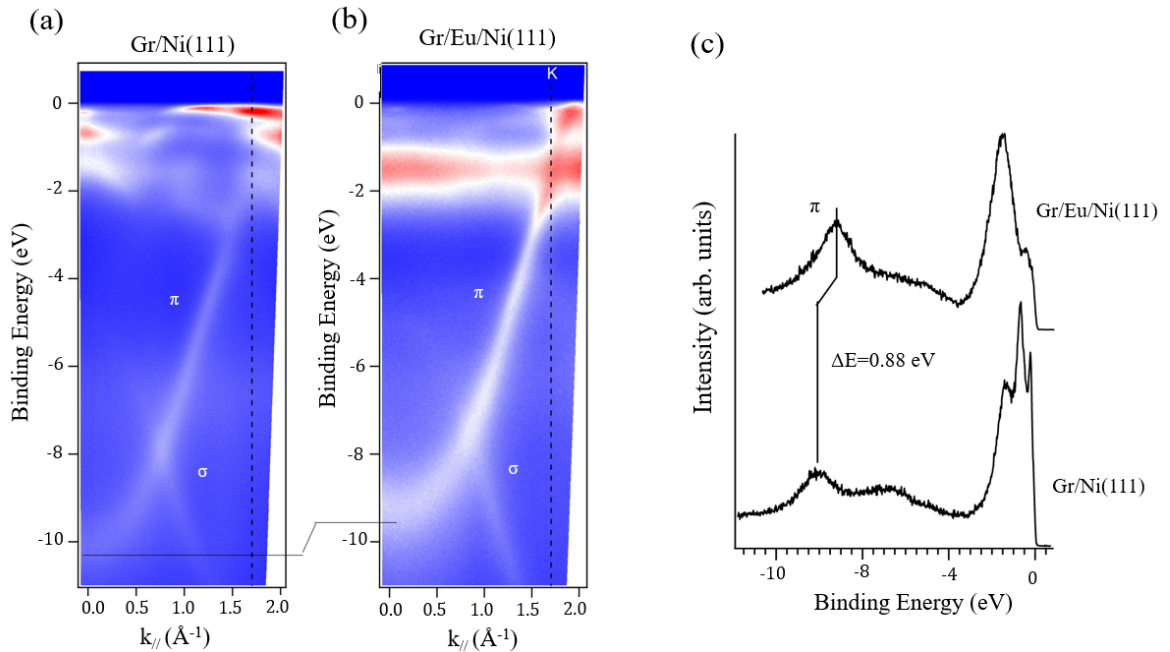


Figure 2.18: ARPES measurements performed at RT (a) before and (b) after Eu intercalation on Gr/Ni(111), with 70 eV of photon energy. (c) Normal emission EDC spectra extracted from panels (a) and (b), respectively.

In Fig. 2.18 we report ARPES measurements taken along ΓK direction of the Brillouin zone at RT and with 70 eV of photon energy, performed on Gr/Ni, panel (a), and after 1ML of Eu intercalation, panel (b). By comparison, we observe some modification of the electronic band structure. After Eu intercalation, the graphene π state is shifted to lower binding energy, indicating a weakening of the graphene interaction with the substrate. The π band of graphene crosses the σ band at $k=0.85 \text{ \AA}^{-1}$ and at 7.5 eV of binding energy. In panel (c) of Fig.2.18 we report the comparison between normal emission EDC spectra extracted from panels (a) and (b); we can clearly see the effect of intercalation in terms of upper shift of the bottom of π state by about 900 meV.

In Fig. 2.19 we report ARPES measurements performed on Gr/Eu/Ni(111) with 40 eV of

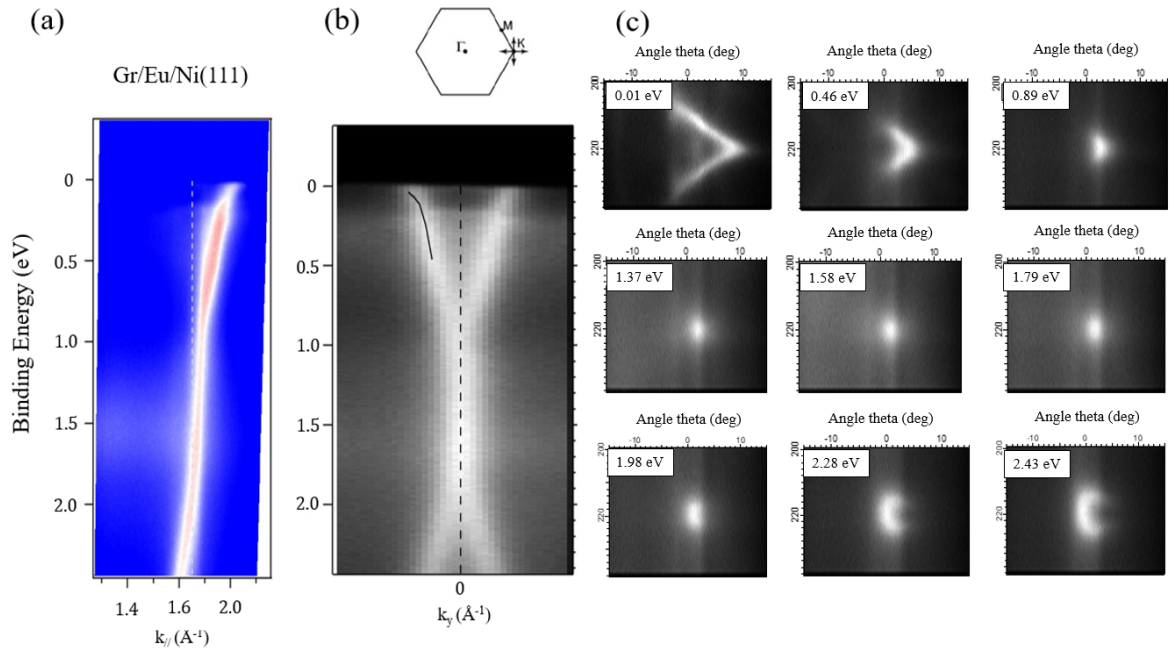


Figure 2.19: ARPES measurements performed on Gr/Eu/Ni(111) with 40 eV of photon energy at low temperature: (a) along ΓK direction and (b) perpendicularly to it. (c) Constant energy cuts at different binding energy extracted from measurements of panel (b).

photon energy, at 18 K, along ΓK direction and perpendicularly to it. From panel (b), it is clear that the dispersion at the Dirac point, i.e. the intersection of the cones, is not characterized by a single point, but the π and π^* states are separated by a region of constant intensity. In this region, according to DFT calculations reported in Fig. 2.17, the Dirac cones intersect the Eu $4f$ states.

Our preliminary ARPES measurements of Gr/1 ML Eu/Ni revealed that the rare-earth metal intercalation induces a strong n -type doping of graphene π band with respect to the free-standing ones and weakens the interaction with the d -bands of the substrate. Data analysis on the present system is currently underway.

The results here shown are reported in the manuscript: "*Dirac cone structure of Europium-intercalated Graphene on Ni(111)*", **I. Grimaldi**, G. Contini, A. K. Kundu, P. Moras, P. M. Sheverdajeva, N. Atodiresei, G. Bihlmayer, D. Pacilè, C. Carbone and L. Ferrari, *in preparation*.

References

- [1] A. K. Geim and K. S. Novoselov. “The rise of graphene”. In: *Nature Materials* 6.3 (Mar. 2007), pp. 183–191. DOI: 10.1038/nmat1849.
- [2] E. Cobas, A. L. Friedman, O. M. J. van’t Erve, J. T. Robinson, and B. T. Jonker. “Graphene As a Tunnel Barrier: Graphene-Based Magnetic Tunnel Junctions”. In: *Nano Letters* 12.6 (May 2012), pp. 3000–3004. DOI: 10.1021/nl3007616.
- [3] D. Klar, S. Bhandary, A. Candini, L. Joly, P. Ohresser, S. Klyatskaya, M. Schleberger, M. Ruben, M. Affronte, O. Eriksson, B. Sanyal, and H. Wende. “Field-regulated switching of the magnetization of Co-porphyrin on graphene”. In: *Phys. Rev. B* 89 (14 Apr. 2014), p. 144411. DOI: 10.1103/PhysRevB.89.144411.
- [4] A. Candini, V. Bellini, D. Klar, V. Corradini, R. Biagi, V. De Renzi, K. Kummer, N. B. Brookes, U. del Pennino, H. Wende, and M. Affronte. “Ferromagnetic Exchange Coupling between Fe Phthalocyanine and Ni(111) Surface Mediated by the Extended States of Graphene”. In: *The Journal of Physical Chemistry C* 118.31 (July 2014), pp. 17670–17676. DOI: 10.1021/jp5041663.
- [5] C. Vo-Van, S. Schumacher, J. Coraux, V. Sessi, O. Fruchart, N. B. Brookes, P. Ohresser, and T. Michely. “Magnetism of cobalt nanoclusters on graphene on iridium”. In: *Applied Physics Letters* 99.14 (Oct. 2011), p. 142504. DOI: 10.1063/1.3646480.
- [6] S. Lisi, P. Gargiani, M. Scardamaglia, N. B. Brookes, V. Sessi, C. Mariani, and M. G. Betti. “Graphene-Induced Magnetic Anisotropy of a Two-Dimensional Iron Phthalocyanine Network”. In: *The Journal of Physical Chemistry Letters* 6.9 (Apr. 2015), pp. 1690–1695. DOI: 10.1021/acs.jpcllett.5b00260.
- [7] O. V. Yazyev and A. Pasquarello. “Magnetoresistive junctions based on epitaxial graphene and hexagonal boron nitride”. In: *Phys. Rev. B* 80 (3 July 2009), p. 035408. DOI: 10.1103/PhysRevB.80.035408.
- [8] P. U. Asshoff, J. L. Sambricio, A. P. Rooney, S. Slizovskiy, A. Mishchenko, A. M. Rakowski, E. W. Hill, A. K. Geim, S. J. Haigh, V. I. Fal’ko, I. J. Vera-Marun, and I. V. Grigorieva. “Magnetoresistance of vertical Co-graphene-NiFe junctions controlled by charge transfer and proximity-induced spin splitting in graphene”. In: *2D Materials* 4.3 (June 2017), p. 031004. DOI: 10.1088/2053-1583/aa7452.
- [9] Miguel Fuentes-Cabrera, M. I. Baskes, Anatoli V. Melechko, and Michael L. Simpson. “Bridge structure for the graphene/Ni(111) system: A first principles study”. In: *Phys. Rev. B* 77 (3 Jan. 2008), p. 035405. DOI: 10.1103/PhysRevB.77.035405.
- [10] D. Pacilé, S. Lisi, I. Di Bernardo, M. Papagno, L. Ferrari, M. Pisarra, M. Caputo, S. K. Mahatha, P. M. Sheverdyeva, P. Moras, P. Lacovig, S. Lizzit, A. Baraldi, M. G. Betti, and C. Carbone. “Electronic structure of graphene/Co interfaces”. In: *Phys. Rev. B* 90 (19 Nov. 2014), p. 195446. DOI: 10.1103/PhysRevB.90.195446.

- [11] D. Usachov, A. Fedorov, M. M. Otrokov, A. Chikina, O. Vilkov, A. Petukhov, A. G. Rybkin, Y. M. Koroteev, E. V. Chulkov, V. K. Adamchuk, A. Grüneis, C. Laubschat, and D. V. Vyalikh. “Observation of Single-Spin Dirac Fermions at the Graphene/Ferromagnet Interface”. In: *Nano Letters* 15.4 (Mar. 2015), pp. 2396–2401. DOI: 10.1021/nl504693u.
- [12] D. Marchenko, A. Varykhalov, J. Sánchez-Barriga, O. Rader, C. Carbone, and G. Bihlmayer. “Highly spin-polarized Dirac fermions at the graphene/Co interface”. In: *Phys. Rev. B* 91 (23 June 2015), p. 235431. DOI: 10.1103/PhysRevB.91.235431.
- [13] J. Lahiri and M. Batzill. “Graphene destruction by metal-carbide formation: An approach for patterning of metal-supported graphene”. In: *Applied Physics Letters* 97.2 (July 2010), p. 023102. DOI: 10.1063/1.3464173.
- [14] M. Sicot, S. Bouvron, O. Zander, U. Rüdiger, Yu. S. Dedkov, and M. Fonin. “Erratum: “Nucleation and growth of nickel nanoclusters on graphene Moiré on Rh(111)” [Appl. Phys. Lett. 96, 093115 (2010)an]”. In: *Applied Physics Letters* 97.7 (Aug. 2010), p. 079901. DOI: 10.1063/1.3481374.
- [15] X. Liu, C.-Z. Wang, M. Hupalo, H.-Q. Lin, K.-M. Ho, and M. Tringides. “Metals on Graphene: Interactions, Growth Morphology, and Thermal Stability”. In: *Crystals* 3.1 (Jan. 2013), pp. 79–111. DOI: 10.3390/cryst3010079.
- [16] S. Sarkar, M. L. Moser, X. Tian, X. Zhang, Y. Fadel Al-Hadeethi, and R. C. Haddon. “Metals on Graphene and Carbon Nanotube Surfaces: From Mobile Atoms to Atomtronics to Bulk Metals to Clusters and Catalysts”. In: *Chemistry of Materials* 26.1 (Oct. 2013), pp. 184–195. DOI: 10.1021/cm4025809.
- [17] X. Liu, Y. Han, J. W. Evans, A. K. Engstfeld, R. J. Behm, M. C. Tringides, M. Hupalo, H.-Q. Lin, L. Huang, K.-M. Ho, D. Appy, P. A. Thiel, and C.-Z. Wang. “Growth morphology and properties of metals on graphene”. In: *Progress in Surface Science* 90.4 (Dec. 2015), pp. 397–443. DOI: 10.1016/j.progsurf.2015.07.001.
- [18] Stephen Blundell and David Thouless. “Magnetism in Condensed Matter”. In: *American Journal of Physics* 71.1 (Jan. 2003), pp. 94–95. DOI: 10.1119/1.1522704.
- [19] G. van der Laan. “Zen and the art of dichroic photoemission”. In: *Journal of Electron Spectroscopy and Related Phenomena* 200 (Apr. 2015), pp. 143–159. DOI: 10.1016/j.elspec.2015.06.001.
- [20] M. V. Gomoyunova, G. S. Grebenyuk, I. I. Pronin, S. M. Solov’ev, O. Yu. Vilkov, and D. V. Vyalykh. “Formation and magnetic properties of the silicon-cobalt interface”. In: *Physics of the Solid State* 55.2 (Feb. 2013), pp. 437–442. DOI: 10.1134/s1063783413020091.
- [21] G. van der Laan. “Dichroism in the angle-resolved X-ray photoemission from magnetic materials”. In: *Journal of Magnetism and Magnetic Materials* 148.1-2 (July 1995), pp. 53–57. DOI: 10.1016/0304-8853(95)00146-8.
- [22] Ch. Roth, F. U. Hillebrecht, H. Rose, and E. Kisker. “Linear magnetic dichroism in angular resolved Fe 3p core level photoemission”. In: *Phys. Rev. Lett.* 70 (22 May 1993), pp. 3479–3482. DOI: 10.1103/PhysRevLett.70.3479.

- [23] S. Bhandary, O. Eriksson, and B. Sanyal. “Defect controlled magnetism in FeP/graphene/Ni(111)”. In: *Scientific Reports* 3.1 (Dec. 2013). DOI: 10.1038/srep03405.
- [24] S. Marocchi, P. Ferriani, N. M. Caffrey, F. Manghi, S. Heinze, and V. Bellini. “Graphene-mediated exchange coupling between a molecular spin and magnetic substrates”. In: *Phys. Rev. B* 88 (14 Oct. 2013), p. 144407. DOI: 10.1103/PhysRevB.88.144407.
- [25] A. Barla, V. Bellini, S. Rusponi, P. Ferriani, M. Pivetta, F. Donati, F. Patthey, L. Persichetti, S. K. Mahatha, M. Papagno, C. Piamonteze, S. Fichtner, S. Heinze, P. Gambardella, H. Brune, and C. Carbone. “Complex Magnetic Exchange Coupling between Co Nanostructures and Ni(111) across Epitaxial Graphene”. In: *ACS Nano* 10.1 (Nov. 2015), pp. 1101–1107. DOI: 10.1021/acsnano.5b06410.
- [26] T.-C. Chiang. “Photoemission studies of quantum well states in thin films”. In: *Surface Science Reports* 39.7-8 (Sept. 2000), pp. 181–235. DOI: 10.1016/S0167-5729(00)00006-6.
- [27] M. Milun, P. Pervan, and D. P. Woodruff. “Quantum well structures in thin metal films: simple model physics in reality?” In: 2002.
- [28] D. Topwal, U. Manju, D. Pacilé, M. Papagno, D. Wortmann, G. Bihlmayer, S. Blügel, and C. Carbone. “Quantum electron confinement in closely matched metals: Au films on Ag(111)”. In: *Phys. Rev. B* 86 (8 Aug. 2012), p. 085419. DOI: 10.1103/PhysRevB.86.085419.
- [29] P. M. Sheverdyeva, R. Requist, P. Moras, S. K. Mahatha, M. Papagno, L. Ferrari, E. Tosatti, and C. Carbone. “Energy-momentum mapping of *d*-derived Au(111) states in a thin film”. In: *Phys. Rev. B* 93 (3 Jan. 2016), p. 035113. DOI: 10.1103/PhysRevB.93.035113.
- [30] D. Wegner, A. Bauer, and G. Kaindl. “Electronic Structure and Dynamics of Quantum-Well States in Thin Yb Metal Films”. In: *Phys. Rev. Lett.* 94 (12 Apr. 2005), p. 126804. DOI: 10.1103/PhysRevLett.94.126804.
- [31] M. Becker and R. Berndt. “Scattering and lifetime broadening of quantum well states in Pb films on Ag(111)”. In: *Phys. Rev. B* 81 (20 May 2010), p. 205438. DOI: 10.1103/PhysRevB.81.205438.
- [32] J. S. Park, A. Quesada, Y. Meng, J. Li, E. Jin, H. Son, A. Tan, J. Wu, C. Hwang, H. W. Zhao, A. K. Schmid, and Z. Q. Qiu. “Determination of spin-polarized quantum well states and spin-split energy dispersions of Co ultrathin films grown on Mo(110)”. In: *Phys. Rev. B* 83 (11 Mar. 2011), p. 113405. DOI: 10.1103/PhysRevB.83.113405.
- [33] F. Patthey and W.-D. Schneider. “Layer-by-layer-resolved quantum-well states in ultrathin silver islands on graphite: A photoemission study”. In: *Phys. Rev. B* 50 (23 Dec. 1994), pp. 17560–17563. DOI: 10.1103/PhysRevB.50.17560.

- [34] D. Pacilé, P. Leicht, M. Papagno, P. M. Sheverdyaeva, P. Moras, C. Carbone, K. Krausert, L. Zielke, M. Fonin, Y. S. Dedkov, F. Mittendorfer, J. Doppler, A. Garhofer, and J. Redinger. “Artificially lattice-mismatched graphene/metal interface: Graphene/Ni/Ir(111)”. In: *Phys. Rev. B* 87 (3 Jan. 2013), p. 035420. DOI: 10.1103/PhysRevB.87.035420.
- [35] D. Nobis, M. Potenz, D. Niesner, and T. Fauster. “Image-potential states of graphene on noble-metal surfaces”. In: *Phys. Rev. B* 88 (19 Nov. 2013), p. 195435. DOI: 10.1103/PhysRevB.88.195435.
- [36] W. Jolie, F. Craes, and C. Busse. “Graphene on weakly interacting metals: Dirac states versus surface states”. In: *Phys. Rev. B* 91 (11 Mar. 2015), p. 115419. DOI: 10.1103/PhysRevB.91.115419.
- [37] P. Leicht, L. Zielke, S. Bouvron, R. Moroni, E. Voloshina, L. Hammerschmidt, Y. S. Dedkov, and M. Fonin. “In Situ Fabrication Of Quasi-Free-Standing Epitaxial Graphene Nanoflakes On Gold”. In: *ACS Nano* 8.4 (Apr. 2014), pp. 3735–3742. DOI: 10.1021/nn500396c.
- [38] J. Tesch, P. Leicht, F. Blumenschein, L. Gagnaniello, M. Fonin, L. E. M. Steinkasserer, B. Paulus, E. Voloshina, and Y. Dedkov. “Structural and electronic properties of graphene nanoflakes on Au(111) and Ag(111)”. In: *Scientific Reports* 6.1 (Mar. 2016). DOI: 10.1038/srep23439.
- [39] J. Tesch, E. Voloshina, M. Jubitz, Y. Dedkov, and M. Fonin. “Local electronic properties of the graphene-protected giant Rashba-split BiAg₂ surface”. In: *Phys. Rev. B* 95 (15 Apr. 2017), p. 155428. DOI: 10.1103/PhysRevB.95.155428.
- [40] Z. I. Alferov. “Nobel Lecture: The double heterostructure concept and its applications in physics, electronics, and technology”. In: *Rev. Mod. Phys.* 73 (3 Oct. 2001), pp. 767–782. DOI: 10.1103/RevModPhys.73.767.
- [41] I. I. Klimovskikh, M. M. Otrokov, V. Yu. Voroshnin, D. Sostina, L. Petaccia, G. Di Santo, S. Thakur, E. V. Chulkov, and A. M. Shikin. “Spin–Orbit Coupling Induced Gap in Graphene on Pt(111) with Intercalated Pb Monolayer”. In: *ACS Nano* 11.1 (Jan. 2017), pp. 368–374. DOI: 10.1021/acsnano.6b05982.
- [42] M. Gao, Y. Pan, L. Huang, H. Hu, L. Z. Zhang, H. M. Guo, S. X. Du, and H.-J. Gao. “Epitaxial growth and structural property of graphene on Pt(111)”. In: *Applied Physics Letters* 98.3 (Jan. 2011), p. 033101. DOI: 10.1063/1.3543624.
- [43] P. Moras, D. Wortmann, G. Bihlmayer, L. Ferrari, G. Alejandro, P. H. Zhou, D. Topwal, P. M. Sheverdyaeva, S. Blügel, and C. Carbone. “Probing the electronic transmission across a buried metal/metal interface”. In: *Phys. Rev. B* 82 (15 Oct. 2010), p. 155427. DOI: 10.1103/PhysRevB.82.155427.
- [44] A. M. Shikin, D. V. Vyalikh, Yu. S. Dedkov, G. V. Prudnikova, V. K. Adamchuk, E. Weschke, and G. Kaindl. “Extended energy range of Ag quantum-well states in Ag(111)/Au(111)/W(110)”. In: *Phys. Rev. B* 62 (4 July 2000), R2303–R2306. DOI: 10.1103/PhysRevB.62.R2303.

- [45] M. Kralj. “Hybridization schemes for Ag films on V(100)”. In: *Surface Science* 599.1-3 (Dec. 2005), pp. 150–159. DOI: 10.1016/j.susc.2005.09.043.
- [46] A. Varykhalov, A. M. Shikin, W. Gudat, P. Moras, C. Grazioli, C. Carbone, and O. Rader. “Probing the Ground State Electronic Structure of a Correlated Electron System by Quantum Well States: Ag/Ni(111)”. In: *Phys. Rev. Lett.* 95 (24 Dec. 2005), p. 247601. DOI: 10.1103/PhysRevLett.95.247601.
- [47] J. Klier. “Dimensionality Effects in the Lifetime of Surface States”. In: *Science* 288.5470 (May 2000), pp. 1399–1402. DOI: 10.1126/science.288.5470.1399.
- [48] R. Paniago, R. Matzdorf, G. Meister, and A. Goldmann. “Temperature dependence of Shockley-type surface energy bands on Cu(111), Ag(111) and Au(111)”. In: *Surface Science* 336.1-2 (Aug. 1995), pp. 113–122. DOI: 10.1016/0039-6028(95)00509-9.
- [49] A. Varykhalov, D. Marchenko, M. R. Scholz, E. D. L. Rienks, T. K. Kim, G. Bihlmayer, J. Sánchez-Barriga, and O. Rader. “Ir(111) Surface State with Giant Rashba Splitting Persists under Graphene in Air”. In: *Phys. Rev. Lett.* 108 (6 Feb. 2012), p. 066804. DOI: 10.1103/PhysRevLett.108.066804.
- [50] G. Neuhold and K. Horn. “Depopulation of the Ag(111) Surface State Assigned to Strain in Epitaxial Films”. In: *Phys. Rev. Lett.* 78 (7 Feb. 1997), pp. 1327–1330. DOI: 10.1103/PhysRevLett.78.1327.
- [51] T. Tomanic, C. Sürgers, R. Heid, M. Alcántara Ortigoza, K.-P. Bohnen, D. Stöffler, and H. v. Löhneysen. “Local-strain mapping on Ag(111) islands on Nb(110)”. In: *Applied Physics Letters* 101.6 (Aug. 2012), p. 063111. DOI: 10.1063/1.4745011.
- [52] H. Hövel, B. Grimm, and B. Reihl. “Modification of the Shockley-type surface state on Ag(111) by an adsorbed xenon layer”. In: *Surface Science* 477.1 (Apr. 2001), pp. 43–49. DOI: 10.1016/S0039-6028(01)00704-X.
- [53] M. Papagno, P. Moras, P. M. Sheverdyeva, J. Doppler, A. Garhofer, F. Mittendorfer, J. Redinger, and C. Carbone. “Hybridization of graphene and a Ag monolayer supported on Re(0001)”. In: *Phys. Rev. B* 88 (23 Dec. 2013), p. 235430. DOI: 10.1103/PhysRevB.88.235430.
- [54] G. Giovannetti, P. A. Khomyakov, G. Brocks, V. M. Karpan, J. van den Brink, and P. J. Kelly. “Doping Graphene with Metal Contacts”. In: *Phys. Rev. Lett.* 101 (2 July 2008), p. 026803. DOI: 10.1103/PhysRevLett.101.026803.
- [55] P. A. Khomyakov, G. Giovannetti, P. C. Rusu, G. Brocks, J. van den Brink, and P. J. Kelly. “First-principles study of the interaction and charge transfer between graphene and metals”. In: *Phys. Rev. B* 79 (19 May 2009), p. 195425. DOI: 10.1103/PhysRevB.79.195425.
- [56] H. Vita, S. Böttcher, K. Horn, E. N. Voloshina, R. E. Ovcharenko, Th. Kampen, A. Thissen, and Yu. S. Dedkov. “Understanding the origin of band gap formation in graphene on metals: graphene on Cu/Ir(111)”. In: *Scientific Reports* 4.1 (July 2014). DOI: 10.1038/srep05704.

- [57] A. Bostwick, T. Ohta, T. Seyller, K. Horn, and E. Rotenberg. “Quasiparticle dynamics in graphene”. In: *Nature Physics* 3.1 (Dec. 2006), pp. 36–40. DOI: 10.1038/nphys477.
- [58] S. Y. Zhou, G.-H. Gweon, A. V. Fedorov, P. N. First, W. A. de Heer, D.-H. Lee, F. Guinea, A. H. Castro Neto, and A. Lanzara. “Substrate-induced bandgap opening in epitaxial graphene”. In: *Nature Materials* 6.10 (Sept. 2007), pp. 770–775. DOI: 10.1038/nmat2003.
- [59] E. Rotenberg, A. Bostwick, T. Ohta, J. L. McChesney, T. Seyller, and K. Horn. “Origin of the energy bandgap in epitaxial graphene”. In: *Nature Materials* 7.4 (Apr. 2008), pp. 258–259. DOI: 10.1038/nmat2154a.
- [60] A. Bostwick, J. L. McChesney, K. V. Emtsev, T. Seyller, K. Horn, S. D. Kevan, and E. Rotenberg. “Quasiparticle Transformation during a Metal-Insulator Transition in Graphene”. In: *Phys. Rev. Lett.* 103 (5 July 2009), p. 056404. DOI: 10.1103/PhysRevLett.103.056404.
- [61] M. Papagno, S. Rusponi, P. M. Sheverdyaeva, S. Vlaic, M. Etzkorn, D. Pacilé, P. Moras, C. Carbone, and H. Brune. “Large Band Gap Opening between Graphene Dirac Cones Induced by Na Adsorption onto an Ir Superlattice”. In: *ACS Nano* 6.1 (Dec. 2011), pp. 199–204. DOI: 10.1021/nn203841q.
- [62] A. Varykhalov, M. R. Scholz, Timur K. Kim, and O. Rader. “Effect of noble-metal contacts on doping and band gap of graphene”. In: *Phys. Rev. B* 82 (12 Sept. 2010), p. 121101. DOI: 10.1103/PhysRevB.82.121101.
- [63] C. Enderlein, Y. S. Kim, A. Bostwick, E. Rotenberg, and K. Horn. “The formation of an energy gap in graphene on ruthenium by controlling the interface”. In: *New Journal of Physics* 12.3 (Mar. 2010), p. 033014. DOI: 10.1088/1367-2630/12/3/033014.
- [64] P. R. Wallace. “The Band Theory of Graphite”. In: *Phys. Rev.* 71 (9 May 1947), pp. 622–634. DOI: 10.1103/PhysRev.71.622.
- [65] S. Schumacher, F. Huttmann, M. Petrovic, C. Witt, D. F. Forster, C. Vo-Van, J. Coraux, A. J. Martinez-Galera, V. Sessi, I. Vergara, R. Ruckamp, M. Gruninger, N. Schleheck, F. Meyer zu Heringdorf, P. Ohresser, M. Kralj, T. O. Wehling, and T. Michely. “Europium underneath graphene on Ir(111): Intercalation mechanism, magnetism, and band structure”. In: *Phys. Rev. B* 90 (23 Dec. 2014), p. 235437. DOI: 10.1103/PhysRevB.90.235437.
- [66] F. Huttmann, D. Klar, N. Atodiresei, C. Schmitz-Antoniak, A. Smekhova, A. J. Martinez-Galera, V. Caciuc, G. Bihlmayer, S. Blugel, T. Michely, and H. Wende. “Magnetism in a graphene-4f – 3d hybrid system”. In: *Phys. Rev. B* 95 (7 Feb. 2017), p. 075427. DOI: 10.1103/PhysRevB.95.075427.

III-VI layered semiconductors

During the last decade, III-VI layered mono-chalcogenides (MX) have emerged as potential candidates for various applications, such as FET and optoelectronic devices.

The properties of this class of layered materials are strongly dependent on their structure, and the existence of different polytypes makes it necessary the identification of the structural phase. In this context, in the first part of the chapter, I report a detailed investigation on the crystal structure and morphology of bulk InSe, by means of X-ray diffraction (XRD), Transmission Electron Microscopy (TEM) and Raman spectroscopy. We demonstrate that only by crossing the information of each technique it is possible to unambiguously discern between similar polytypes. The combination of the employed techniques allowed to identify the structural phase of InSe samples (ϵ polytype).

In the second part of the chapter, I report a comparison of the electronic structure of bulk ϵ -InSe and ϵ -GaSe, by means of ARPES measurements and DFT calculations. We focus our attention to the top valence band of the two compounds along main symmetry directions, discussing the effect of spin-orbit coupling and contributions from metal (Ga or In) and Se atoms.

3.1 Introduction

The discovery of graphene has opened the way to the investigation of two-dimensional (2D) layered materials with comparable properties, such as high mobility, high conductivity, high mechanical strength and long spin diffusion length for spintronic devices. In recent years, layered materials have been widely studied due to their unique optical, electronic and mechanical properties [1, 2]. Besides graphene, some typical 2D materials, which have been explored both experimentally and theoretically, include transition metal dichalcogenides (TMDCs), black phosphorus (BP), hexagonal boron nitride (h-BN) and III-VI semiconductors [3, 4].

Metal mono-chalcogenides (MX, where M stands for the post transition metal and X represents the chalcogen atom) have recently been rediscovered, as 2D materials with electronic properties that strongly depend on the number of layers. Among them, InSe and GaSe,

which have been synthesized via physical and chemical methods [5–8], exhibit promising properties in the field of microelectronic, optical and optoelectronic applications [9, 10]. The two compounds exhibit a direct bandgap in the bulk (GaSe of about 2.1 eV and InSe of about 1.2 eV), while they acquire an indirect bandgap in few layers regime. The variable width of the bandgap as a function of the thickness, due to strong quantum confinement effects, makes them optically active in the IR and visible region, thus allowing their use as active components in photodetectors [8, 11–16]. InSe exhibits a carrier mobility reaching the value of $10^3 \text{ cm}^2\text{V}^{-1}\text{s}^{-1}$ at RT, highest among the other TMDCs and superior to BP [17]. It has been demonstrated also that III-VI materials can be used in solar energy conversion devices, field-effect transistors and photodetectors. Recently, these materials have been also included into novel heterostructures for the development of new transistors, sensors etc. [10, 18–20]. More generally, vertical van der Waals (vdW) heterostructures obtained by combining different 2D materials have been investigated in order to create novel functionalities [21–24], or to increase the carrier mobility, which, in MX compounds, strongly increases with the number of layers [17, 25].

However, the possibility to manipulate vertical vdW heterostructures requires a detailed knowledge of the single components, starting from the bulk counterpart down to the single-layer.

Mono-chalcogenides possess different basic polytypes; they differ in stoichiometry [26] and also in the structural phase (ϵ -MSe, β -MSe, γ -MSe, δ -MSe) [27, 28]. Besides the confirmation of the stoichiometric ratio, the accurate knowledge of the structural phase is required in order to understand and simulate all the macroscopic properties of the crystal. For this purpose, in section 3.2, we report an experimental investigation of InSe and GaSe in order to identify unambiguously the phase of the two compounds.

In the second part of the chapter, section 3.3, we compare the electronic band structure of bulk ϵ -GaSe and ϵ -InSe layered semiconductors, focusing on the top valence band of the two compounds along main surface symmetry directions, in order to discuss the effect of spin-orbit coupling and contributions from metal (Ga or In) and Se atoms.

3.2 Structural investigation of III-VI layered semiconductors

Here we report the experimental investigation of semiconductors InSe and GaSe by means of X-ray diffraction (XRD), Transmission Electron Microscopy (TEM), selected area electron diffraction (SAED) and Raman spectroscopy. We show that, due to the existence of similar polytypes, only combining the findings of each technique the structural phase can be unambiguously determined. Overall, our study provides a useful guide to discern between polytypes of mono-chalcogenides layered semiconductors.

3.2.1 Experimental details

The InSe crystals were grown in double wall ampoules by means of the Bridgman method starting from a nonstoichiometric melt, containing an In excess of about 5%. More details are

available in Ref. [29].

The high quality of the as-grown ingots was characterized by X-ray diffraction (XRD) by using a Bruker AXS D8 Discover diffractometer with Cu K α radiation ($\lambda = 1.5418 \text{ \AA}$). Measurements were taken at room temperature for 2θ values over $2^\circ - 70^\circ$ in steps of $0.01^\circ/0.004^\circ$, with a step time of 1 s. These measurements were performed at the LiCryl laboratory CNR c/o, University of Calabria.

In order to study the layered morphology of InSe, we performed transmission electron microscopy (TEM). Samples were embedded in Araldite epoxy resin (Fluka, Buchs, Switzerland). Ultrathin sections were prepared using a diamond knife and collected on formvar/carbon copper grids (G 300 Cu). TEM measurements were conducted using a transmission electron microscope Jeol JEM-1400 Plus, operated at an acceleration voltage of 80 kV in TEM mode. Selected area diffraction (SAED) patterns were recorded using a selected area aperture 2 mm in diameter.

Raman spectra were collected by using a Horiba-Jobin Yvon microprobe apparatus with spectral resolution of about 2 cm^{-1} , equipped with a CCD (256×1024 pixels) detector cooled at about 200 K, and a diode laser of 532 nm, with an emitted power of 50mW and with its notch filter. Two M-plan Olympus objectives, $100\times$ and $50\times$, were used, focusing a laser spot of about $2 \mu\text{m}$ of apparent diameter. In addition, to avoid structural changes due to laser heating, filters with different optical density were used (from OD 2:0 to OD 0:6). InSe samples were reduced to thin films, by means of the scotch-tape based mechanical exfoliation, followed by the deposition on a SiO₂ substrate. Raman measurements were performed at the Raman Spectroscopy laboratory, of the University of Calabria.

3.2.2 Results and Discussion

The crystal structure of mono-chalcogenides III-VI compounds consists of basic quadruple-layers (about 8 \AA of thickness), held together by weak van der Waals forces; each quadruple-layer is formed by covalently bonded atoms (Se-In-In-Se); this peculiar structure makes easy the mechanical exfoliation of the sample. The three-dimensional lattices are built by stacking quadruple-layers in different way, yielding selected polytypes.

InSe crystals, with 1:1 indium/selenium ratio, exhibit three common polytypes ϵ , β and γ , which differ in the stacking of the quadruple-layers. In Fig. 3.1 we report a schematic representation realized using the software Avogadro [30]. The ϵ phase has hexagonal lattice and belongs to the D^1_{3h} non-centrosymmetric space group; it is formed by two quadruple-layers, with ABAB alternating stacking; the second quadruple-layers is shifted with respect to the first one along the horizontal plane, as reported in Fig. 3.1(a). The β phase has also a hexagonal crystal structure, but belongs to the D^4_{6h} centrosymmetric space group; it is formed by two quadruple-layers, in which the upper one is counterclockwise rotated by 60° around the vertical axis, as reported in Fig. 3.1(b). The two hexagonal phases are hardly distinguishable, as they exhibit a similar composition of the unit cell and same lattice parameters (i.e., for InSe, $a = b = 4.00 \text{ \AA}$, $c = 16.68 \text{ \AA}$ [31]), although they belong to different symmetry groups. The γ polytype has rhombohedral crystal structure and belongs to the C^5_{3v} non-centrosymmetric

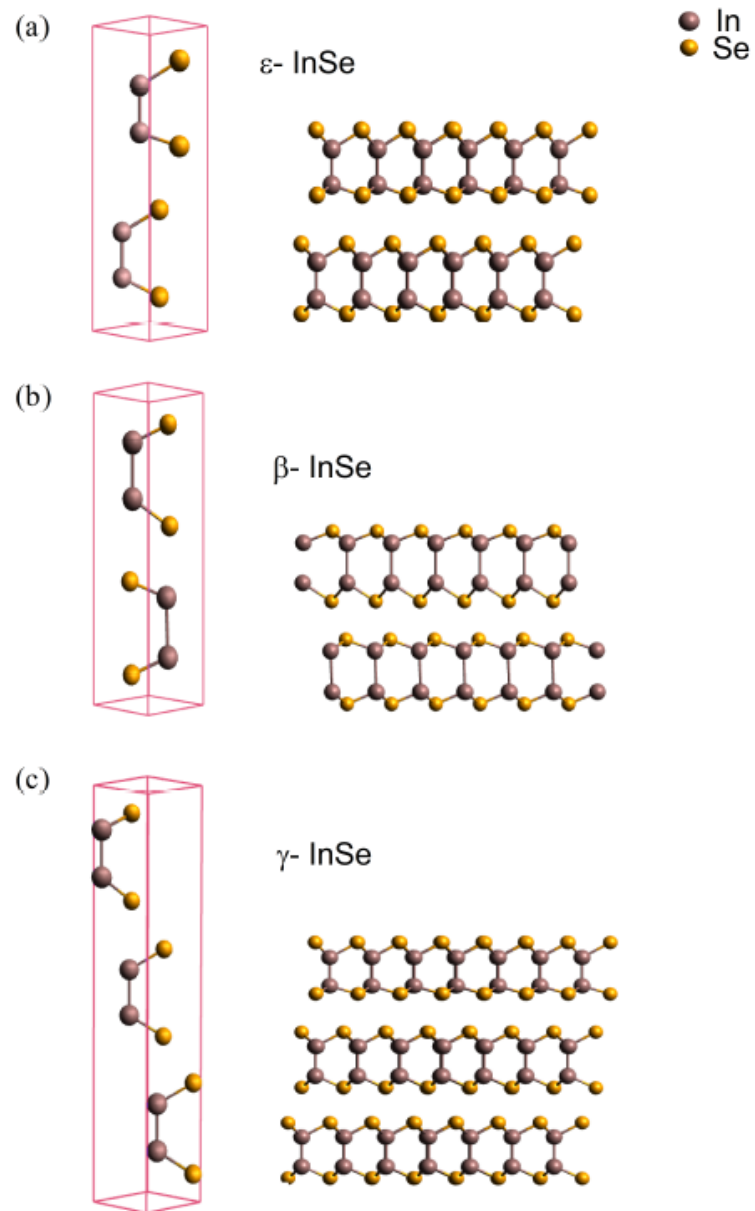


Figure 3.1: Crystal structure of three common polytypes of InSe: unit cell (left) and side view (right) of: (a) ϵ -InSe; (b) β -InSe; (c) γ -InSe.

space group. It is composed by three quadruple-layers with ABCABC alternated stacking; each layer is shifted with respect to the other along the horizontal plane as we can see in Fig. 3.1(c). The non-primitive hexagonal cell shares the same planar lattice parameters of ϵ and β phases, while the orthogonal unit cell parameter is about 1.5 times higher, c is about 25 Å [26, 32, 33] for γ -InSe.

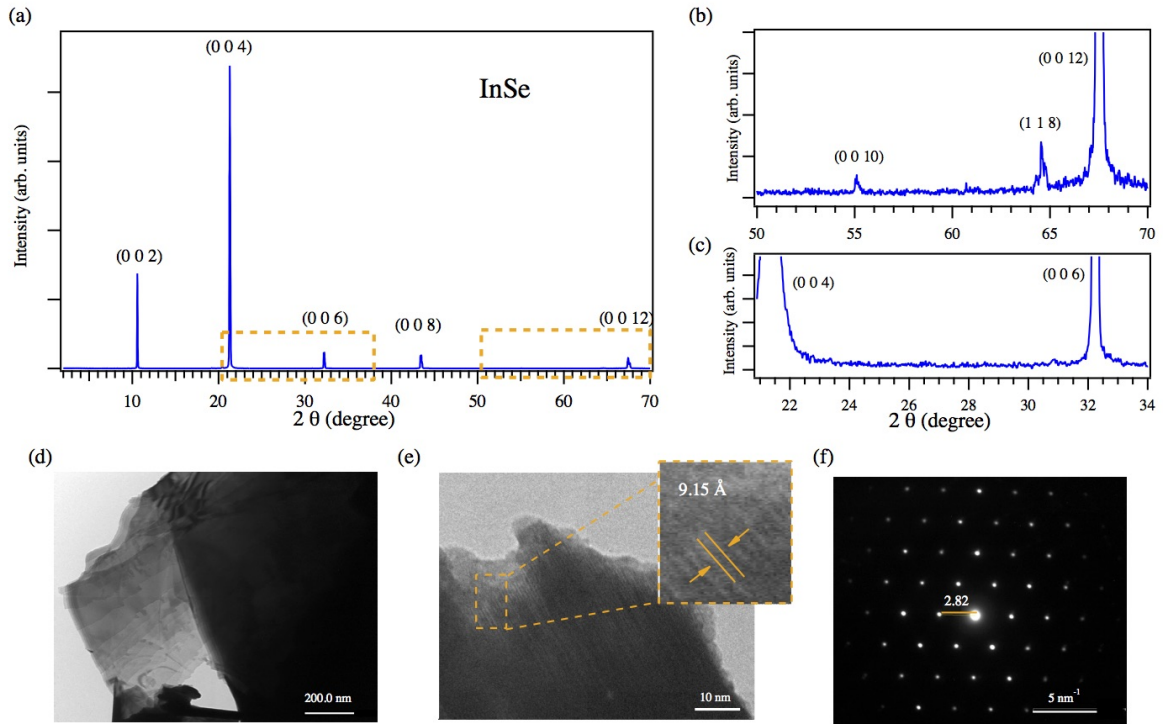


Figure 3.2: (a) XRD spectrum of InSe crystal. In panels (b) and (c) we report selected zoom extracted from (a) and highlighted by dashed yellow box. Representative TEM images of InSe: (d) 40000 \times and (e) 300000 \times magnification. The inset shows a zoom-in of panel (e) highlighting the distance between quadruple-layers. (f) SAED pattern of InSe crystal.

To gain information on the bulk structure of InSe samples, we have first employed the XRD technique. The room temperature XRD pattern, reported in Fig. 3.2(a), exhibits five main peaks at 10.576°, 21.290°, 32.247°, 43.482° and 67.441°. According to the existing literature and to international diffraction databases, these angles correspond to (0, 0, 2*n*) planes of the hexagonal polytypes, ϵ or β [34, 35], and to (0, 0, 3*n*) of γ -InSe [36]. The experimental observation of highly (0, 0, *n*) oriented diffracted peaks with narrow full-width at half-maximum (FWHM) (i.e. 0.120°) reveals the preferential orientation of the crystal planes, as well as the high-quality of the investigated samples.

However, on the basis of the main peaks only one cannot distinguish between different polytypes. Fig. 3.2(b) displays a zoom-in of the XRD spectrum in the angular range of 50° - 70°, showing one additional diffraction peak due to a residual polycrystalline phase located at 64.532°. The angular position of this peak turned out to be crucial in distinguishing between hexagonal and rhombohedral phases. We report in TABLE 3.1 the angular position of the observed peaks, their relative intensity and the calculated distance between planes (d_{hkl}). XRD relative intensity was calculated by defining the intensity of (0 0 4) peak, the strongest

$2\theta(^{\circ})$	$(h\ k\ l)$	Rel. intensity (%)	d_{hkl} (Å)
10.576	(0 0 2)	19.31	8.365
21.290	(0 0 4)	100	4.173
32.247	(0 0 6)	7.07	2.776
43.482	(0 0 8)	7.32	2.081
55.207	(0 0 10)	0.18	1.664
64.532	(1 1 8)	0.55	1.444
67.441	(0 0 12)	6.94	1.389

Table 3.1: Diffraction peaks position, corresponding diffraction planes, intensity normalized to the main peak and calculated planar distance.

peak, as 100%. The last column has been obtained according to the Bragg's relation, starting from the experimental angular position of the peaks. For main (0 0 n) peaks the calculated distances provide the c parameter by either $c = 2 n d_{hkl}$ or $c = 3 n d_{hkl}$, for hexagonal and rhombohedral phases, respectively. By comparing our data with the JCPDS-ICDD (Joint Committee on Powder Diffraction Standards-International Centre for Diffraction Data, card No.: 34-1431) standard database, it is possible to relate the diffraction peak detected at 64.532° with the planes (1 1 8) of the hexagonal phases, thus all the main peaks to planes: (0 0 2), (0 0 4), (0 0 6), (0 0 8), (0 0 10) and (0 0 12), as labeled in Fig. 3.2(a)-(c) and reported in TABLE 3.1. Indeed, the calculated distance for the diffraction peak detected at 64.532° which is 1.444 Å, well agrees with the theoretical one $\frac{1}{d^2} = \frac{4}{3} \left(\frac{h^2+hk+k^2}{a^2} \right) + \frac{l^2}{c^2}$, expected for the hexagonal phase, with c parameter of either ϵ or β phases. Starting from our experimental data, we deduced the value of the unit cell parameter $c = 16.672$ Å (± 0.045 Å) from main (0 0 $2n$) peaks; from the (1 1 8) peak, using the corresponding experimental planar distance and the c parameter previously calculated, we found the value of the lattice parameter $a = 4.005$ Å (± 0.022 Å). This result is in good agreement with values reported in the literature [26, 37], as well as in the JCPDS-ICDD database we used for indexing the diffraction peaks (card No.: 34-1431: $c = 16.640$ Å, $a = 4.005$ Å). We point out that no characteristic peaks of secondary phases of indium selenide In_xSe_y ($x \neq y$) were observed [37, 38]. Thus, from the analysis of the XRD spectra we confirm the high quality of the crystal, we rule out the γ phase and we evaluate the value of the volume of lattice parameters a and c , expected for the hexagonal phases; however, it is worth noting that the sequence of the peaks here observed is representative of an hexagonal 1:1 phase, which can be either ϵ or β . Thus, on the basis of the XRD results only, the phase identification is not complete.

To explore the microstructure and morphology further, TEM was performed. In Fig. 3.2(d)-(e) we report TEM images of InSe with 40000× and 300000× magnification, respectively. As shown in Fig. 3.2(d), the color (in greyscale), nearly transparent in extended regions, suggests the stratification of the sample. The cross-sectional TEM image, reported in Fig. 3.2(e), clearly reveals the alternation of bright and less bright grey columns. Starting from this, we estimate an A-B distance, i.e. half value of the c parameter, of about 9.15 Å (± 1.80 Å), in agreement with our XRD findings.

From selected area electron diffraction (SAED) measurements, reported in Fig. 3.2(f), we

can observe a well defined six sided pattern, which confirms the hexagonal structure and it is also index of high crystalline quality. In order to obtain a good quality diffraction image, the thinner areas of the sample have been selected. Starting from a spatial frequency (yellow line in Fig. 3.2(f)) of about 2.82 nm^{-1} ($\pm 0.14 \text{ nm}^{-1}$), evaluated from the spatial distance between the central spot and the first-neighbor ones, we have obtained the value of the reciprocal lattice vector of about 1.772 \AA^{-1} , and consequently the value of the lattice parameter $a=4.09 \text{ \AA}$ ($\pm 0.20 \text{ \AA}$). The last value is in agreement with our XRD findings and with the JCPDS-ICDD database.

It is worth nothing that XRD and TEM measurements have allowed us to exclude the rhombohedral γ phase, to obtain the values of the planar and volume lattice parameters, a and c , respectively, and to confirm the good crystalline quality of the samples. However, these techniques failed to untangle between the β and ϵ hexagonal phases. We notice that a high-resolution cross-sectional STEM image can provide locally the sequence of quadruple-layers [39].

At last, Raman spectroscopy has been employed to characterize the phonon and electronic properties of our crystals. For this class of compounds, vibrational modes are a unique fingerprint of different polytypes, because each space group allows selected vibrational modes [40, 41].

In Fig. 3.3 we report the optical images of InSe and the corresponding Raman spectra on areas of different thickness, taken with a 532 nm line, in the range of wavenumbers from 100 to 275 cm^{-1} . In both spectra, we observe three main peaks, at about 115, 176 and 226 cm^{-1} , corresponding to the $A_1(\Gamma_1^2)$, $E(\Gamma_3^3)/E(\Gamma_3^1)$ -(TO) and $A_1(\Gamma_1^3)$ vibrational modes, respectively. These vibrational modes are common to all three InSe phases with 1:1 stoichiometry, i.e. ϵ , β and γ [40, 42, 43]. Thus, from a first inspection no information can be gained on the structural phase of InSe samples. Going from a thick flake, Fig. 3.3(a), to a thinner one, Fig. 3.2(b), a weaker peak is detected at about 199 cm^{-1} . This peak has been associated to $A_1(\Gamma_1^1)$ -LO vibrational mode, and assumed as characteristic of non-centrosymmetric phases, i.e. ϵ and γ ones [32, 40, 44].

On the basis of our Raman results only, we would recognize a different couple of possible polytypes, that is ϵ and γ . However, XRD results have lead us to unequivocally rule out the rhombohedral γ phase. Thus, by crossing the information obtained from all the employed techniques, we can conclude that our InSe samples belong to the ϵ polytype and exhibit good crystallinity.

We further discuss the discriminant mode A_1 -(LO) at about 199 cm^{-1} . It has been recently shown that the intensity of Raman scattering for this vibrational mode is enhanced in resonant conditions, which is better met with incident light of 514.5 nm, and, further, by strain effects on the sample [45]. By means of Raman mapping, we have found that the A_1 -LO vibrational mode of InSe emerges gradually with decreasing thickness, as deduced from Fig. 3.3(b). This findings have been carefully monitored in previous publications [7, 46], and also used to quantify the number of InSe layers. Two different trends have been observed for the InSe above-mentioned vibrational modes: from one side a thickness-dependent intensity variation, on the other side a frequency shift toward higher or lower values, due to significant changes

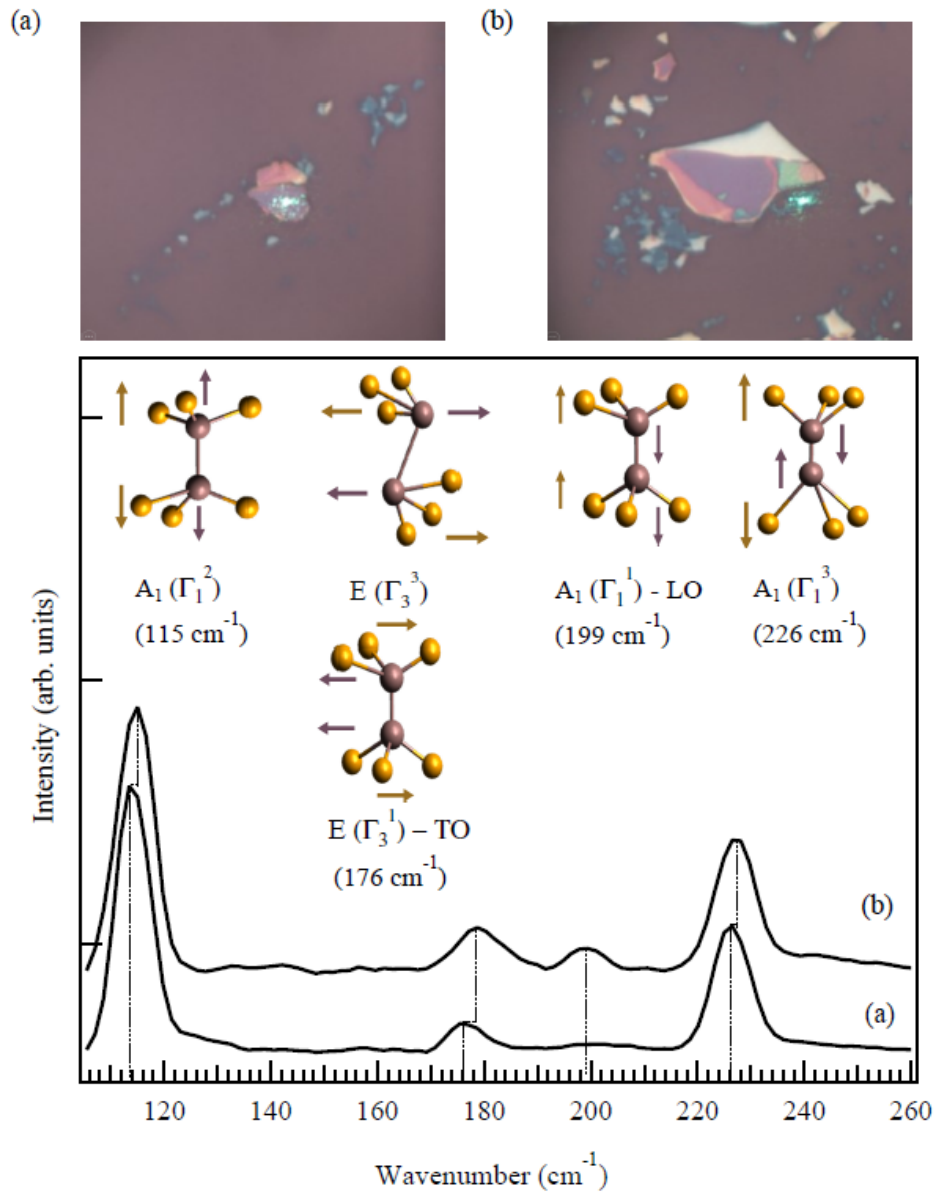


Figure 3.3: Optical images of InSe and corresponding Raman spectra taken on thick (a) and thinner (b) areas, as seen by optical contrast. The laser spot shows the point of detection.

in oscillator strengths in few-layer regime compared to the bulk structure.

In this work, we provide a detailed investigation of the crystal structure and morphology of bulk InSe, by means of XRD, TEM and Raman techniques. XRD results allowed to identify the hexagonal phase, typical of ϵ and β polytypes, and discard the rhombohedral one, i.e. γ polytype; in addition to this, we proved the single-phase and good crystalline quality of the sample and provide the value of the lattice parameters: $c = 16.672 \text{ \AA} (\pm 0.045 \text{ \AA})$ and $a = 4.005 \text{ \AA} (\pm 0.022 \text{ \AA})$. TEM measurements lead us to observe and confirm the layered structure of the sample and to measure the distance between quadruple-layers, that is $9.15 \text{ \AA} (\pm 1.80 \text{ \AA})$. The SAED technique confirms the hexagonal surface symmetry and provides the planar lattice parameter, $a = 4.09 \text{ \AA} (\pm 0.20 \text{ \AA})$, in agreement with XRD results. Finally, the Raman technique was used to untangle the similar ϵ and β polytypes. Indeed, the A_1 -LO vibrational mode, which is only detected in thin flakes, can act as a characteristic fingerprint of non-centrosymmetric symmetry groups. By crossing our results, we can unambiguously identify the predominantly ϵ -character of InSe samples and, most importantly, we show that the identification of the polytype within the family of III-VI semiconductors requires a careful use of complementary techniques. Moreover, as the symmetry and structure of each polytype affect the nonlinear optical properties, the identification of the structural phase is of wide interest for the realization of 2D heterostructures.

The results here shown are reported in the manuscript: "*Structural investigation of InSe layered semiconductors*", I. Grimaldi, T. Gerace, M. M. Pipita, I. D. Perrotta, F. Ciuchi, H. Berger, M. Papagno, M. Castriota, and D. Pacilè, *Solid State Communications* **311** (2020) 113855. The manuscript is available [here](#).

3.3 Electronic investigation of InSe and GaSe layered semiconductors

The structural characterization of InSe semiconductors, reported in section 3.2, allowed us to unambiguously identify the ϵ phase of our samples. Same phase characterization has been performed for bulk GaSe compounds (not reported), which confirms the prevailing ϵ -character of the samples. Starting from this, it was possible to address the DFT calculations in order to compare the electronic band structures of the two compounds.

In this section, by means of ARPES measurements and DFT calculations, we compare the electronic band structure of bulk ϵ -InSe and ϵ -GaSe layered semiconductors. The present study aims at clarifying the effect of spin-orbit and unveil the role of the different third group metal.

From the literature, we know that both ϵ -GaSe and ϵ -InSe have band edges located at the Γ point in the bulk structure, while decreasing the number of layers the valence band maximum (VBM) slightly shifts away from Γ point, creating a bow-shaped valence band, called inverted "Mexican hat". The band structure in the few-layers regime has attracted most of the attention as the peculiar shape yields high density of states (DOS) and Van Hove singularity near

the VBM, which may lead to unconventional superconductivity or ferromagnetic phase transition, according to recent theoretical studies [47]. The band structure of bulk ϵ -GaSe and ϵ -InSe has also been reported in the literature [21, 22, 48]. It has been shown that the spin-orbit interaction in the band structure of MX compounds does lift band degeneracies, causing a splitting of several hundreds meV just below the VBM, yielding measurable differences in high-energy photoluminescence transition energies and in angle-resolved photoemission spectroscopy (ARPES) experiments. However, still more work is needed to unveil the role of different post-transition metal atoms in modulating the electronic structure across the Fermi level.

3.3.1 Experimental details

The InSe and GaSe crystals were grown in double wall ampoules by means of the Bridgman method, as aforementioned in section 3.2.1.

The ARPES experiments were performed at the VUV-Photoemission beamline of the Elettra synchrotron radiation facility in Trieste (see chapter 1 section A.4.1). ARPES and XPS measurements were performed at RT. The energy and angular resolution of ARPES were set to 15 meV and 0.3 degrees, respectively. In order to better resolve the band structure of the presented samples, ARPES investigation was performed after an accurate photon energy scan (not reported) which allow us to choose a suitable photon energy. All the presented measurements were performed on a fresh mirror-like surface obtained by cleavage *in-situ* at RT and in UHV conditions (base pressure of 1×10^{-11} mbar), before the related ARPES measurements. The high quality of the achieved (111) surfaces were verified and confirmed by the (1×1) sharp features in the LEED pattern which allow us to determine also the sample orientation. To unveil possible surface contaminants, we have performed detailed XPS measurements after cleavage.

All the ARPES experimental results have been compared with electronic structure calculations provided by the group lead by Prof. Evgueni Chulkov and Dr. Sergey V. Ereameev.

3.3.2 Results and discussion

In Figs. 3.4 (a)-(c) and (e), we report the ϵ -InSe bulk band structure; the measurements were collected with 30 eV, 40 eV and 60 eV of photon energy, respectively. All measurements were performed at RT. In panel (a), we report the ARPES spectrum along the $\bar{M} \bar{\Gamma} \bar{M}'$ path of the Brillouin zone, while in the bottom panels we extended our measurements to the second Brillouin zone. The main feature of InSe band structure are the two band centered at the $\bar{\Gamma}$ point; the upper band is characterized by a downward dispersing paraboloid feature, which constitutes the valence band maximum. From DFT calculations, reported below in Fig. 3.7, one can observe that for both compounds, the paraboloid feature has prevalent selenium p_z character, while an admixture contribution of selenium p_x and a p_y orbitals prevails in the inner bands located at higher distance from the valence band maximum (about 1.5 eV below).

To better visualize the band dispersion of InSe and to enhance the contrast, in panels (b)-(d) and (f) of Fig. 3.4, we present also the corresponding second derivatives along the

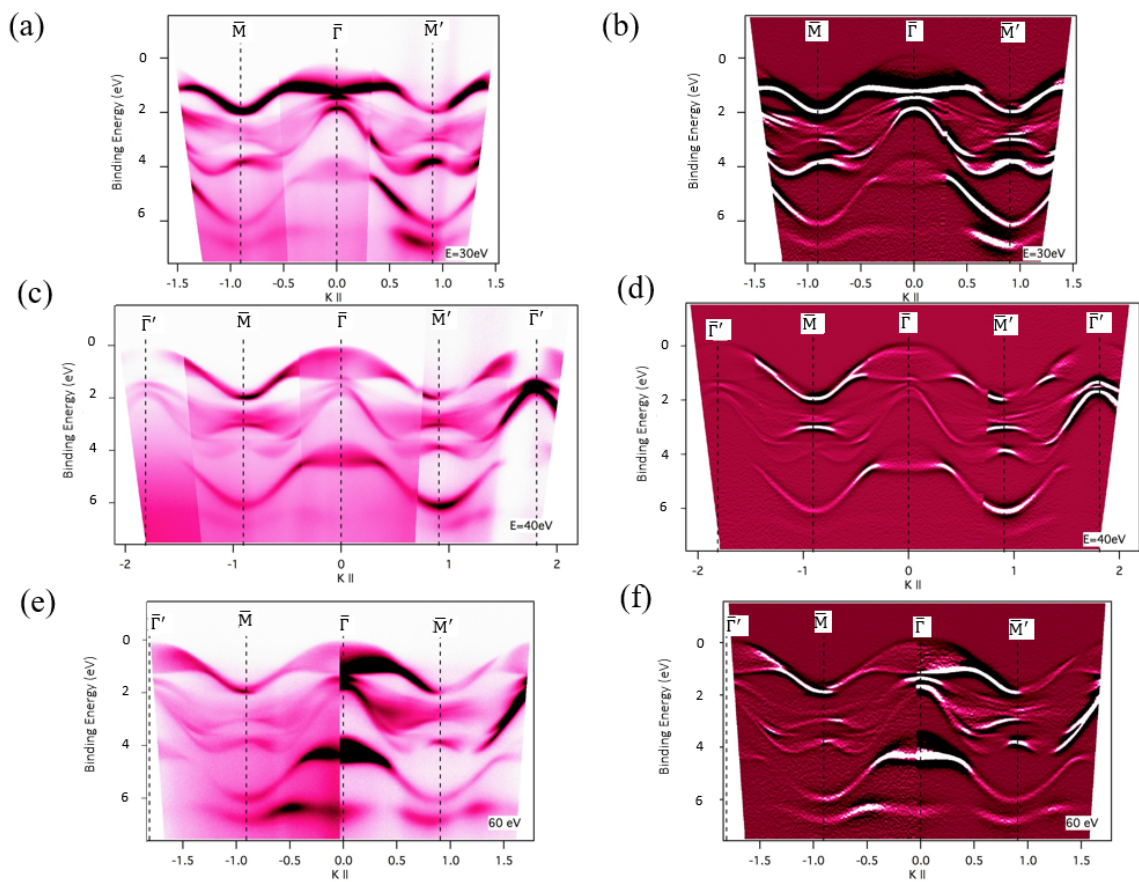


Figure 3.4: Electronic band structure and corresponding second derivatives along the energy axis of InSe measured with (a)-(b) 30 eV, (c)-(d) 40 eV and (e)-(f) 60 eV of photon energy.

binding energy axis; besides the distinctive features of the VBM, a multitude of downward dispersing bands has been emphasized, as we can observe at about $k_{\parallel} \pm 0.5 \text{ \AA}^{-1}$. Starting from the $\bar{\Gamma}$ point and moving towards \bar{M} (or \bar{M}') symmetry point, the main upper band changes from a parabolic dispersion (hole-like) to electron-like dispersion, with a minimum located at \bar{M} point ($k_{\parallel} \simeq 0.9 \text{ \AA}^{-1}$). Moreover, one can observe that many bands, located at lower kinetic energy, remain doubly degenerate, while others undergo to a split. It has been shown that the spin-orbit interaction in the band structure of MX compounds does lift band degeneracies, causing a splitting of several hundreds meV just below the VBM, yielding measurable differences. Indeed, in the absence of spin-orbit interaction (SOI), the p_x and a p_y states (we are referring to the bands that are at about 1.5 eV below the VBM) should be degenerate at the $\bar{\Gamma}$ point; SOI lifts the energy degeneracy with a spin-orbit splitting of about 0.34 eV, as showed in the zoom reported in Fig. 3.5. This value is in good agreement with previous works reported in Refs. [48–50]. Such spin-splitting confirms also that we are probing a non-centrosymmetric crystal (i.e. ϵ phase) [49].

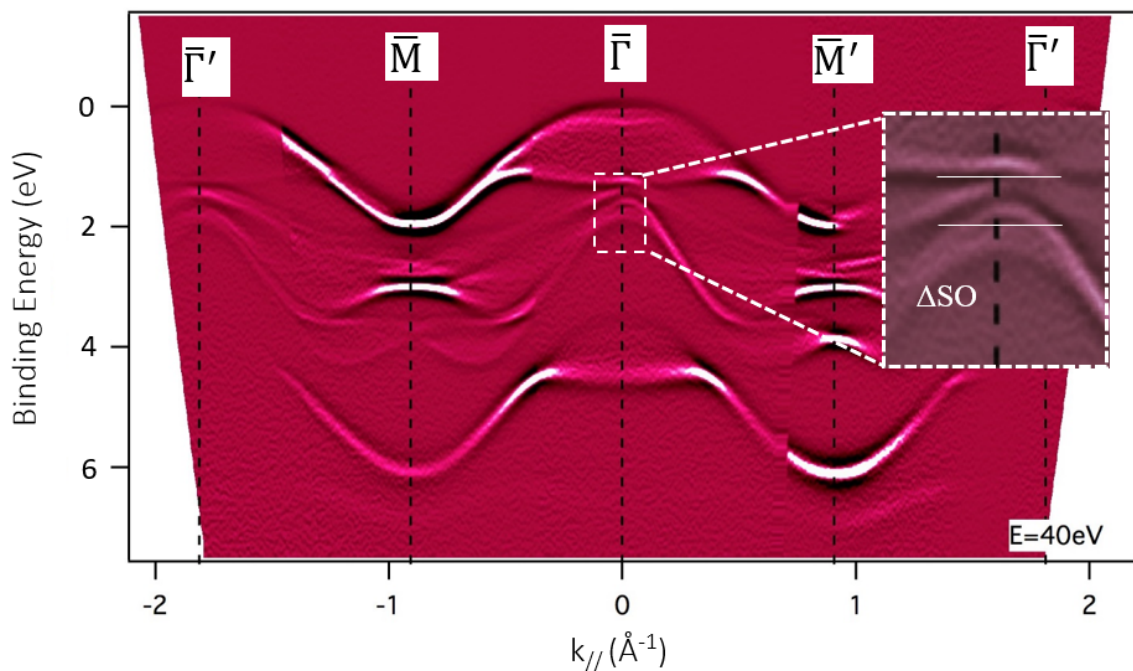


Figure 3.5: ARPES image of InSe (collected with 40 eV of photon energy) and zoom at $\bar{\Gamma}$ point: spin-orbit interaction induces an energy splitting of 0.34 eV.

In the following, we focus the attention on a comparative study between InSe and GaSe. In Fig. 3.6 we report the band structure of GaSe along (a) $\bar{\Gamma} \bar{K}$ and (b) $\bar{\Gamma} \bar{M}$ symmetry directions of the first Brillouin zone. The measurements were performed at RT and collected with 45 eV of photon energy. At first glance one can observe that the band structure is very similar to the one reported for InSe; indeed we can recognize the main distinctive dispersing feature centered at $\bar{\Gamma}$ point, which constitute the VBM, and a multitude of downward dispersing bands that spread from $\bar{\Gamma}$ point to the high symmetry points.

In Fig. 3.7 we report the DFT calculations for (a) InSe and (b) GaSe with the respective

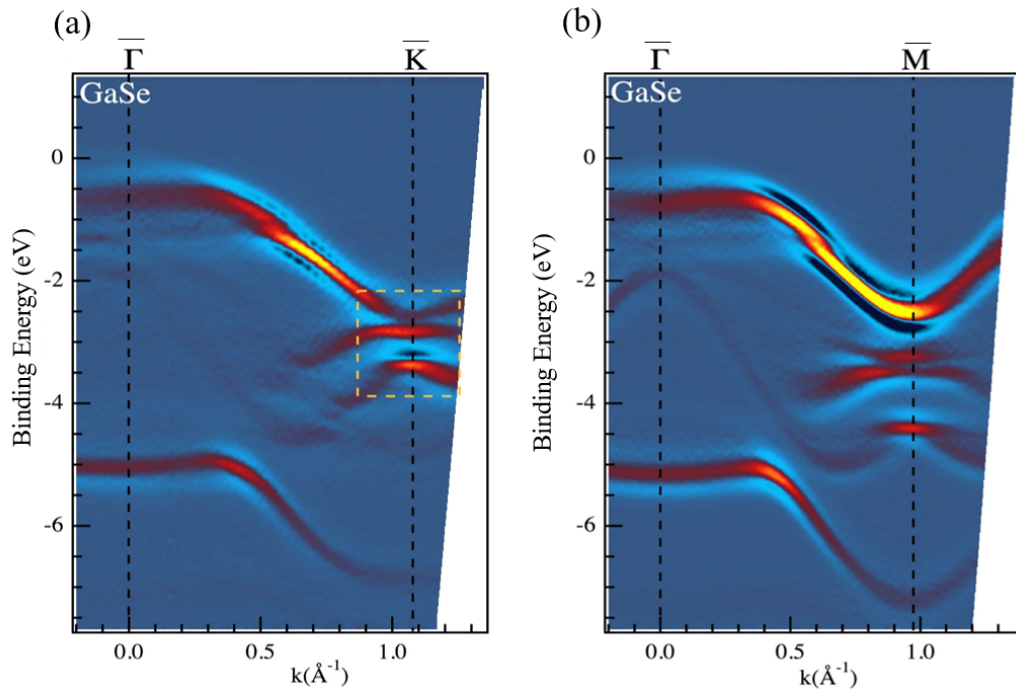


Figure 3.6: Electronic band structure of GaSe along (a) $\bar{\Gamma}$ \bar{K} and (b) $\bar{\Gamma}$ \bar{M} direction of the first Brillouin zone collected with 45 eV of photon energy.

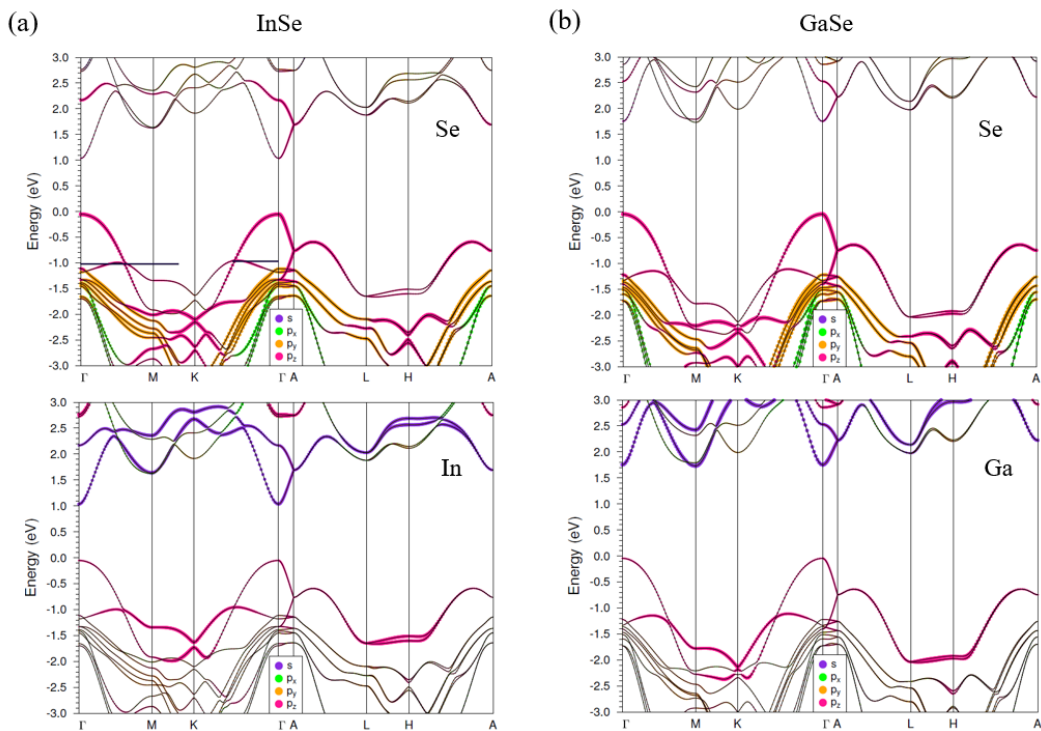


Figure 3.7: Calculated electronic band structure of (a) InSe and (b) GaSe. Upper panels show the Se atoms contribution, while below panels the third group metal one. The thickness of the lines gives the indication of the relative weights of the orbitals.

contribution of Se atoms (upper panels) and third group metals (bottom panels); the thickness of the lines indicate the weights of each orbitals. From DFT calculations, one can observe that p_x , p_y and p_z orbitals (In, Ga and Se) are more relevant in the formation of the valence band structure, while s orbital character prevails in the conduction band. The p_z character of Se, for each compound, contributes mainly in the formation of the top valence band (main paraboloid feature), indeed we expect a similar trend (such as band width, effective mass, etc.) for the two samples. Nevertheless, we expect some differences in the electronic band structure due to different contribution of third group metals (In or Ga). These differences should be more evident in the points where the weight of the orbitals of group III metals prevails, i.e. at the corners of the Brillouin zone (K and H points).

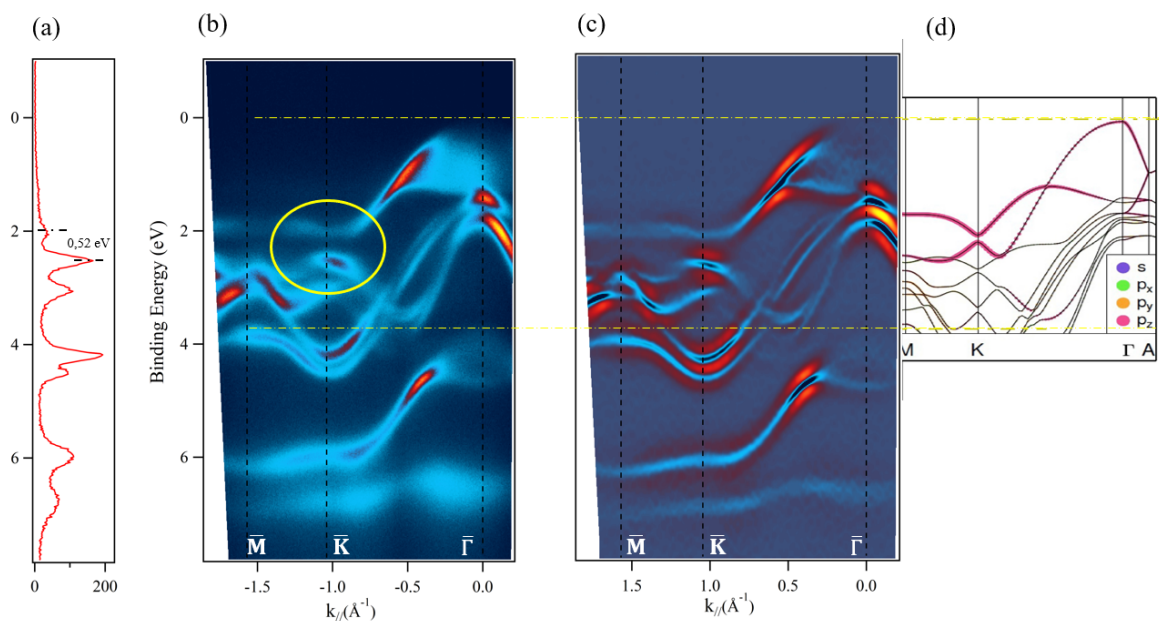


Figure 3.8: Insight to \bar{K} point of InSe: (a) EDC extracted at \bar{K} point, (b) as-acquired spectrum, (c) second derivative along the energy axis and (d) DFT calculation in the region outlined by yellow dotted lines.

For this purpose, we report for InSe and GaSe, in Figs. 3.8 and 3.9, the comparison between (b) the as-acquired spectra, (c) the second derivative (along the energy axis) and (d) DFT calculations in the area outlined by yellow dotted lines. In panels (a), we report also the EDC extracted at \bar{K} point for each compound. From DFT calculations one can observe that for InSe the upper band at \bar{K} point is well separated from the one below, while it undergoes to a kind of crossing for GaSe. Such difference is large enough to be experimentally appreciate, indeed we measured 0.52 eV for InSe and 0.20 eV for GaSe (see panels (a) of Figs. 3.8 and 3.9).

Following, we discuss the shape of the top of the valence band. The shape of the VBM close to the Γ point in bulk InSe and GaSe results from the close proximity of multiple subbands, originated from the interlayer coupling and decreasing in number in the few-layers regime, up to the Mexican hat structure characteristic of a single tetra-layer [51]. These narrowly spaced subbands are clearly visible in our measurements, due to the high quality of the crystal samples. In Fig. 3.10 we show the electronic band dispersion for (a)-(b) InSe and

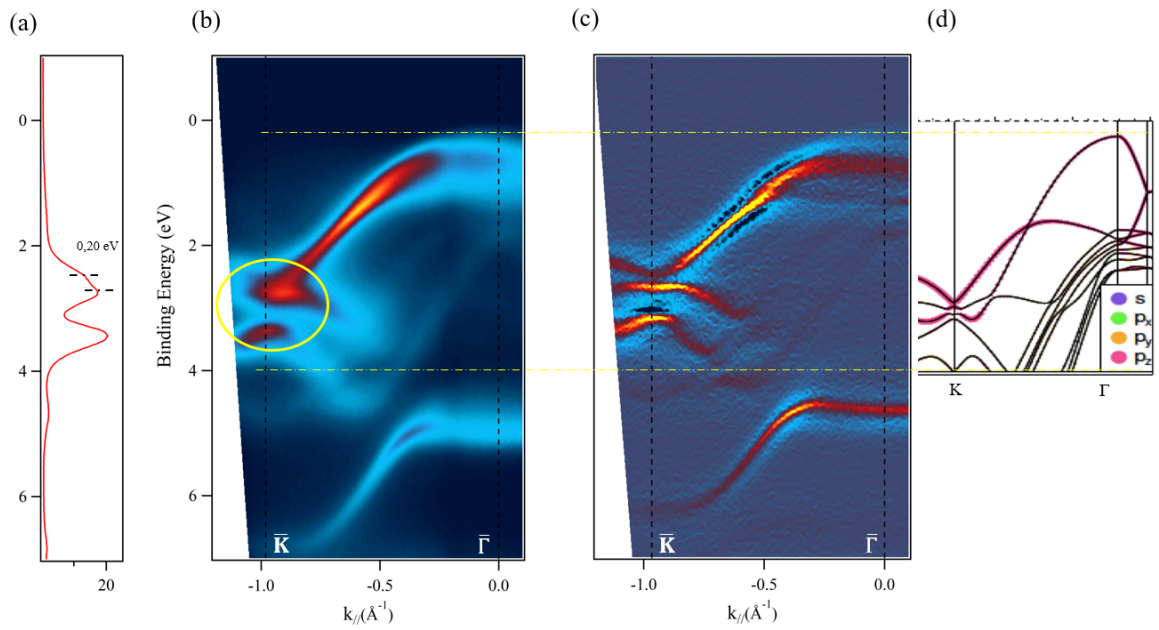


Figure 3.9: Insight to \bar{K} point of GaSe: (a) EDC extracted at \bar{K} , (b) as-acquired spectrum, (c) second derivative along the energy axis and (d) DFT calculation in the region outlined by yellow dotted lines.

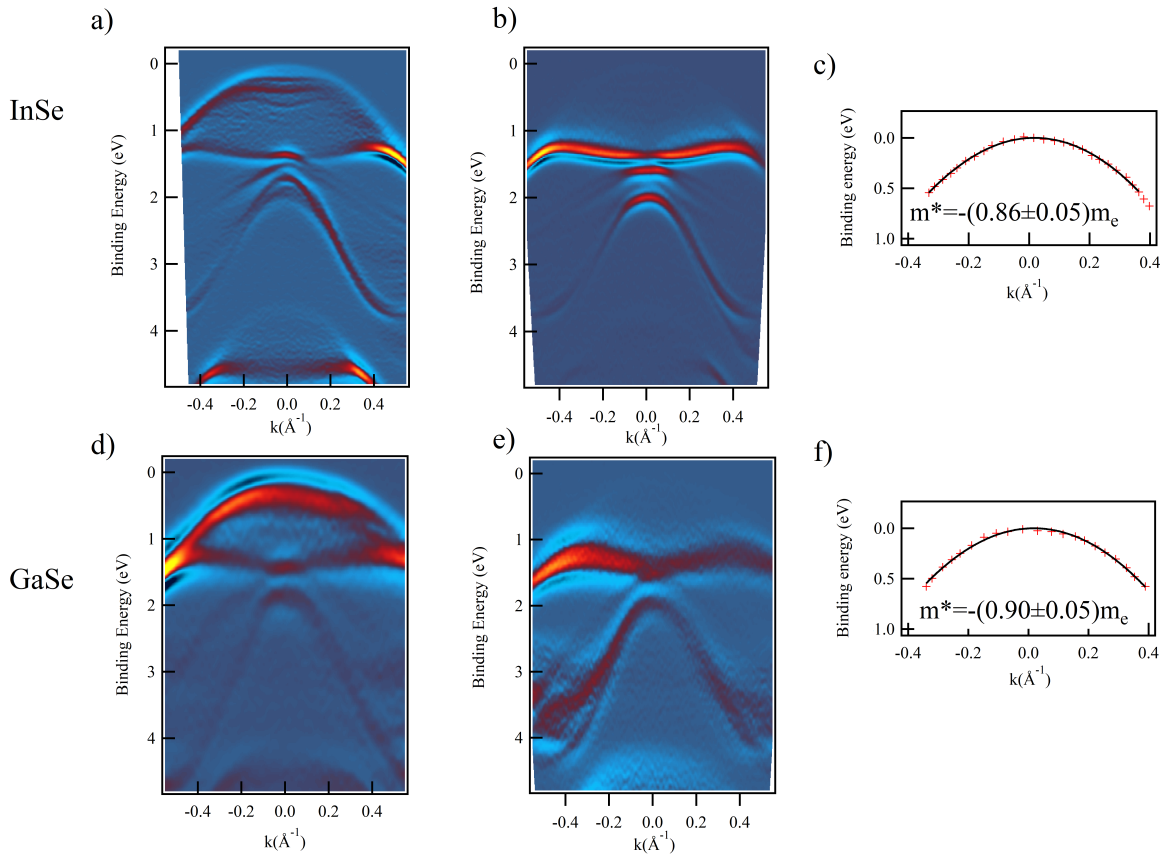


Figure 3.10: Matrix-element effect of the VBM: ARPES images at (a) 40 eV and (b) 30 eV of photon energy for InSe; ARPES images at (d) 40 eV and (e) 30 eV of photon energy for GaSe. Effective masses fit for (c) InSe and (f) GaSe.

(d)-(e) GaSe. In panels (a) and (d), either for InSe and GaSe, we recognize the typical parabolic structure centered at the $\bar{\Gamma}$ point (measurements collected with 40 eV of photon energy); by changing the photon energy (30 eV), panels (b) and (e), we observe a strong modulation of the signal intensity (matrix-element effects); the shape of the paraboloid upper structure almost vanishes giving way to a structured trend *very similar* to the Mexican hat. However, this results driven exclusively by the response in photoemission yield (matrix-element effect) which leads to a change in the relative intensities of the mentioned above subbands.

An analysis of the curvature of the top paraboloid band centered at the $\bar{\Gamma}$ point, allows to estimate the effective mass¹; the experimental dispersions (reported in panels (a) and (d)) have been fitted by using a parabola and yield an effective mass of $m^* = 0.86 m_e (\pm 0.05)$ for InSe, and of $m^* = 0.90 m_e (\pm 0.05)$ for GaSe; see panels (c) and (f) of Fig. 3.10. The values obtained for InSe are in good agreements with previous works [48].

In summary, our investigation on the band structure of bulk ϵ III-VI monochalcogenides show that the top of valence band, at $\bar{\Gamma}$ point, is mainly dominated by Se p_z states of either InSe and GaSe compounds; the main effect of different third group metal atoms (Ga or In) appears more deeply in binding energy and at the corner of the Brillouin zone (\bar{K} point), resulting in a different measurable value of spin-orbit split. Data analysis and comparison with on going theoretical calculations is in progress.

The results here shown are reported in the manuscript: "*Insight into the electronic structure of semiconducting ϵ -GaSe and ϵ -InSe*", S. V. Eremeev, M. Papagno, **I. Grimaldi**, O. De Luca, L. Ferrari, Asish K. Kundu, P. M. Sheverdyeva, P. Moras, G. Avvisati, A. Crepaldi, H. Berger, I. Vobornick, M. G. Betti, M. Grioni, C. Carbone, E. V. Chulkov, and D. Pacilè, *submitted to Physical Review B*.

¹The effective mass of electrons in a band with a given (E,k) relationship is given by: $m^* = \frac{\hbar^2}{d^2 E_k / dk^2}$.

References

- [1] A. K. Geim and I. V. Grigorieva. “Van der Waals heterostructures”. In: *Nature* 499.7459 (July 2013), pp. 419–425. DOI: 10.1038/nature12385.
- [2] S. Das, J.A. Robinson, M. Dubey, H. Terrones, and M. Terrones. “Beyond Graphene: Progress in Novel Two-Dimensional Materials and van der Waals Solids”. In: *Annual Review of Materials Research* 45.1 (July 2015), pp. 1–27. DOI: 10.1146/annurev-matsci-070214-021034.
- [3] K. S. Novoselov, A. Mishchenko, A. Carvalho, and A. H. Castro Neto. “2D materials and van der Waals heterostructures”. In: *Science* 353.6298 (July 2016), aac9439. DOI: 10.1126/science.aac9439.
- [4] W. Zhang, Q. Wang, Y. Chen, Z. Wang, and A. T. S. Wee. “Van der Waals stacked 2D layered materials for optoelectronics”. In: *2D Materials* 3.2 (Apr. 2016), p. 022001. DOI: 10.1088/2053-1583/3/2/022001.
- [5] Z. Yang, W. Jie, C.-H. Mak, S. Lin, H. Lin, X. Yang, F. Yan, S. P. Lau, and J. Hao. “Wafer-Scale Synthesis of High-Quality Semiconducting Two-Dimensional Layered InSe with Broadband Photoresponse”. In: *ACS Nano* 11.4 (Mar. 2017), pp. 4225–4236. DOI: 10.1021/acsnano.7b01168.
- [6] S. Shigetomi and T. Ikari. “Crystalline InSe Films Prepared by RF-Sputtering Technique”. In: *Japanese Journal of Applied Physics* 30.Part 2, No. 12B (Dec. 1991), pp. L2127–L2129. DOI: 10.1143/jjap.30.12127.
- [7] S. Lei, L. Ge, S. Najmaei, A. George, R. Koppera, J. Lou, M. Chhowalla, H. Yamaguchi, G. Gupta, R. Vajtai, A. D. Mohite, and P. M. Ajayan. “Evolution of the Electronic Band Structure and Efficient Photo-Detection in Atomic Layers of InSe”. In: *ACS Nano* 8.2 (Jan. 2014), pp. 1263–1272. DOI: 10.1021/nn405036u.
- [8] S. L. Stoll and A. R. Barron. “Metal-Organic Chemical Vapor Deposition of Indium Selenide Thin Films”. In: *Chemistry of Materials* 10.2 (Feb. 1998), pp. 650–657. DOI: 10.1021/cm970638i.
- [9] D. K. Sang, H. Wang, M. Qiu, R. Cao, Z. Guo, J. Zhao, Y. Li, Q. Xiao, D. Fan, and H. Zhang. “Two Dimensional β -InSe with Layer-Dependent Properties: Band Alignment, Work Function and Optical Properties”. In: *Nanomaterials* 9.1 (Jan. 2019), p. 82. DOI: 10.3390/nano9010082.
- [10] Z. Yang and J. Hao. “Recent Progress in 2D Layered III-VI Semiconductors and their Heterostructures for Optoelectronic Device Applications”. In: *Advanced Materials Technologies* 4.8 (May 2019), p. 1900108. DOI: 10.1002/admt.201900108.
- [11] C. Song, F. Fan, N. Xuan, S. Huang, G. Zhang, C. Wang, Z. Sun, H. Wu, and H. Yan. “Largely Tunable Band Structures of Few-Layer InSe by Uniaxial Strain”. In: *ACS Applied Materials & Interfaces* 10.4 (Jan. 2018), pp. 3994–4000. DOI: 10.1021/acsam.7b17247.

- [12] D. V. Rybkovskiy, N. R. Arutyunyan, A. S. Orekhov, I. A. Gromchenko, I. V. Vorobiev, A. V. Osadchy, E. Yu. Salaev, T. K. Baykara, K. R. Allakhverdiev, and E. D. Obraztsova. “Size-induced effects in gallium selenide electronic structure: The influence of interlayer interactions”. In: *Physical Review B* 84.8 (Aug. 2011). DOI: 10.1103/physrevb.84.085314.
- [13] S. Lei, L. Ge, Z. Liu, S. Najmaei, G. Shi, G. You, J. Lou, R. Vajtai, and P. M. Ajayan. “Synthesis and Photoresponse of Large GaSe Atomic Layers”. In: *Nano Letters* 13.6 (June 2013), pp. 2777–2781. DOI: 10.1021/nl4010089.
- [14] T. Wang, J. Li, Q. Zhao, Z. Yin, Y. Zhang, B. Chen, Y. Xie, and W. Jie. “High-Quality GaSe Single Crystal Grown by the Bridgman Method”. In: *Materials* 11.2 (Jan. 2018), p. 186. DOI: 10.3390/ma11020186.
- [15] P. Hu, Z. Wen, L. Wang, P. Tan, and K. Xiao. “Synthesis of Few-Layer GaSe Nanosheets for High Performance Photodetectors”. In: *ACS Nano* 6.7 (June 2012), pp. 5988–5994. DOI: 10.1021/nn300889c.
- [16] X. Li, M.-W. Lin, A. A. Puretzky, J. C. Idrobo, C. Ma, M. Chi, M. Yoon, C. M. Rouleau, I. I. Kravchenko, D. B. Geohegan, and K. Xiao. “Controlled Vapor Phase Growth of Single Crystalline, Two-Dimensional GaSe Crystals with High Photoresponse”. In: *Scientific Reports* 4.1 (June 2014). DOI: 10.1038/srep05497.
- [17] D. A. Bandurin, A. V. Tyurnina, G. L. Yu, A. Mishchenko, V. Zólyomi, S. V. Morozov, R. K. Kumar, R. V. Gorbachev, Z. R. Kudrynskiy, S. Pezzini, Z. D. Kovalyuk, U. Zeitler, K. S. Novoselov, A. Patané, L. Eaves, I. V. Grigorieva, V. I. Fal’ko, A. K. Geim, and Y. Cao. “High electron mobility, quantum Hall effect and anomalous optical response in atomically thin InSe”. In: *Nature Nanotechnology* 12.3 (Nov. 2016), pp. 223–227. DOI: 10.1038/nnano.2016.242.
- [18] D. J. Terry, V. Zólyomi, M. Hamer, A. V. Tyurnina, D. G. Hopkinson, A. M. Rakowski, S. J. Magorrian, N. Clark, Y. M. Andreev, O. Kazakova, K. Novoselov, S. J. Haigh, V. I. Fal’ko, and R. Gorbachev. “Infrared-to-violet tunable optical activity in atomic films of GaSe, InSe, and their heterostructures”. In: *2D Materials* 5.4 (Sept. 2018), p. 041009. DOI: 10.1088/2053-1583/aadfc3.
- [19] P.-H. Ho, Y.-R. Chang, Y.-C. Chu, M.-K. Li, C.-A. Tsai, W.-H. Wang, C.-H. Ho, C.-W. Chen, and P.-W. Chiu. “High-Mobility InSe Transistors: The Role of Surface Oxides”. In: *ACS Nano* 11.7 (July 2017), pp. 7362–7370. DOI: 10.1021/acsnano.7b03531.
- [20] J. Jiang, J. Li, Y. Li, J. Duan, L. Li, Y. Tian, Z. Zong, H. Zheng, X. Feng, Q. Li, H. Liu, Y. Zhang, T.-L. Ren, and L. Han. “Stable InSe transistors with high-field effect mobility for reliable nerve signal sensing”. In: *npj 2D Materials and Applications* 3.1 (July 2019). DOI: 10.1038/s41699-019-0110-x.
- [21] Z. B. Aziza, H. Henck, D. Pierucci, M. G. Silly, E. Lhuillier, G. Patriarche, F. Sirotti, M. Eddrief, and A. Ouerghi. “van der Waals Epitaxy of GaSe/Graphene Heterostructure: Electronic and Interfacial Properties”. In: *ACS Nano* 10.10 (Oct. 2016), pp. 9679–9686. DOI: 10.1021/acsnano.6b05521.

- [22] Z. B. Aziza, D. Pierucci, H. Henck, M. G. Silly, C. David, M. Yoon, F. Sirotti, K. Xiao, M. Eddrief, J.-C. Girard, and A. Ouerghi. “Tunable quasiparticle band gap in few-layer GaSe/graphene van der Waals heterostructures”. In: *Phys. Rev. B* 96 (3 July 2017), p. 035407. DOI: 10.1103/PhysRevB.96.035407.
- [23] C. Hee Lee, S. Krishnamoorthy, D. J. O’Hara, M. R. Brenner, J. M. Johnson, J. S. Jamison, R. C. Myers, R. K. Kawakami, J. Hwang, and S. Rajan. “Molecular beam epitaxy of 2D-layered gallium selenide on GaN substrates”. In: *Journal of Applied Physics* 121.9 (Mar. 2017), p. 094302. DOI: 10.1063/1.4977697.
- [24] F. Yan, L. Zhao, A. Patanè, P. Hu, X. Wei, W. Luo, D. Zhang, Q. Lv, Q. Feng, C. Shen, K. Chang, L. Eaves, and K. Wang. “Fast, multicolor photodetection with graphene-contacted p-GaSe/n-InSe van der Waals heterostructures”. In: *Nanotechnology* 28.27 (June 2017), 27LT01. DOI: 10.1088/1361-6528/aa749e.
- [25] W. Li, Samuel Poncè, and F. Giustino. “Dimensional Crossover in the Carrier Mobility of Two-Dimensional Semiconductors: The Case of InSe”. In: *Nano Letters* 19.3 (Feb. 2019), pp. 1774–1781. DOI: 10.1021/acs.nanolett.8b04799.
- [26] G. Han, Z.-G. Chen, J. Drennan, and J. Zou. “Indium Selenides: Structural Characteristics, Synthesis and Their Thermoelectric Performances”. In: *Small* 10.14 (Apr. 2014), pp. 2747–2765. DOI: 10.1002/smll.201400104.
- [27] R. Longinhos and J. Ribeiro-Soares. “Ultra-weak interlayer coupling in two-dimensional gallium selenide”. In: *Physical Chemistry Chemical Physics* 18.36 (2016), pp. 25401–25408. DOI: 10.1039/c6cp03806a.
- [28] N.C. Fernelius. “Properties of gallium selenide single crystal”. In: *Progress in Crystal Growth and Characterization of Materials* 28.4 (Jan. 1994), pp. 275–353. DOI: 10.1016/0960-8974(94)90010-8.
- [29] A. Chevy, A. Kuhn, and M.-S. Martin. “Large InSe monocrystals grown from a non-stoichiometric melt”. In: *Journal of Crystal Growth* 38.1 (Apr. 1977), pp. 118–122. DOI: 10.1016/0022-0248(77)90381-5.
- [30] *Avogadro: an open-source molecular builder and visualization tool. Version 1.2.0 Web page.* <http://avogadro.cc/>.
- [31] K. S. Urmila, T. A. Namitha, R. R. Philip, and B. Pradeep. “Optical and low-temperature thermoelectric properties of phase-pure p-type InSe thin films”. In: *Applied Physics A* 120.2 (May 2015), pp. 675–681. DOI: 10.1007/s00339-015-9237-6.
- [32] M. Wu, Q. Xie, Y. Wu, J. Zheng, W. Wang, L. He, X. Wu, and B. Lv. “Crystal structure and optical performance in bulk γ -InSe single crystals”. In: *AIP Advances* 9.2 (Feb. 2019), p. 025013. DOI: 10.1063/1.5086492.
- [33] G. W. Mudd, S. A. Svatek, T. Ren, A. Patanè, O. Makarovskiy, L. Eaves, P. H. Beton, Z. D. Kovalyuk, G. V. Lashkarev, Z. R. Kudrynskiy, and A. I. Dmitriev. “Tuning the Bandgap of Exfoliated InSe Nanosheets by Quantum Confinement”. In: *Advanced Materials* 25.40 (Aug. 2013), pp. 5714–5718. DOI: 10.1002/adma.201302616.

- [34] S. R. Tamalampudi, Y.-Y. Lu, R. Kumar U., R. Sankar, C.-D. Liao, K. Moorthy B., C.-H. Cheng, F. C. Chou, and Y.-T. Chen. “High Performance and Bendable Few-Layered InSe Photodetectors with Broad Spectral Response”. In: *Nano Letters* 14.5 (Apr. 2014), pp. 2800–2806. DOI: 10.1021/nl500817g.
- [35] B. Gürbulak, M. Şata, S. Dogan, S. Duman, A. Ashkhasi, and E. F. Keskenler. “Structural characterizations and optical properties of InSe and InSe:Ag semiconductors grown by Bridgman/Stockbarger technique”. In: *Physica E: Low-dimensional Systems and Nanostructures* 64 (Nov. 2014), pp. 106–111. DOI: 10.1016/j.physe.2014.07.002.
- [36] A. Milutinović, Z. Ž. Lazarević, M. Jakovljević, B. Hadžić, M. Petrović, M. Gilić, W. D. Dobrowolski, and N. Ž. Romčević. “Optical properties of layered III-VI semiconductor γ -InSe: M (M = Mn, Fe, Co, Ni)”. In: *Journal of Physics and Chemistry of Solids* 89 (Feb. 2016), pp. 120–127. DOI: 10.1016/j.jpccs.2015.10.020.
- [37] S. Popović, A. Tonejc, B. Gržeta-Plenković, B. Čelustka, and R. Trojko. “Revised and new crystal data for indium selenides”. In: *Journal of Applied Crystallography* 12.4 (Aug. 1979), pp. 416–420. DOI: 10.1107/s0021889879012863.
- [38] G. Liu, K. Chen, and J. Li. “Combustion synthesis of InSe, In₂Se₃, and GaSe”. In: *Journal of the American Ceramic Society* 101.1 (Sept. 2017), pp. 36–39. DOI: 10.1111/jace.15223.
- [39] C. H. Lee, S. Krishnamoorthy, D. J. O’Hara, M. R. Brenner, J. M. Johnson, J. S. Jamison, R. C. Myers, R. K. Kawakami, J. Hwang, and S. Rajan. “Molecular beam epitaxy of 2D-layered gallium selenide on GaN substrates”. In: *Journal of Applied Physics* 121.9 (Mar. 2017), p. 094302. DOI: 10.1063/1.4977697.
- [40] S. Jandl and C. Carlone. “Raman spectrum of crystalline InSe”. In: *Solid State Communications* 25.1 (Jan. 1978), pp. 5–8. DOI: 10.1016/0038-1098(78)91157-2.
- [41] F. E. Faradev, N. M. Gasanly, B. N. Mavrin, and N. N. Melnik. “Raman scattering in some III-VI layer single crystals”. In: *Physica Status Solidi (b)* 85.1 (Jan. 1978), pp. 381–386. DOI: 10.1002/pssb.2220850142.
- [42] M. Dai, H. Chen, R. Feng, W. Feng, Y. Hu, H. Yang, G. Liu, X. Chen, J. Zhang, C.-Y. Xu, and P. Hu. “A Dual-Band Multilayer InSe Self-Powered Photodetector with High Performance Induced by Surface Plasmon Resonance and Asymmetric Schottky Junction”. In: *ACS Nano* 12.8 (Aug. 2018), pp. 8739–8747. DOI: 10.1021/acsnano.8b04931.
- [43] C. Carlone and S. Jandl. “Second order Raman spectrum and phase transition in InSe”. In: *Solid State Communications* 29.1 (Jan. 1979), pp. 31–33. DOI: 10.1016/0038-1098(79)90145-5.
- [44] C. Song, F. Fan, N. Xuan, S. Huang, G. Zhang, C. Wang, Z. Sun, H. Wu, and H. Yan. “Largely Tunable Band Structures of Few-Layer InSe by Uniaxial Strain”. In: *ACS Applied Materials and Interfaces* 10.4 (2018), pp. 3994–4000. DOI: 10.1021/acsmi.7b17247.

- [45] C. Song, F. Fan, N. Xuan, S. Huang, C. Wang, G. Zhang, F. Wang, Q. Xing, Y. Lei, Z. Sun, H. Wu, and H. Yan. “Drastic enhancement of the Raman intensity in few-layer InSe by uniaxial strain”. In: *Phys. Rev. B* 99 (19 May 2019), p. 195414. DOI: 10.1103/PhysRevB.99.195414.
- [46] J. F. Sánchez-Royo, G. Muñoz-Matutano, M. Brotons-Gisbert, J. P. Martínez-Pastor, A. Segura, A. Cantarero, R. Mata, J. Canet-Ferrer, G. Tobias, E. Canadell, J. Marqués-Hueso, and B. D. Gerardot. “Electronic structure, optical properties, and lattice dynamics in atomically thin indium selenide flakes”. In: *Nano Research* 7.10 (Oct. 2014), pp. 1556–1568. ISSN: 1998-0000. DOI: 10.1007/s12274-014-0516-x.
- [47] T. Cao, Z. Li, and S. G. Louie. “Tunable Magnetism and Half-Metallicity in Hole-Doped Monolayer GaSe”. In: *Phys. Rev. Lett.* 114 (23 June 2015), p. 236602. DOI: 10.1103/PhysRevLett.114.236602.
- [48] H. Henck, D. Pierucci, J. Zribi, F. Bisti, E. Papalazarou, J.-C. Girard, J. Chaste, F. Bertran, P. Le Fèvre, F. Sirotti, L. Perfetti, C. Giorgetti, A. Shukla, J. E. Rault, and A. Ouerghi. “Evidence of direct electronic band gap in two-dimensional van der Waals indium selenide crystals”. In: *Physical Review Materials* 3.3 (Mar. 2019). DOI: 10.1103/physrevmaterials.3.034004.
- [49] D. T. Do, S. D. Mahanti, and C. W. Lai. “Spin splitting in 2D monochalcogenide semiconductors”. In: *Scientific Reports* 5.1 (Nov. 2015). DOI: 10.1038/srep17044.
- [50] M. Zhou, R. Zhang, J. Sun, W.-K. Lou, D. Zhang, W. Yang, and K. Chang. “Multiband k·p theory of monolayer XSe (X = In, Ga)”. In: *Physical Review B* 96.15 (Oct. 2017). DOI: 10.1103/physrevb.96.155430.
- [51] I. A. Kibirev, A. V. Matetskiy, A. V. Zotov, and A. A. Saranin. “Thickness-dependent transition of the valence band shape from parabolic to Mexican-hat-like in the MBE grown InSe ultrathin films”. In: *Applied Physics Letters* 112.19 (May 2018), p. 191602. DOI: 10.1063/1.5027023.

Black-Phosphorus and analogue materials

Beyond graphene, a wide class of 2D materials with different properties has been investigated, including quasi-2D topological insulators, transition metal dichalcogenides (TMD), monochalcogenides (MX) and very recently, black phosphorous (BP) and analogue materials.

Recently, BP has been widely studied as it possesses high charge carrier mobility, tunable band-gap and peculiar anisotropic structure.

In the first part of the chapter, I report the results of Time- and Angle-Resolved PhotoElectron Spectroscopy investigations on BP, in order to shed light on the electronic response to an ultrafast laser excitation; the observation of a shift of the valence band (VB) maximum is indicative of band-gap renormalization; the relaxation time of holes, near VB maximum, and electrons at the CB minimum have been estimated.

In the second part of the chapter, I report some preliminary investigation on SnSe, which has triggered much interest due to its thermoelectric dimensionless figure of merit (ZT) (maximum value of Seebeck coefficient). We focused also on SnS, whose thermoelectric performances are also large and on substitutional alloys with different percentages of Pb.

4.1 Introduction

The family of 2D-layered materials has been expanding rapidly in the last years. Among all, Black Phosphorus (BP), with its tunable band-gap and its peculiar crystal structure opens opportunities for optoelectronic applications [1–4]. BP is a layered semiconductor which has attracted attention due to its high carrier mobility (comparable to graphene) [5] and peculiar structure which infers in-plane anisotropic physical properties. It is considered as a promising material for many applications, such as in transistors, photonics, optoelectronics, sensors, batteries and catalysis. BP has the capability to combine the optoelectronic properties of gapless graphene [6] with the wide-gap characteristic of the transition metal dichalcogenides (TMDs) [7].

One of the most interesting aspects of BP resides in its unique structural arrangement, which has a strong in-plane covalent bonding but weak vdWs interlayer interactions, and also

in its tunable layer-dependent bandgap of 0.3 - 2.0 eV, which makes it attractive in electronics, optoelectronics and photovoltaics applications.

Despite the great interest in the excellent properties of BP, unfortunately it has found to degrade within a few hours when exposed to oxygen and water vapour in air [8].

This is the reason why more stable layered semiconductors are of significant interest; among these it makes its way orthorhombic tin selenide (SnSe), which is representative of group IV-VI binary compounds. SnSe is robust and share the same peculiar structure with black phosphorus. As the electronic band structure of SnSe has been subject of several studies, both theoretical and experimental [9], there are no theoretical calculations and/or experimental studies on the parental compounds $\text{Pb}_{1-x}\text{Sn}_x\text{S}$. In this chapter I show preliminary ARPES measurements on SnSe and SnS (which is isostructural to SnSe and BP) and substitutional alloys with 25% and 50% of Pb.

Our results will also help modelling interface between ultra-thin layers semiconductors, in search for advantageous properties or enhancements of thermoelectric properties. *Ab initio* calculations are ongoing, as well as our data analysis. The combined theory and experiment will unravel the origin of the large figure of merit of SnSe, by comparison with SnS whose thermoelectric performances are large but smaller with respect to SnSe [10, 11].

Further measurements are also in progress.

4.2 TR-ARPES investigation of Black Phosphorus

In this section, the electronic and optoelectronic properties of BP have been discussed. BP layered material is composed of layers of atoms organized in a stable structure, where the layers are held together by van der Waals forces, which allow to an easy exfoliation of the sample. Bulk BP have a base-centered orthorhombic (Cmca space group (No. 64)) crystal structures and symmetry point group D_{2h}^{18} [12].

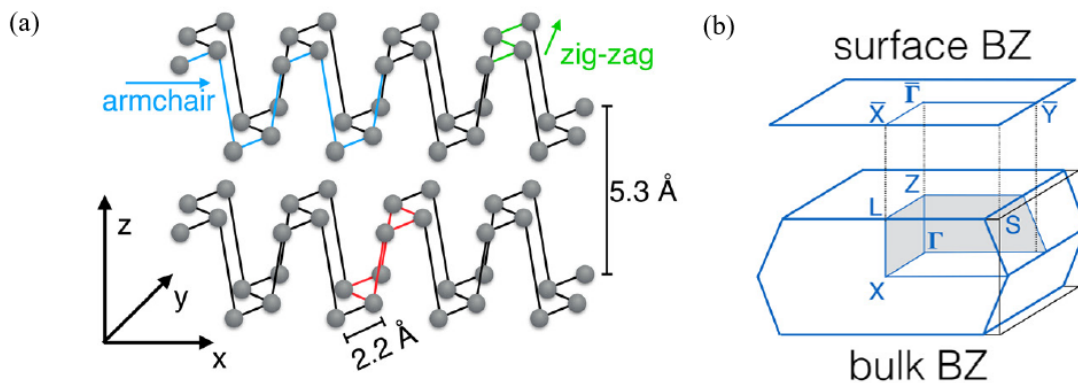


Figure 4.1: (a) Crystal structure of BP. (b) Bulk and surface-projected Brillouin zone.

The unit cell of BP is formed by two puckered bilayers; the flat honeycomb structure is distorted with armchair (along x) and zig-zag (along y) in-plane modulations, as showed in panel (a) of Fig. 4.1 [13]. The peculiar trait of BP is its highly anisotropic crystal structure,

which leads to a sizeable in-plane asymmetry of optical and electronic properties [14]. We report also the Brillouin zone schemes of bulk and surface BP in panel (b) of Fig. 4.1, where high-symmetry points are highlighted.

Interest on this material has been renewed since 2014, when its exfoliation into few-layers was first demonstrated, allowing for the fabrication as an atomically thin semiconductor, whose optical band gap and electronic properties are controllable by the number of layers. The strength of BP is the band-gap tunability, making it a promising material for optoelectronic devices. For instance, the experimental¹ band gap of BP is found to range from 0.33 eV [18–20], in bulk BP, up to almost 2.0 eV for its monolayer counterpart, called "phosphorene". Its band-gap can be engineered to cover mid- and near-infrared (IR) [15, 21–23], with various applications, such as tunable photodetector, solar cell and thermoelectric-power generators [14, 24–26].

Moreover, the observed high carrier mobilities of the order of $10^5 \text{ cm}^2 \text{ V}^{-1} \text{ s}^{-1}$ makes it promising for electronic applications, and, despite the value decreases by one/two orders of magnitude in the monolayer regime, it appears to be larger than that of many TMDs [12, 27–30]; BP advantageously bridges the optoelectronic properties of graphene [6] with the wide gap of TMDs [7, 30]. Beside this, BP has been successfully implemented also in laser technology [31–33] and polarization-sensitive photodetector, in order to exploit its strong in-plane absorption dichroism [4, 34].

It is worth noted that although the conductivity properties are related to the stationary state of the system², for other applications which require light absorption, knowledge of the dynamics of the charge carriers in VB and CB is mandatory. In this context, we have investigated the electronic properties of photoexcited BP by means of TR-ARPES (with laser excitation of 1.55 eV) and compared our results with *ab initio* calculations. A clear shift of the VB maximum has been observed, which indicates the band-gap renormalization (BGR) effect; it was also possible to determine the lifetimes of the excited electrons and hole population.

4.2.1 Experimental details

The experiments were performed at the EPFL LACUS, at the ASTRA end station of the Harmonium beamline; further details are available in section A.5.2. All the TR-ARPES measurements were carried out at 80 K with an overall temporal resolution of 200 fs an energy and angular resolution of 130 meV and 0.3° , respectively. Static ARPES measurements were performed at 80 K using He II α emission line of He discharge lamp (see section A.5.2). The samples have been acquired from hq Graphene Groningen Netherlands and cleaved *in situ* in UHV condition by scotch tape method.

The *ab initio* calculations were performed by A. Marini et al. by using the quantum espresso suite [35] to compute the equilibrium properties of BP. Structural and electronic properties have been obtained by DFT calculation.

¹The theoretical value is slightly larger, 0.44 eV from Refs. [15–17].

²The conductivity properties are determined by the properties of the charges at the Fermi surface, i.e. limited to the knowledge of the steady-state.

Density-functional-perturbation-theory has been used to compute electron-phonon matrix elements.

The experimental pump pulse has been simulated by using a narrow band pump laser pulse; for frequency, intensity and width the experimental values have been used. In order to be sure that the pump is correctly absorbed, the screened-exchange SEX approximation has been used [36].

4.2.2 Results and discussion

A three-dimensional ARPES map (energy vs momentum cuts) acquired with 40.8 eV (He II α) of photon energy is reported in Fig. 4.2. The top surface shows the Fermi surface and the sides of the cube present the band dispersion along the main zig-zag and armchair directions; the presented measurements are in agreement with earlier studies reported in Refs. [2, 19]. The valence band maximum (VBM) is located exactly in correspondence of the Γ point of the first surface Brillouin zone (sketch represented in Fig. 4.1).

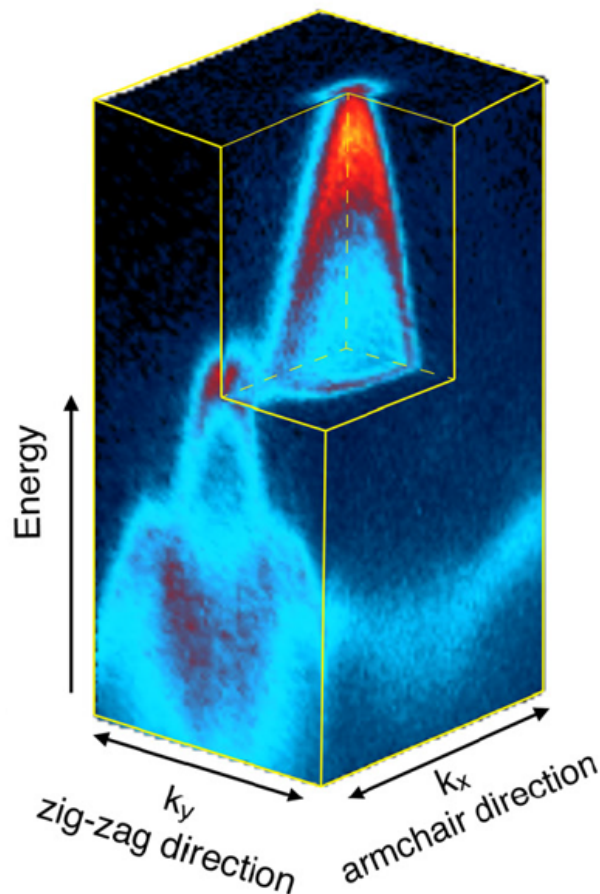


Figure 4.2: Electronic band structure of BP in energy vs momentum cuts at 40.8 eV of photon energy.

Fig. 4.3 shows the measured and calculated parabolic band dispersion along the two symmetry directions: zig-zag direction in panels (a) and (b), and armchair in panels (c) and (d). The experimental data correspond to the ΓY and ΓX directions of the Brillouin

zone, respectively. The parabolic dispersion along the two directions has different shape and different effective masses; *ab initio* DFT calculations (panels (b) and (d)) are in good agreement with experimental data. The DFT calculations were integrated over the k_z wave vector to take into account the intrinsic momentum broadening of ARPES along the surface normal.

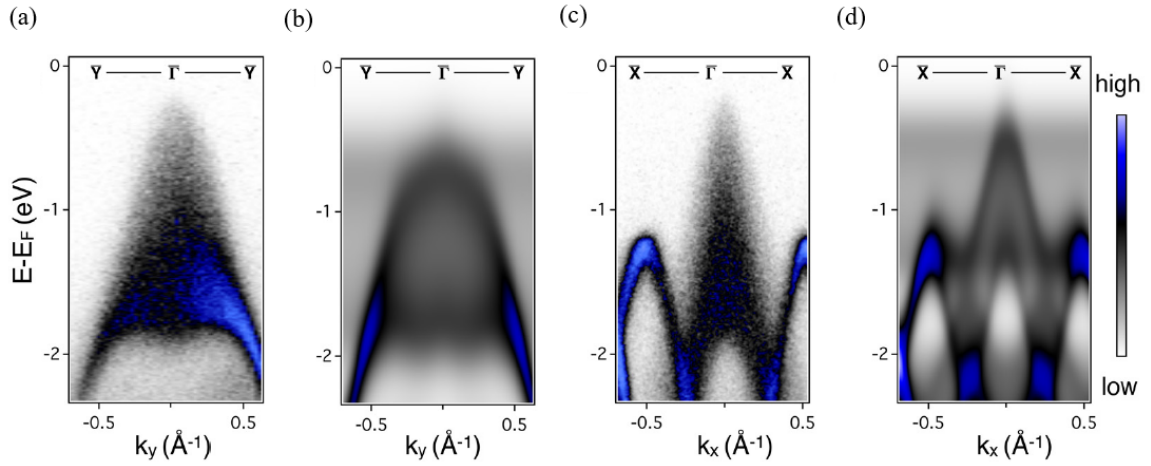


Figure 4.3: Measured and calculated VB dispersion along the zig-zag, panels (a) and (b), and armchair, panels (c) and (d), direction, respectively.

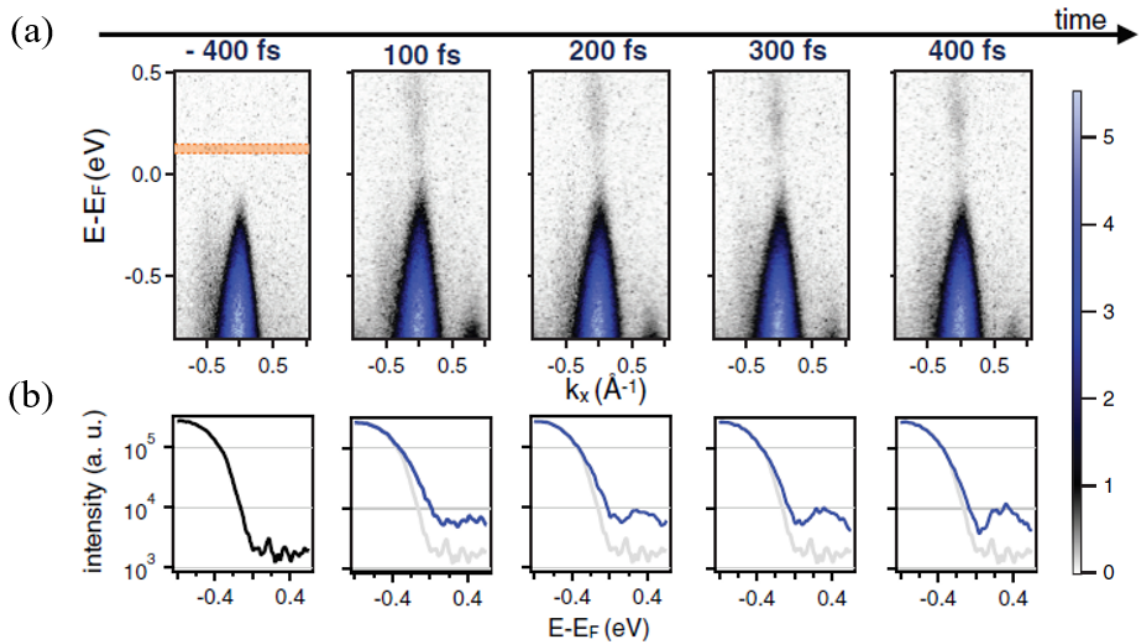


Figure 4.4: Out-of-equilibrium dynamics of BP. (a) snapshots at different delay times. (b) EDCs extracted at Γ point from each delay time.

For the out-of-equilibrium dynamic, only in the armchair direction (ΓX) has been taken into account; along which, in addition to the intense and prominent central band, one also can observe two well defined sharp sidebands with maximum located at 1.35 eV of binding energy and $k \simeq \pm 0.5 \text{\AA}^{-1}$.

In Fig. 4.4 the out-of equilibrium dynamics of BP is showed. In panel (a) series one can appreciate the temporal snapshots of the ARPES signal before (-400 fs) and after (from 100 fs up to 400 fs) optical excitation with an absorbed fluence of about 0.15 mJ cm^{-2} ; in order to minimize the Laser Assisted Photoelectric Effect (LAPE)³ contributions to the spectra, the data have been acquired using s-polarized optical excitation. The first snapshot, of the panel (a) series, show that at -400 fs (before pulse) the VB is fully occupied; following the arrival of the pulse, the electrons are removed from VB and populate the bottom of the CB. This dynamic can be better understood by following the evolution of the EDCs extracted for each delay time and reported in the panel series (b); indeed, in order to appreciate the temporal evolution, for each snapshot the EDC extracted at the related delay time has been reported and, superimposed, the EDC extracted at -400 fs, i.e. before the signal arrives. Starting from 100 fs (second panel) we observe a sudden increase of intensity above the VBM across the Fermi level as well as an upward shift of the VB.

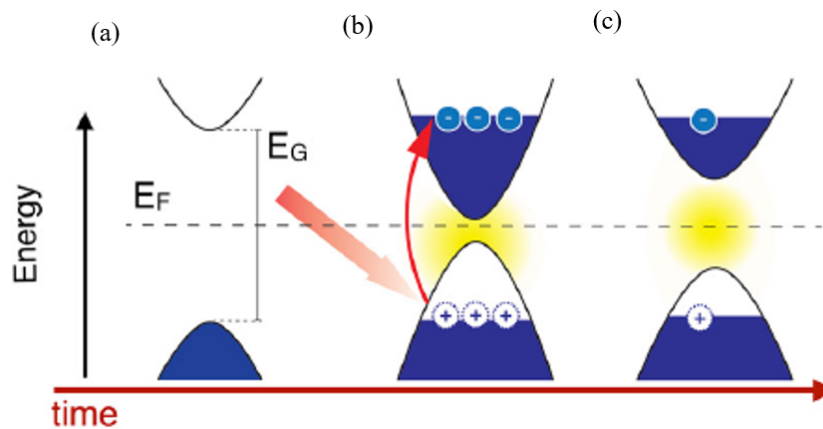


Figure 4.5: Representation of the band-gap renormalization mechanism.

The response of BP to external optical excitation is not just a variation of the occupancy of the VB and CB states; indeed, we observe a sudden change in the energy position of the top of VB after the pump pulse. This complex behaviour has been attributed to an ultrafast band-gap renormalization (BGR), as schematically illustrated in Fig. 4.5. Before optical excitation E_F lies within the band-gap and the VB is fully occupied, panel (a). Upon optical excitation electrons are photoexcited in the CB and high-energy holes are left in the VB. These high-mobility charges are responsible for the band-gap reduction, as we can see in panel (b). The system relaxes and equilibrium band-gap energy is recovered on a longer timescale, panel (c). From literature, it is known that the BP energy gap can be modified by external parameters, such as a static electric field [37–41], pressure [42–44], strain [17, 26, 45, 46] and also the surface Stark effect upon alkali deposition [19, 20, 47–51]. But, our findings demonstrate that optical excitation with laser light may offer another promising way to tune the band-gap, making BP potentially applicable to ultrafast optical devices.

³Laser Assisted Photoelectric Effect is driven by the interaction of the photoemitted electron with the electric field of the IR pulse during. LAPE leads to generation of higher-energies replicas of the photoemission spectral features. The replica, with lower intensity, is spaced by the energy of the pump photon.

Thanks to the support of theoretical calculations, it is possible to state that the BGR mechanism is the product of an upward shift of the VB and a downward one of the CB; the two shifts are driven by combined mechanisms: (i) alteration of the screening effect of electron-electron Coulomb interaction and (ii) reduction of the final state available for scattering processes (Pauli blocking) [52, 53].

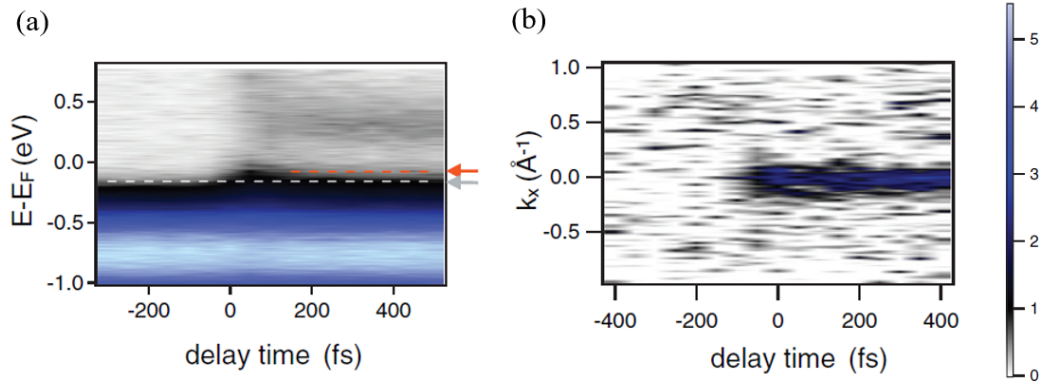


Figure 4.6: Temporal evolution of the ARPES intensity (a) over a wave vector region of $\pm 0.1 \text{ \AA}^{-1}$ around the Γ point and (b) over an energy window between 100 meV and 150 meV above the Fermi level.

Fig. 4.6 shows the temporal evolution of ARPES intensity and integrated (a) over a wave vector region of $\pm 0.1 \text{ \AA}^{-1}$ around at Γ point and (b) over an energy window between 100 meV and 150 meV above the Fermi level. The temporal evolution of the energy-dependent ARPES intensity, panel (a), well illustrate the BGR dynamic; it is worth noted that a precise experimental determination of the VBM is not possible due to the k_z broadening. However, an estimation of the time-dependent shift of the VBM by following a standard procedure in semiconductor physics [54] is possible: for each delay time we extrapolate the spectral leading edge with respect to the baseline and extract the intersection as a proxy for the VBM, as reported in Fig. 4.7 (a). The white dashed line (highlighted by light grey arrow) superimposed on panel (a), stands for the position of the VBM evaluated at -300 fs. During the optical excitation, at time of about 50 fs, we observe a a shift of the VB of about 60 meV towards lower binding energy, along with a broad distribution of excited electrons within the gap region. The orange dashed line indicates the VBM position at 400 fs. In panel (b) we report the temporal evolution of the ARPES intensity integrated in an energy range between 100 meV and 150 meV above Fermi level; such energy range is highlighted in orange in the first snapshot of Fig. 4.4 panel (a). It helps to observe that electrons accumulate at the bottom of CB upon optical pulse.

Below, we focused on the comparison between experimental and theoretical results on ultrafast BGR. Panel (a) of Fig. 4.7 show the EDCs at Γ point extracted from the data reported in panel (b) of Fig. 4.4; the three experimental curves refer to different delay time, -300 fs (blue markers), 100 fs (light blue markers) and 400 fs (red markers). Superimposed light blue and red curves stand for the linear interpolation of the VB intensity at -300 fs and 400 fs, respectively. The solid green line is the exponential fit of the tail of the 400 fs EDC (red

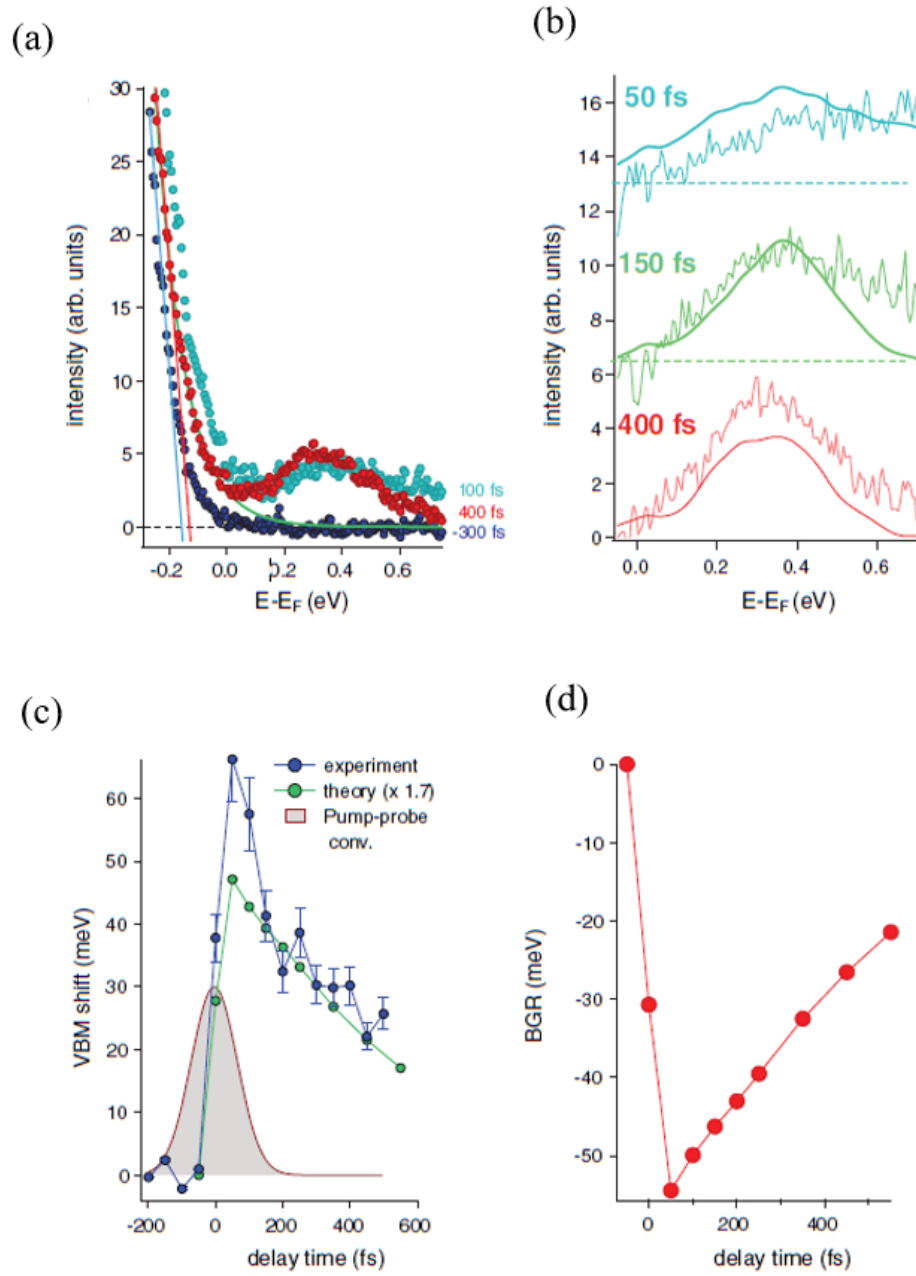


Figure 4.7: Ultrafast BGR results: (a) comparison between experiment and theory of the EDCs extracted at Γ point for different delay times; (b) experimental (thin lines) and theoretical (thick lines) EDCs after subtracting the high energy tail of the VB, for different delay times; (c) comparison between experimental (blues) and theoretical (green) temporal evolution of the VB shift; (d) calculated dynamics of the BGR.

markers). The position of the VBM has been estimated as the intercept at the baseline of the linearly extrapolated spectral edge. It is clear that after the arrival of the pump there is a large increase in the spectral intensity into the band-gap region, as one can observe starting for 100 fs delay time.

Panel (b) of Fig. 4.7 compares the experimental EDC extracted at Γ point (thin lines) with theoretical simulations (thick lines) for three delay times: 50 fs (light blue), 150 fs (green) and 400 fs (red). Experimental curves are plotted after the subtraction of an exponential function that fit the tail of VB spectrum, as the green curve reported in panel (a) for 400 fs delay time. The 50 fs spectrum presents a wide and undefined structure distribution, which is a signature of the excitation of electrons at high energy in the CB. The theoretical simulation show that bottom CB receive most of the excited carriers. On a longer time scale, electron-electron scattering mediates the relaxation of charges towards the CBM. For 150 fs and 400 fs delay time we found a good agreement between experiment and theory, which indicates that the measured ARPES peak reflects the CB density of states. The population evolves at larger delay times due to electron-hole with the VB recombination.

A precise estimation of the CBM is not possible due to the broadening of experimental energy and momentum and also to the unknown intrinsic line shape of the CB; the aforementioned extrapolation from the intersection with the baseline underestimates the correct value of the CBM. The central point of the rising slope of the curve constitutes an upper limit of the CBM. Following this result, it was possible to evaluate the value of the band-gap, which is of about 0.29 eV at 400 fs delay time, in comparison with the experimental and theoretical values at the equilibrium, 0.33 eV and 0.45 eV respectively [2, 15, 16, 50].

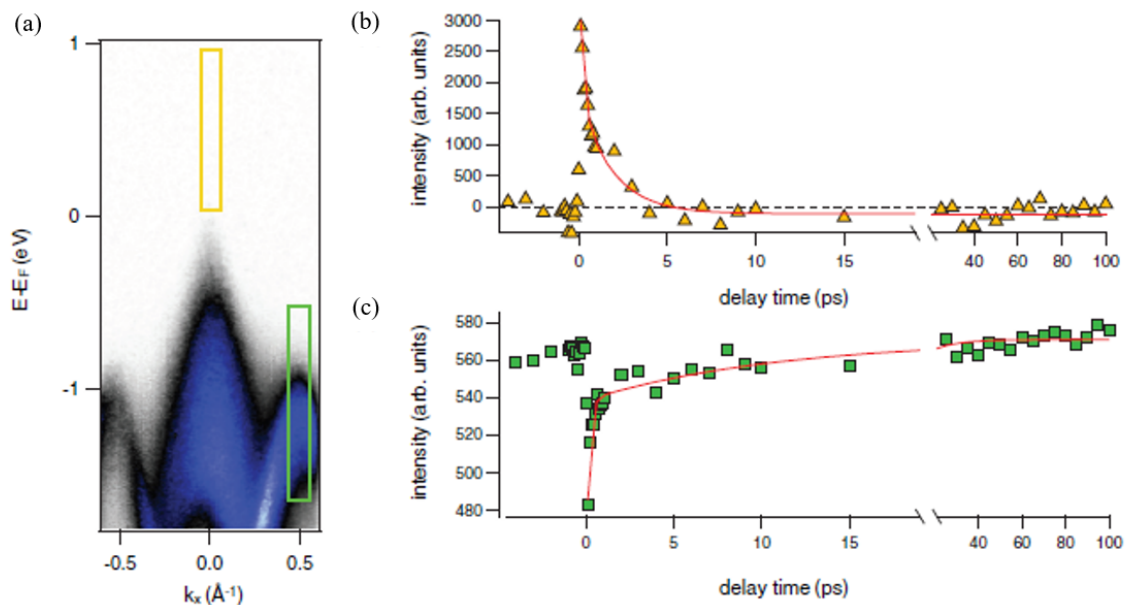


Figure 4.8: Charge carriers dynamics extracted from (a) ARPES image of BP along armchair direction and integrated for (b) CB minimum and (c) VB maximum.

Panel (c) of Fig. 4.7 presents the comparison between theoretical and experimental temporal evolution of the shift of VBM. The experimental dynamics (blue lines) is only partially

reproduced by theoretical calculations (green lines); in fact for absorbed fluence of 0.18 mJ cm^{-2} the calculated BGR is 20 meV, which is 1.7 times lower than the experimental result (green curve $\times 1.7$ to facilitate comparison). This difference indicates that BGR is probably driven by other mechanism, which need to take into account. One possibility is that the intense electric field induced by laser pump could be responsible of the Stark effect; one additional term is the asymmetry in distribution of the charge carriers inside the BP unit cell. The latter has been observed experimentally by ARPES after alkali metal deposition [19, 49, 51, 55]: extra electrons populate the CB in the top-most layer and this allow to the formation of a transient dipole responsible of the BGR [48]. We suppose that a similar effect can be caused by the photodoping induced by optical excitation. The gray filled curve indicates the cross-correlation between pump and probe pulses.

In panel (d) of Fig. 4.7 the calculated temporal dynamics of the BGR is reported; the BRG reaches a maximum of about 55 meV (± 10 meV). Our calculations (not reported) do not exclude a value up to 400 meV, which could lead to a band inversion via optical excitation.

Following, we focused our attention on the hot carriers dynamics; since optical absorption allows electrons in CB and leaves holes in the VB, the study of the two dynamics is of interest. In order to unveil these effects, panel (b) and (c) of Fig. 4.8 show the temporal evolution of the integrated ARPES intensity into two energy region: at the CBM (yellow rectangle) and top of the sideband VB (green rectangle) extracted from the ARPES image (along the armchair symmetry direction) in panel (a). The carrier dynamics of both curves are well reproduced by decaying exponential function with the same fast component $\tau = 0.2 \text{ ps}$ ($\pm 0.1 \text{ ps}$). From these spectra it is possible to determine the relaxation times for holes generated near the VB maximum, $\tau_{VB} = 10.2 \text{ ps}$ ($\pm 1 \text{ ps}$), and for electrons accumulated at the CB minimum, $\tau_{CB} = 1.95 \text{ ps}$ ($\pm 0.2 \text{ ps}$). The difference in the dynamics implies that electron-hole recombination is not the only relaxation methods but other effects need to take into account, such as diffusion from surface, carrier multiplication dynamics, carrier-phonon scattering, interband scattering etc. [56–61]. Our results allow to a clear estimation of the lifetime of the excited electrons and holes population.

The results here shown are reported in the manuscript: "*Photocarrier-induced band-gap renormalization and ultrafast charge dynamics in black phosphorus*", S. Roth, A. Crepaldi, M. Puppini, G. Gatti, D. Bugini, **I. Grimaldi**, T. R. Barrilot, C. A. Arrell, F. Frassetto, L. Poletto, M. Chergui, A. Marini and M. Grioni, 2D Mater. 6 (2019) 031001. The manuscript is available [here](#).

4.3 Electronic structure of SnSe, SnS and analogue materials

Tin selenide (SnSe) layered semiconductor has a relevant interest for thermoelectric applications due to its high Seebeck coefficient⁴, as a consequence of the record maximum

⁴The Seebeck coefficient, or thermoelectric power, is an indication of how much a material can manifest the Seebeck effect (a temperature difference generates electricity). It gives a measures of the magnitude of an induced thermoelectric voltage in response to a difference of temperature across that material, as induced by the Seebeck

value of the dimensionless figure of merit (ZT)⁵ (2.6 along a specific crystalline orientation (b-axis) at 923 K), as reported by L. D. Zhao et al. in Refs. [62, 63].

The electronic structure and related properties of SnSe have been extensively studied [9] but so far, there is no ARPES studies addressing on Tin-based binary chalcogenide compounds; in particular on SnS (isostructural to SnSe and BP), whose thermoelectric performances are significant [10, 11].

Starting from the well known SnSe, we report some preliminary ARPES measurements of the comparative study with SnS and the parental compounds $Pb_{1-x}Sn_xS$ ($x=0.5, 0.75$).

Data analysis and *ab initio* calculations are ongoing and further measurements are also in progress. The combined theory and experiments will shade light on the origin of the large figure of merit of SnSe, by comparison with SnS.

4.3.1 Experimental details

The experiments were carried out at the Band Dispersion and Electron-Phonon coupling (BaDElPh) beamline of the Elettra Synchrotron of Trieste. BaDElPh beamline provides photons in the low energy range, from 4.6 eV up to 40 eV with high flux, high resolving power, and horizontal-vertical linear polarization⁶. The availability of low photon energies makes BaDElPh unique among the other ARPES beamlines at Elettra and allow us to perform high-resolution experiments. For further details on beamline performance, see Refs. [64, 65].

We have successfully cleaved and measured SnSe, SnS and substitutional alloys with 25% and 50% of Pb instead of Sn in different experimental conditions such as a function of the temperature, of the photon energy and along different high symmetry directions. The layered samples have been cleaved in UHV environment. The clean and ordered substrate has been monitored by LEED measurements, which also allowed us to orient the sample along the main symmetry directions. Suitable energies for the ARPES investigation have been chosen after an accurate photon energy scan (not reported) in order to enhance the photoemission intensity from the electronic band dispersion (matrix-element effect). ARPES measurements were performed at low temperature (about 100 K).

On pristine samples, Fermi level was determined with a reference from the Cu plate on the sample holder; in the second part of the experiments, we evaporated alkali-metals on SnSe and SnS to estimate the value of the electronic gap and study the band gap evolution along one selected symmetry direction, and, further, the renormalization (as in the case of the BP) as a function of alkali content.

4.3.2 Results and discussion

The layered orthorhombic SnSe belongs to group IV-VI binary compounds. It is isoelectronic and shares the same structure of BP, given by two double layers (P_{nma} space group).

effect.

⁵The dimensionless figure of merit, $ZT = S^2\rho^{-1}K^{-1}T$, is calculated from the Seebeck coefficient (S), electrical resistivity (ρ), and thermal conductivity (K).

⁶Photon with energy lower than 15 eV has enhanced bulk sensitivity, very useful in tuning matrix elements which vary rapidly at low energy.

Its perspective view is different along the axial directions, as in the case of BP: along b-axis it has zig-zag structure while armchair along the c-axis. This peculiar structure leads to its anisotropic nature.

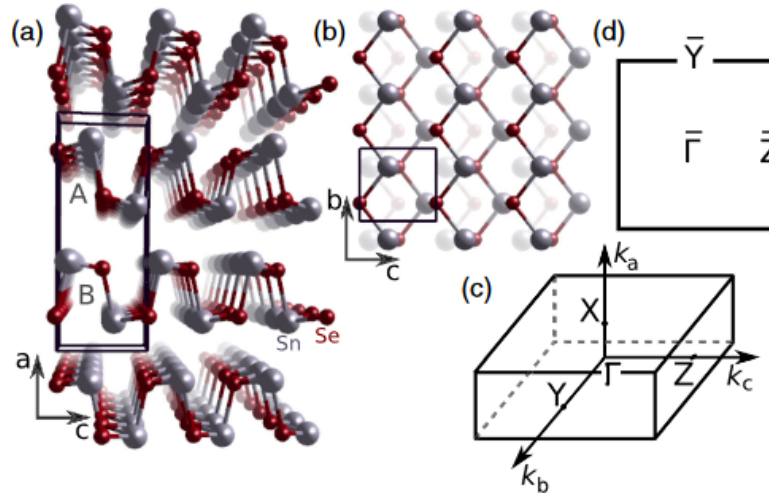


Figure 4.9: Crystal structure of SnSe (a) along and (b) perpendicular to the layers. (c) Bulk and (d) surface Brillouin zone. Figure extracted from ref. [9].

In Fig. 4.9 we report the crystal structure of SnSe along (a) and perpendicular (b) to the layers, from Ref. [9]. The red and gray balls correspond to Se (or S) and Sn atoms, respectively. The crystal structure of the $\text{Pb}_{1-x}\text{Sn}_x\text{S}$ ($x=0.25, 0.5, 1$) compounds is similar as the one here depicted for SnSe, where Pb to Sn substitution occurs.

One of the most important feature that the compounds IV-VI share is the narrow bandgap; it is well known that optoelectronic properties strongly depend on it. The alkali evaporation on SnSe and SnS, allow us to estimate a bandgap value of about 1.3 eV.

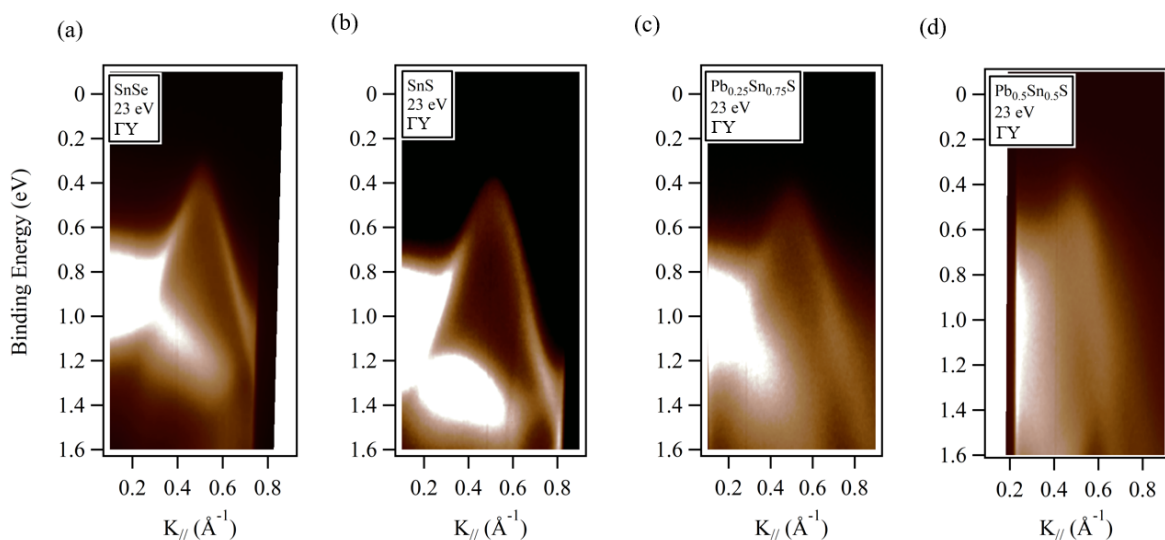


Figure 4.10: ARPES measurements of (a) SnSe, (b) SnS, (c) $\text{Pb}_{0.25}\text{Sn}_{0.75}\text{S}$ and (d) $\text{Pb}_{0.5}\text{Sn}_{0.5}\text{S}$ along ΓY direction of the Brillouin zone and performed at 23 eV of photon energy.

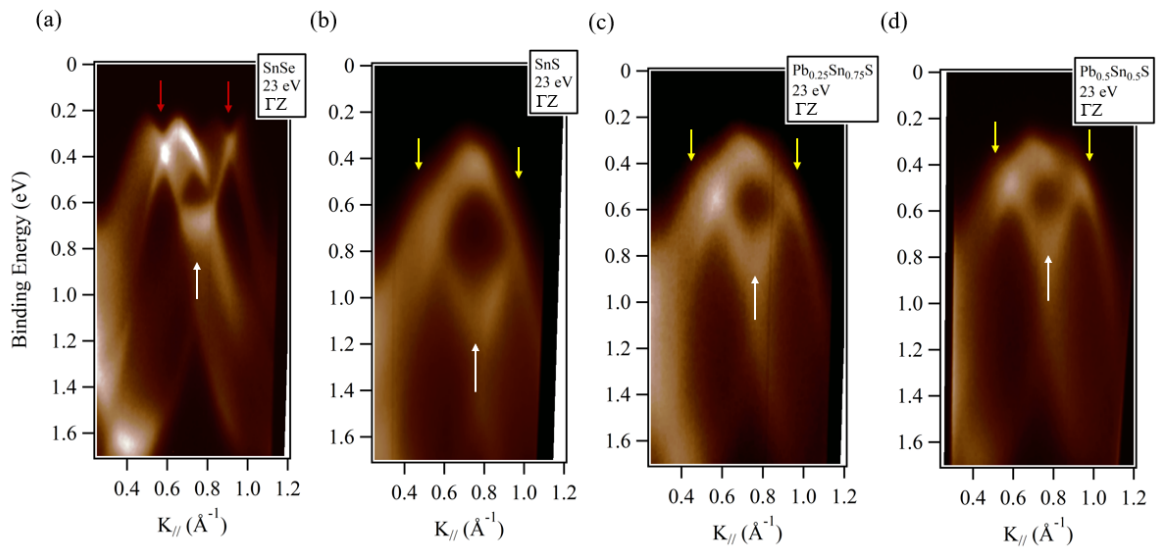


Figure 4.11: ARPES measurements of (a) SnSe, (b) SnS, (c) $\text{Pb}_{0.25}\text{Sn}_{0.75}\text{S}$ and (d) $\text{Pb}_{0.5}\text{Sn}_{0.5}\text{S}$ along ΓZ direction of the Brillouin zone and performed at 23 eV of photon energy.

Our electronic band structure studies on SnS and $\text{Pb}_{1-x}\text{Sn}_x\text{S}$ ($x=0.25, 0.5$) parental compounds, reveal a band dispersion very similar to SnSe [9].

From the dispersion along the ΓY and ΓZ high-symmetry directions, we could observe several hole like bands. In Fig. 4.10 we report the experimental results of our samples along the ΓY high-symmetry direction of the Brillouin zone, measured with 23 eV of photon energy, at 100 K and with linear horizontal polarization. Along ΓY direction all the samples exhibit a similar single parabolic-like dispersion with a hole pocket centered at about 0.5 \AA^{-1} ; the top of the VB, along ΓY direction, has been estimated to be at about 0.5 \AA^{-1} .

Along the ΓZ direction of the Brillouin zone, the samples display several downward dispersing bands. For each compound, the central crossing point (highlighted by white arrows) is located between $0.75 - 0.8 \text{ \AA}^{-1}$, as one can observe from panels (a)-(d) of Fig. 4.12. Concerning SnSe, at lower binding it presents at least four downwards dispersing bands, intersect two by two at 0.58 and 0.91 \AA^{-1} (red arrows), respectively: this is the so called *pudding-mold-like* shape. Along this direction, the compound does not have a single top of the VB but the four bands have the maximum at the same binding energy. The band structure of the SnS and $\text{Pb}_{1-x}\text{Sn}_x\text{S}$ ($x=0.25, 0.5$) samples is very different with respect to SnSe; according the preliminary theoretical calculations (not reported) the multiple upper bands appear to be degenerate with a single VB maximum located at about 0.77 \AA^{-1} and two lower "shoulders" on the sides, highlighted by yellow arrows.

We known that effective mass and group velocity are the factors that affect the charge carrier mobility and consequently the value of ZT; in this context we started analysis of effective mass along ΓY direction for SnSe and SnS, by fitting with an asymmetric parabola the maximum of intensity extracted from the EDCs. Some preliminary results are reported in Figs. 4.12 and 4.13; fit results are superimposed on EDCs and on the ARPES spectra. Red markers stand for the maximum intensity extracted from each EDC, the white curve is the

fit result. We estimated an effective mass for SnSe and SnS of $m^*=0.210 m_e$ and $m^*=0.170 m_e$, respectively; the value for SnSe is in good agreements with previous works [66]. Further measurements as well as *ab initio* calculations are also in progress.

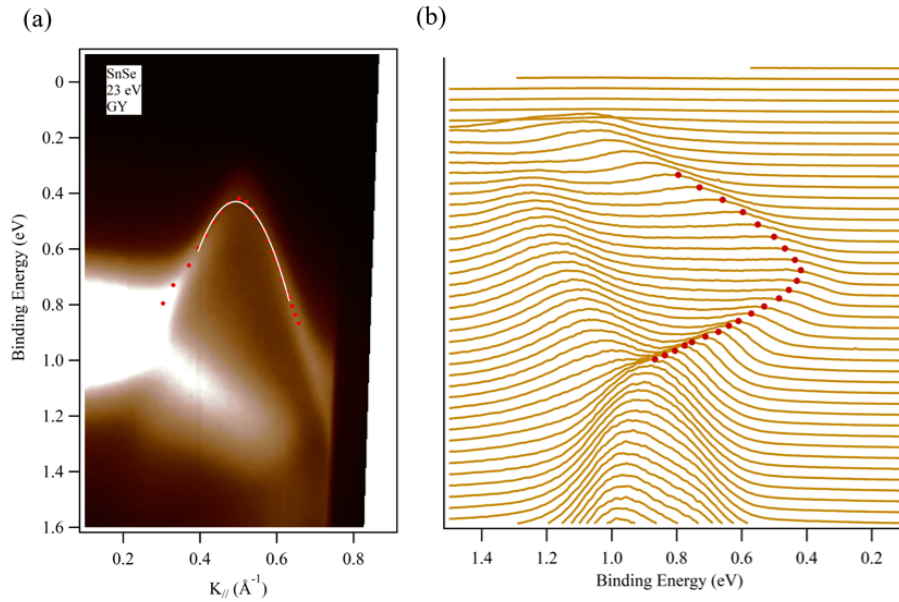


Figure 4.12: Estimation of the effective mass of valence bands in SnSe along ΓY direction.

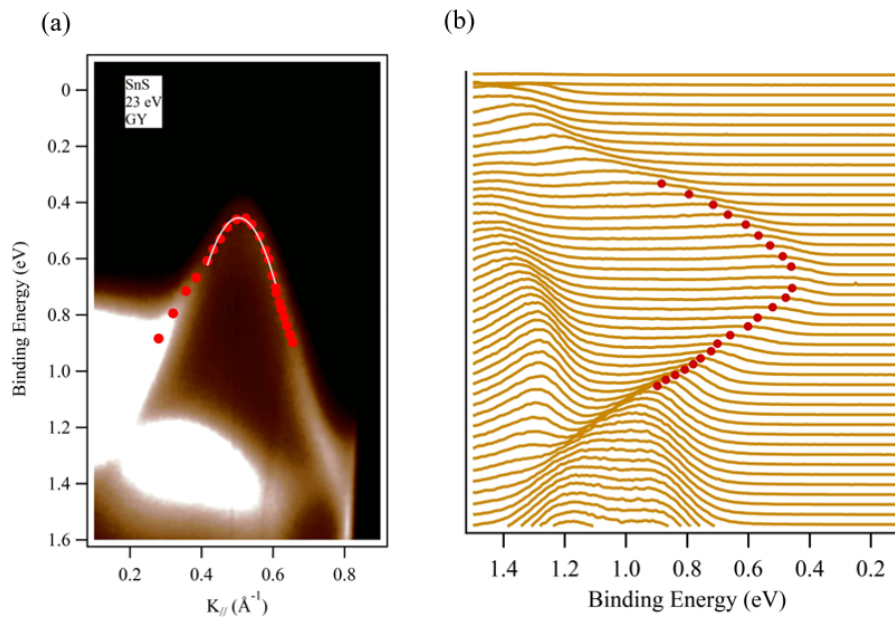


Figure 4.13: Estimation of the effective mass of valence bands in SnS along ΓY direction.

References

- [1] A. Castellanos-Gomez, L. Vicarelli, E. Prada, J. O. Island, K. L. Narasimha-Acharya, S. I. Blanter, D. J. Groenendijk, M. Buscema, G. A. Steele, J. V. Alvarez, H. W. Zandbergen, J. J. Palacios, and H. S. J. van der Zant. “Isolation and characterization of few-layer black phosphorus”. In: *2D Materials* 1.2 (June 2014), p. 025001. DOI: 10.1088/2053-1583/1/2/025001.
- [2] L. Li, Y. Yu, G. Jun Ye, Q. Ge, X. Ou, H. Wu, D. Feng, X. H. Chen, and Y. Zhang. “Black phosphorus field-effect transistors”. In: *Nature Nanotechnology* 9.5 (Mar. 2014), pp. 372–377. DOI: 10.1038/nnano.2014.35.
- [3] H. Liu, A.T. Neal, Z. Zhu, Z. Luo, X. Xu, D. Tománek, and P.D. Ye. “Phosphorene: An Unexplored 2D Semiconductor with a High Hole Mobility”. In: *ACS Nano* 8.4 (Mar. 2014), pp. 4033–4041. DOI: 10.1021/nn501226z.
- [4] F. Xia, H. Wang, and Y. Jia. “Rediscovering black phosphorus as an anisotropic layered material for optoelectronics and electronics”. In: *Nature Communications* 5.1 (July 2014). DOI: 10.1038/ncomms5458.
- [5] A. K. Geim and K. S. Novoselov. “The rise of graphene”. In: *Nature Materials* 6.3 (Mar. 2007), pp. 183–191. DOI: 10.1038/nmat1849.
- [6] F. Bonaccorso, Z. Sun, T. Hasan, and A. C. Ferrari. “Graphene photonics and optoelectronics”. In: *Nature Photonics* 4.9 (Aug. 2010), pp. 611–622. DOI: 10.1038/nphoton.2010.186.
- [7] K. F. Mak, K. He, J. Shan, and T. F. Heinz. “Control of valley polarization in monolayer MoS₂ by optical helicity”. In: *Nature Nanotechnology* 7.8 (June 2012), pp. 494–498. DOI: 10.1038/nnano.2012.96.
- [8] Y. Huang, J. Qiao, K. He, S. Bliznakov, E. Sutter, X. Chen, D. Luo, F. Meng, D. Su, J. Decker, W. Ji, R. S. Ruoff, and P. Sutter. “Interaction of Black Phosphorus with Oxygen and Water”. In: *Chemistry of Materials* 28.22 (Nov. 2016), pp. 8330–8339. DOI: 10.1021/acs.chemmater.6b03592.
- [9] I. Pletikosić, F. von Rohr, P. Pervan, P. K. Das, I. Vobornik, R. J. Cava, and T. Valla. “Band Structure of the IV-VI Black Phosphorus Analog and Thermoelectric SnSe”. In: *Physical Review Letters* 120.15 (Apr. 2018). DOI: 10.1103/physrevlett.120.156403.
- [10] B. Zhou, S. Li, W. Li, J. Li, X. Zhang, S. Lin, Z. Chen, and Y. Pei. “Thermoelectric Properties of SnS with Na-Doping”. In: *ACS Applied Materials & Interfaces* 9.39 (Sept. 2017), pp. 34033–34041. DOI: 10.1021/acsmi.7b08770.
- [11] R. Guo, X. Wang, Y. Kuang, and B. Huang. “First-principles study of anisotropic thermoelectric transport properties of IV-VI semiconductor compounds SnSe and SnS”. In: *Physical Review B* 92.11 (Sept. 2015). DOI: 10.1103/physrevb.92.115202.
- [12] X. Ling, H. Wang, S. Huang, F. Xia, and M. S. Dresselhaus. “The renaissance of black phosphorus”. In: *Proceedings of the National Academy of Sciences* 112.15 (Mar. 2015), pp. 4523–4530. DOI: 10.1073/pnas.1416581112.

- [13] A. Brown and S. Rundqvist. “Refinement of the crystal structure of black phosphorus”. In: *Acta Crystallographica* 19.4 (Oct. 1965), pp. 684–685. DOI: 10.1107/s0365110x65004140.
- [14] J. He, D. He, Y. Wang, Q. Cui, M. Z. Bellus, H.-Y. Chiu, and H. Zhao. “Exceptional and Anisotropic Transport Properties of Photocarriers in Black Phosphorus”. In: *ACS Nano* 9.6 (May 2015), pp. 6436–6442. DOI: 10.1021/acsnano.5b02104.
- [15] V. Tran, R. Soklaski, Y. Liang, and L. Yang. “Layer-controlled band gap and anisotropic excitons in few-layer black phosphorus”. In: *Physical Review B* 89.23 (June 2014). DOI: 10.1103/physrevb.89.235319.
- [16] A. N. Rudenko, S. Yuan, and M. I. Katsnelson. “Toward a realistic description of multilayer black phosphorus: From GW approximation to large-scale tight-binding simulations”. In: *Physical Review B* 92.8 (Aug. 2015). DOI: 10.1103/physrevb.92.085419.
- [17] L. Liang, J. Wang, W. Lin, B. G. Sumpter, V. Meunier, and M. Pan. “Electronic Bandgap and Edge Reconstruction in Phosphorene Materials”. In: *Nano Letters* 14.11 (Oct. 2014), pp. 6400–6406. DOI: 10.1021/nl502892t.
- [18] R. W. Keyes. “The Electrical Properties of Black Phosphorus”. In: *Physical Review* 92.3 (Nov. 1953), pp. 580–584. DOI: 10.1103/physrev.92.580.
- [19] J. Kim, S. S. Baik, S. H. Ryu, Y. Sohn, S. Park, B.-G. Park, J. Denlinger, Y. Yi, H. J. Choi, and K. S. Kim. “Observation of tunable band gap and anisotropic Dirac semimetal state in black phosphorus”. In: *Science* 349.6249 (Aug. 2015), pp. 723–726. DOI: 10.1126/science.aaa6486.
- [20] A. Sanna, A. V. Fedorov, N. I. Verbitskiy, J. Fink, C. Krellner, L. Petaccia, A. Chikina, D. Yu Usachov, A. Grüneis, and G. Profeta. “First-principles and angle-resolved photoemission study of lithium doped metallic black phosphorus”. In: *2D Materials* 3.2 (June 2016), p. 025031. DOI: 10.1088/2053-1583/3/2/025031.
- [21] J. Qiao, X. Kong, Z.-X. Hu, F. Yang, and W. Ji. “High-mobility transport anisotropy and linear dichroism in few-layer black phosphorus”. In: *Nature Communications* 5.1 (July 2014). DOI: 10.1038/ncomms5475.
- [22] T. Low, A. S. Rodin, A. Carvalho, Y. Jiang, H. Wang, F. Xia, and A. H. Castro Neto. “Tunable optical properties of multilayer black phosphorus thin films”. In: *Physical Review B* 90.7 (Aug. 2014). DOI: 10.1103/physrevb.90.075434.
- [23] L. Li, J. Kim, C. Jin, G. Jun Ye, D. Y. Qiu, F. H. da Jornada, Z. Shi, L. Chen, Z. Zhang, F. Yang, K. Watanabe, T. Taniguchi, W. Ren, S. G. Louie, X. H. Chen, Y. Zhang, and F. Wang. “Direct observation of the layer-dependent electronic structure in phosphorene”. In: *Nature Nanotechnology* 12.1 (Sept. 2016), pp. 21–25. DOI: 10.1038/nnano.2016.171.
- [24] M. Engel, M. Steiner, and P. Avouris. “Black Phosphorus Photodetector for Multispectral, High-Resolution Imaging”. In: *Nano Letters* 14.11 (Oct. 2014), pp. 6414–6417. DOI: 10.1021/nl502928y.

- [25] J. Dai and X. C. Zeng. “Bilayer Phosphorene: Effect of Stacking Order on Bandgap and Its Potential Applications in Thin-Film Solar Cells”. In: *The Journal of Physical Chemistry Letters* 5.7 (Mar. 2014), pp. 1289–1293. DOI: 10.1021/jz500409m.
- [26] R. Fei and L. Yang. “Strain-Engineering the Anisotropic Electrical Conductance of Few-Layer Black Phosphorus”. In: *Nano Letters* 14.5 (May 2014), pp. 2884–2889. DOI: 10.1021/nl500935z.
- [27] Q. Zeng, H. Wang, W. Fu, Y. Gong, W. Zhou, P. M. Ajayan, J. Lou, and Z. Liu. “Band Engineering for Novel Two-Dimensional Atomic Layers”. In: *Small* 11.16 (Dec. 2014), pp. 1868–1884. DOI: 10.1002/smll.201402380.
- [28] M. Batmunkh, M. Bat-Erdene, and J. G. Shapter. “Phosphorene and Phosphorene-Based Materials - Prospects for Future Applications”. In: *Advanced Materials* 28.39 (July 2016), pp. 8586–8617. DOI: 10.1002/adma.201602254.
- [29] G. Fiori, F. Bonaccorso, G. Iannaccone, T. Palacios, D. Neumaier, A. Seabaugh, S. K. Banerjee, and L. Colombo. “Electronics based on two-dimensional materials”. In: *Nature Nanotechnology* 9.10 (Oct. 2014), pp. 768–779. DOI: 10.1038/nnano.2014.207.
- [30] M. Buscema, D. J. Groenendijk, G. A. Steele, H. S. J. van der Zant, and A. Castellanos-Gomez. “Photovoltaic effect in few-layer black phosphorus PN junctions defined by local electrostatic gating”. In: *Nature Communications* 5.1 (Aug. 2014). DOI: 10.1038/ncomms5651.
- [31] J. Sotor, G. Sobon, W. Macherzynski, P. Paletko, and K. M. Abramski. “Black phosphorus saturable absorber for ultrashort pulse generation”. In: *Applied Physics Letters* 107.5 (Aug. 2015), p. 051108. DOI: 10.1063/1.4927673.
- [32] Y. Chen, G. Jiang, S. Chen, Z. Guo, X. Yu, C. Zhao, H. Zhang, Q. Bao, S. Wen, D. Tang, and D. Fan. “Mechanically exfoliated black phosphorus as a new saturable absorber for both Q-switching and Mode-locking laser operation”. In: *Optics Express* 23.10 (May 2015), p. 12823. DOI: 10.1364/oe.23.012823.
- [33] D. Li, H. Jussila, L. Karvonen, G. Ye, H. Lipsanen, X. Chen, and Z. Sun. “Polarization and Thickness Dependent Absorption Properties of Black Phosphorus: New Saturable Absorber for Ultrafast Pulse Generation”. In: *Scientific Reports* 5.1 (Oct. 2015). DOI: 10.1038/srep15899.
- [34] H. Yuan, X. Liu, F. Afshinmanesh, W. Li, G. Xu, J. Sun, B. Lian, A. G. Curto, G. Ye, Y. Hikita, Z. Shen, S.-C. Zhang, X. Chen, M. Brongersma, H. Y. Hwang, and Y. Cui. “Polarization-sensitive broadband photodetector using a black phosphorus vertical p-n junction”. In: *Nature Nanotechnology* 10.8 (June 2015), pp. 707–713. DOI: 10.1038/nnano.2015.112.
- [35] P. Giannozzi, S. Baroni, N. Bonini, M. Calandra, R. Car, C. Cavazzoni, D. Ceresoli, G. L. Chiarotti, M. Cococcioni, I. Dabo, A. Dal Corso, S. de Gironcoli, S. Fabris, G. Fratesi, R. Gebauer, U. Gerstmann, C. Gougoussis, A. Kokalj, M. Lazzeri, L. Martin-Samos, N. Marzari, F. Mauri, R. Mazzarello, S. Paolini, A. Pasquarello, L. Paulatto, C. Sbraccia, S.

- Scandolo, G. Sclauzero, A. P. Seitsonen, A. Smogunov, P. Umari, and R. M Wentzcovitch. “QUANTUM ESPRESSO: a modular and open-source software project for quantum simulations of materials”. In: *Journal of Physics: Condensed Matter* 21.39 (Sept. 2009), p. 395502. DOI: 10.1088/0953-8984/21/39/395502.
- [36] C. Attaccalite, M. Grüning, and A. Marini. “Real-time approach to the optical properties of solids and nanostructures: Time-dependent Bethe-Salpeter equation”. In: *Physical Review B* 84.24 (Dec. 2011). DOI: 10.1103/physrevb.84.245110.
- [37] Y. Li, S. Yang, and J. Li. “Modulation of the Electronic Properties of Ultrathin Black Phosphorus by Strain and Electrical Field”. In: *The Journal of Physical Chemistry C* 118.41 (Oct. 2014), pp. 23970–23976. DOI: 10.1021/jp506881v.
- [38] Q. Liu, X. Zhang, L. B. Abdalla, A. Fazzio, and A. Zunger. “Switching a Normal Insulator into a Topological Insulator via Electric Field with Application to Phosphorene”. In: *Nano Letters* 15.2 (Jan. 2015), pp. 1222–1228. DOI: 10.1021/nl5043769.
- [39] B. Ghosh, B. Singh, R. Prasad, and A. Agarwal. “Electric-field tunable Dirac semimetal state in phosphorene thin films”. In: *Physical Review B* 94.20 (Nov. 2016). DOI: 10.1103/physrevb.94.205426.
- [40] Y. Liu, Z. Qiu, A. Carvalho, Y. Bao, H. Xu, S. J. R. Tan, W. Liu, A. H. Castro Neto, K. P. Loh, and J. Lu. “Gate-Tunable Giant Stark Effect in Few-Layer Black Phosphorus”. In: *Nano Letters* 17.3 (Feb. 2017), pp. 1970–1977. DOI: 10.1021/acs.nanolett.6b05381.
- [41] B. Deng, V. Tran, Y. Xie, H. Jiang, C. Li, Q. Guo, X. Wang, H. Tian, S. J. Koester, H. Wang, J. J. Cha, Q. Xia, L. Yang, and F. Xia. “Efficient electrical control of thin-film black phosphorus bandgap”. In: *Nature Communications* 8.1 (Apr. 2017). DOI: 10.1038/ncomms14474.
- [42] Z. J. Xiang, G. J. Ye, C. Shang, B. Lei, N. Z. Wang, K. S. Yang, D. Y. Liu, F. B. Meng, X. G. Luo, L. J. Zou, Z. Sun, Y. Zhang, and X. H. Chen. “Pressure-Induced Electronic Transition in Black Phosphorus”. In: *Physical Review Letters* 115.18 (Oct. 2015). DOI: 10.1103/physrevlett.115.186403.
- [43] R. Fei, V. Tran, and L. Yang. “Topologically protected Dirac cones in compressed bulk black phosphorus”. In: *Physical Review B* 91.19 (May 2015). DOI: 10.1103/physrevb.91.195319.
- [44] P. Di Pietro, M. Mitrano, S. Caramazza, F. Capitani, S. Lupi, P. Postorino, F. Ripanti, B. Joseph, N. Ehlen, A. Grüneis, A. Sanna, G. Profeta, P. Dore, and A. Perucchi. “Emergent Dirac carriers across a pressure-induced Lifshitz transition in black phosphorus”. In: *Physical Review B* 98.16 (Oct. 2018). DOI: 10.1103/physrevb.98.165111.
- [45] A. S. Rodin, A. Carvalho, and A. H. Castro Neto. “Strain-Induced Gap Modification in Black Phosphorus”. In: *Physical Review Letters* 112.17 (May 2014). DOI: 10.1103/physrevlett.112.176801.

- [46] Z. Zhang, L. Li, J. Horng, N. Zhou Wang, F. Yang, Y. Yu, Y. Zhang, G. Chen, K. Watanabe, T. Taniguchi, X. H. Chen, F. Wang, and Y. Zhang. “Strain-Modulated Bandgap and Piezo-Resistive Effect in Black Phosphorus Field-Effect Transistors”. In: *Nano Letters* 17.10 (Sept. 2017), pp. 6097–6103. DOI: 10.1021/acs.nanolett.7b02624.
- [47] J. Kim, S. S. Baik, S. W. Jung, Y. Sohn, S. H. Ryu, H. J. Choi, B.-J. Yang, and K. S. Kim. “Two-Dimensional Dirac Fermions Protected by Space-Time Inversion Symmetry in Black Phosphorus”. In: *Physical Review Letters* 119.22 (Nov. 2017). DOI: 10.1103/physrevlett.119.226801.
- [48] S. S. Baik, K. S. Kim, Y. Yi, and H. J. Choi. “Emergence of Two-Dimensional Massless Dirac Fermions, Chiral Pseudospins, and Berry’s Phase in Potassium Doped Few-Layer Black Phosphorus”. In: *Nano Letters* 15.12 (Nov. 2015), pp. 7788–7793. DOI: 10.1021/acs.nanolett.5b04106.
- [49] N. Ehlen, B. V. Senkovskiy, A. V. Fedorov, A. Perucchi, P. Di Pietro, A. Sanna, G. Profeta, L. Petaccia, and A. Grüneis. “Evolution of electronic structure of few-layer phosphorene from angle-resolved photoemission spectroscopy of black phosphorous”. In: *Physical Review B* 94.24 (Dec. 2016). DOI: 10.1103/physrevb.94.245410.
- [50] J. Kim, M. Huh, S. W. Jung, S. H. Ryu, Y. Sohn, and K. S. Kim. “Electronic band structure of surface-doped black phosphorus”. In: *Journal of Electron Spectroscopy and Related Phenomena* 219 (Aug. 2017), pp. 86–91. DOI: 10.1016/j.elspec.2016.12.001.
- [51] N. Ehlen, A. Sanna, B. V. Senkovskiy, L. Petaccia, A. V. Fedorov, G. Profeta, and A. Grüneis. “Direct observation of a surface resonance state and surface band inversion control in black phosphorus”. In: *Physical Review B* 97.4 (Jan. 2018). DOI: 10.1103/physrevb.97.045143.
- [52] N. Peyghambarian, S. W. Koch, and A. Mysyrowicz. *Introduction to Semiconductor Optics*. Upper Saddle River, NJ, USA: Prentice-Hall, Inc., 1993. ISBN: 0-13-638990-2.
- [53] C. F. Klingshirn. *Semiconductor Optics*. Springer Berlin Heidelberg, 2012. DOI: 10.1007/978-3-642-28362-8.
- [54] A. D. Katnani and G. Margaritondo. “Microscopic study of semiconductor heterojunctions: Photoemission measurement of the valance-band discontinuity and of the potential barriers”. In: *Physical Review B* 28.4 (Aug. 1983), pp. 1944–1956. DOI: 10.1103/physrevb.28.1944.
- [55] M. Kang, B. Kim, S. H. Ryu, S. W. Jung, J. Kim, L. Moreschini, C. Jozwiak, E. Rotenberg, A. Bostwick, and K. S. Kim. “Universal Mechanism of Band-Gap Engineering in Transition-Metal Dichalcogenides”. In: *Nano Letters* 17.3 (Feb. 2017), pp. 1610–1615. DOI: 10.1021/acs.nanolett.6b04775.
- [56] Y. Wang, G. Huang, H. Mu, S. Lin, J. Chen, S. Xiao, Q. Bao, and J. He. “Ultrafast recovery time and broadband saturable absorption properties of black phosphorus suspension”. In: *Applied Physics Letters* 107.9 (Aug. 2015), p. 091905. DOI: 10.1063/1.4930077.

- [57] K. Wang, B. M. Szydłowska, G. Wang, X. Zhang, J. J. Wang, J. J. Magan, L. Zhang, J. N. Coleman, J. Wang, and W. J. Blau. “Ultrafast Nonlinear Excitation Dynamics of Black Phosphorus Nanosheets from Visible to Mid-Infrared”. In: *ACS Nano* 10.7 (June 2016), pp. 6923–6932. DOI: 10.1021/acsnano.6b02770.
- [58] V. Iyer, P. Ye, and X. Xu. “Mid-infrared ultrafast carrier dynamics in thin film black phosphorus”. In: *2D Materials* 4.2 (June 2017), p. 021032. DOI: 10.1088/2053-1583/aa74ab.
- [59] R. J. Suess, M. M. Jadidi, T. E. Murphy, and M. Mittendorff. “Carrier dynamics and transient photobleaching in thin layers of black phosphorus”. In: *Applied Physics Letters* 107.8 (Aug. 2015), p. 081103. DOI: 10.1063/1.4929403.
- [60] B. Liao, H. Zhao, E. Najafi, X. Yan, He Tian, J. Tice, A. J. Minnich, H. Wang, and A. H. Zewail. “Spatial-Temporal Imaging of Anisotropic Photocarrier Dynamics in Black Phosphorus”. In: *Nano Letters* 17.6 (May 2017), pp. 3675–3680. DOI: 10.1021/acs.nanolett.7b00897.
- [61] S. Ge, C. Li, Z. Zhang, C. Zhang, Y. Zhang, J. Qiu, Q. Wang, J. Liu, S. Jia, J. Feng, and D. Sun. “Dynamical Evolution of Anisotropic Response in Black Phosphorus under Ultrafast Photoexcitation”. In: *Nano Letters* 15.7 (June 2015), pp. 4650–4656. DOI: 10.1021/acs.nanolett.5b01409.
- [62] L.-D. Zhao, S.-H. Lo, Y. Zhang, H. Sun, G. Tan, C. Uher, C. Wolverton, V. P. Dravid, and M. G. Kanatzidis. “Ultralow thermal conductivity and high thermoelectric figure of merit in SnSe crystals”. In: *Nature* 508.7496 (Apr. 2014), pp. 373–377. DOI: 10.1038/nature13184.
- [63] L.-D. Zhao, G. Tan, S. Hao, J. He, Y. Pei, H. Chi, H. Wang, S. Gong, H. Xu, V. P. Dravid, C. Uher, G. J. Snyder, C. Wolverton, and M. G. Kanatzidis. “Ultrahigh power factor and thermoelectric performance in hole-doped single-crystal SnSe”. In: *Science* 351.6269 (Nov. 2015), pp. 141–144. DOI: 10.1126/science.aad3749.
- [64] L. Petaccia, P. Vilmercati, S. Gorovikov, M. Barnaba, A. Bianco, D. Cocco, C. Masciovecchio, and A. Goldoni. “BaD ElPh: A 4m normal-incidence monochromator beamline at Elettra”. In: *Nuclear Instruments and Methods in Physics Research Section A: Accelerators, Spectrometers, Detectors and Associated Equipment* 606.3 (July 2009), pp. 780–784. DOI: 10.1016/j.nima.2009.05.001.
- [65] *BaDElPh beamline. Web page.* <https://www.elettra.trieste.it/it/lightsources/elettra/elettra-beamlines/badelph/badelph.html>.
- [66] C. W. Wang, Y. Y. Y. Xia, Z. Tian, J. Jiang, B. H. Li, S. T. Cui, H. F. Yang, A. J. Liang, X. Y. Zhan, G. H. Hong, S. Liu, C. Chen, M. X. Wang, L. X. Yang, Z. Liu, Q. X. Mi, G. Li, J. M. Xue, Z. K. Liu, and Y. L. Chen. “Photoemission study of the electronic structure of valence band convergent SnSe”. In: *Physical Review B* 96.16 (Oct. 2017). DOI: 10.1103/physrevb.96.165118.

Basic principles of Angle-Resolved PhotoEmission Spectroscopy and Synchrotron Radiation

In the present thesis work, the electronic band structure of selected materials has been investigated through Angle-Resolved PhotoEmission Spectroscopy (ARPES).

ARPES is a powerful experimental technique to directly extract and visualise the momentum-resolved electron dispersion in the reciprocal space of solid material surface. The electronic band structure of materials reflects the electrical, magnetic and optical properties of the investigated sample.

In the last years, the advances in instrumentation and the emergency of Synchrotron Light sources have significantly improved the accuracy and efficiency of ARPES experiments; these advantages have allowed a deeper knowledge of the physical properties and behaviour of new materials.

This chapter has been focused on a brief introduction on the basic principles of Angle-Resolved PhotoEmission Spectroscopy and Synchrotron Light sources, since the data reported in this thesis were mostly acquired by means of ARPES technique and on Synchrotron facilities. In order to study the evolution in time of the electronic properties a time resolved approach is needed. In this chapter I introduced also Time-Resolved ARPES (TR-ARPES) technique with some basic details to interpret the experiments reported in chapter 4 of this thesis.

A.1 Introduction to PhotoEmission Spectroscopy

Several spectroscopy techniques are based on the interaction of the electromagnetic radiation (probe) with matter (target): spectroscopy includes a variety of complementary techniques that gives informations about physical and chemical properties of matter, providing a wide description of the system under investigation. PhotoEmission Spectroscopy (PES) is a general term which refers to all the techniques based on the *photoelectric effect* originally observed by Hertz (1887), among them Ultraviolet Photoelectron Spectroscopy (UPS), X-ray

Photoelectron Spectroscopy (XPS), and Angle-Resolved PhotoElectron Spectroscopy (ARPES) [1–3]. The *photoelectric effect* was later explained by Einstein (1905) as a manifestation of the quantum nature of light. PES technique uses photons of energy $\hbar\omega$ impinging upon a surface and unbinding electrons from the system with a maximum kinetic energy of $\hbar\omega - \phi$, where ϕ is the work function¹. It is not a characteristic of a bulk material, but rather a property of the surface of the material. The light, impinging on the sample, excites electrons which are collected by an electrostatic analyser as a function of their kinetic energy E_{kin} and momentum \mathbf{p} . Knowing both the photon energy and work function it is possible to extract the binding energy E_B of electrons using Einstein equation:

$$E_{kin} = \hbar\omega - \phi - E_B \tag{A.1.1}$$

The momentum \mathbf{p} of the outgoing electrons could be extracted from kinetic energy:

$$E_{kin} = \frac{p^2}{2m} \quad p = \sqrt{2mE_{kin}} \tag{A.1.2}$$

An important aspect of PES is the energy of the incoming photons. By changing the photon energy, one can use PES technique to examine core-levels (in the X-ray regime, 100 eV up to > 1000 eV) or valence energy levels (ultraviolet regime, from 5 eV to 100 eV, Ultraviolet Photoemission Spectroscopy - UPS). In the energy range of 50 - 100 eV, the *escape depth of the electrons* is only a few Å, as shown in Fig. A.1, so the electrons are mainly extracted from the surface. Since we are interested in investigating the surface of materials, we need to work at the minimum of the curve using the correspondent energy.

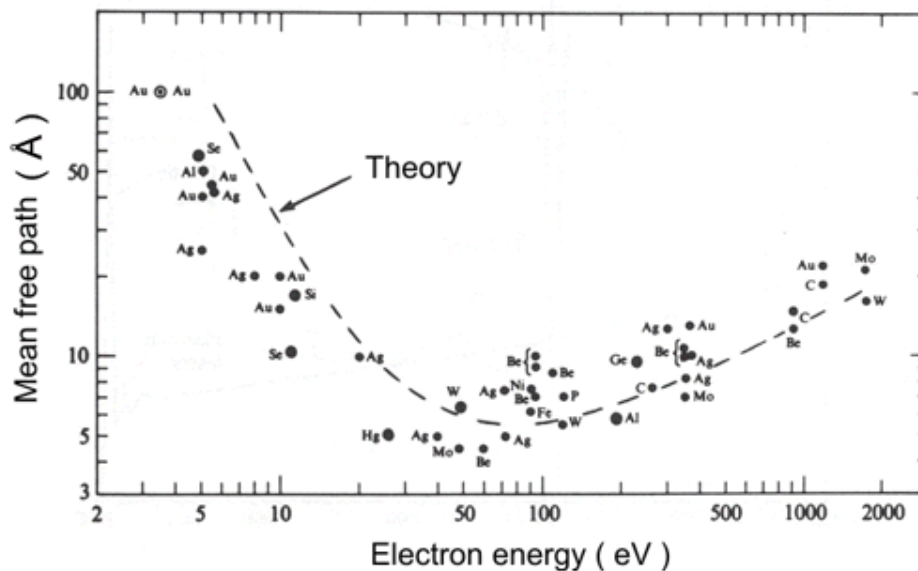


Figure A.1: Electron mean free path as a function of kinetic energy for various metals. The curve has a minimum at about 6 Å for kinetic energies of 50 - 100 eV.

Working with electrons requires an excellent vacuum. The Ultra-High Vacuum (UHV)

¹Work function represents the minimum thermodynamic energy needed to remove an electron from a solid to a point in the vacuum immediately outside the solid surface.

is mandatory in order to perform PES experiments. The investigation of surface states or adsorbed molecules requires UHV condition to prevent interferences from adsorbed contaminants. Photoemission techniques are therefore performed in UHV chambers in order to obtain and analyse a clean surface and to ensure that gas molecules do not scatter the low energy photoemitted electrons.

A.2 Angle-resolved Photoemission Spectroscopy

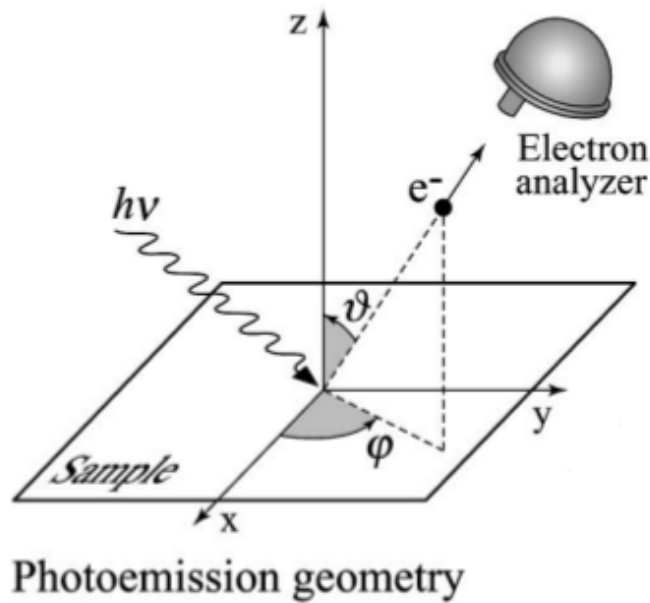


Figure A.2: Geometry of an ARPES experiment: the direction of the emitted photoelectron is specified by the polar θ and azimuthal ϕ angles. Figure adapted from Ref. [4].

A typical ARPES experiment is illustrated in Fig. A.2: a beam of monochromatized radiation, $h\nu$, produced by a light source, such as a gas-discharge lamp or a synchrotron beamline, impinges on the sample and electrons are emitted by photoelectric effect [4, 5]. The direction of the emitted photoelectron is specified by the polar θ and azimuthal ϕ angles. It is necessary to work in a vacuum sufficiently rarefied (typically better than 10^{-10} Torr) to increase the mean free path of electrons and to secure the sample cleaning from residual gas atoms and molecules. Photoelectrons escape from the surface, propagate into the vacuum and are collected by an electron energy analyzer characterized by a finite acceptance angle. The relevance of the θ angle becomes clear when the photoelectron wave vector \mathbf{k} is decomposed into its parallel and orthogonal (to the surface normal) components:

$$\mathbf{k} = \mathbf{k}_{\parallel} + \mathbf{k}_{\perp} = \begin{cases} \mathbf{k}_{\parallel} = \frac{1}{\hbar} \sqrt{2mE_{kin}} \sin \theta \\ \mathbf{k}_{\perp} = \frac{1}{\hbar} \sqrt{2mE_{kin}} \cos \theta \end{cases} \quad (\text{A.2.1})$$

The components of the photoelectron wave vector are related to the electron kinetic energy

E_{kin} , which is one of the experimental accessible quantity, and to the θ angle, also experimentally defined. The component parallel to the surface of the electron crystal momentum is given by:

$$\mathbf{p}_{\parallel} = \hbar \mathbf{k}_{\parallel} = \sqrt{2mE_{kin}} \sin \theta \quad (\text{A.2.2})$$

It is important to take note that \mathbf{k}_{\perp} component is not conserved across the sample surface because there is no translational symmetry along the surface normal. This implies that the experiments do not give a complete determination of the total crystal wave vector \mathbf{k} . The electronic dispersion is then almost exclusively determined by \mathbf{k}_{\parallel} as in the case of the 2D system. We have sufficient informations to map out in detail the electronic dispersion relation $E(\mathbf{k}_{\parallel})$ by tracking the energy position of the peaks detected in the ARPES for different angles as a function of \mathbf{p}_{\parallel} . The azimuthal angle ϕ represents the rotation angle with respect to the surface normal of the sample and from its value one can determine the reciprocal space direction. ARPES experiment allows to obtain a mapping of the photoelectron intensity as a function of the parallel momentum of the electron in the surface, along a defined space direction, and its binding energy E_B .

Because of the number of interacting particles is on the order of Avogadro's constant ($N \simeq 10^{23} \text{ mol}^{-1}$), the description of the photoemission process is very tricky; there are some models that helps us to describe the process: *Three-step model* and *One-step model*. The *One-step model* provides a more realistic picture of the photoemission process in which photon absorption, electron removal and detection are treated as a single process. The Hamiltonian will include bulk, surface and vacuum terms and it involves also many-body effects, self-energy and relativistic corrections, etc. However, the most intuitive approach is the *Three-step model*. The steps are (i) photoexcitation of electrons, (ii) transport to the surface and (iii) escape of photoelectrons.

In evaluating the first step and therefore photoemission intensity, it is necessary to calculate the transition probability w_{fi} between the N -electron ground state Ψ_i^N and one possible final states Ψ_f^N using *Fermi's golden rule*:

$$w_{fi} = \frac{2\pi}{\hbar} |\langle \Psi_f^N | H_{int} | \Psi_i^N \rangle|^2 \delta(E_f^N - E_i^N - \hbar\omega) \quad (\text{A.2.3})$$

where $E_i^N = E_i^{N-1} - E_B^{\mathbf{k}}$ and $E_f^N = E_f^{N-1} + E_{kin}$ are the initial and final-state energies of the N -particle system. The delta $\delta(E_f^N - E_i^N - \hbar\omega)$ ensures the conservation of energy E during the photoemission process. In the initial-state energy we take into account the binding energy $E_B^{\mathbf{k}}$ of the electron (with momentum \mathbf{k}), while in the final-state the term of kinetic energy E_{kin} of photoelectron appears. The interaction Hamiltonian operator ² has the following form:

$$H_{int} = -\frac{e}{mc} \mathbf{A} \cdot \mathbf{p} \quad (\text{A.2.4})$$

²The interaction with photon is treated as a perturbation

where \mathbf{A} is the electromagnetic vector potential and \mathbf{p} is the electronic momentum operator. We are working in the Coulomb gauge³ and we are using the commutator relation $[\mathbf{p}, \mathbf{A}] = 0^4$.

After excitation, we assume a *sudden approximation*⁵, so that we can factorize the final state term Ψ_f^N as the product of the final state wave function of the $(N-1)$ -electrons system Ψ_f^{N-1} and the wave function of the escaped electron $\phi_f^{\mathbf{k}}$ with momentum \mathbf{k} :

$$\Psi_f^N = A \phi_f^{\mathbf{k}} \Psi_f^{N-1} \quad (\text{A.2.5})$$

A is an antisymmetric operator which ensures that the Pauli principle is satisfied. It is worth noting that the final state Ψ_f^{N-1} is one of the m excited final states Ψ_m^{N-1} with energy E_m^{N-1} . The total transition probability is given by the sum over all possible m final excited states. We assume that Ψ_i^N is a Slater determinant (i.e. Hartree-Fock formalism), so the initial state can be factorized as the product of one-electron orbital $\phi_i^{\mathbf{k}}$ and the $(N-1)$ -particles term:

$$\Psi_i^N = A \phi_i^{\mathbf{k}} \Psi_i^{N-1} \quad (\text{A.2.6})$$

At this point the matrix element in Eq. A.2.3 can be written as:

$$\langle \Psi_f^N | H_{int} | \Psi_i^N \rangle = \langle \phi_f^{\mathbf{k}} | H_{int} | \phi_i^{\mathbf{k}} \rangle \langle \Psi_m^{N-1} | \Psi_i^{N-1} \rangle \quad (\text{A.2.7})$$

where $\langle \phi_f^{\mathbf{k}} | H_{int} | \phi_i^{\mathbf{k}} \rangle \equiv M_{f,i}^{\mathbf{k}}$ is the one-electron dipole matrix element and $\langle \Psi_m^{N-1} | \Psi_i^{N-1} \rangle$ is the $(N-1)$ electron overlap integral. In Eq. A.2.7 the Ψ_f^N has been replaced with Ψ_m^N as mentioned before.

ARPES detector will measure the intensity current proportional to the transition probability, i.e.:

$$I(\mathbf{k}, E_{kin}) \propto \sum_{f,i} |M_{f,i}^{\mathbf{k}}|^2 \sum_m |c_{m,i}|^2 \delta(E_{kin} + E_m^{N-1} - E_i^N - \hbar\omega) \quad (\text{A.2.8})$$

$|c_{m,i}|^2 = \left| \langle \Psi_m^{N-1} | \Psi_i^{N-1} \rangle \right|^2$ is the probability for an electron to be excited from an initial state i to a final state m .

In the *non-interacting particles* case, it can be assumed that $\Psi_i^{N-1} = \Psi_{m_0}^{N-1}$ for a particular state $m = m_0$; the value of $|c_{m,i}|^2$ is 1 and the other $c_{m,i}$ terms are zero: consequently, see Fig. A.3(a), we can see in ARPES spectra a delta function at the energy $E_B^{\mathbf{k}}$ ⁶. This is a good

³In this model, the gauge with $\Phi = 0$ for the scalar potential was chosen. The quadratic term of \mathbf{A} can be neglected in the linear optical regime.

⁴The commutator relation is $[\mathbf{p}, \mathbf{A}] = -i\hbar \nabla \cdot \mathbf{A}$ that is zero if $\nabla \cdot \mathbf{A} = 0$, which is the case of the coulomb gauge.

⁵The relation between the time scale of the process τ and the typical energy splittings among the energy levels involved in transition ΔE is $\tau \ll \hbar / \Delta E$. It means that the electron is instantaneously removed and there is no interaction between the photoelectron and the system left behind. The sudden approximation is not appropriate for low kinetic energy photoelectrons. In this case Ψ_f^N can not be factorized into two independent terms: *adiabatic limit*.

⁶We assume that $N - 1$ electrons in the final state have the same spatial distribution and the same energy

approximation but we need to take into account the $N-1$ electrons after photoemission. In the case of *strongly correlated system* many of $|c_{m,i}|^2$ terms are different from zero because Ψ_i^{N-1} will overlap with many Ψ_m^{N-1} states. The ARPES spectra show not only a single delta function but a main line with some satellite peaks, Fig. A.3(b).

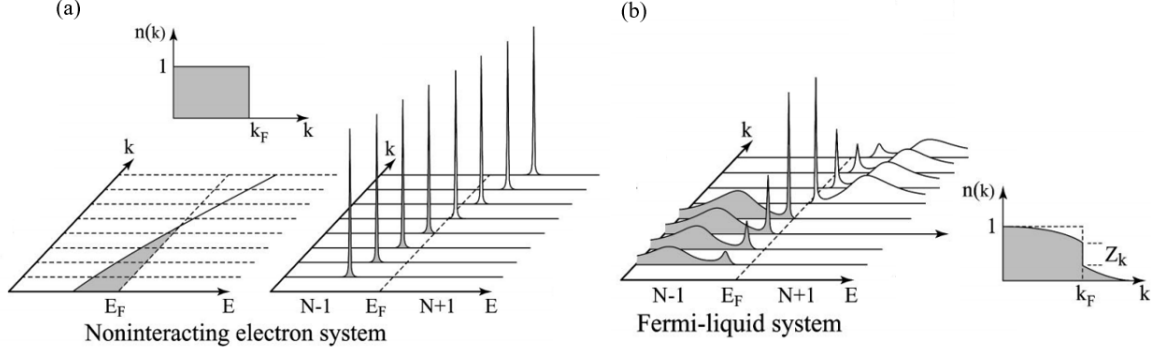


Figure A.3: (a) Non-interacting particle system. We can observe delta function at the corresponding energy E_B . The groundstate (at $T=0$ K) momentum distribution function $n(\mathbf{k})$ is also reported. (b) An interacting Fermi-liquid system with momentum distribution. Figure adapted from Ref. [4].

A general treatment of process which takes into account the interaction between electrons is based on the *Green's-function formalism* in energy-momentum representation⁷; the one-electron addition and removal Green's function has the following form:

$$G^\pm(\mathbf{k}, \omega) = \sum_m \frac{|\langle \Psi_m^{N\pm 1} | c_{\mathbf{k}}^\pm | \Psi_i^N \rangle|^2}{\omega - E_m^{N\pm 1} + E_i^N \pm i\eta} \quad (\text{A.2.9})$$

The operators $c_{\mathbf{k}}^\pm$ create/annihilate an electron with energy ω and momentum \mathbf{k} (note that $\hbar = 1$) and the sum runs over all the possible $(N \pm 1)$ -particles eigenstates $\Psi_m^{N\pm 1}$ with eigenvalue $E_m^{N\pm 1}$ and η is a positive infinitesimal number.

We can introduce the *one-particle spectral function*⁸ which is related to the imaginary part of Green's function:

$$A(\mathbf{k}, \omega) = -\frac{1}{\pi} \text{Im} G(\mathbf{k}, \omega) \quad (\text{A.2.10})$$

Our interest is on the one-electron removal term $A^-(\mathbf{k}, \omega)$, as it refers to the photoemission process; using this we can rewrite the photocurrent:

$$I(\mathbf{k}, \omega) = I_0(\mathbf{k}, \nu, \mathbf{A}) A^-(\mathbf{k}, \omega) f(\omega) \quad (\text{A.2.11})$$

that had before electron emission: *frozen-orbital approximation*. Therefore their binding energy is equal to the orbital energy (changing in sign) $E_B^k = -\epsilon_k$. This is the Koopmans' theorem which, however neglects the electron relaxation and relativistic effects.

⁷The propagation of the electron in many-body system is described by the time-ordered one-electron Green's-function $G(t-t')$: it represents the amplitude probability that an electron in a Bloch state, with momentum \mathbf{k} , stay in the same state after a time $|t-t'|$. By taking the Fourier transform $G(t-t')$ can be expressed in energy-momentum representation: $G(\mathbf{k}, \omega)$

⁸ $A^\pm(\mathbf{k}, \omega) = \sum_m |\langle \Psi_m^{N\pm 1} | c_{\mathbf{k}}^\pm | \Psi_i^N \rangle|^2 \delta(\omega - E_m^{N\pm 1} + E_i^N)$

$\mathbf{k}=\mathbf{k}_{\parallel}$ is the in-plane electron momentum (2D system), $I_0(\mathbf{k}, \nu, \mathbf{A})$ is proportional to the matrix element⁹ $|M_{f,i}^{\mathbf{k}}|^2$; we introduced also the *Fermi function* which assures that the photoemission probes only the occupied electronic states:

$$f(\omega) = \frac{1}{e^{\omega/k_B T} + 1} \quad (\text{A.2.12})$$

Rearranging the eq. A.2.10, by integration on complex plane, we obtain:

$$A(\mathbf{k}, \omega) = -\frac{1}{\pi} \delta(\epsilon - E_B^{\mathbf{k}}) \quad (\text{A.2.13})$$

The electron-electron correlations can be introduced as a correction term to the Green's function. By introducing the *complex self energy*¹⁰, we can express Green's function and spectral function as follow:

$$G(\mathbf{k}, \omega) = \frac{1}{\omega - \epsilon_{\mathbf{k}} - \Sigma(\mathbf{k}, \omega)} \quad (\text{A.2.14})$$

$$A(\mathbf{k}, \omega) = -\frac{1}{\pi} \frac{\Sigma''(\mathbf{k}, \omega)}{[\omega - \epsilon_{\mathbf{k}} - \Sigma'(\mathbf{k}, \omega)]^2 + [\Sigma''(\mathbf{k}, \omega)]^2} \quad (\text{A.2.15})$$

where $\epsilon_{\mathbf{k}}$ is the electron binding energy. Now we are able to express the total formula for the intensity:

$$I(\mathbf{k}, \omega) \propto |M_{f,i}^{\mathbf{k}}|^2 A(\mathbf{k}, \omega) f(\omega) \quad (\text{A.2.16})$$

In conclusion, the intensity current results proportional to: (i) the matrix element $|M_{f,i}^{\mathbf{k}}|^2$, which depends on experimental geometry and on energy and polarization of impinging radiation; (ii) the spectral function $A(\mathbf{k}, \omega)$, which represents the probability to extract an electron with energy ω and momentum \mathbf{k} from a system of N -electron and it reproduces the density of states, i.e. the band structure; (iii) $f(\omega)$ that is the Fermi-Dirac distribution: it determines the statistical distribution of electrons and take into account that direct photoemission can measure only occupied electronic states.

A.3 Experimental ARPES setup

In the following section we briefly discuss the main part of an ARPES experimental setup. Despite the differences that may exist between various experimental setups aimed to perform ARPES measurements, we can recognize some common fundamental elements:

- **Photon sources:** typical photon sources for ARPES experiments are discharge lamp, synchrotron radiation (see section A.4) and laser. The most common discharge lamp is the He lamp¹¹, with the main He I α (21.2 eV), He I β (23.1 eV) and He II α (40.8 eV)

⁹This term depends on the electron momentum and on the energy polarization of the incoming photon.

¹⁰ $\Sigma(\mathbf{k}, \omega) = \Sigma'(\mathbf{k}, \omega) + i\Sigma''(\mathbf{k}, \omega)$: real and imaginary parts contain all the information on the energy renormalization and lifetime of an electron with banding energy $\epsilon_{\mathbf{k}}$ and momentum \mathbf{k} .

¹¹The gas inside of the lamp, in this case He, was ionized by high voltage or microwave radiation generating plasma; the excited ions have enough time to relax back to ground state and they emit photons with discrete energies, depending on the used gas.

emission lines. He lamp has one important disadvantage, i.e. the inability of tuning the photon energy; such obstacle that has been overcome by the advent and using of synchrotron radiation, which instead extends over a broad energy range.

- **Vacuum system:** in ARPES experiments, the sample can be prepared *ex-situ* or *in-situ*; those prepared *ex-situ* must be cleaved inside the chamber in order to obtain a fresh and clean surface. Indeed UHV conditions are mandatory to ensure the cleaved surface and also a sufficient free path for the emitted electrons. The interconnected chambers work in UHV conditions, and these conditions are kept by using different pumping systems, such as: scroll pump, turbo-molecular and ion pump. The combination of these pumps provides the ideal pressure required for ARPES measurements (in the order of 10^{-10} Torr).
- **Sample manipulator:** the beamline designer can choose how the sample should move with respect to the incident radiation and/or the detector. In some case the manipulators achieve the maximum flexibility as it possesses 6 degrees of freedom (3 rotational and 3 translational). Generally the manipulator is also equipped with a cooling system, such as a cryostat, and a thermostat to read the sample temperature.
- **Analyser:** the electrons emitted by photoelectric effect pass through the vacuum chamber until they reach the analyser. According to the direction or cut of the entrance slit, the analyser will take the data; then, the electrons enter two concentric inner hemispheres which act as capacitor and deflect the electrons path. The pass energy determines the central energy that the analyser will read; it is a kind of retarding parameter that alter the electrons kinetic energy but not their distribution.

A.4 Introduction to Synchrotron radiation

When electrons or charged particles, moving with speed close to c , and forced to magnetic field to follow curved trajectories, they emit electromagnetic radiation with peculiar characteristics (in the direction of their motion) known as *Synchrotron radiation*. Such radiation is extremely intense and extend over a broad energy range, from IR through visible and ultraviolet, up to soft and hard x-ray region. Synchrotron radiation was first observed in 1946 by Elder et al. [6, 7], and then theoretically described by Schwinger [8]. The sources of this radiation are accelerators like storage rings; they consist of evacuated pipes where electrons are forced to move along the circular path under the action of magnets (bending magnets). The optimization of the radiation sources led to the realization of new synchrotron radiation sources, the so called *third generation sources*¹². Synchrotron radiation produced by sources of third generation represents the most used coherent light source for physics

¹²The first generation of synchrotron radiation sources were realized and optimized for high energy physics; these sources were not dedicated to synchrotron radiation studies; the second generation facilities were dedicated for this purpose with the use of magnetic field devices.

matter¹³; the main difference compared to the older sources is the usage of *wigglers* and *undulators* which increase the brightness by a factor N and N^2 respectively (N is the number of magnetic periods).

While improvements in third generation sources are still possible; fourth generation sources are being developed, mainly based on free electron lasers (FELs), sources able to produce very short light pulses of high intensity and brightness, and on diffraction-limited storage rings (DLSR), which operate in the soft to hard x-ray range 8100 eV - 100 keV with extremely high brilliance (10^{21} - 10^{22} photons/s/mm²7mrad²/0.1%BW) [9–11]. Fourth generation light sources are characterized by a relative high coherent flux (order of 10^{14} - 10^{15} photons/s/0.1%BW for DLSR) [12].

The main properties of synchrotron radiation are:

- Continuous emission spectrum from infra-red to hard x-ray;
- High brilliance that reaches values like 10^{20} ph s⁻¹ mrad⁻² mm⁻² (0.1% BW)⁻¹ ¹⁴;
- Highly collimated photon beam;
- High polarized beam;
- Pulsed temporal structure.

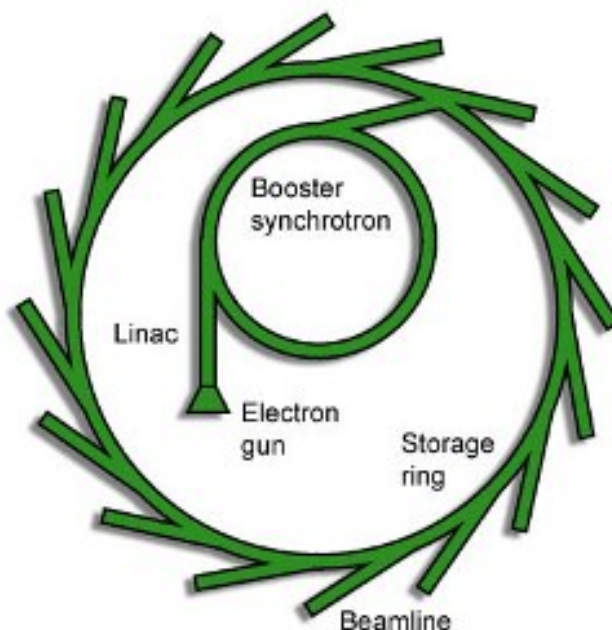


Figure A.4: Schematic representation of a synchrotron radiation light source.

¹³The coherent fraction of the light produced by an undulator depends by energy and the characteristic of the source, and even in the most advanced light sources is far from being 100% coherent.

¹⁴It takes into account number of photons produced per second, the angular divergence and the cross-sectional area of the beam and the bandwidth (BW) of 0.1%. The formula is $\text{brilliance} = \frac{n_{\text{photons}}}{\text{s mrad}^2 \text{ mm}^2 0.1\% \text{ BW}}$. The value obtained in synchrotron radiation sources is 10^{12} times greater than brilliance of common sources.

A schematic Synchrotron Radiation source, represented in Fig. A.4, basically consists of following components:

- **Electron gun:** electrons are produced here. There is the cathode that is heated up until it reaches a temperature at which electrons are released from its surface: this is called thermionic emission.
- **Linac:** linear accelerator is the place where they are accelerated to a speed close to c ¹⁵ using energy provided by microwave radio frequency fields. Electrons are not slowed down by collision with atoms or molecules since they are in vacuum.
- **Booster ring:** as the electrons are accelerated to the required speed they are put into a circular ring called Booster ring. The shape of the ring is not a perfect circle but it is like an N-polygon where each section is connected to the other by bending magnets. Electrons are accelerated in the straight sections (using radio waves) and the energy are boosted from about 250 MeV to 2 GeV up to 6 GeV. Booster ring increase the speed of electrons about 99:9999985% of c by means radio frequency (RF) cavity.
- **Storage ring:** this is the main ring. An injection system transfers the electrons from Booster to Storage ring. The shape of this storage ring is once again a N-polygon made of short straight sections joined together at an angle. This structure is equipped by undulators and wigglers. In this section, electrons energy is compensated for the loss they experience in the light production process. The top-up mode, responsible for the continuous refill of electrons in the storage ring, compensates the loss of electrons due to scattering with residual gas molecules in the pipes and their consequent loss of trajectory. Due to this process, it is possible to give constant light at each beamline.
- **Beamline:** this is the part where X-ray will be manipulate and used for experiments. After the undulators, the light beam is refined by monochromators, silicon mirrors, slits and crystals (used as a filter) and finally shine on the sample¹⁶. By varying the parameters of these devices, the users can select the wavelength required for the experiments.

The ARPES experiments reported in this thesis have been performed mainly on VUV and APE beamline of Elettra Synchrotron radiation source situated in the AREA Science Park of Trieste, Italy. The description of the beamlines will be reported in next subsections, A.4.1 and A.4.2. Below there are some specifications on Elettra radiation source.

Elettra is the third generation storage ring operating since October 1993. The storage ring has been optimized to produce radiation from UV to hard X-rays with spectral brightness of up to 10^{19} ph s⁻¹ mrad⁻² mm⁻² (0.1% BW)⁻¹. Elettra consists of a small Linac (66 meters of length), and a Booster ring that accelerates and injects electrons at the final energy of 2 GeV

¹⁵Electrons enter the Linac at a velocity of $0.6c$ and they are emitted with speed very close to the speed of light.

¹⁶There are some conditioning devices which are used for check the thermal load (heating caused by the beam) and devices which absorb significant power from the beam may need to be cooled by water, or liquid nitrogen.

and 2.4 GeV. The Linac operates at the frequency of 3 GHz and it produces electrons bunches of 5.4 mm or 7 mm of length: it depends on the operative modality. The temporal distance between bunches is 2 ns and the maximum number of bunches is 432. The circumference of storage ring is 259.2 m and there are 12 groups of bending magnet and 11 section for insertion devices. There are also 4 resonant cavity with the aim to provide the beam of the energy lost because of the electromagnetic energy emission. Currently there are 30 experimental stations sharing 27 beamlines.

A.4.1 VUV beamline

The VUV Photoemission beamline at Elettra is a photoemission dedicated beamline. It is mainly addressed to surface and solid state experiments by high resolution photoemission. In particular the following types of experiments can be carried out:

- Band mapping by high energy and angle-resolved photoemission;
- High resolution photoemission on core levels and valence band;
- Photoelectron diffraction.

The light source is an undulator which provides an energy range from 20 eV to 750 eV; the minimum energy for 2.4 GeV of energy ring is about 25 eV. The undulator consists of 36 periods and the high energy part of the spectrum is like a wiggler, i.e. continuous and fairly smooth. The measured flux goes to $1.4 \cdot 10^{13}$ to $5 \cdot 10^{10}$ ph s⁻¹ (0.1% BW)⁻¹ 200 mA, in a spot of maximum size 0.5 mm, for energies between 100 eV and 900 eV. The Spherical Grating Monochromator has five interchangeable gratings for pre- and post-focusing optics. VUV is equipped with five evaporation sources, two of them can be replaced without venting the chamber and the other three are mounted directly inside.

The VUV photoemission end station consists of several interconnected vacuum chambers:

- **Heating station:** it operates in 10^{-10} mbar regime. The load lock allows easy insertion of samples; the chamber is dedicated to high temperature annealing up to 2000 ° C by electron bombardment. High pressure treatment are also possible up to 10^{-2} mbar of oxygen. In case of no high temperature or pressure treatments, it can be used as a sample parking hosting up to 3 samples.
- **Preparation chamber:** the base pressure is 2×10^{-10} mbar. The sample can be cooled down to 100 K and heated up to 500 K. It is equipped with some facilities such as LEED, quartz microbalance, mass analyzer, sputter gun and evaporators. The manipulator has five degrees of freedom (no azimuthal rotation).
- **Measurement chamber:** the base pressure is about 10^{-11} mbar. The motorized vertical manipulator, with 5 degree of freedom¹⁷, allows to acquire automatically Fermi surfaces with an angle step less than 0.01° and angular range $\pm 160^\circ$. The Helium closed-cycle

¹⁷The stage (Vab Vacuum) allows linear motion along the X, Y, and Z axes and polar rotation (360° with 0.2° accuracy) and the azimuthal rotation is made possible through piezoelectric rotary stage.

cryostat allows to work in temperature range from 9 to 450 K. The electron analyser is a **Scienta R4000-WAL** with variable acceptance angle (7 – 30 degrees) and it is mounted at 45 ° with respect to the beam direction.

More information are available in Ref. [13].

A.4.2 APE beamline

The Advanced Photoelectric Effect (APE) beamline is a facility dedicated for advanced spectroscopies. It comprises two distinct beamlines, low and high energy end station, using radiation in the ultraviolet and soft X-ray range. The UHV interconnected chambers include facilities for sample preparation and characterization, such as Ar ion sputtering, annealing, controlled evaporation, LEED and Auger. It is also possible to perform, on the same surface, atomic resolution Scanning Tunneling Microscopy (STM). The low energy beamline hosts VG-Scienta DA30 analyzer which has been completed by VESPA (Very Efficient Spin Polarization Analysis) in order to perform spin-resolved ARPES¹⁸. The APE low-energy beamline (APE-LE) covers 8-120 eV photon energy range. The high energy dedicated branch (APE-HE) covers 150-1600 eV photon energy range, suitable for soft-X-ray absorption (XAS), magnetic dichroism (XMCD, XMLD) and X-ray photoelectron spectroscopy (XPS). APE beamline has also specific chambers for sample growth which are directly connected to off-beam and on-beam facilities. Both end stations are equipped with cryostats: the minimum sample temperature is 16 K at APE-LE and 30 K at APE-HE. More details and information about the beamline are available in Ref. [14].

A.5 Time-resolved ARPES Spectroscopy

Standard ARPES technique has the ability to probe the equilibrium electronic band structure of materials in momentum space, as those studied in the present thesis; the related informations are contained in the *spectral function* $A(\mathbf{k}, \omega)$. Indeed, by measuring the momentum \mathbf{k} and kinetic energy of the photoemitted electrons we are able to obtain the energy-momentum dispersion of the investigated materials. The knowledge on the time evolution of the system is not allowed.

However, in order to obtain information on the time evolution of the electronic properties of materials, triggered by the photo-excitation process, a time resolved approach is needed. The use of ultra-short laser pulses allow the possibility to study the unfilled electronic states of materials and how electrons behave in time. So, combining ARPES with short wavelength high-harmonics (in order to drive the photoemission processes) it is possible to obtain a direct investigation of a wide range of electronic states and momenta; this is called time-resolved ARPES (TR-ARPES).

One of the first applications of TR-ARPES made use of a *pump-probe approach*, which is a method for perturbing the system with light and, after that, watching the response.

¹⁸It consists of two VLEED-based scattering chambers for the determination of spin direction of the photo-emitted electrons, becoming the first facility for spin-resolved ARPES at Elettra.

A schematic representation of the pump-probe setup is reported in Fig. A.5 and it will be explained in section A.5.1.

After the first pulse, the excited electrons get thermalized through relaxation processes that can be described by a hot-thermal distribution function: *Hot-Fermi Dirac Distribution*. As mentioned before, the photoemission intensity is proportional to the product $A(\mathbf{k}, \omega) f(\omega)$; in order to extend the formalism to the non-equilibrium approach we need to add the following approximations, besides the sudden approximation treated before: electron-electron interaction, responsible for e-e scattering processes, is faster than the duration of both the pump and probe pulses (~ 100 fs). If the conditions are both satisfied we can describe the evolution of the electronic states in energy and time domains separately; in this case the photoemission intensity results proportional to $A(\mathbf{k}, \omega, t) f(\omega, t)$, where t is the delay time and $f(\omega, t)$ the Hot-Fermi Dirac distribution.

For static ARPES, the conventional way to analyse the spectra in the momentum-energy domains is to extract the Energy Distribution Curves (EDCs), i.e. data at constant energy, and Momentum Distribution Curves (MDCs), data at constant momentum; in a TR-ARPES experiments this procedure must be extended for each time delay.

In chapter 4 the results obtained on Black Phosphorus by using time-resolved ARPES technique are presented.

A.5.1 Experimental TR-ARPES setup

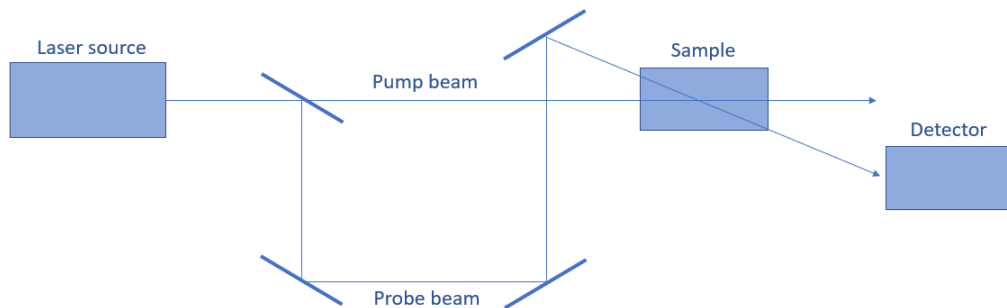


Figure A.5: Sketch of the pump-probe spectroscopy setup.

In this section, we report a schematic representation of the pump-probe setup. A first ultrashort pulse *pumps* the electrons into unfilled bands (or non-equilibrium states) and subsequently a second pulse *probes* them via photoemission. Such *pump-and-probe* sequence is repeated until a sufficient signal is accumulated. By changing the delay time δt with respect to the first pulse, i.e. the time between pump and probe pulses, the ARPES spectra can illustrate the evolution of excitation and relaxation dynamics up to the ground state of the investigated system, as we can observe in the example reported Fig. A.6. The delay time is controlled by changing the path length difference between the pulses: $dT = dX/c$ where dX is the path length difference; this is possible by changing geometry of the beamline through the placement of different mirrors.

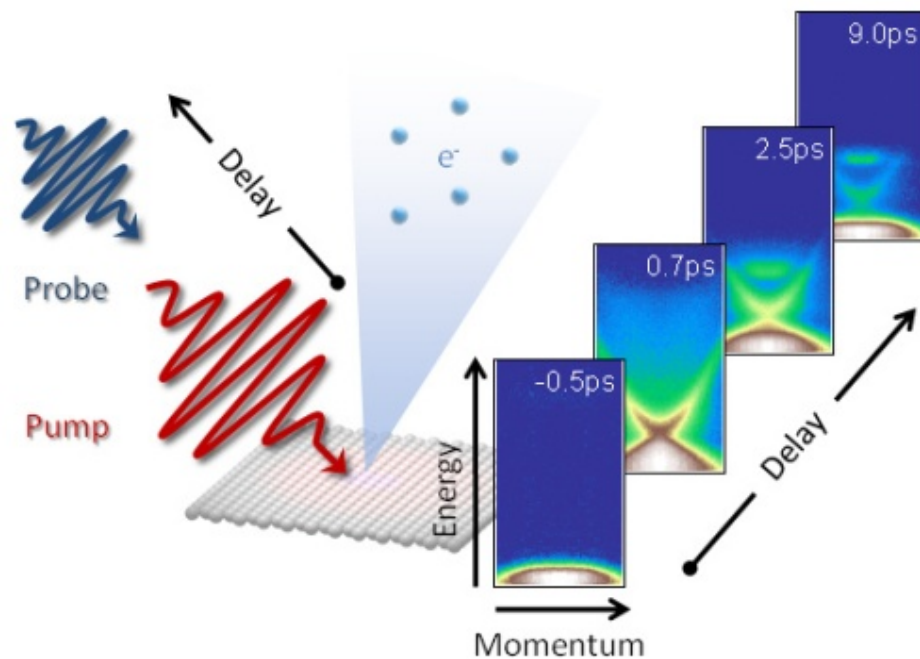


Figure A.6: Schematic representation of a time-resolved ARPES experiment. Figure extracted from Ref. [15].

More detailed analysis allows to obtain information on the electron-electron and electron-phonon coupling, in complementary way to the spectral analysis of standard ARPES data. It is clear that TR-ARPES extends and complements conventional ARPES by adding time-resolution.

A.5.2 ASTRA end station

The TR-ARPES experiments reported in chapter 4 were carried out at the ASTRA (ARPES Spectrometer for Time-Resolved Applications) end station of Harmonium beamline, at the Lausanne Centre for Ultrafast Science (LACUS) of the Ecole Polytechnique Fédérale de Lausanne (EPFL). TR-ARPES experiment requires pulsed laser sources providing ultra-short pulses with duration of about ~ 100 fs ($1 \text{ fs} = 10^{-15} \text{ s}$). However, owing to the technical difficulty of achieving high flux and stable harmonic generation, only a few VUV TR-ARPES instruments are operational until now.

Since detailed information of the laser source and of the Harmonium setup has been widely described in Ref. [16], here I provide some technical information about ASTRA end station, which allows to perform static and TR-ARPES measurements.

The linear polarization of the HHG can be either vertical (V) or horizontal (H); by selecting the polarization we can take advantage of polarization-dependent matrix elements during the photoemission experiment. The experiment has been performed in UHV condition; the HHG probe beam is focused on the surface of the sample with a spot size smaller than $100 \times 100 \mu\text{m}^2$. We used a Specs Phoibos 150 electrostatic hemispherical electron analyzer with angular resolution. The energy and angular resolution were set to 10 meV for static

ARPES and 0.3 degrees, respectively; for TR-ARPES experiments we used 120 meV energy resolution. The bandwidth of the HHG pulses has been estimated to be lower than 100 meV, which correspond to the temporal duration of 240 fs (for the grating of 900 gr/mm used in the presented experiments). It is particularly useful to determine the band structure (static ARPES) of the investigated materials prior to the TR-ARPES experiments; this could be done *in-situ* and on the same exposed surface because the ASTRA set-up is equipped with a He discharge lamp with a monochromator (Gammadata Burklint AB, Sweden) providing high-brilliance He I α and He II α emission lines of 21.2 eV and 40.8 eV, respectively. The pump at 800 nm was H polarized and the fluence on the sample surface was $\sim 0.5 \text{ mJcm}^{-1}$.

References

- [1] Stefan Hüfner. *Photoelectron Spectroscopy*. Springer Berlin Heidelberg, 2003. DOI: 10.1007/978-3-662-09280-4.
- [2] Hans Lüth. *Surfaces and Interfaces of Solid Materials*. Springer Berlin Heidelberg, 1995. DOI: 10.1007/978-3-662-03132-2.
- [3] Phil Woodruff. *Modern Techniques of Surface Science*. Cambridge University Press, 2016. DOI: 10.1017/cbo9781139149716.
- [4] Andrea Damascelli, Zahid Hussain, and Zhi-Xun Shen. “Angle-resolved photoemission studies of the cuprate superconductors”. In: *Reviews of Modern Physics* 75.2 (Apr. 2003), pp. 473–541. DOI: 10.1103/revmodphys.75.473.
- [5] Haifeng Yang, Aiji Liang, Cheng Chen, Chaofan Zhang, Niels B. M. Schroeter, and Yulin Chen. “Visualizing electronic structures of quantum materials by angle-resolved photoemission spectroscopy”. In: *Nature Reviews Materials* 3.9 (Aug. 2018), pp. 341–353. DOI: 10.1038/s41578-018-0047-2.
- [6] F. R. Elder, A. M. Gurewitsch, R. V. Langmuir, and H. C. Pollock. “Radiation from Electrons in a Synchrotron”. In: *Physical Review* 71.11 (June 1947), pp. 829–830. DOI: 10.1103/physrev.71.829.5.
- [7] F. R. Elder, R. V. Langmuir, and H. C. Pollock. “Radiation from Electrons Accelerated in a Synchrotron”. In: *Physical Review* 74.1 (July 1948), pp. 52–56. DOI: 10.1103/physrev.74.52.
- [8] Julian Schwinger. “On the Classical Radiation of Accelerated Electrons”. In: *Physical Review* 75.12 (June 1949), pp. 1912–1925. DOI: 10.1103/physrev.75.1912.
- [9] *International Year of Light*. Web page. <http://www.light2015.org/>.
- [10] *Lightsources.org*. Web page. <http://www.lightsources.org/>.
- [11] *The european lightsources single entry point: way for light*. Web page. <http://www.wayforlight.eu/>.
- [12] I. A. Vartanyants and A. Singer. “Coherence Properties of Third-Generation Synchrotron Sources and Free-Electron Lasers”. In: *Synchrotron Light Sources and Free-Electron Lasers: Accelerator Physics, Instrumentation and Science Applications*. Cham: Springer International Publishing, 2018, pp. 1–38.
- [13] *VUV beamline*. Web page. <https://www.elettra.trieste.it/it/lightsources/elettra/elettra-beamlines/vuv/vuv.html>.
- [14] *APE beamline*. Web page. <http://www.elettra.trieste.it/elettra-beamlines/ape.html>.
- [15] *Stanford. Shen Laboratory*. Web page. <https://arpes.stanford.edu/research/tool-development/time-resolved-arpes>.

- [16] J. Ojeda, C. A. Arrell, J. Grilj, F. Frassetto, L. Mewes, H. Zhang, F. van Mourik, L. Poletto, and M. Chergui. “Harmonium: A pulse preserving source of monochromatic extreme ultraviolet (30–110 eV) radiation for ultrafast photoelectron spectroscopy of liquids”. In: *Structural Dynamics* 3.2 (Oct. 2015), p. 023602. DOI: 10.1063/1.4933008.

This chapter contains conclusive remarks, and summarizes the main results of the work thesis.

The first part of my work, Chapter 1, is focused on the study of a class of Topological Insulators. We proved that a tailoring of the topological states is possible by controlling either the stoichiometry and the atomic composition of the compounds. Starting from topological insulators with the same atomic composition and different stoichiometry, our combined theoretical and experimental investigations were addressed to shed light on the effect of stoichiometry on the band structure of the compounds. Following, the comparison between compounds with same stoichiometry and different atoms, proves that it is possible to built a topological insulator with the desired properties and to obtain a tailoring of the topological states and related electronic properties. Our investigation proves the high potential of this family of compounds for novel topological phenomena which require the tunability of the Dirac states.

In Chapter 2, the electronic band structures of different graphene-based systems have been reported. Starting from the study of the magnetic coupling between different ferromagnetic metals, we proved a shielding effect of a graphene layer towards FM clusters. We focused also on the study of the electron quantum confinement effects of Ag-film underneath a graphene layer and we proved that the growth of uniform films with well-defined electronic states is possible. In the last part of the chapter, I reported some measurements on a work in progress focused on the interaction between graphene and a $4f$ rare-earth metal.

Concerning Chapter 3, the electronic investigation of InSe and GaSe layered semiconductors have been reported; since the properties of this class of materials strongly depend on their structure, we started from the crystal structure and morphology. Indeed we proved

that by crossing the experimental results obtained from different techniques, it is possible to unambiguously discern between similar polytypes. Further, we have investigated the main differences between InSe and GaSe, focusing on the valence band maximum (crucial for optical and optoelectronic applications) of the two compounds along main symmetry directions; we discussed also the effect of spin-orbit coupling and contributions from Se atoms and the different third group metal.

In Chapter 4 I have reported the results of Time- and Angle-Resolved PhotoElectron Spectroscopy investigations on Black Phosphorus, in order to study the out-of-equilibrium dynamics and to shed light on the electronic response to an ultrafast laser excitation; we observe that the effect of band gap renormalization can be induced by laser excitation. In the second part of the chapter I reported some preliminary measurements on the electronic investigation of SnSe, SnS and analogue compounds.

In the following paragraph, I report corresponding list of publications.

List of Publications

- "*Magnetic decoupling of ferromagnetic metals through a graphene spacer*",
I. Grimaldi, M. Papagno, L. Ferrari, P. M. Sheverdyeva, S. K. Mahatha, D. Pacilè and C. Carbone,
Journal of Magnetism and Magnetic Materials Volume **426**, 15 March 2017, Pages 440-443.
- "*Deep Insight Into the Electronic Structure of Ternary Topological Insulators: A Comparative Study of $PbBi_4Te_7$ and $PbBi_6Te_{10}$* ",
D. Pacilè, S. V. Eremeev, M. Caputo, M. Pisarra, O. De Luca, **I. Grimaldi**, J. Fujii, Z. S. Aliev, M. B. Babanly, I. Vobornik, R. G. Agostino, A. Goldoni, E. V. Chulkov and M. Papagno,
Physica Status Solidi - Rapid Research Letter Volume **12**, 10 October 2018, Page 1800341.
- "*Electron Confinement Effects in Silver Films Embedded between Graphene and Metallic Substrates*",
L. Ferrari, **I. Grimaldi**, P. M. Sheverdyeva, Asish K. Kundu, P. Moras, M. Papagno, C. Carbone and D. Pacilè,
Journal of Physical Chemistry C Volume **123**, 29 March 2019, Pages 9764-9769.
- "*Photocarrier-induced band-gap renormalization and ultrafast charge dynamics in black phosphorus*",
S. Roth, A. Crepaldi, M. Puppini, G. Gatti, D. Bugini, **I. Grimaldi**, T. R. Barrilot, C. A. Arrell, F. Frassetto, L. Poletto, M. Chergui, A. Marini and M. Grioni,
2D Mater. **6** (2019) 031001.
- "*Structural investigation of InSe layered semiconductors*",
I. Grimaldi, T. Gerace, M. M. Pipita, I. D. Perrotta, F. Ciuchi, H. Berger, M. Papagno, M. Castriota, and D. Pacilè,
Solid State Communications **311** (2020) 113855.

- "*Electronic band structure of three-dimensional topological insulators with different stoichiometry composition*",
I. Grimaldi, D. Pacilè, S. V. Eremeev, O. De Luca, A. Policicchio, P. Moras, P. M. Sheverdyaeva, A. Kumar Kundu, Z. S. Aliev, P. Rudolf, R. G. Agostino, E. V. Chulkov and M. Papagno,
Physical Review B., Accepted.
- "*Dirac cone structure of Europium-intercalated Graphene on Ni(111)*",
I. Grimaldi, G. Contini, A. K. Kundu, P. Moras, P. M. Sheverdajeva, N. Atodiresei, G. Bihlmayer, D. Pacilè, C. Carbone and L. Ferrari,
in preparation.
- "*Insight into the electronic structure of semiconducting ϵ -GaSe and ϵ -InSe*",
S. V. Eremeev, M. Papagno, **I. Grimaldi**, O. De Luca, L. Ferrari, Asish K. Kundu, P. M. Sheverdyaeva, P. Moras, G. Avvisati, A. Crepaldi, H. Berger, I. Vobornick, M. G. Betti, M. Grioni, C. Carbone, E. V. Chulkov, and D. Pacilè,
submitted to Physical Review B.

Manuscript not included in this thesis:

- "*Zinc(II) Tetraphenylporphyrin on Au(111) Investigated by Scanning Tunnelling Microscopy and Photoemission Spectroscopy Measurements*",
O. De Luca, T. Caruso, **I. Grimaldi**, A. Policicchio, V. Formoso, J. Fujii, I. Vobornik, D. Pacilè, M. Papagno and R. G. Agostino,
Nanotechnology 31 (2020) 365603.